REPORT DOCUMENTATION PAGE

Form Approved
OMB No. 0704-0188

1. AGENCY USE ONLY *(Leave blank)*	2. REPORT DATE	3. REPORT TYPE AND DATES COVERED
	7.Oct.03	DISSERTATION

4. TITLE AND SUBTITLE
"THE ROLE OF TERRAIN AND CONVECTION ON MICROFRONT FORMATION LEADING TO SEVERE LOW-LEVEL TURBULENCE"

5. FUNDING NUMBERS

6. AUTHOR(S)
MAJ CETOLA JEFFREY D

7. PERFORMING ORGANIZATION NAME(S) AND ADDRESS(ES)
NORTH CAROLINA STATE UNIVERSITY

8. PERFORMING ORGANIZATION REPORT NUMBER

CI02-1292

9. SPONSORING/MONITORING AGENCY NAME(S) AND ADDRESS(ES)
THE DEPARTMENT OF THE AIR FORCE
AFIT/CIA, BLDG 125
2950 P STREET
WPAFB OH 45433

10. SPONSORING/MONITORING AGENCY REPORT NUMBER

11. SUPPLEMENTARY NOTES

12a. DISTRIBUTION AVAILABILITY STATEMENT
Unlimited distribution
In Accordance With AFI 35-205/AFIT Sup 1

DISTRIBUTION STATEMENT A
Approved for Public Release
Distribution Unlimited

12b. DISTRIBUTION CODE

13. ABSTRACT *(Maximum 200 words)*

20031104 031

14. SUBJECT TERMS	15. NUMBER OF PAGES
	340
	16. PRICE CODE

17. SECURITY CLASSIFICATION OF REPORT	18. SECURITY CLASSIFICATION OF THIS PAGE	19. SECURITY CLASSIFICATION OF ABSTRACT	20. LIMITATION OF ABSTRACT

The Role of Terrain and Convection on Microfront Formation Leading to Severe Low-Level Turbulence

by

J.D. Cetola

A dissertation submitted to the Graduate Faculty of
North Carolina State University
in partial fulfillment of the
requirements for the Degree of
Doctor of Philosophy

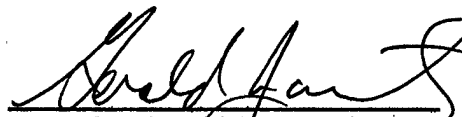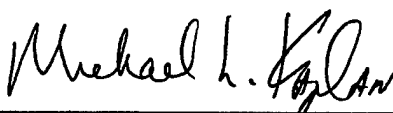## DEPARTMENT OF MARINE, EARTH, AND ATMOSPHERIC SCIENCES

Raleigh

2003

APPROVED BY:

_____
Dr. Allen J. Riordan

_____
Dr. Gerald S. Janowitz

_____
Dr. Michael L. Kaplan
Co-chair of Advisory Committee

_____
Dr. Yuh-Lang Lin
Co-chair of Advisory Committee

ABSTRACT

CETOLA, JEFFREY DAVID. The Role of Terrain and Convection on Microfront Formation Leading to Severe Low-level Turbulence.
(Under the direction of Yuh-Lang Lin and Michael L. Kaplan)

Two low-level convectively-induced turbulence (CIT) events east of the Appalachian Mountains are investigated utilizing observations, satellite, radar, and numerical simulations. Both events had an inordinate amount of low-level turbulence reported, but one event had more than twice as many severe or greater reports. The events were compared—to include the 72 hours leading up to the turbulence reports—and similarities and differences at the various scales from the synoptic to meso-α, meso-β, meso-γ, and microscale are noted. The case of weaker turbulence featured a meridional wave pattern with ridging over the East Coast and a single upper-level jet closely coupled with the large-scale frontal system. The stronger turbulence case possessed a zonal wave pattern with a vortex over eastern Canada and both a polar jet and subtropical jet. These differences are reflected in the low-level temperature and potential vorticity patterns and affected the hydraulic structures as well—with the stronger turbulence environment more prone to a blocking-type regime. Hydrostatic mountain waves were observed for both events. Stronger cross-mountain flow combined with a strong low-level leeside inversion resulted in a more vigorous mountain wave with a stronger downstream isentropic upfold (mid-level cold pool) in the stronger turbulence event. This mid-level cold pool was deformed by the large-scale jet resulting in a mid-level cold front (downstream from the surface cold front), surface pressure rises to the lee of the Allegheny Mountains, and ultimately a surface cold surge (edgewave) that merges with warm air from the south. The phasing of the mid-level cold pool and the convergence with the northerly cold surge

and southerly warm air results in kata-frontogenesis and cellular convection that transits the severe turbulence location in space and time. Convection in the weaker turbulence case was lineal in structure and tied to the large-scale cold anafront. Vorticity, enstrophy, turbulent kinetic energy, and Richardson number analyses indicated maxima were lineal in structure and upstream from the convection in the weaker case and arc-like in appearance and downstream from convection in the stronger case. A turbulence index was formulated based on three-dimensional vorticity (enstrophy), vertical wind shear, and static stability.

BIOGRAPHY

Major Jeffrey D. Cetola was born in Myrtle Beach, South Carolina. He graduated from J.E.B. Stuart High School in Falls Church, Virginia in 1984 and received a Bachelor of Science degree in Electrical Engineering from Clemson University in 1988.

He was commissioned a 2nd Lieutenant in the United States Air Force in December 1988 and was assigned to the Air Force Institute of Technology's Basic Meteorology Program. He completed the one-year program at Florida State University in 1989 and was assigned to Carswell Air Force Base, Texas as a Wing Weather Officer. In 1992, he was transferred to Royal Air Force Base Mildenhall, United Kingdom where he worked as chief of the Special Support Cell supporting aviation reconnaissance missions until July of 1995.

As a Captain, Jeff entered Florida State University in the Fall of 1995 where he earned a Master of Science degree in Synoptic Meteorology in 1997. His thesis work directly supported research efforts by the 45th Weather Squadron and was titled "A Climatology of the Sea Breeze at Cape Canaveral, Florida".

In 1997, he was assigned to the newly relocated Air Force Combat Climatology Center in Asheville, North Carolina. He served as Chief, Climatological Applications Team where he was responsible for all specially-tailored climatological support.

As a Major, he entered North Carolina State University in the Fall of 2000 where he began work on his PhD.

Jeff is married and has two children—a daughter and a son.

TABLE OF CONTENTS

LIST OF TABLES

LIST OF FIGURES

Chapter 3

Chapter 4

CHAPTER 1

INTRODUCTION

1.1 Introduction

According to the Federal Aviation Administration (FAA), turbulence is the leading cause of nonfatal accidents to airline passengers and flight attendants. The cost to commercial airlines in the United States is an estimated $100 million a year. Major air carriers in the United States reported over 250 turbulence incidents between 1981 and 1996. Of these, two resulted in deaths and 63 passengers or flight attendants were seriously injured. Overall, nearly 1,000 people sustained injuries as a result of aircraft turbulence during this 16-year period (Cowen 1998). In addition, there is a significant increase in fuel consumption during travel through turbulent regions and in cases of severe or extreme turbulence, aircraft may be structurally damaged (Ellrod and Knapp 1992, Keller and Haines 1981). Advanced detection and accurate forecasts of turbulence would not only calm nerves but would enable passengers and flight attendants to adequately stow loose objects and buckle themselves in (the majority of serious turbulence-related injuries stems from objects (including passengers) flying through the cabin). Obviously, accurate detection (other than by the aircraft itself) and forecasts of turbulence would be beneficial to the aviation industry. Unfortunately, the fine spatial and temporal scale of turbulence combined with the relatively coarse nature of atmospheric observations make both observing and forecasting turbulence extremely difficult. In order to bridge this gulf, large-scale precursors to severe turbulence must be identified.

The East Coast region of the United States is one of the most frequently traversed aerospace regions in the world. Complicating meteorological systems in this region is the

1

complex topography that features the Appalachian Mountains to the west and the warm Gulf Stream to the east (see Fig. 1). Of particular interest to this research is the role the Appalachian Mountain chain plays in generating convection and waves; the effect of terrain on frontal systems and momentum traversing the mountains (as well as downstream of the mountains), and how the combination of these terrain-induced features can create an environment favorable for severe low-level turbulence in this region.

To better study these scale interactions and resultant low-level turbulence, two events where an inordinate amount of low-level turbulence was reported by aircraft will be investigated in great detail. In one event, the vast majority of low-level turbulence reports are of the light to moderate variety. In the other, nearly half of the turbulence reports are for severe low-level turbulence. Differences in environment to include jet-front systems, frontogenesis, frontal structure, orographic effects, vorticity, and resultant turbulence will be examined across spatial and temporal scales and highlighted. In order to attack the low-level turbulence problem east of the Appalachian Mountains, a detailed hypothesis has been developed to explain the scale interactive processes which can lead to myriad reports of moderate to severe turbulence in this very busy flight corridor. From this hypothesis, it is hoped a better understanding of the larger scale dynamics which lead to the scale contractions described within will enable more advanced and accurate forecasts of low-level turbulence in this region (and elsewhere).

It is hypothesized that the orography of the East Coast of the United States in combination with identifiable meteorological signals of decreasing scale can combine in the following, logical scenario and result in convection and the generation of severe low-level turbulence:

2

(1) Strong flow orthogonal to the Appalachian Mountains results in large amplitude hydrostatic mountain wave formation.

(2) Vertical motions induced by mountain waves produce a downstream isentropic upfold (i.e., a mid-level cold pool). This cold pool is deformed by the background jet and its concomitant ageostrophic motions (to include an indirect circulation that enhances the cold pool). This process is similar to that described by Kaplan and Karyampudi (1992a) although applied on the Appalachians instead of the Rockies.

(3) Intensification of the cold pool aloft and mass flux convergence results in a leeside pressure ridge and a building edgewave that propagates to the south-southeast in a manner previously described by Tilley (1990) and Colle and Mass (1995). This wave response leads to increased surface convergence and frontogenesis as the front at the surface is now oriented ENE-WSW.

(4) Leeside warming due to downslope adiabatic effects results in a temperature ridge (leeside trough) east of the Appalachians.

(5) These features (leeside trough, cold front aloft, edgewave) coalesce to form a system somewhat similar to a cold occlusion and result in a lapse rate much greater than moist adiabatic as cold air resides over low-level warm air in a region of tightening surface temperature gradient and convergence.

(6) This combination in the vertical results in convection, cold downdrafts, formation of a density current-like feature (capable of producing a narrow cold frontal rainband (NCFR)), and ultimately breaking vortices. Frontogenesis analyses will aid in locating these features and their causes. These microscale features are believed to result in a helicity rich low-level environment highly predisposed to strong low-level turbulence near their level of

3

interaction, i.e., 800-700 hPa.

The downstream effects of mountain-induced cold pools and their interaction with other terrain-induced features have been largely ignored in the literature. It is believed these interactions along the East Coast (and likely other regions) can play an important role in convective development, scale contraction, and turbulence generation. It is the goal of this research to thoroughly investigate this hypothesis and the various interactions within. This is accomplished through a combination of observational data and numerical simulations of two case studies. Furthermore, although both cases studied in the research contained an inordinate number of low-level turbulence reports, one of the cases exhibited a much greater propensity for severe low-level turbulence reports. It is believed that a combination of inter-scale signals, to include differences in jet-front signatures and pre- and post-mountain stability structures, along with different frontal slopes (anafront vs. katafront) and resultant convection (linear vs. cellular) delineate the difference in turbulence intensities reported for these two events. Although the amalgamation of processes to be discussed have not been broadly covered in the literature, to some extent the individual components have.

1.2 Literature Review

Turbulence can most easily be described as a random fluctuation or perturbation superimposed on the mean wind. There are several different types of turbulence to include both clear air turbulence (CAT) and convectively-induced turbulence (CIT). Clear air turbulence is generally described as bumpiness encountered in flight through clear air. More precisely, CAT is all atmospheric turbulence of interest in aerospace operations that is not in or adjacent to visible convective activity (Hopkins 1977). Convectively-induced turbulence can best be described as turbulence caused by or closely related to convection, to include turbulence outside of convective cells.

There are several different intensities of turbulence reported by aircrews. Primary concern rests with turbulence in excess of light (because that is the realm where the vast majority of injuries and damage to aircraft occur). The following definitions are offered for turbulence intensity (Lee et al., 1984, Hopkins 1977):

Moderate: Moderate changes are experienced in aircraft attitude and/or altitude, but the aircraft remains in positive control at all times. Usually, small variations in air speed and changes in accelerometer readings of 0.5 g to 1.0 g at the aircraft's center of gravity occur. Occupants feel strain against seat belts or have difficulty walking and loose objects move about.

Severe: Abrupt changes are experienced in aircraft attitude and/or altitude. Aircraft may be out of control for short periods. Usually, large variations in airspeed and changes in accelerometer readings greater than 1.0 g to 2.0 g at the aircraft's center of gravity occur. Occupants are forced violently against seat belts and loose objects are tossed about (including passengers if they're not buckled in).

Extreme: Very rare. The aircraft is violently tossed about and practically impossible to control. Structural damage may occur. Changes in accelerometer readings greater than 2.0 g occur at the aircraft's center of gravity.

Aircraft respond differently depending on the scale of the turbulence. Aircraft tend to

5

move fairly smoothly in the vertical with large eddy flow and often barely notice the effects of small eddies. It should be pointed out that aerodynamic parameters, such as aircraft design, altitude, speed, and weight also determine how much buffeting an aircraft receives (McCann 1999). In general, the following conditions tend to increase the effects of turbulence: decreased weight of the aircraft, decreased air density (i.e., higher altitude), decreased wing sweep angle, increased wing surface area, and increased airspeed (Lee et al. 1984). As a result, aircraft type and other parameters need to be considered when determining the intensity of turbulence reported by aircraft.

Multiple researchers have concluded that jet entrance regions are preferred locations of turbulence (Reiter and Nania 1964, Mancuso and Endlich 1966, Roach 1970, Reed and Hardy 1972, Shapiro 1976, Gidel and Shapiro 1979, Uccellini et al. 1986, Keller 1990, Ellrod and Knapp 1992). Observations of turbulence around jet streams by specially instrumented aircraft (see Kennedy and Shapiro 1975, 1980) have confirmed the preferred location of turbulence to be in the shear zones above and below the jet stream. Additionally, these studies clearly indicated the patchy and intermittent quality of turbulence and found considerable variation between jet streams (Pepler et al. 1998). Turbulence can be considered the combination of the internal and frictional dissipation of total energy following a parcel of air spanning a well-defined turbulent shear layer (Keller 1986). Theoretical and observational considerations suggest that most turbulence is in the form of unstable waves due to Kelvin-Helmholtz instability (KHI) which develops with low static stability for quasi-horizontal flows in the presence of strong shear (Starr and Kemp 1974). Through the years, several theories as to possible causes of aviation turbulence have been proffered.

In general, vertical shear of the horizontal wind is recognized as a primary cause of

6

turbulence (Knox 1997). Many investigators have identified KHI as the principal mechanism responsible for turbulence (Ellrod and Knapp 1992, Keller 1990, Hopkins 1977, Fairall et al. 1991, Jinliang and Jianzhong 1996). When large shear exists between two layers of an inhomogeneously stratified fluid, the boundary can become distorted into an amplifying wave or billow which ultimately breaks down into turbulence in order to alleviate the shear. Turbulence associated with this strong vertical wind shear in a inhomogenously stratified layer is the result of amplified, breaking waves (KHI). The energy source for KHI is the mechanical energy produced by the vertical wind shear. Sinks include the dissipating small-scale eddies and the negative buoyancy of the stable layer. This is, however, not the only explanation.

Bender and Panofsky (1976) noted the association between strong thermal gradients and the high probability of turbulence. Keller (1990) and others have noted that the dissipation of large-scale kinetic energy in the free atmosphere is usually associated with turbulence. Of course, this takes us back to wind shear. Wind shear is the only contributor to Turbulent Kinetic Energy (TKE) production that is always positive. Vertical instability accompanying neutrally-stratified layers could also aid in the production of TKE as positive buoyancy production occurs with a superadiabatic lapse rate (negative in stable conditions).

Theory and observations have demonstrated that gravity waves can locally modify wind shear and stability such that turbulence is produced. Additionally, numerical output for turbulence events suggests turbulence is highly correlated with indicators of large-scale atmospheric imbalance (McCann 1998). Unbalanced flow is typically associated with ageostrophic motions and geostrophic adjustment—hypothesized to be a cause of gravity waves. McCann (1998, 1999) and others (e.g., Fairall et al. 1991) have suggested that

7

turbulence may be caused by these gravity waves. Fairall et al. (1991) have suggested that the gravity wave spectrum is sufficiently energetic to cause local overturning and that this process dominates the production of turbulence in the free atmosphere.

Several authors (Reiter and Nania 1964, Uccellini et al. 1986, and others) have suggested that turbulence could be the result of undercutting jet features (e.g., the polar jet undercutting the subtropical jet). These layers of strong winds (often from different directions) possess strong shear in thermally stable layers and could be responsible for a gravity-wave type mechanism immanent in turbulence perturbations (described previously).

From this, it is clear certain conditions are important for turbulence formation and continuation. These include large variations in the vertical and horizontal wind vectors, vertical motions, and often the existence of a stably stratified layer. These conditions tend to occur more often for curved flow than straight flow (Endlich 1964, Ellrod 1985) and can be very difficult to detect by the conventional observation network.

In a series of papers, Kaplan et al. (2003a,b,c) examined 44 accident-producing turbulence events and determined that turbulence should be forecast (or expected) in regions with the following synoptic signatures: jet stream entrance region, upstream curvature, cold advection, and nearby convection. Kaplan et al. (2003b) speculated that ageostrophic motions enhancing the environment for the development of horizontal vortex tubes may have been responsible for reported severe turbulence in four case studies. Kaplan et al. (2003c) concluded that turbulence is likely along convectively-generated microfronts where convergence and vorticity maximized. Convergence intensified vorticity until it broke down into strong vortex tubes which can be a locus for severe turbulence as they are most likely invisible to aircrews and possess very large velocity gradients. It is believed that horizontal

8

vorticity, when tilted and stretched (at small scales) into vortex tubes plays a major role in the generation of severe low-level turbulence.

Smolarkiewicz and Rotunno (1989) used a three-dimensional numerical model and found that a vertical component of vorticity developed on the leeside of a mountain due to tilting of baroclinically-produced horizontal vorticity as isentropes folded in response to flow over the mountain. Kaplan and Karyampudi (1992b) noted that narrow maxima of relative vorticity (vortex tubes) developed as model and terrain resolution increased. These vortex tubes are forced by the tilting of horizontal vorticity into the vertical and by the convergence of vorticity due to an along-stream frontogenesis process. They concluded that this process was due to the superposition of folding isentropes on which increased convergence occurred leading to large components of the convergence term in the isentropic vorticity equation.

Clark et al. (2000) discussed horizontal vortex tube formation accompanying flow near mountain waves. They found that large-magnitude cross-stream horizontal wind shear and along-stream curvature could create a horizontal region of rapidly changing vertical velocity in an area where a jet streak is imbedded in curved flow and result in a sharp gradient of vorticity and concentration of horizontal vortex tubes. This situation can be enhanced when two jet entrance regions interact in the vertical leading to increased momentum.

Aside from Clark et al. (2000) and Kaplan et al. (2003b,c), there has been very little written in the meteorological journals regarding vortex tubes and/or their relationship to incipient turbulence. Several companion fluid dynamics papers (e.g., Andreassen et al. 1998; Fritts et al. 1998) have covered the subject in a discussion of vorticity in a breaking wave, as well as vortex interactions and turbulence. Additionally, to the best of the author's

knowledge there is an absence of material in the literature detailing the inter-scale relationships between frontogenesis, along-stream frontogenesis, frontal tilt, and the role of convection on microfront formation leading to severe low-level turbulence—particularly along the East Coast of the United States, downstream from the Appalachian Mountains. Essentially, a summary of aircraft turbulence literature provides consensus that turbulence is generally found near thermal gradients, wind shear, relative vorticity gradients, and convection. These become more significant as curvature (and angular momentum) is enhanced, forcing becomes more along-stream, and the scale is contracted.

Atmospheric fronts and associated jets are well-known focal points of temperature gradients and wind shear. An excellent review of quasi-geostrophic (QG) frontal dynamics and frontogenesis can be found in Keyser and Shapiro (1986). Fronts are defined as relatively long and narrow zones of enhanced thermal gradient. They may also be characterized by large horizontal gradients of static stability and absolute vorticity, and are often accompanied by vertical wind shear. Variations tend to be much greater across the front in QG flow (where accelerations are minimal and the front is spatially more compact) than along the front (although, as will be shown, along-front variations can be instrumental to the turbulence process). Fronts can be identified in cross sections as sloping zones of isentropes (baroclinicity), with vertical thickness of 1-2 km. Formation is favored near quasi-horizontal boundaries such as the earth's surface and the tropopause. Sawyer (1955) and Eliassen (1959, 1962) noted that horizontal non-divergent primary circulations (driven by horizontal deformation) force secondary vertical circulations possessing horizontal and vertical components of velocity, which act to either accelerate or retard the rate of frontogenesis. One frequently used tool for diagnosing frontogenetical properties and

budgets is the frontogenesis equation (Miller 1948):

$$F = \frac{1}{|\nabla \theta|} \left[\frac{\partial \theta}{\partial x} \left(-\frac{\partial u}{\partial x} \frac{\partial \theta}{\partial x} - \frac{\partial v}{\partial x} \frac{\partial \theta}{\partial y} \right) + \frac{\partial \theta}{\partial y} \left(-\frac{\partial u}{\partial y} \frac{\partial \theta}{\partial x} - \frac{\partial v}{\partial y} \frac{\partial \theta}{\partial y} \right) + \frac{\partial \theta}{\partial p} \left(-\frac{\partial \theta}{\partial x} \frac{\partial \omega}{\partial x} - \frac{\partial \theta}{\partial y} \frac{\partial \omega}{\partial y} \right) \right] \quad (1.1)$$

where the terms inside the first parentheses represent the contribution due to confluence/divergence, the terms inside the second parentheses represent contributions due to deformation, and the terms inside the last parentheses represent the contribution of tilting to overall frontogenesis. An increase in the horizontal temperature gradient due to differential advection as a result of the horizontal deformation field results in frontogenesis. The subsequent mass perturbation may cause a thermally direct circulation (warm air rising, cold air sinking) in order to produce the corresponding increase in vertical wind shear and maintain thermal wind balance (Namias and Clapp 1949). Additionally, thermally indirect ageostrophic cross-stream circulations can lead to frontogenesis via the tilting process. Thus, deformation, confluence, and tilting dominate QG frontogenetical cross-stream circulations. These same circulations occur with jet streaks and are coupled at upper and lower levels.

The jet stream has been defined as a strong, narrow current of air concentrated along a quasi-horizontal axis characterized by strong lateral and vertical wind shears (Reiter 1963). Upper-level jet streaks are often instrumental in driving surface frontogenesis and surface weather (Keyser and Shapiro 1986). Divergence patterns associated with upper-level jet-front systems play an active role in surface features by contributing to low-level mass changes. Therefore, knowledge of jet streak dynamics and accompanying ageostrophic circulations is essential to understanding frontogenesis and frontal structure.

Features, structure, and circulations associated with the jet stream have been widely discussed in the literature. These will vary depending on the geometry and advection

patterns in and around the jet stream as well as the number and location (in the vertical and horizontal) of jet streaks (and attendant circulation patterns) present.

The most straightforward to describe is the straight jet model. The straight jet (assume negligible centripetal accelerations due to flow curvature) can be broken down into four quadrants—the left entrance, right entrance, left exit, and right exit regions with accelerating flow in the entrance regions and decelerating flow in the exit regions. Namias and Clapp (1949) first demonstrated the thermally direct circulation associated with the jet stream forced by confluent geostrophic deformation. Reed and Sanders (1953), Newton (1954), Bosart (1970) and Shapiro (1970) all demonstrated that an indirect circulation was also associated with a jet stream. For the case of a straight jet streak, a thermally direct circulation is found in the entrance region and a thermally indirect circulation in the exit region (Riehl 1952; Murry and Daniels 1953; Newton 1958; Reiter 1969; Uccellini and Johnson 1979). The direct circulation consists of warm air rising in the right entrance region and cold air sinking in the left entrance region. This circulation pattern results in flow (and mass transport) from the right entrance region to the left entrance region at higher levels and flow from the left entrance region to the right entrance region in the lower level—essentially an isallobaric response due to mass flux convergence below the sinking jet (see Fig. 2). The indirect circulation in the exit region is essentially the reverse with flow from left to right in the exit region aloft and flow from right to left in the exit region at low levels and consists of rising motion in the cold air and sinking motion in the warmer air (Fig. 2).

The thermally direct circulation acts to decrease the cross-front thermal contrast, increase westerly momentum aloft and increase easterly momentum at lower levels thereby increasing the vertical wind shear of the along-front component. The indirect circulation acts

12

to increase the cross-front thermal contrast, decrease the westerly momentum aloft, and increase westerly momentum at lower levels. These mass adjustments (ageostrophic circulations) develop in order to maintain a balance between the mass and momentum fields in the atmosphere's neverending quest for quasi-geostrophy. The circulations (and mass adjustments) as described result in divergence aloft in the right entrance and left exit regions and convergence aloft in the left entrance and right exit regions. Consequently, by mass continuity (Dines' compensation), convergence aloft (sinking motion) will result in divergence at lower levels and divergence aloft (rising motion) will result in convergence in the lower levels.

The upper-level jet streak and ageostrophic circulations discussed above are coupled with the lower level circulation (Reiter 1969; Uccellini and Johnson 1979) with the inertial-advective component dominating the transverse circulation at the upper level and the isallobaric component dominating at the lower level. These circulations can be explained through use of the equations of motion (as described above), quasi-geostrophic omega equation (vorticity advection argument), and energy conservation (potential energy converted to kinetic energy leading to jet streak (accelerating flow) and kinetic energy converted to potential energy from jet streak to exit region (decelerating flow)).

Curvature embedded in the jet stream complicates matters somewhat as can be seen in the gradient wind equation:

$$V_{gr} = \frac{V_g}{1 + \frac{R V_{gr}}{f}} \qquad (1.2)$$

where R represents curvature effects and is positive for cyclonic shear and negative for

13

anti-cyclonic shear. Thus, winds will be subgeostrophic (accelerating) in regions of cyclonic curvature and supergeostrophic (decelerating) in anti-cyclonic regions. This setup will result in convergence upstream from the base of a cyclonically curved trough and divergence downstream. In essence, the combination of curvature with the previously discussed straight jet model yields enhanced convergence aloft in the left entrance region (expect largest surface pressure rises here) and enhanced divergence aloft in the right exit region (which helps explain why this region is often favored for convective development). Horizontal shear and thermal effects further complicate matters and result in along-front thermal gradients. Hence, for highly ageostrophic flow, curvature effects can be important in frontogenesis. These are the types of flow often associated with turbulence. In a detailed observational and numerical study, Kaplan et al. (2003 a,b,c) found that the juxtaposition of a curved and a straight jet entrance region created a highly ageostrophic state and organized the potential for supergradient wind flow thereby establishing a favorable environment for ageostrophically-forced frontogenesis (on the meso-β scale) and fine scale along-stream temperature and density gradients. They found that these regions were roughly coincident with accident (severe turbulence) locations.

Along-front thermal gradients are not always sufficiently small to be neglected when compared to cross-front thermal gradients (Eliassen 1962). At the mesoscale, and particularly when the flow is out of geostrophic balance, substantial temperature gradients in the along-stream direction can exist. Curvature enhances this effect. Convergence or deformation in the along-stream flow can result in along-stream frontogenesis. A review of the literature indicates a dearth of material dealing with along-stream frontogenesis. Kaplan and Karyampudi (1992a) and Karyampudi et al. (1995) have both documented cases where

14

indirect ageostrophic circulations occurred primarily in the along-stream direction as opposed to the large-scale circulation in the cross-stream direction. Kaplan and Karyampudi (1992a) suggested that along-stream differential vertical motions could tilt vertical gradients of potential temperature into the horizontal, thereby increasing the along-stream horizontal temperature gradient (and as a result, the pressure gradient) as part of a scale contraction process. They described this process as follows: (1) increasing vertical wind shear in the along-stream plane results in increased non-uniform vertical variation of horizontal temperature advection as the ageostrophic wind component grows in magnitude downstream of a mesoscale terrain-induced isentropic downfold and upfold (hydrostatic mountain wave); (2) increasing along-stream differential vertical motions tilt the vertical gradient of isentropes into the horizontal as the vertical temperature gradient increases in proximity to horizontal gradients in the along-stream component of the ageostrophic wind; and (3) tilting motions act to increase the along-stream horizontal temperature gradient, and along-stream confluence non-uniformly increases the along-stream pressure gradient force resulting in accelerations, ageostrophy, and frontal steepening as part of a scale contraction process. Mountain waves, convective complexes, propagating internal gravity waves, and mountain-plains solenoid phenomena have all been observed to force along-stream temperature and wind perturbations at length scales much less than the Rossby radius of deformation above the planetary boundary layer (Koch 1979; Maddox et al. 1981; Uccellini and Kocin 1987; Tripoli and Cotton 1989; Kaplan and Karyampudi 1992a, Karyampudi et al. 1995a). In addition to jet-front systems and the relative roles of cross- and along-stream frontogenesis, the vertical structure of frontal systems can have an impact on ensuing weather events.

Bergeron (1937) introduced the terms anafront and katafront based on the vertical

motion occurring at the front. An anafront was defined as a front in which the warm air ascends relative to the cold air (cold air advances more rapidly than the warm air recedes). A katafront was defined as a front in which the warm air descends relative to the cold air. Sanson (1951) investigated 50 cold fronts traversing the United Kingdom and identified them as either anafronts or katafronts based on airflow relative to the frontal surface (generally, cold air rises behind an anafront and sinks behind a katafront). He also identified weather conditions associated with these two types of fronts. Godske et al. (1957) differentiated between anafronts and katafronts based on whether precipitation fell behind (anafront) or ahead (katafront) of the frontal system. Browning (1986) conceptualized anafronts based on "rearward" sloping ascent and katafronts based on "forward" sloping ascent. He introduced the conveyor belt paradigm based on the cloud and precipitation patterns associated with mid-latitude systems and used flow relative to the front to determine frontal type.

When air in the warm conveyor belt moves forward relative to cold frontal motion, the primary ascent and precipitation occur in advance of the cold front (katafront). If the air in the warm conveyor belt moves rearward relative to the cold frontal motion, precipitation will primarily fall behind the rearward sloping surface (anafront). In general, it has been found that the front-normal component of the wind increases above the surface for katafronts and decreases for anafronts (Sanson 1951; Manton 1985; Moore and Smith 1989).

Although it's been suggested that anafronts are more preferred in the atmosphere, many researchers have recently documented the presence of katafronts—particularly downstream of elevated terrain (e.g., Locatelli et al. 1989; Mass and Schultz 1993; Colle and Mass 1995; Schultz and Steenbrugh 1998; Stoelinga et al. 2002, 2003). Various explanations for forward tilting frontal systems have been proffered to include presence of prefrontal

16

inversions (Bedard and Sanders 1978), interaction with mid- to upper-tropospheric baroclinic zones (Schultz and Steenburgh 1998), adiabatic cooling or diabatic effects (Mass and Schultz 1993), preexisting static stability contrast with greater stability ahead of the front (Stoelinga et at. 2002), and orographic retardation of an advancing surface front by a mountain range (Bergeron 1937). Terrain can slow the front at low levels while the upper-level frontal support advances unimpeded downstream and can adjust the vertical frontal structure.

It is well known that terrain can significantly impact both upstream and, in particular, downstream weather. The Appalachian Mountains in the Eastern United States are no exception. The Appalachian Mountain Range is made up of three mountain chains, each prominent in height—the Allegheny Mountains, the Blue Ridge Mountains, and the Shenandoah Mountains (see Fig. 3). The Allegheny Mountains are a prominent western ridge of the Appalachians extending from the West Virginia and Virginia border to the north through central Pennsylvania. At the end of the mountain range is the Allegheny Plateau which covers a large portion of northwestern Pennsylvania and a small portion of western New York (the Allegheny National Forest). The Blue Ridge Mountains are a prominent eastern ridge of the Appalachians extending from northern Georgia, along the Tennessee/North Carolina border, through western Virginia (east of the Shenandoah River Valley), and into western Maryland. The Shenandoah Mountain is a smaller mountain ridge—the first prominent ridge west of the Shenandoah River Valley, located on the West Virginia/Virginia border east of the Allegheny Mountains. While not nearly as extensive as the Rocky Mountains in the western United States, the Appalachian Mountains (particularly considering their proximity to the Atlantic Ocean and Gulf of Mexico) can have a significant impact on the weather of the East Coast of the United States.

17

A brief summary of terrain effects related to this research will be presented (a more detailed description of terrain effects can be found in Smith (1979)). A review of observational synoptic data reveals two common effects of orography on the atmosphere—a hydrostatically generated pressure difference across the mountains (high pressure windward, low pressure leeward) and a deflection of air to the left (in the Northern Hemisphere) as it approaches the mountain (Smith 1982a). Numerical simulations have also shown this mesohigh-mesolow couplet (Lin et al. 1992).

Various authors have demonstrated that the movement of a deep front approaching a mountain range is altered and that the front advances irregularly when compared to the expected propagation absent the mountain range (Buzzi and Tibaldi 1978; Smith 1982a; Davies 1984; Blumen and Gross 1986; Schumann 1987; Zehnder and Bannon 1988; Egger and Hoika 1992; Gross 1994; Steenburgh and Blazek 2001). In fact, Charney and Fritsch (1999) showed that discrete frontal propagation can occur downstream of complex terrain. Numerous researchers have concluded that frontal motion is retarded on the windward side of mountains and is accelerated on the leeside (Smith 1982b, Davies 1984; Bannon 1984; Zehnder and Bannon 1988; Heimann 1990; Hoinka et al. 1990; Williams et al. 1992). Additionally, Gross (1994) noted research utilizing two-dimensional stratified models demonstrated that frontal interaction with orography can result in weakened frontogenesis on the windward side and enhanced frontogenesis on the leeside of mountains due to interactions between the ageostrophic cross-frontal circulation and the circulation produced by flow across the ridge. Mountain-forced divergence upwind and convergence on the leeside results in a reduced thermal gradient windward and an increased thermal gradient and enhanced frontogenesis to the lee (Williams et al. 1992). The presence of a leeside trough

18

(due to downslope warming, advection, insolation) can further enhance this frontogenetical effect downstream of mountains. Gross (1994) found that the magnitude of frontogenesis was more than an order of magnitude larger than that without terrain (based on numerical simulations with and without terrain).

According to hydraulic theory, there are four categories for two-layer flow over mountains: supercritical, partially blocked, completely blocked, and subcritical (see Fig. 4). For partially blocked flow, flow transitions from subcritical to supercritical at mountain crest and can result in hydraulic jumps and long waves of expansion (Rottman and Simpson 1989; Simpson 1997).

Durran (1986) noted that the presence of an upstream inversion enhanced the existence of tropospheric waves as well as the pressure drag due to terrain and that increased mountain height greatly increased terrain drag (similar to that predicted in hydraulic theory as the height of a mountain becomes sufficient to force a transition from subcritical to supercritical flow at the crest, see Fig. 5). This transition from subcritical to supercritical flow has been associated with a sharp increase in leeside wind speeds. Results from numerical modeling studies suggest that mountain-induced frontal distortions are most pronounced when the Froude number ($Fr = U/Nh$, where U is the cross-mountain wind, N is Brunt-Väisälä frequency, and h is mountain height) is much less than one (Schumann 1987; Gross 1994). Low Froude number favors low-level blocking and this blocking is enhanced by increased mountain height and static stability, and decreased cross-mountain winds. Additionally, weaker fronts (those with smaller temperature/density/pressure gradients) tend to be more frequently blocked than stronger fronts with faster propagation speeds (Gross 1994). Additionally, Garner (1999) concluded that large-scale warm advection enhances

blocking and cold advection weakens it. He found that the northern Appalachians (i.e., Alleghenies) could block incident flow of 10 ms^{-1} for realistic choices of static stability and baroclinicity. He also found that the Appalachian Mountains' large length to width ratio and strong inland static stability during the winter months enhanced the likelihood of blocking in that region. In addition, several authors have shown that cold, blocked air can wrap around terrain (on the left, downstream side) or squeeze through gaps in the terrain when effectively blocked (Buzzi and Tibaldi 1978; Smith 1982a; Egger and Hoika 1992; Gross 1994). Of particular interest is the relationship of terrain blocking to flow at lower and upper levels.

Smith (1982b), Gross (1994), and others found that the presence of terrain effectively slowed (decelerated) incoming flow at low levels (near the surface) while the cold air aloft was unimpeded resulting in "differential advection" and mountain-induced vertical shear. As the cold air aloft overrides the relatively warmer air at low levels, instability results downstream from the mountains. Although infrequently presented in the literature, scale interaction effects due to terrain interference (or disruptance) can play an important role in weather downstream from mountains. Karyampudi et al. (1995a) noted interaction of the Rocky Mountains with specific larger-scale flow patterns and the vertical structure of the atmosphere produced a scale-interactive process from large-scale baroclinic to mesoscale to microscale downstream. This could have important implications for turbulence. Convection can have a similar impact in acting as a blocking mechanism and altering the balance of forces governing parcel motions through initiation of an outflow jetlet. The combination of terrain-induced upfolds and downfolds, dual-jet entrance regions (incorporating upstream curvature), ageostrophic along-stream frontogenesis, convection, scale interactive processes, and breaking vortices are likely elemental to the generation of severe low-level turbulence

downstream of the Appalachian Mountains.

1.3 Overview

Specifically, this research will use available observations and a mesoscale model (to include various sensitivity tests) to differentiate between the large-scale, and scale-interactive processes responsible for different low-level turbulence intensities and to identify root causes of low-level turbulent signals for two cases of widespread low-level turbulence east of the Appalachian Mountains. This dissertation contains five chapters: Chapter Two will focus on the larger-scale signals and dynamics (to include observational and model analysis as well as verification) of the two cases. Chapter Three will focus on the role of terrain and convection leading to still smaller scales of interaction. Chapter Four will discuss convectively-induced microfront formation and the organization of possible breaking vortices and implications for turbulence. Chapter Five contains a summary and conclusions.
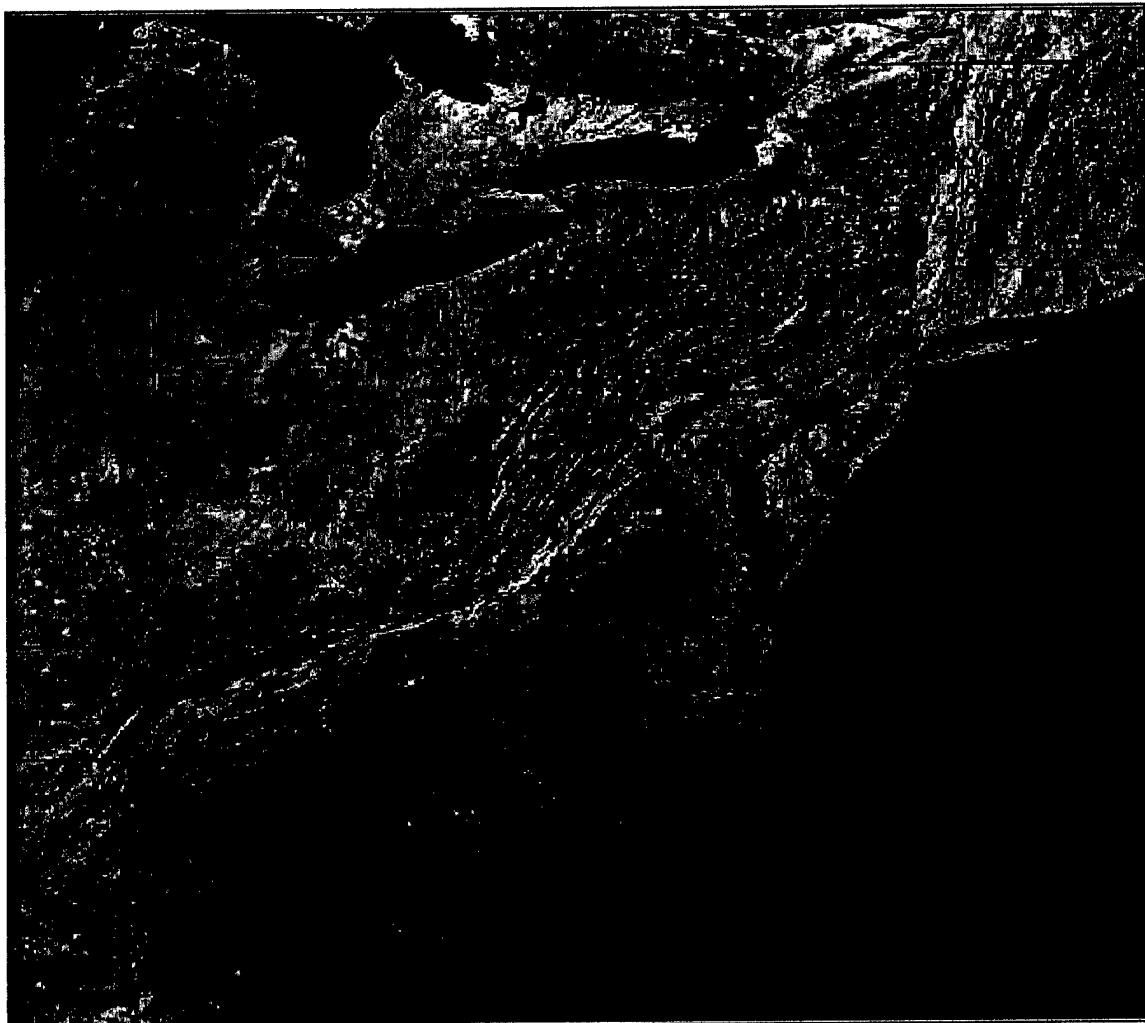
Figure 1. US East Coast with terrain.
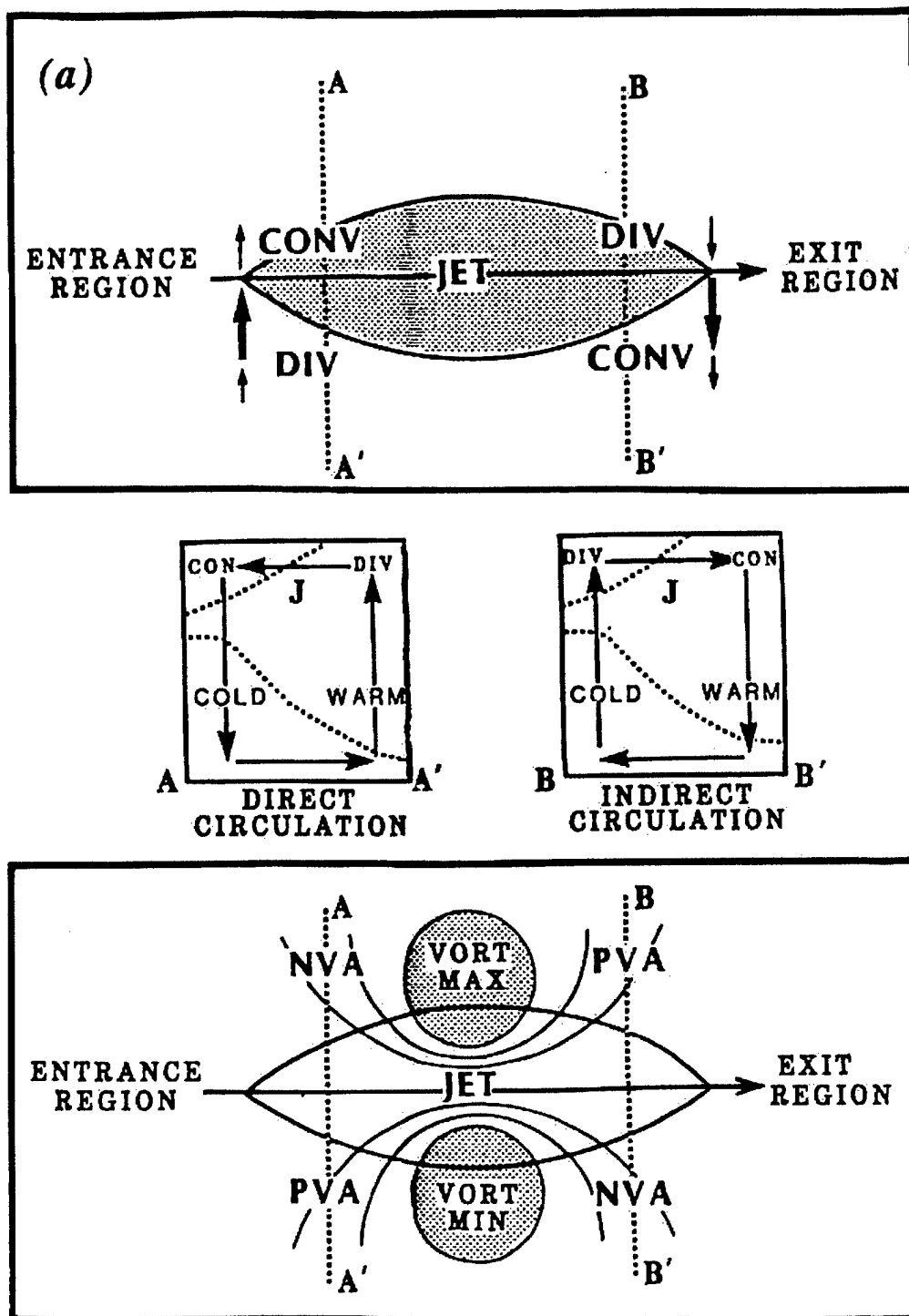
Figure 2. Depiction of horizontal and vertical structures of transverse ageostrophic circulations about jet streaks (from Kaplan et al. 1988)
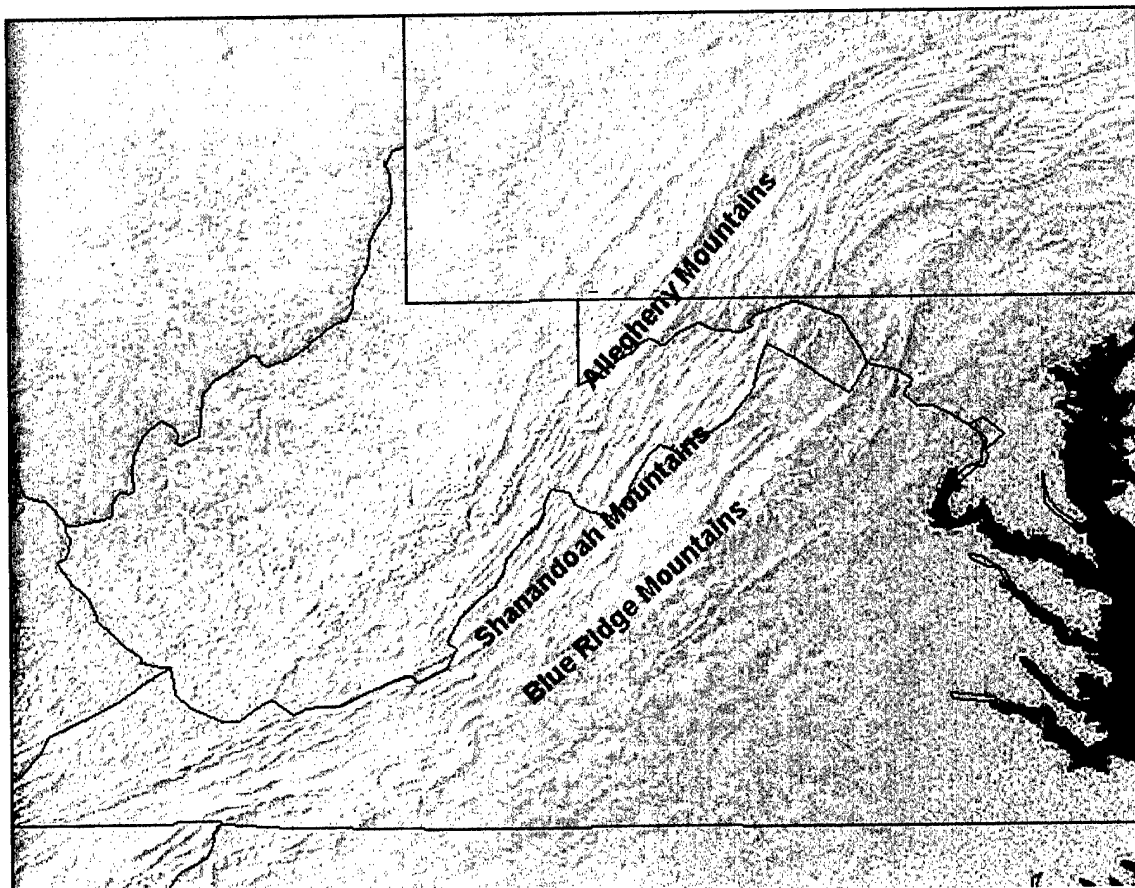
Figure 3. Appalachian Mountain Chain.
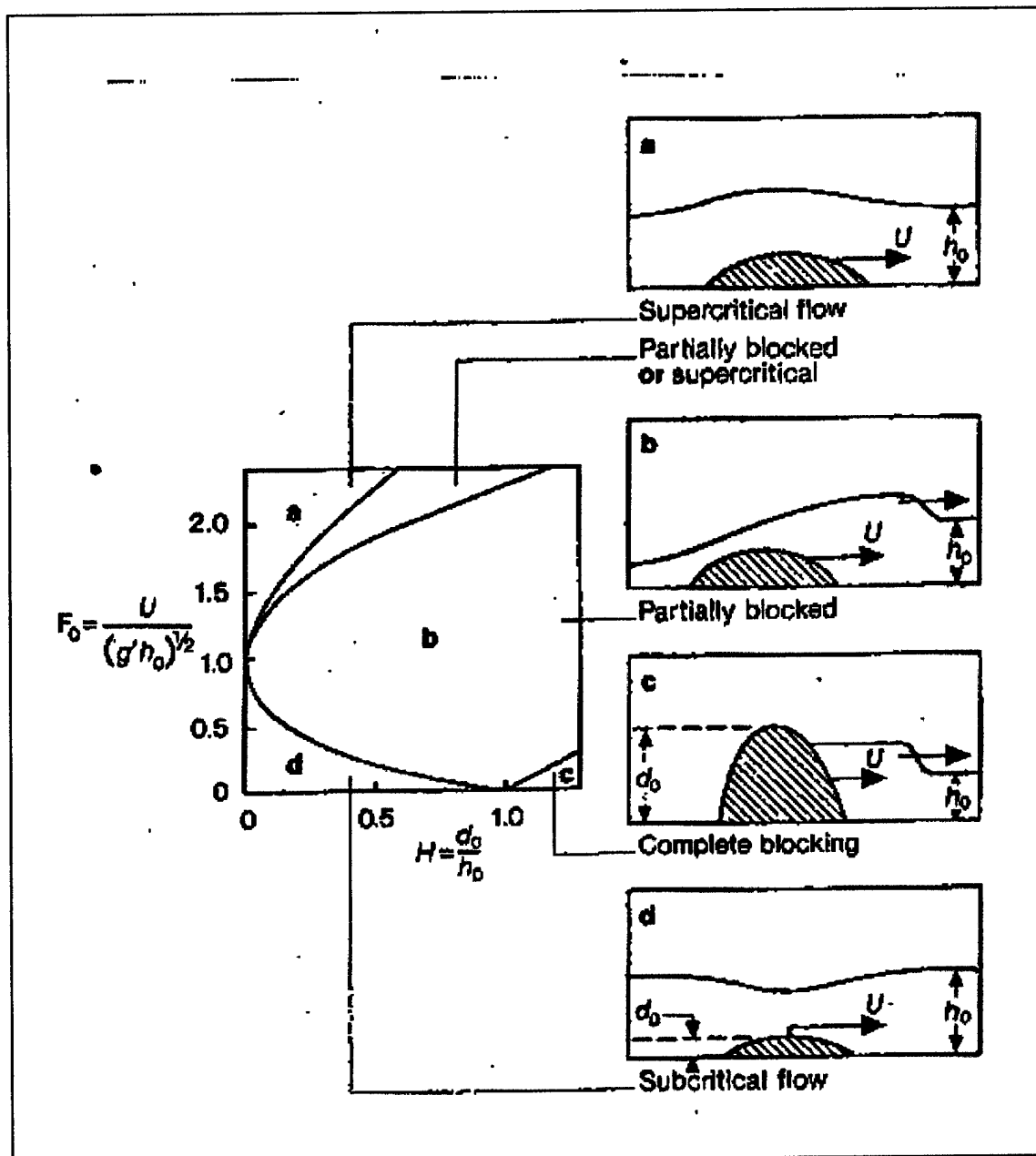
Figure 4. Four types of disturbance which can be generated by a moving obstacle at the interface between two fluids (after Simpson, 1997).
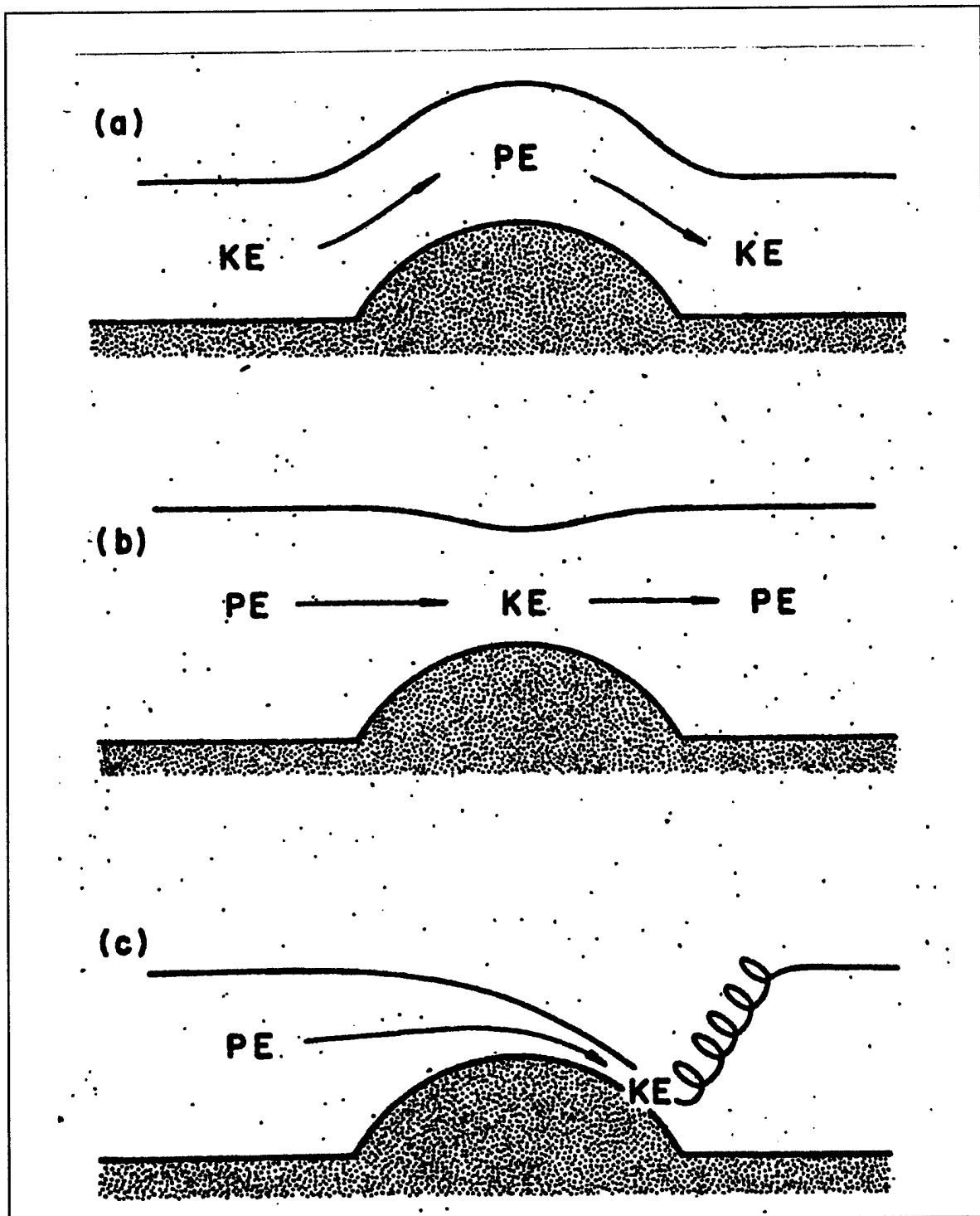
Figure 5. Behavior of water flowing over an obstacle: (a) Supercritical everywhere, (b) Subcritical everywhere, (c) Hydraulic jump (after Durran, 1986)

CHAPTER 2

MESOSCALE SIMULATIONS OF DYNAMICS AND STRUCTURE FOR TWO DIFFERING LOW-LEVEL TURBULENCE EVENTS EAST OF THE APPALACHIAN MOUNTAINS. PART I: QUASI-GEOSTROPHIC JET-FRONT PRECURSORS

2.1 Introduction

Atmospheric turbulence is the leading cause of non-fatal accidents to airline passengers and flight attendants. Over 250 incidents were reported to include nearly 1,000 injuries over a 16-year period from 1981 to 1996 (Cowen 1998). These turbulence encounters resulted in two deaths and 63 serious injuries. Additionally, fuel consumption is significantly increased during travel through turbulent regions and structural damage may occur to aircraft in cases of severe or extreme turbulence (Keller and Hanes 1981, Ellrod and Knapp 1992). Low-level turbulence is particularly alarming as aircraft take-off and landing are considered the most dangerous times of flight and there is much less room to react or compensate for unexpected turbulent motions.

Obviously, accurate forecasts of moderate or greater turbulence would greatly benefit the aviation field. Unfortunately, the very fine scale nature of turbulence combined with the rather coarse observational network conspire against us. Precursors at the larger scale (i.e., observable) must be identified and related to the various scale-interactive processes leading to the turbulence in order to adequately predict and identify regions prone to this dangerous phenomenon.

Numerous explanations and expected locations for turbulence (both clear air turbulence (CAT) and convectively-induced turbulence (CIT)) have been proffered in the literature (see review in Chapter 1). These include entrance regions of jet streaks (Reiter and

28

Nania 1964, Mancuso and Endlich 1966, Roach 1970, Reed and Hardy 1972, Shapiro 1976, Gidel and Shapiro 1979, Uccellini et al. 1986, Keller 1990, Ellrod and Knapp 1992), shear zones above and below jet streaks (Kennedy and Shapiro 1975, 1980), undercutting jet features (Uccellilni et al. 1986), vertical shear of the horizontal wind (Knox 1997), Kelvin-Helmholtz instabilities (Hopkins 1977, Keller 1990, Fairall et al. 1991, Ellrod and Knapp 1992, Jingliang and Jianzhong 1996), large-scale atmospheric imbalance (McCann 1998), and gravity waves (Fairall et al. 1991, McCann 1998, 1999). Conditions crucial for turbulence formation and continuation include large variations in the vertical and horizontal wind vectors, vertical motions, and often the existence of a stably stratified layer. These conditions tend to occur more often for curved flow than straight flow (Endlich 1964, Ellrod 1985). Recently, Kaplan et al. (2003a,b,c) determined that turbulence should be forecast in regions with the following synoptic signatures: jet stream entrance region, upstream curvature, cold advection, and nearby convection.

The purpose of this chapter is to identify the large-scale signals present in two cases where an inordinate amount of moderate or greater low-level turbulence was reported in the busy flight corridor east of the Appalachian Mountains. As expected, these cases exhibit many similarities, but also some fairly significant differences which ultimately result in different frontal structures, convective patterns, and turbulence intensities.

The first case is from 28 December 1988 and has been studied previously in the literature (Koch and Kocin 1991, Chen et al. 1997) as an event where a strong narrow cold frontal rainband (NCFR) formed east of the Appalachians and resulted in brief, heavy rainfall and some substantial low-level winds. The amount of low-level turbulence reports for this event was significant (top 5% in number of reports when compared to an aircraft turbulence

29

climatology for the same region) yet the majority of reports were of moderate or lighter intensity. The second case investigated in this paper is from 13 January 2000 in the same region. This case also involved a multitude of low-level turbulence reports (also in the top 5% numerically) with the vast majority of reports being of the severe variety.

In order to better understand and identify the dynamic and kinematic links from the large-scale to the much smaller scale (where turbulence occurs), larger-scale features leading to turbulence/breaking vortices must first be identified. This chapter will form the building blocks for this step-by-step process for two cases of reported low-level turbulence east of the Appalachian Mountains by beginning with a discussion of the larger scale features (similarities and differences) for both cases. This chapter will focus on the synoptic and meso-α precursors leading to the turbulence events and delineate early, key differences in the two cases, which ultimately resulted in different hydraulic structures, frontal structures, convective structures, and turbulence intensities. The remainder of this chapter is set up as follows: Section 2 provides an observational summary of both cases. Section 3 describes the numerical models, numerical experiments (sensitivity tests), and visualization tools used in this study. Model verification and discussion of numerical simulations of the different jet-front systems, advection patterns, and stability structures for the two cases studied is provided in section 4. Large-scale similarities and differences are described in section 5. Section 6 provides a summary of results for this chapter.

2.2 Observational Summary

2.2.1 The 28 December 1988 Event (D88)

On December 28, 1988 there were over 40 reports of moderate or greater turbulence in a region in the northeast United States (Fig. 1). All but three of these turbulence events occurred after 1245 UTC and 80% occurred after 1500 UTC. The vast majority (over 90%) of reported turbulence was at low levels (below 2500 m) and there were six reports of low-level wind shear. Seven of the reports were for moderate to severe turbulence and five were reported as severe with a total of six reports of moderate or greater turbulence between 16 – 20 UTC. In contrast, there were 12 reports of moderate to severe turbulence and 12 reports of severe or greater turbulence (19 for moderate or greater during the 16 – 20 UTC time frame) in the same region for the second case (13 January 2000) to be studied in this paper. The 28 December 1988 weather event (henceforth D88) has previously been studied by Koch and Kocin (1991, henceforth KK91) and Chen et al. (1997) in an effort to determine the cause of an intense narrow cold frontal rainband (NCFR) that formed east of the Appalachians (successfully modeled in this research). No reference to the myriad low-level turbulence observed on this day is mentioned by either author although extensive damage to trees, windows, and power lines as a result of strong winds is discussed. The larger scale details and turbulence precursors for both cases studied in this research will be discussed in this chapter with smaller scale details (to include meso-β and meso-γ) covered in later chapters.

Surface analysis from 28/1400 UTC indicates a slow moving cold front along the Appalachian Mountains with low pressure centered in southwestern Pennsylvania (see Fig. 2a). At this time, a second front (referred to as an arctic front in KK91) is located through

31

central Ohio and eastern Kentucky just west and north of the slow-moving Appalachian front. This front possesses a temperature gradient of 20 ^{0}C (from eastern West Virginia to central Ohio) and is rapidly approaching the downstream front. By 1900 UTC, these two fronts have essentially merged as the system presses through the Blue Ridge Mountains (Fig. 2b). A subjective mesoanalysis (KK91) indicated a sub-synoptic pressure ridge through central Maryland and western Virginia by this time—a feature KK91 attributed to increasing mass flux convergence associated with a tropopause fold tied to cross-front jet circulations in the left entrance region of the polar jet. Passage of the arctic front was marked by strong westerly winds and significant pressure jumps (to be discussed in more detail in a later chapter). Sub-synoptic pressure surges and a concomitant surge in westerly momentum along the frontal system are closely related to the formation of the NCFR along this system downstream from the Appalachian Mountains.

An analysis of satellite imagery and radar indicates several lines of convective precipitation with the strongest storms occurring after 2000 UTC (see Figs. 3a and 3b). Earlier imagery (1700 – 1730 UTC) indicates a secondary line of convection developed between Elkins and Martinsburg, West Virginia which may have contributed to the generation of a density current-like feature emanating ahead of the arctic front as the system contracted and moved eastward. There is some evidence in visible satellite imagery of mountain wave activity visible through North Carolina. Unfortunately, mid- and upper-level cloudiness obscures any unambiguous mountain-wave signals through Virginia, Maryland, and Pennsylvania although downslope clearing is evident in later imagery. Cloud cover is much more substantial in this case than in the 13 January 2000 case.

Upper air analyses prior to NCFR formation and the bulk of the turbulence reports is

very revealing—both in terms of synoptic precursors to turbulence and for highlighting the major differences between the two cases studied in this and subsequent chapters. For starters, flow at the lower levels (850 and 700 hPa) clearly exhibits some of the signals identified by Kaplan et al. (2003 a,b) as conducive to turbulence. The 28/1200 UTC 850 hPa plot indicates a low height center over eastern Ontario with a trough extending southward through central Ohio and Tennessee. The region east of the Appalachian Mountains where the majority of low-level turbulence was reported is clearly in a rather strong low-level jet entrance region with upstream curvature and winds in excess of 35 ms^{-1} (Fig. 4). Additionally, very strong cold advection is evident as the temperatures upstream of the Appalachians (Michigan/Indiana) are more than 23 ^{0}C colder than those east of the mountains. By 29/00 UTC, the 850 hPa trough is located just off the East Coast.

The 28/1200 UTC 700 hPa analysis indicates a slightly westward location for the low center and trough. Additionally, the eastern corridor is located in the entrance region of a very strong, straight low-level jet with winds in excess of 40 ms^{-1} (Fig. 5). Flow at both 850 hPa and 700 hPa possesses a cross-mountain component although the orthogonality is much less (and the momentum greater) that that of the second case studied in this research.

The 28/1200 UTC 500 hPa analysis indicates a continuing westward tilt of the trough (and cold air) and increasing winds to nearly 50 ms^{-1} with steady eastward progression through 29/00 UTC. Cross sectional analyses in KK91 verify this rearward-sloping (anafront) structure and indicate the strongest subsidence is located well behind the surface front at 450 hPa. Analysis at 300 hPa indicates a strong jet streak over southern Ohio at 28/1200 UTC where winds approach 75 ms^{-1} (Fig. 6). KK91 used the National Center for Environmental Prediction (NCEP) Regional Analysis and Forecast System (RAFs) to show

that this 300 – 250 hPa jet propagated northeastward into eastern Pennsylvania by 1800 UTC and New York by 29/00 UTC. KK91's cross-sectional analysis indicated a thermally-direct circulation in the entrance region of this upper-level jet with transverse ageostrophic flow in excess of 20 ms^{-1} with strong subsidence on the cyclonic (north) side and mid- and upper-tropospheric ascent beneath and to the warm (south) side of the upper-level jet-front system. It is important to note that analyses at 300, 250, and 200 hPa for 27 and 28 December indicate this is a single jet-front system at upper levels (see Figs. 7 and 8). This single-jet structure is in stark contrast to the 13 January 2000 case also studied in this research where two jets are present at upper levels and this dual-jet structure has, as will be shown in later chapters, a significant impact on the intensity of the low-level turbulence ultimately reported in these two cases. Another factor of import to subsequent turbulence intensities and mountain wave formation is the degree of orthogonality the winds possess in relation to the Appalachian Mountain chain. In general, upper-level winds in this case are strong and contain a component perpendicular to the mountains. This orthogonality increases between 28/12 and 29/00 UTC and with altitude although the cross-mountain component is not as significant as that for the other case (13 Jan 2000) investigated in this research.

2.2.2 The 13 January 2000 Event (J00)

On January 13, 2000 at 1931 UTC a commercial aircraft (US Airways 737) encountered severe turbulence at a flight level of 2300 m ($\approx$ 775 hPa) approximately 30 miles southeast of Wilmington, Delaware (KILG). This aircraft carried NASA flight instrumentation to measure turbulence gust loads and recorded an acceleration of 2g (i.e., twice the force of gravity). The vertical acceleration changes as an aircraft experiences a

change in velocity—an acceleration of 2g would cause those experiencing such a force to weigh twice as much as normal. Additionally, such gravitational forces tend to draw blood downward, away from the head and chest and can result in nausea, tunnel vision, and blackouts. In addition to this reported turbulence, there were multiple reports of moderate and greater turbulence throughout the region on this day (Fig. 9). As mentioned in the previous section, the percentage of severe and greater low-level turbulence reports was significantly higher (27%) than that of the 28 December 1988 case (12%).

NMC Surface analysis from 13 January/1200 UTC indicates a slow moving cold front draped along the eastern Appalachians with a low centered over southwestern Pennsylvania and a secondary trough (arctic front) of much colder air to the west and north through central Ohio, Illinois, and Indiana. There is indication of a meandering warm front through Tennessee and the Carolinas 24 hours earlier which continues to move into the region east of the Appalachians and northward and is located through central Virginia, Maryland, Delaware, and New Jersey by 13/1200 UTC (Fig. 10a). By 1500 UTC, this warm front extends eastward to just south of Wilmington, Delaware (KILG) as the slow-moving cold front lies along the lee of the Appalachians. Additionally, there is strong evidence of leeside warming (and drying) at this time and strong westerly winds are evident as the system slowly propagates to the east (see Fig. 11). Strong cold advection is evident to the north through Pennsylvania as temperatures are generally 20 ^{0}C colder through central Pennsylvania than in Maryland/Northern Virginia by 1800 UTC. Additionally, it is during this time period (18 – 20 UTC) that a surge of cold low-level (surface) air drains to the south, both south and east of the terrain (to be described in more detail in the following chapter). The 1800 UTC surface analysis indicates a 1002 hPa low just off the New Jersey coast with the cold front

and post-frontal trough (arctic front) just north of KILG. Surface mesoanalysis indicates very slow progression of the cold front and a tightening of the temperature gradient along the Pennsylvania-Maryland border (Fig. 11b). In general, this case shows much more of a meridional structure at low-levels east of the Appalachian Mountains.

At 1932 UTC (one minute after the NASA accident report), surface frontal passage was reported at KILG. Satellite imagery from this time indicates some isolated convection was present in the vicinity of KILG, and there is some indication of wave-like activity in the cloud signature east of the Appalachians (Fig. 12). A GOES 1-km visible satellite loop from 1500 UTC unambiguously shows a density current-like feature (convectively-induced and rope-like in appearance) emanating to the southeast from central Pennsylvania and into Maryland/northern Delaware by 1900 UTC (additionally, ASOS 5-minute pressure and temperature traces at both KPHL and KILG indicate a response consistent with density current passage, i.e., rapid pressure increase and temperature decrease. See Fig. 13 for KILG pressure trace). From approximately 1845 UTC (over northeast Maryland) through 1932 UTC, satellite imagery indicates cellular convection traversing northern Delaware through the accident location and into southwest New Jersey before dissipating. Surface observations from KILG during this time indicate light rain began to fall, temperatures dropped 12 ^{0}C in four hours, winds increased from light and variable to WNW at 12 ms^{-1} gusting to 20 ms^{-1}, and the station pressure rose from 1004 hPa to 1019 hPa in four hours (and continued to rise to 1035 hPa less than 20 hours after frontal passage).

Upper air plots in the lower levels (i.e., 850 hPa and 700 hPa) bear some similarity to those from the previous case discussed. However, the large-scale forcing is weaker (i.e., winds are 5-10 ms^{-1} weaker and the temperature spread across the trough is not as large as in

D88) and the flow is generally more orthogonal to the Appalachian Mountains and exhibits more low-level curvature upstream. The 13/1200 UTC 850 hPa plot indicates low pressure in northwest Pennsylvania with strong winds (20 – 30 ms^{-1}) flowing perpendicular to the mountains. Temperatures at 850 hPa are fairly mild (5 ^{0}C) although significantly colder temperatures are present upstream. Analysis indicates this region is in the entrance region of a curved jet (Fig. 14a).

The 13/1200 UTC 700 hPa analysis indicates that the closed low at 850 hPa is not closed at this level and the location of the 700 hPa trough is directly above the 850 hPa trough. Winds at 700 hPa are also perpendicular to the mountains and slightly stronger than those at 850 hPa with the region located in the entrance region of an overlapping straight jet (Fig. 14b). By 14/00 UTC, the 700 hPa trough is located east-southeast of KILG and strong cold advection is evident.

The 500 hPa analysis for 13/1200 UTC exhibits some westward tilt with the trough located through central Indiana. Winds at this altitude are 35 to 45 ms^{-1} and again orthogonal to the Blue Ridge Mountains. Analysis at levels above 500 hPa is particularly revealing in highlighting an important distinction between the two cases of low-level turbulence studied in this research. Whereas the 28 December 1988 (D88) case is essentially a single jet-front system at 300-200 hPa, the 13 January 2000 (J00) case clearly exhibits a strong polar jet-front at 300 hPa and a sub-tropical jet-front at 250-200 hPa (see Fig. 15). As will be shown, the existence of this second jet plays a significant role in setting up and differentiating the turbulence intensity in this case from that of D88. More details of the larger-scale precursors, similarities, and differences will be diagnosed through the use of a mesoscale model and trajectory analyses.

2.3 Numerical Model Description

2.3.1. Experiment Design

In order to increase spatial (both horizontal and vertical) and temporal coverage (necessary to adequately diagnose the multi-scale phenomena at play in the previously discussed scenario), a mesoscale model will be utilized. Although grid spacing and time steps are limited by the CFL criterion and computer resources, a much greater resolution of meteorological parameters in time and space can be achieved in comparison to coarse observational datasets. This increased resolution is particularly valuable as the bulk of turbulence reports occurred directly between the meager existing upper air data. The numerical model chosen for this study is MESO Inc.'s Non-hydrostatic Mesoscale Analysis and Simulation System (NHMASS) version 6.0 (Kaplan et al. 2000, MASS Handbook). Turbulent Kinetic Energy (TKE) PBL physics, mixed-phase moisture physics similar to those given in Lin et al. (1983) and Rutledge and Hobbs (1983), and the Kain-Fritsch cumulus parameterization scheme (see Kain and Fritsch 1993) were employed. Table 1 lists the characteristics of the NHMASS model and microphysical formulation specifics. A nested grid approach was used with a coarse initial grid of 30-km with subsequent finer grids of 15-km, 6-km, 2-km, 1-km, and 500-m resolutions (see Fig. 22 for 30-km/6-km grid locations). Coarse runs were performed over a 100x100 grid. The 15-km and 6-km simulations employed grids of 170x170. All other model simulations were run over 200x200 grids. All model runs employed 46 vertical levels with staggered spacing (highest resolution in the PBL). Terrain following (sigma) coordinates were used and vertical resolution ranged from 25-m to 350-m. NHMASS was run in hydrostatic mode for the 30-km and 15-km runs. All other simulations were performed non-hydrostatically (note: a comparison between 6-km

runs performed both hydrostatically and non-hydrostatically indicated improved fidelity when executed in non-hydrostatic mode for both case studies). A combination of envelope and silhouette terrain representation of 1-km resolution was employed for the control runs. Additionally, in order to generate 72 hours worth of simulated data (for use in the trajectory model and overall analysis), 40-km resolution (horizontal) runs of dimensions 100x100x46 were performed using the hydrostatic option of NHMASS for both cases. Initialization for these runs is as described for the 30-km control runs.

Initialization for the coarse-mesh (30-km) simulations was performed with NCEP reanalysis data for the 28 December 1988 case and ETA analysis data for the 13 January 2000 case. The NCEP Reanalysis Project (Kalnay et al. 1996) dataset employed as initial and 6-hour lateral boundary conditions for the coarse D88 runs is a gridded dataset reanalyzed utilizing available rawinsonde, profiler, satellite, radar, and surface observations using a 3-D Optimal Interpolation (3DOI) scheme (Daley 1991). The ETA data gridded fields employed as initial and 6-hour lateral boundary conditions for the coarse J00 runs were augmented with surface and upper air observations from conventional sources in order to determine the first guess fields. Subsequent finer runs were initialized with output from the previous run (i.e., the 15-km run was initialized with the 30-km output, 6-km initialized with 15-km output, etc.). Lateral boundary conditions were provided from the next coarser simulation output and updated at appropriate time intervals.

To adequately assess the effects of terrain on weather evolution for the cases studied, sensitivity tests were performed. The full physics, terrain runs described above are to be considered the control simulations. Identical simulations with coarse (60-km), smoothed (50-point smoother) terrain are utilized to isolate the effect the Appalachian Mountain chain

has on these two weather events.

Additionally, sensitivity tests were run to assess the effect of latent heating on weather evolution, and in particular, microfront development and turbulence initiation. In order to do this, a 2-km run (for both cases) was initialized with the 6-km control data and latent heating turned off. To accomplish this, all temperature perturbations due to precipitation or moisture processes were set to zero. Simulations of 1-km and 500-m resolution were performed as well utilizing the same initialization and boundary condition processes as in the control run (i.e., the next coarser run). A list of numerical simulations performed during this research is provided in Table 2.

2.3.2 Trajectory Analysis

In addition, in order to ascertain parcel origination and flow patterns, three-dimensional parcel trajectories were plotted and analyzed. The Mesoscale Atmospheric Simulation System Trajectory (MASSTRAJ) software package (Rozumalski 1997) was used to accomplish this. MASSTRAJ is a three-dimensional trajectory model using model simulated mass and momentum fields to retrace or forecast the path of an air parcel. Both forward and backward trajectories can be produced using MASSTRAJ. Trajectory calculations are performed in the x, y, sigma coordinate system and are advected by the following time-dependent iterative scheme:

$$x^{(n+1)\delta t} = x^{n\delta t} + \overline{u}_i^{n\delta t}\left(\frac{m}{\Delta x}\right)\delta t \qquad (2.1)$$

$$y^{(n+1)\delta t} = y^{n\delta t} + \overline{v}_i^{n\delta t}\left(\frac{m}{\Delta y}\right)\delta t \qquad (2.2)$$

40

$$\sigma^{(n+1)\delta t} = \sigma^{n\delta t} + \overline{\sigma}_i^{n\delta t} \delta t \qquad (2.3)$$

where m is the map scale factor (in meters) on a polar stereographic grid, Δx and Δy are model horizontal grid spacing, n is the time step, and δt is the timestep used between dataset updates for the advection of parcels as determined by $\delta t = \Delta t / N$, and represents the time between model updates. The components of advection velocity $(\overline{u}, \overline{v}, \overline{\sigma})$ are determined by the following equations:

$$\overline{u}_i^{n\delta t} = \overline{u}_i^{t_o} + \left[\frac{\overline{u}_i^{t_0 + \Delta t} - \overline{u}_i^{t_0}}{\Delta t} \right] n \delta t \qquad (2.4)$$

$$\overline{v}_i^{n\delta t} = \overline{v}_i^{t_o} + \left[\frac{\overline{v}_i^{t_0 + \Delta t} - \overline{v}_i^{t_0}}{\Delta t} \right] n \delta t \qquad (2.5)$$

$$\overline{\sigma}_i^{n\delta t} = \overline{\sigma}_i^{t_o} + \left[\frac{\overline{\sigma}_i^{t_0 + \Delta t} - \overline{\sigma}_i^{t_0}}{\Delta t} \right] n \delta t \qquad (2.6)$$

The subscript "i" denotes the number of iterations completed to determine the mean advection velocity. Mean velocities between simulated data sets are computed by initially determining a velocity between data sets at t_0. The parcel is then advected (either forward or backward) by δt to a new location in space and time where a new velocity is determined and the parcel is returned to its original position. At this point, the parcel velocities (at t_0 and $t_0 + \delta t$) are averaged and the new mean velocity is used to advect the parcel. This process iterates three times before the final mean velocity vector is determined and final advection of the parcel occurs.

The parcel characteristics are assumed to be the same as the local environment over a model grid cube. Any change in potential temperature is considered due to diabatic heating.

41

A bi-cubic interpolation method is used to interpolate horizontal gridded data to parcel positions.

2.3.3 Visualization

The GEMPAK plotting system (des Jardins and Peterson 1983) is the primary tool used to generate plots for analyses from model output. McIDAS-X has been utilized for satellite looping, Microsoft Excel for meteogram (time series) plots, and MASSTRAJ was modified to plot NHMASS output and employed for plotting trajectories.

2.4 Model Verification and Numerical Simulation of Jet-Front Systems

The MASS/NHMASS numerical model described in section 3 was utilized to produce high resolution simulations of the large- and small-scale meteorological parameters at play during two low-level turbulence events east of the Appalachian Mountains. Obviously, the very small-scale features (meso-β, meso-γ, and below) leading to the myriad low-level aviation turbulence reports cited in these cases are difficult to verify observationally. Nevertheless, if the large-scale features (or precursors) can be simulated with reasonable fidelity, the ensuing smaller-scale features produced and resolved by the mesoscale model can be used to diagnose the evolutionary, inter-scale physical mechanisms that create an environment predisposed to low-level turbulence. Initial model output from the control runs (both cases) as well as the coarse, 72-hour simulations to include temperature, pressure, height, wind, cloud and precipitation patterns, and moisture analyses were subjectively compared to the corresponding National Weather Service (NWS) plots (surface and upper air), RAOB (where available), satellite, and radar summaries. In general, the numerical simulations performed exceedingly well for both cases. More specific details and any deviations are presented in the following subsections.

2.4.1 Verification – 28 December 1988 Case (D88)

Comparison of model output to available observations for this case indicates excellent agreement in terms of wind, pressure, height, and precipitation patterns. Timing of significant features (convective line, pressure surges) is also in good agreement with reality and KK91's mesoscale analyses. The location and evolution of synoptic-scale surface features, to include pressure patterns and frontal features discussed earlier align nearly

43

identically in space and time with simulated pressures within 1-2 hPa of those observed. As the system evolves, fidelity is well-maintained with frontal system approach and timing near the Appalachians and downstream in excellent agreement (both spatially and temporally) with KK91. Development of the NCFR is also very well-produced—particularly in the higher resolution simulations. Although simulated rainfall intensity is less than that reported by KK91 (they reported a radar-derived rainfall rate in the very narrow core of the NCFR for a 5 – 10 minute interval of over 100 mm/hr for a 10-km area), NHMASS produced rainfall rates in the proper location and at the proper time of more than 40 mm/hr (a vast improvement over KK91's NGM-produced 10 mm/hr and Chen et al.'s (1997) simulated rate of 12 mm/hr). Additionally, comparison of model-generated cloud fields with 1-km visible satellite imagery indicates the model adequately portrayed the cloud environment. In addition to surface fields, the control run (as well as subsequent higher resolution simulations) successfully reproduces upper-level synoptic features.

Model output at standard upper levels was compared to NMC observational analyses at 28/1200 UTC for the coarse resolution control run. This simulation compares remarkably well at all levels. The position of the low pressure center east of Hudson Bay is well produced at 850 hPa both in terms of location and intensity as is the general synoptic pattern at this level, with the trough located through central Ohio/Kentucky/Tennessee as in reality (Fig. 16). Temperature and wind patterns (as well as values) are in good agreement with observations to include the curved 30+ ms^{-1} jet streak and upstream cold advection. Heights at this level are within 5 m throughout the region of interest (and elsewhere). Results are similar at 700 hPa where the 40+ ms^{-1} observed straight jet is simulated with the proper intensity, structure, and location (Fig. 17). Synoptic features are well replicated with height

44

troughs and ridges properly located and of the appropriate magnitude. Simulated heights are again within 5 m of observed with the only discrepancy noted being a slightly (less than 100 km) eastward location of the Atlantic High. At 500 hPa, placement of trough, wind, and temperature patterns are well simulated. A 50 ms^{-1} jet is properly located and heights are within 5 m throughout the domain. At 300 hPa, the control simulation for 28/1200 UTC properly reproduces the single-jet system discussed earlier in this chapter. Simulated heights mirror those observed both in magnitude and location (Fig. 18). Plots for 250 hPa and 200 hPa from the control simulation verify the single-jet structure observed for this case and demonstrate proper synoptic signatures in regards to temperature and height patterns. In addition to surface and upper air output, the 28/1200 UTC RAOB/Skew-T for Dulles International (KIAD) was compared to a model-generated sounding at the same location. The simulated sounding verified well in terms of temperature, dewpoint, and wind profiles. Tropopause heights were identical (200 hPa) and a weak low-level inversion is present (at approximately the same altitude) in both soundings. The only obvious discrepancy apparent in the simulated sounding is strong drying observed above 300 hPa in nature.

Output from the higher resolution control simulations also verifies well with observations to include the simulation of a 6 hPa/hr surface pressure jump in close agreement (both in size and location) to the 8 hPa increase noted in KK91. Observed surface parameters (temperature, dewpoint, mean sea level pressure, and cloud cover) for 43 sites within the 6-km domain were compared for 28/1700 UTC for further verification purposes (17 hours into the run). The average temperature difference between modeled and observed was 0.09 ^{0}C (1^{0}C median). Modeled dewpoints were, on average, 1.3 ^{0}C higher than observed, and pressure differences averaged 0.5 hPa (0.6 hPa median). With very few

45

exceptions, sites reporting cloud ceilings were represented by cloud cover in the mesoscale model. Overall, synoptic-scale features were extremely well-simulated for this case. Similar results are shown for the 13 January 2000 case.

2.4.2 Verification – 13 January 2000 Case (J00)

As with the 28 December 1988 case, the MASS/NHMASS simulations of the 13 January 2000 turbulence event verify extremely well when compared to observations. Synoptic features at the surface are well simulated. At 13/1200 UTC, a closed, contoured 1008 hPa low pressure center is simulated in western Pennsylvania as observed. The surface cold front is properly positioned along the West Virginia/Virginia border extending southwest through northern Alabama and central Mississippi. The post frontal trough observed is properly simulated just north of West Virginia through central Ohio and Indiana as is the presence of a meandering warm front through Virginia. Surface temperatures, winds, and isobaric patterns verify as well. The only obvious discrepancy is precipitation coverage and intensity, which is underdone in the model. This discrepancy is very likely the result of poor initial moisture fields in the 13/00 UTC ETA data. Nevertheless, the convection observed near the accident location is simulated by the numerical model at higher resolutions although it lags reality by approximately one hour in timing. It is also noted that modeled cloud fields match those from visible satellite imagery. Upper-level synoptic features are also well produced by the model.

At 850 hPa, the 13/1200 UTC closed, contoured 1380-m low over northwest Pennsylvania is collocated in the simulated and observed height plots (Fig. 19). Similarly, the trough along the Appalachian Mountains and temperature pattern (to include the warm

46

protrusion from the southwest) are well verified. The curved (upstream) 25 - 30 ms^{-1} jet is orthogonal to the Appalachians as observed. Simulated heights are well within 5 m of observed throughout the region of interest. Simulated height and temperature patterns (and values) correspond closely with observations at 700 hPa to include the fairly straight 30 – 40 ms^{-1} jet perpendicular to the Appalachians (Fig. 20). Results are again well simulated at 500 hPa and higher for this case. Position and intensity of the trough over Michigan as well as winds and temperatures throughout the domain are essentially as observed. Heights continue to be within 5 m of observed. The polar front jet (PJ) is well simulated at 300 hPa across the central to northern Appalachians as in reality. Heights and winds as well as weak troughing over Wisconsin/Michigan correlate well with observations (Fig. 21). Additionally, the upper-level double-jet structure in this case is clearly apparent in both simulations and observations at 250 – 200 hPa as the PJ is located across the Appalachian region and the sub-tropical jet (STJ) traverses the Gulf of Mexico and Florida. These jets are unambiguously separated by a minimum in wind speed at 200 and 250 hPa. As verified at the lower levels, simulated wind speeds, temperatures, and heights at the upper levels match well those from the 13/1200 UTC observations. In addition to these comparisons, the 13/1200 UTC sounding for KIAD was compared to a simulated profile at the same location. The simulated profile compares favorably with the observed sounding—a strong inversion is present in both soundings at 925 hPa, tropopause heights are identical (200 hPa), and temperature and wind profiles are nearly identical. The only apparent discrepancy is an increased moisture content in the observed profile (not surprising given the previously mentioned dry bias of the simulation). A quick profile comparison at 14/00 UTC indicates the model continued to simulate reality with a high degree of fidelity. Both observed and modeled soundings depict

an elevated inversion at approximately 700 hPa and wind, temperature, and dewpoint profiles are well matched.

Output from higher resolution simulations verifies with excellent fidelity as well to include the cellular convection that passed within the vicinity of the accident location (observed at 1930 UTC, simulated at 2030 UTC at 1-km resolution—more details to follow in later chapters). As with the previous case, observed surface parameters (temperature, dewpoint, mean sea level pressure, and cloud cover) for multiple sites (36) within the 6-km domain were compared to simulations at the same locations for 13/17 UTC (17 hours into the run) in order to ascertain the degree of model accuracy near and prior to the time of interest. The temperature bias and median for this case were 0.0, dewpoint readings were approximately 1 ^{0}C too low, and pressure readings were 1 hPa too high (on average) for these locations. With only two exceptions (less than 10%), all sites recording low- or mid-level cloud ceilings have simulated ceilings in the model output. As with D88, overall model verification is extremely good. Aside from the minor discrepancy in moisture content and the tardiness of precipitation, the simulations for J00 matched reality to a remarkable degree at the large scale. As a result, we are confident these simulations can be adequately used to diagnose the physical and dynamical forcing mechanisms leading to low-level turbulence in this case.

2.5 Distinguishing Synoptic and Meso-α Signals

Numerical simulations enable a more detailed, higher resolution analysis (spatially and temporally) of the dynamical and physical processes leading to widespread moderate to severe low-level turbulence reported east of the Appalachian Mountains in the two cases studied in this research. Additionally, since the bulk of these turbulence reports occurred between 16 – 20 UTC, simulations allow a much more thorough investigation of upper-level dynamics and kinematics precisely where (and when) observations are absent (i.e., between sounding times). While these cases share many similarities (particularly at the synoptic scale), they also possess some key differences in structure during the early stages prior to turbulence formation. These differences are likely responsible for the varying turbulence intensities (in general) of the myriad turbulence reports for these two cases as well as differences in convective geometry and frontal structure/slope. How well each case matches the turbulence paradigm laid out in Kaplan et al. (2003 a,b)—discussed earlier, and how these cases conform and respond to the various stages presented in the hypothesis (Chapter 1) of this research will be explored in the remainder of this chapter and in the chapters to follow. As will be shown, the synoptic to meso-α set-up and structure—prior to terrain interaction and subsequent, smaller-scale (meso-β, meso-γ) frontogenesis and turbulence—plays a significant, deterministic role in the intensity of the turbulence reported in this region for these two cases (and likely many others).

2.5.1 Early Similarities Between D88 and J00

Both the 28 December 1988 and 13 January 2000 cases possess many of the large-scale signatures previously discussed as being favorable for turbulence. Some similarities

are apparent in the time leading up to the majority of low-level turbulence reports for these cases (16 – 20 UTC) as an examination of simulated output from 12 to 21 UTC (approximately six hours prior to and through the time of most active low-level turbulence reports) on the day of the NASA accident report (13 January 2000) and the numerous turbulence reports on 28 December 1988 will indicate. Both events occurred during the winter months as a cold front was draped along the Appalachian Mountains crossing the region of interest between 18 and 21 UTC. An analysis of precipitation for both cases (as verified in radar and satellite) indicates convection was well within 100 km of the low-level turbulence reports in both these cases although the convection was deeper and more intense for D88. Strong cold advection was also present in both cases. At the approximate level of two low-level moderate to severe turbulence reports for the D88 case (775 to 700 hPa near Hagerstown, Maryland and Harrisonburg, Virginia at approximately 1830 UTC), the temperature dropped 13 ^{0}C between 15 and 21 UTC. Similarly, in J00, the temperature dropped 11 ^{0}C during the same time frame prior to the NASA accident report southeast of Wilmington, Delaware. Both cases occur in or near the entrance region of fairly strong jets at 775 hPa with upstream curvature although the curvature (as will be shown in more detail in the following chapters) is greater for the J00 case. Fig. 23 depicts simulated 850 hPa winds valid at 1800 UTC on 13 Jan 2000 and 28 Dec 1988. Winds in the region of low-level turbulence reports for D88 are generally from the southwest at 30 to 35 ms^{-1} with westerly and northwesterly flow upstream and the strongest flow (40 ms^{-1}) from the southwest along and off the east coast. Flow is more westerly (cross-mountain) and curvature stronger for the J00 event with winds generally westerly at 30 ms^{-1}. North to northwesterly winds are evident just upstream and the strongest flow is from the southwest along and off the east coast at 35

50

to 40 ms^{-1}. In addition to exhibiting these similarities at low levels, both cases bear some resemblance at upper levels as well.

Upper-level simulations (and analyses straddling the event—12 UTC and 00 UTC) indicate the polar jet entrance region (and its concomitant, leftward-directed ageostrophy) is approaching the Appalachians. The 1800 UTC 28 Dec 1988 300 hPa plot indicates west-southwesterly flow at 70 to 75 ms^{-1}. A similar pattern is apparent at 200 hPa with winds becoming more westerly at 60 to 65 ms^{-1} (see Fig. 24). The 13 Jan 2000 case also exhibits the approach of a polar jet streak upstream from the Appalachians at and prior to the time of the NASA accident report. The 1800 UTC 13 Jan 2000 300 hPa plot depicts 70+ ms^{-1} winds impinging upon the Appalachians and a similar pattern is apparent in the 200 hPa analysis (see Fig. 25). Flow is more westerly for this case (as it was at lower levels). In spite of these similarities and the presence of multiple parameters identified as turbulence precursors, resultant turbulence intensities (as well as frontal structure and convection geometry) at low levels east of the Appalachian Mountains differ for these two cases. In order to begin to identify root causes of these differences, it's necessary to identify early (12 to 72 hours prior to turbulence formation) differences in the atmosphere at both upper and lower levels for these two cases.

2.5.2 Differences in Large-Scale Wave Patterns

As will be demonstrated in the following chapters, early differences in synoptic and meso-α patterns play a vital role in the determination of the low-level turbulence intensity east of the Appalachian Mountains for two cases of widespread low-level turbulence studied in this research. A fairly clear difference between these two cases can be seen in an

examination of the large-scale wave patterns in the 48 hours prior to Appalachian frontal passage, convective initiation, and low-level turbulence inception in the region to the east of the Appalachians. These patterns affect the incident angle of the wind's approach to the mountains prior to any mountain wave formation and subsequent downstream response, as well as the atmosphere's propensity for frontogenesis/frontolysis east of the Appalachians. Observational analysis and simulations at 300 hPa for 1200 UTC 26 Dec 1988 and 1200 UTC 11 Jan 2000 are indicative of the early differences in large-scale wave patterns for these two cases.

These early plots depict a meridional pattern with a strong, deep trough in the western US and ridging through the central US (and points East) for the December 1988 case and an essentially zonal pattern with weak troughing through the eastern half of the US and some indication of a vortex located in south-eastern Canada in the 24 hours preceding the turbulence event on 13 Jan 2000. Analysis from 00 UTC 27 Dec 1988 clearly demonstrates the high amplitude wave pattern over the US with a 55+ ms^{-1} northerly jet along the West Coast and a stronger, southwesterly PJ streak (75+ ms^{-1}) stretching from Baja California through the central US into Wisconsin. This pattern exhibits an amplifying ridge over the eastern half of the US which inhibits frontogenesis and persists in a robust fashion at all times prior to surface frontal passage (east of the Appalachians), NCFR formation, and turbulence associated with the strong QG PJ-front system itself (see Fig. 26). In contrast, the wave pattern for J00 is of much smaller amplitude over the US and exhibits a zonal pattern as it traverses the US.

Analysis from 00 UTC 12 Jan 2000 depicts essentially west to east flow across the contiguous United States with several 70+ ms^{-1} PJ streaks evident between 35^0 and 45^0 N

52

latitude (discussed in more detail in the next section). Additionally, the subtropical jet (STJ) is evident in this case throughout the period from 11 Jan 2000 to 14 Jan 2000. It is absent in the D88 case. The presence of the STJ and its associated transverse circulations distinguishes this case and ultimately plays an important role in the advection of low-level warm air along and east of the Appalachians (as is detailed in the following two sections). In addition, the existence of this southern stream in combination with a low/vortex over Quebec (and resulting west-northwesterly flow to the south) creates a confluent zone and enhances synoptic-scale frontogenesis over the Ohio Valley and the Atlantic States. Such a zone does not exist east of the large-scale jet front system for the Dec 1988 event. The large-scale wave patterns described for these two cases persist and translate to the east as time advances toward the dates of the turbulence events.

Winds for the D88 case become more southwesterly on the 28th (i.e., less orthogonal to the terrain) as the entrance region of the massive meridional PJ impinges upon the Appalachians between 12 UTC and 18 UTC on 28 Dec 1988 (Fig. 27). The strength of this classical QG system is reflected in analyses at lower levels essentially depicting the same pattern of southwesterly flow with the jet streak and west to northwesterly flow behind the trough. In contrast, low-level flow for the 13 Jan 2000 event does not simply mimic upper-level flow patterns. While flow at 200 and 300 hPa for the 13th remains essentially zonal, there's more directional variation at the lower levels, although flow impinging on the Appalachians continues to be from the west (i.e., orthogonal) at 700 and 850 hPa. This contrast can be clearly seen in the backward trajectories from 12 UTC on the days of interest (i.e., 28 Dec 1988 and 13 Jan 2000) and run for 60 hours at multiple levels in the vertical for a point in south-central Pennsylvania east of the Alleghenies (see Figs. 28 and 29).

Trajectories for D88 essentially trace parcel origination back to the south-southwest at all levels. On the other hand, trajectories for J00 indicate multiple directions for parcel origination at these varying altitudes. This large-scale shear (i.e., parcels at different altitudes arriving from different directions) predisposes the 13 Jan 2000 environment to frontogenesis east of the Appalachians as it is conducive to quasi-geostrophic deformation.

Clearly, there are some significant large-scale differences between these two cases in the hours leading up to the hydrostatic mountain wave formation, isentropic upfold, convective initiation, and subsequent downstream turbulence described in the hypothesis for this research (Chapter 1). The 28 Dec 1988 case exhibited a meridional wave structure. Flow was less orthogonal to the mountains, was generally from the same direction in the vertical at points east of the Appalachians, and was a single jet-front system. The 13 Jan 2000 event possessed an essentially zonal wave structure with flow perpendicular to the Appalachians, and arriving from various directions in the vertical at points east of the mountains. Additionally, this case had both a polar jet and a subtropical jet present. The importance of this difference in jet structure will be explored in more detail in the next section.

2.5.3 Early Differences in Jet-Front Structures

An examination of early jet-front structures and subsequent mass and momentum adjustments associated with these features for both cases is very revealing. One early elemental difference readily apparent between the D88 and J00 low-level turbulence events is the difference in upper-level jet-front systems present on the day of the event and in the 48 to 72 hours preceding the turbulence reports. Both observations and simulations reveal a

54

single-jet structure in the upper levels for the 28 Dec 1988 low-level turbulence event. Analysis at 300 hPa, 250 hPa, and 200 hPa for 26 Dec 1988 depicts a fairly vigorous polar jet (PJ) amplifying south along the Western US coast with winds of 65 to 75 ms^{-1} with a trough extending from Idaho through Southern California (Fig. 30). This jet turns northeast and is depicted as several streaks—a southwest 70 ms^{-1} pulse across the Midwest and a westerly streak of similar magnitude across the eastern half of the US. There is no compelling evidence of a subtropical jet (STJ) at this time. By 06 UTC on the 26th, there is evidence of ridging and anti-cyclonic curvature associated with the southwest (65 ms^{-1}) jet streak's right exit region located in Kansas. This ridging is reflected in the now west-northwesterly flow in the western Gulf of Mexico at 12 UTC 26 Dec 1988 (Fig. 31). This northerly surge of momentum and ridging over the central Gulf (e.g., 00 UTC 27 Dec 1988, see Fig. 26) prohibits development of the STJ in this case and as will be shown, constrains the strongest southerly flow at lower levels (i.e., 850 hPa) and warm advection to the west of the Appalachians in the hours prior to 12 UTC 28 Dec 1988. This single-jet front pattern propagates slowly to the east throughout the period as the entrance region associated with the southwesterly jet streak approaches the Ohio Valley with speeds in excess of 70 ms^{-1} by 00 UTC on the 28th and the entrance region of this strong PJ-front system impinges upon the Appalachians between 12 and 18 UTC 28 Dec 1988. Upper-level winds associated with this jet are from the southwest at 75+ ms^{-1} and become more westerly (i.e., orthogonal to the terrain) between 12 and 18 UTC on the 28th. These upper-level conditions (and subsequent low-level response discussed later) are in stark contrast to those observed for the 13 Jan 2000 case.

A significant early difference between these two low-level turbulence events is

evident in the upper air analysis for 00 UTC 11 Jan 2000. Both observations and simulations clearly depict the presence of the STJ in addition to the PJ (see Fig. 15). The key interactions for this case can be broken down into three distinct jet streak features—two PJ streaks and the STJ. Analysis from 00 UTC 11 Jan 2000 clearly depicts the STJ with its confluent left jet entrance region situated over northeast Mexico, south Texas and the western Gulf of Mexico (this feature likely formed in response to height rises over the Mexican plateau). Leftward directed ageostrophy is apparent (as expected) in this entrance region and the STJ exit region is located off the northeast coast of Florida as implied by diminishing winds and rightward directed ageostrophy. These circulations are verified by trajectory analysis of parcels injected into this region with leftward flow (entrance region) south of Texas/Louisiana and rightward flow (exit region) off the East Coast (see Fig. 32). Winds associated with the STJ are from the west at 50 to 55 ms^{-1}. The STJ continues to slowly propagate to the east and by 00 UTC 12 Jan 2000, the entrance region is located through southeast Texas and along the Louisiana coast as 45 to 50 ms^{-1} westerlies transit the Gulf Coast states. By 12 UTC 12 Jan 2000, the now 40 to 45 ms^{-1} westerly entrance region is located along the Mississippi/Florida coast. At this time (12/00 – 12/12 UTC), the first of two PJ streaks to transit the Appalachians during the period from 12/00 to 14/00 UTC possesses a fairly straight right exit region (WNW flow at 60 ms^{-1}) with rightward directed ageostrophy located in the southern plains (Fig. 33). The second PJ streak to play a significant role in organizing the dynamics ultimately responsible for low-level turbulence in J00 exhibits more curvature than the first PJ streak which transitted 24 to 36 hours earlier. This second PJ streak encroaches upon the Appalachians (as it amplifies) between 12 UTC 13 Jan 2000 and 00 UTC 14 Jan 2000 with winds orthogonal to the Appalachians (from the west) and increasing from 50 to 70 ms^{-1} at

300 hPa (Fig. 34). This QG polar jet-front system's left entrance region helps bring stratospheric, high IPV air to the mid- and lower-levels and drives the surface front off the East Coast. Unlike the 28 Dec 1988 case, upper-level flow is essentially perpendicular to the terrain throughout the day of the accident. Although the incident angle of the jet to the Appalachians (particularly at low levels) and overall large-scale wave pattern play a role in the generation of a hydrostatic mountain wave and an accompanying cold upfold (as will be discussed in the following chapter), as well as influencing the Appalachian leeside's frontogenesis/frontolysis (as discussed in the previous section), the interaction between the multiple upper-level jet streaks present in the 13 Jan 2000 case (absent in the 28 Dec 1988 case) is also important to the subsequent intensity response of turbulence to the earliest stages of the hypothesis presented in Chapter 1. The key interactions between the PJ streaks and the STJ present in the hours and days (11/00 – 14/00 UTC) prior to the NASA accident report (13/1931 UTC) ultimately result in an environment more predisposed to severe to extreme low-level turbulence than does the classical QG, single-jet antecedent environment in the 28 Dec 1988 event.

These key interactions begin with the STJ entrance region and its concomitant transverse ageostrophic circulation. This direct circulation increases low-level heights over Texas and the northern Gulf of Mexico in the left entrance region as it slowly propagates to the east from 00 UTC 11 Jan 2000 through 12 Jan 2000 (Fig. 35). During this time, the first PJ's relatively straight, right exit region maintains high heights (through mass flux convergence) over the Southern Plains until early on 12 January. Additionally, from 16 UTC 11 Jan 2000, low-level warm advection is apparent from the Mexican Plateau and east of the Rocky Mountains through the central United States (Fig. 36). The STJ left entrance region

57

acts to cap this warm air along the Gulf Coast late on the 11th and early on the 12th. Between 00 UTC and 12 UTC on 12 January (at approximately 09 UTC), the rapidly transitting first PJ's right exit region moves off the east coast and its right entrance region becomes aligned with the more slowly propagating STJ's left entrance region (Fig. 37). As a result, heights begin to fall to the right of the PJ's right entrance region and rise to the left of the STJ's left entrance region. This scenario sets up a relative lower-tropospheric pressure gradient force between the warm, capped Mexican plume of air along the Gulf and the colder continental air to the left of the first PJ streak. This relative gradient from East Texas to Tennessee enables the warm air along the Gulf to move to the north through the Tennessee Valley (as indicated in simulations, 12 UTC 12 Jan 2000 850 hPa analysis, and the 12 and 13 Jan 2000 soundings for Nashville, TN). Meanwhile, the second, more curved PJ streak begins moving across the Central United States (exit region located in central – east Nebraska at 06 UTC 12 Jan 2000). This second PJ streak plays a vital role in setting up the pre-turbulence environment in this case as well. The combination of the STJ and the first PJ streak's entrance regions enable the warm Mexican air to be transported northeast along the Piedmont region from approximately 09 UTC on 12 January to the Southern Appalachians early on the 13th (Fig. 38). By 12 UTC 13 Jan 2000, the second PJ streak's right exit region and its accompanying transverse ageostrophic circulation crosses the Appalachians along the West Virginia/Pennsylvania border. This exit region circulation is fairly vigorous (see Fig. 39) and facilitates the continued transport of the previously supplanted warm air (from the pressure gradient force set up between the STJ and first PJ streak on the 12th) as well as a second surge of warm air to the north into northern Virginia, western Maryland, and south-central Pennsylvania—east of the Appalachians where it resides atop the southward moving colder surface air (Fig. 40).

This low-level warm air east of the Alleghenies alters the hydraulic environment and affects the strength of terrain blocking and the subsequent mountain-wave induced isentropic upfold east of the mountains so crucial to the early stages of the hypotheses described in Chapter 1 and detailed in Chapter 3. The presence of the STJ in J00 clearly distinguishes it from the D88 case and is significant in differentiating the pre-turbulence environments along and east of the Appalachian Mountains. The STJ's left entrance region acts to cap warm low-level Mexican air along the Texas and Louisiana coasts until the first PJ streak's right entrance region and its accompanying ageostrophic circulation and height falls associated with mass flux divergence allow the northward transport of this warm air into the Tennessee Valley and Piedmont region after 09 UTC 12 Jan 2000. The second PJ streak's right exit region completes this process by moving this warm air into western Maryland and south-central Pennsylvania (Bedford County) in advance of the mountain wave dynamics and upfold discussed in the next chapter. The lack of a STJ in D88 results in the absence of warm air from the Mexican Plateau east of the Appalachians and affects the environmental response that ultimately determines the type of convection and intensity of turbulence observed. Additionally, the warm low-level air is transported above cold surface air that dammed against the Appalachians in the aftermath of the first PJ. A more detailed analysis of low-level temperatures for these two cases is presented in the next section.

2.5.4 Differences in Low-level Temperatures

As discussed in the previous section, a primary difference between the two cases studied in this research is the absence of a STJ in D88. This difference in the hours leading up to hydrostatic mountain wave formation, convection, and turbulence manifests itself in the

59

different temperature patterns through Maryland and south-central Pennsylvania. The 28 Dec 1988 case only possesses a single upper-level jet structure and as a result, has only a single surge of warm air located to the west of the Appalachians prior to the formation of a narrow cold frontal rainband (NCFR) and subsequent low-level turbulence east of the Appalachians. The surge of warm air in D88 is essentially coupled to the single PJ-frontal system and its exit region's transverse ageostrophic circulation as described in KK91. Output from the 40-km simulation was examined for the 72 hours from 00 UTC 26 Dec 1988 through 00 UTC 29 Dec 1988 in order to determine the advection pattern at the lower levels as well as the behavior and translation of the PJ-front system. Due to the absence of a STJ in this case, low-level return flow was essentially dominated by the QJ PJ-front system and as a result, there is only one discernible fetch of warm air present in this region. This warm air is transported northward through the central portion of the United States on 27 Dec 1988 after 15 UTC. This swath of warm air moves north and east as the QG system moves from west to east. As a result, the warmer temperatures tend to be west of the Appalachians prior to mountain wave formation and preceding frontal passage on the 28th. In other words, there is no warm advection east of the Appalachians downstream from the advection coupled to the primary QG system. Essentially, temperatures in south-central Pennsylvania (the region of focus in the next chapter) on both sides of the Alleghenies prior to terrain/low-level jet interaction are essentially equivalent for this case and the low-level inversion is set up west of the mountains, not to the east as in J00. In fact, the temperature spread across the Alleghenies for 28 Dec 1988 never exceeds 4 ^{0}C. On the other hand, there are essentially two surges of warm air at low levels (850 hPa) in J00 case, one of the two surges is located along and east of the Appalachians (due to the early presence of the STJ).

The presence of the STJ early in the J00 case has a profound effect on low-level temperatures east of the Appalachian Mountains leading up to the pre-turbulence environment. As discussed in the previous section, alignment of the first PJ streak's right entrance region with enhanced heights over the Gulf Coast associated with the STJ enabled warm air from the Mexican Plateau to move to the northeast through the Tennessee Valley and along the southern Appalachians. Upper air observations from the Nashville (BNA) RAOB site for this period show the temperature climbing from 7 ^{0}C to 15 ^{0}C between 12 UTC on the 12th and 00 UTC on the 13th at 850 hPa. This is rather warm air for January at this altitude and latitude and is 9 ^{0}C warmer than that of 00 UTC on the 12th and more than 15 ^{0}C greater than the climatological average. A skew-T sounding for BNA at 00 UTC 13 Jan 2000 (Fig. 41) clearly indicates this warm, elevated mixed layer—consistent with the notion that warm Mexican air is overrunning the surface layer at 850 hPa as it moves from the southwest and ultimately reaches south-central Pennsylvania (Bedford County) by 12 UTC 13 Jan 2000 after interacting with the second PJ streak's right exit region and a secondary warm surge associated with it (moving in from the west). Temperatures at 850 hPa in this region have a cross-mountain variation twice that of the 28 Dec 1988 case (7 to 8 ^{0}C) with temperatures west of the Alleghenies near 0 ^{0}C and temperatures to the east greater than 7 ^{0}C. Analysis of a 72-hr 850-hPa temperature trend from 00 UTC 11 Jan 2000 through 00 UTC 14 Jan 2000 indicates warm advection of Mexican Plateau air through BNA and east of the Appalachians (advected in the manner previously described) as well as warm advection attached to the PJ-front system and its exit region (in a manner similar to that of D88). As will be shown in the following chapters, it is the warm advection east of the Appalachians overrunning cold surface air that distinguishes J00 from D88 thus producing a

61

stable layer in J00 that is absent in D88. Consistent with differences in temperature advection and temperature patterns along the Appalachians, these two cases also exhibit differences in low-level potential vorticity. These differences reflect the quasi-geostrophic differences in jet structures, i.e., multiple jet streaks with geostrophic deformation in J00 and a single jet streak in D88.

2.5.5 Differences in Potential Vorticity

As with the different low-level temperature structures for the two low-level turbulence cases studied, there are some distinctive differences in the low-level potential vorticity (PV) structures as well—both in terms of advection patterns and origins of low-level PV. These differences can be related to the different jet-front structures previously described.

Analysis of low-level PV for D88 is performed for the 72 hours prior to NCFR and low-level turbulence formation. Low-level PV in this case is almost entirely associated with the large-scale QG system and the tropopause fold and stratospheric intrusion associated with the left entrance region of the polar jet—in the manner previously described by KK91 and Danielsen (1968). The low-level PV is broad in meridional extent, essentially coexisting with the large-scale surface frontal system, and is fairly coherent and indicated as early as 00 UTC on 27 Dec 1988 east of the Rocky Mountains in the central US (Fig. 42). This low-level PV maximum tracks east with the large-scale system—there is no significant, independent secondary PV maximum east of the Appalachians prior to surface frontal passage for this case.

On the other hand, the presence of the STJ and southern position of the PJ early in the

period (i.e., 60 – 70 hours prior to the reported turbulence) for J00 create a very different low-level PV pattern. A trace of low-level PV from 00 UTC 11 Jan 2000 through 14 Jan 2000 is very revealing. Low-level PV maxima are visible east of the Rocky Mountains through Oklahoma and Texas as early as 11/02 UTC. By 11/06 UTC, a 1.5 to 2.0 PVU maximum is evident along the Edwards Plateau in west Texas (Fig. 43). The origin of this low-level PV maximum is likely the result of confluence between the right exit region of the first PJ streak and the left entrance region of the STJ. An analysis of PV at 200 hPa during this time indicates PV greater than 5.5 PVU throughout west Texas. Additionally, low-level flow across this region (and points West) is generally from the west (i.e., orthogonal to elevated terrain) indicating probable mountain downslope contribution to low-level PV in the region. This low-level PV maximum, initially apparent in the Edwards Plateau, is coherently traceable (as it moves east in advance of low-level thickness increases associated with the mass flux convergence of the PJ/STJ circulations) through east Texas, northern Louisiana/Arkansas by 12/05 UTC and into the Tennessee Valley and through the Piedmont region by 12/12 UTC (see Fig. 44) where it progresses to the northeast and arrives in northern Virginia, Maryland, and south-central Pennsylvania in advance of a secondary PV maximum associated with the large-scale tropopause fold with the second PJ's left entrance region. This upstream PV maximum is similar to the low-level PV maximum in D88. This phasing creates an environment east of the Alleghenies that is high in cyclonic vorticity ahead of the large-scale surface cold front for J00. In contrast, the atmosphere in advance of the cold front for D88 does not possess this enhanced cyclonic vorticity. As a result, microscale tilting and vertical convergence processes have more large-scale cyclonic vorticity to work with for J00—thus, X- and Y- space vorticity, necessary for microvortex

formation, will be larger for J00 than for D88 (as Chapter 4 will demonstrate). This enhanced cyclonic vorticity is also consistent with the low-level frontal system already in place east of the Appalachians for J00 and absent in D88.

2.6 Summary and Conclusions

The synoptic scale atmospheric environments prior to two cases of widespread low-level turbulence east of the Appalachian Mountains have been examined in this chapter. Both events occurred during the winter months, during the same time of day, and at similar altitudes. Surface analyses for both cases indicated a cold front along the Appalachians that moved through the region of interest between 17 and 21 UTC. Observations and simulations indicate these cases possess many of the large-scale turbulence precursors detailed in Kaplan et al. (2003 a,b,c) as favorable for turbulence formation. Both the 28 Dec 1988 and 13 Jan 2000 events occurred in jet entrance regions with upstream curvature (although curvature is more substantial in J00). Both occurred in a region of strong cold advection with convection within 100 km of the turbulence reports based on radar, satellite, and simulations. In spite of these similarities and the presence of multiple parameters identified as turbulence precursors, resultant turbulence intensities (as well as frontal structure and convection geometry—to be discussed in the remaining chapters) at low-levels east of the Appalachian Mountains differ for these two cases (e.g., there is a similar number of low-level turbulence reports, but the percentage of severe and greater turbulence reports for 13 Jan 2000 is more than twice that for 28 Dec 1988). In an effort to identify some of the causes of these differences, early deviations in the large-scale wave patterns and overall jet-front systems were identified through the use of available observations and simulations.

Large-scale wave patterns display some distinct differences. The D88 event displays a meridional wave pattern with ridging over the East Coast—such a pattern does not favor frontogenesis east of the Appalachians. The J00 wave pattern is much more zonal with a vortex over Quebec and a southern stream (associated with the STJ) combining to enhance

65

deformation, convergence, and frontogenesis east of the Appalachians. Additionally, flow for D88 is essentially uni-directional at all levels. The J00 event displays flow/parcels arriving from different directions at different altitudes. The large-scale shearing and stretching deformation further predisposes the 13 Jan 2000 environment to frontogenesis east of the Appalachians Mountains. Additionally, these wave patterns affect the orthogonality of the winds to the terrain—the flow for 28 Dec 1988 is generally from the southwest with flow for 13 Jan 2000 much more westerly and hence, more perpendicular to the elevated terrain. In addition to these differences in overall large-scale wave structure, these two cases have rather different jet-front structures in the 24 to 72 hours prior to the turbulence events.

The primary difference in the jet-front structures for these two cases is the presence of the STJ in J00 (absent in D88). The STJ and its associated transverse ageostrophic circulations distinguishes J00 event from that of D88 and ultimately plays an important role in the advection of low-level warm air along and east of the Appalachians. Due to the absence of a STJ in D88 case, the surge of low-level warm air (i.e., 850 hPa) is essentially coupled to the single PJ-frontal system and its exit region's transverse ageostrophic circulation. As a result, there is only one discernible fetch of warm air present in this case as this warm air moves north and east as the QG system proceeds from west to east. Thus, the warmer temperatures tend to be west of the Appalachians prior to mountain wave formation and prior to frontal passage on the 28th. There is no warm advection east of the Appalachians downstream from the advection coupled to the primary QG system. On the other hand, there are essentially two surges of warm air at low levels in J00 case, including an additional surge along and east of the Appalachians (due to the early presence of the STJ).

For J00, alignment of the first PJ streak's right entrance region, along with enhanced

66

heights over the Gulf Coast associated with the STJ on 12 Jan 2000, enabled warm air from the Mexican Plateau to advect to the east and northeast through the Tennessee Valley and along the southern Appalachians. This warm air from the southwest is east of the Appalachians and ultimately combines with a second fetch of warm air associated with the second PJ streak's right exit region. This warm air—east of the Alleghenies, overrides colder surface air, which increases the static stability, and plays a significant role in the blocking of flow over the elevated terrain and the subsequent strength of the isentropic upfold shown to be important to low-level mesoscale and microscale frontogenesis, convection, and turbulence formation in Chapters 3 and 4. In addition to these differences in low-level temperature patterns, these two cases display similar differences in low-level potential vorticity maxima.

Differences in low-level PV structure and advection patterns are readily apparent for the two low-level turbulence cases studied in this research. These differences are coupled to the different upper-level wave patterns and jet structures present prior to, and leading up to the events. The low-level PV advection in D88 is almost entirely associated with the large-scale QG jet-front system and the tropopause fold associated with the PJ's left entrance region. This low-level PV maximum is essentially meridional in extent and tracks east with the system as it advances. As with the low-level warm air for this case, there is no secondary significant low-level PV maximum east of the Appalachians prior to frontal passage. On the other hand, and in a fashion similar to the low-level warm advection pattern, two distinct low-level PV maxima are evident for J00. The first, associated with the STJ and first PJ streak, is coherent and traceable from along the Edwards Plateau in west Texas (early on 11 Jan 2000) to the east (in advance of low-level height rises) and ultimately to the northeast

67

through Tennessee and the Carolinas. This first PV maximum ultimately ends up in south-central Pennsylvania in advance of a second low-level PV maximum associated with the left entrance region of the second PJ streak. The presence of the additional low-level PV maximum in this case (absent in D88) creates an environment that is high in cyclonic vorticity ahead of the large-scale cold front.

Both the 28 Dec 1988 and 13 Jan 2000 cases contained an inordinate number of low-level turbulence reports. These cases were similar in many ways and possessed many of the large-scale signals found in Kaplan et al. (2003 a,b,c) to be precursors to turbulence formation. In spite of these similarities, the general intensity of the reported low-level turbulence was significantly different for these two events. Some large-scale differences were identified, to include wave patterns, jet-front structures, low-level temperature advection, and low-level PV. How these differences affect the turbulence-formation hypothesis presented in Chapter 1 and how well each case conforms to the early stages of this hypothesis is the focus of the following chapter.

Table 1. MASS/NHMASS Model (version 6.0b2) Characteristics

MODEL NUMERICS

- Non-hydrostatic primitive equation model (hydrostatic option for coarse runs)
- 3-D equations for u, v, T, q, and p
- Cartesian grid on a polar stereographic map
- Sigma-p terrain-following vertical coordinate system
- Vertical coverage from approximately 10m to 16,000m
- Energy-absorbing sponge layer near top of domain
- Fourth-order horizontal space differencing on an unstaggered grid
- Split-explicit time integration schemes (a) forward-backward for the gravity mode and (b) Adams-Bashforth for the advective mode
- Time-dependent lateral boundary conditions
- Positive-definite advection scheme for scalar variables
- Massless tracer equations for ozone and aerosol transport

INITIALIZATION

- First guess/lateral boundary conditions from NCEP Reanalysis data (D88) or ETA data (J00)
- First guess from next larger-scale simulation
- High resolution terrain database derived from observations
- High resolution satellite or climatological sea surface temperature database
- High resolution land use classification scheme
- High resolution climatological subsoil moisture database derived from antecedent precipitation
- High resolution normalized difference vegetation index

PBL SPECIFICATION

- 1.5-order Turbulence Kinetic Energy PBL
- Surface energy budget
- Soil hydrology scheme
- Atmospheric radiation attenuation scheme

MOISTURE PHYSICS

- Grid-scale prognostic equations for cloud water and ice, rainwater, and snow
- Kain-Fritsch convective parameterization scheme

69

Table 2. MASS/NHMASS Numerical Simulations Performed

Initialized (UTC)	Duration (hours)	Resolution (km)	Grid Dimensions (x,y,z)	Modifica-tions	Hydrostatic /Non-Hydrostatic
01/13/00 0000	24	30	100,100,46	None	H
01/13/00 0000	24	30	100,100,46	Smooth Terrain	H
12/28/88 0000	24	30	120,100,46	None	H
12/28/88 0000	24	30	120,100,46	Smooth Terrain	H
01/13/00 0600	18	15	150,150,46	None	H
01/13/00 0600	18	15	150,150,46	Smooth Terrain	H
12/28/88 0600	18	15	150,150,46	None	H
12/28/88 0600	18	15	150,150,46	Smooth Terrain	H
01/13/00 1200	12	6	170,170,46	None	NH
01/13/00 1200	12	6	170,170,46	Smooth Terrain	NH
12/28/88 1200	8	6	200,200,46	None	NH
12/28/88 1200	8	6	200,200,46	Smooth Terrain	NH
01/13/00 1630	5	2	200,200,46	None	NH
01/13/00 1630	5	2	200,200,46	Smooth Terrain	NH
01/13/00 1630	5	2	200,200,46	No Latent Heat	NH
12/28/88 1600	4	2	200,200,46	None	NH
12/28/88 1600	4	2	200,200,46	Smooth Terrain	NH
12/28/88 1600	4	2	200,200,46	No Latent Heat	NH
01/13/00 1830	3	1	200,200,46	None	NH
01/13/00 1830	3	1	200,200,46	Smooth Terrain	NH
01/13/00 1830	3	1	200,200,46	No Latent Heat	NH
12/28/88 1800	2	1	200,200,46 *	None	NH
12/28/88 1800	2	1	200,200,46	Smooth Terrain	NH
12/28/88 1800	2	1	200,200,46	No Latent Heat	NH
01/13/00 1915	1.67	0.5	200,200,46	None	NH
01/13/00 1915	1.67	0.5	200,200,46	Smooth Terrain	NH
01/13/00 1915	1.67	0.5	200,200,46	No Latent Heat	NH
12/28/88 1840	1	0.5	200,200,46	None	NH
12/28/88 1840	1	0.5	200,200,46	Smooth Terrain	NH
12/28/88 1840	1	0.5	200,200,46	No Latent Heat	NH
01/11/00 0000	72	40	100,100,46	None	H
12/26/88 0000	72	40	120,100,46	None	H
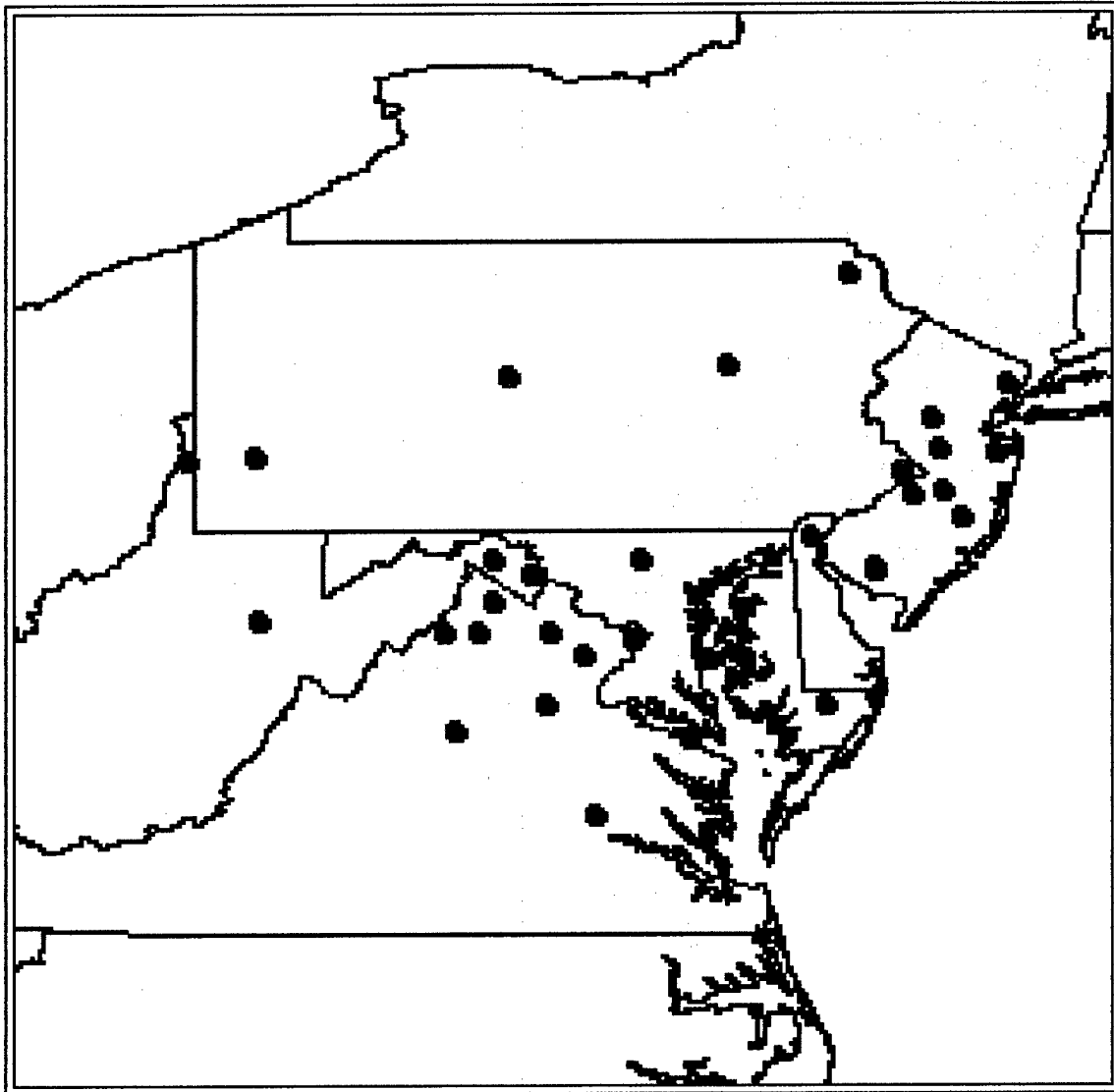
Figure 1. Moderate to Severe turbulence reports for 28 Dec 1988.
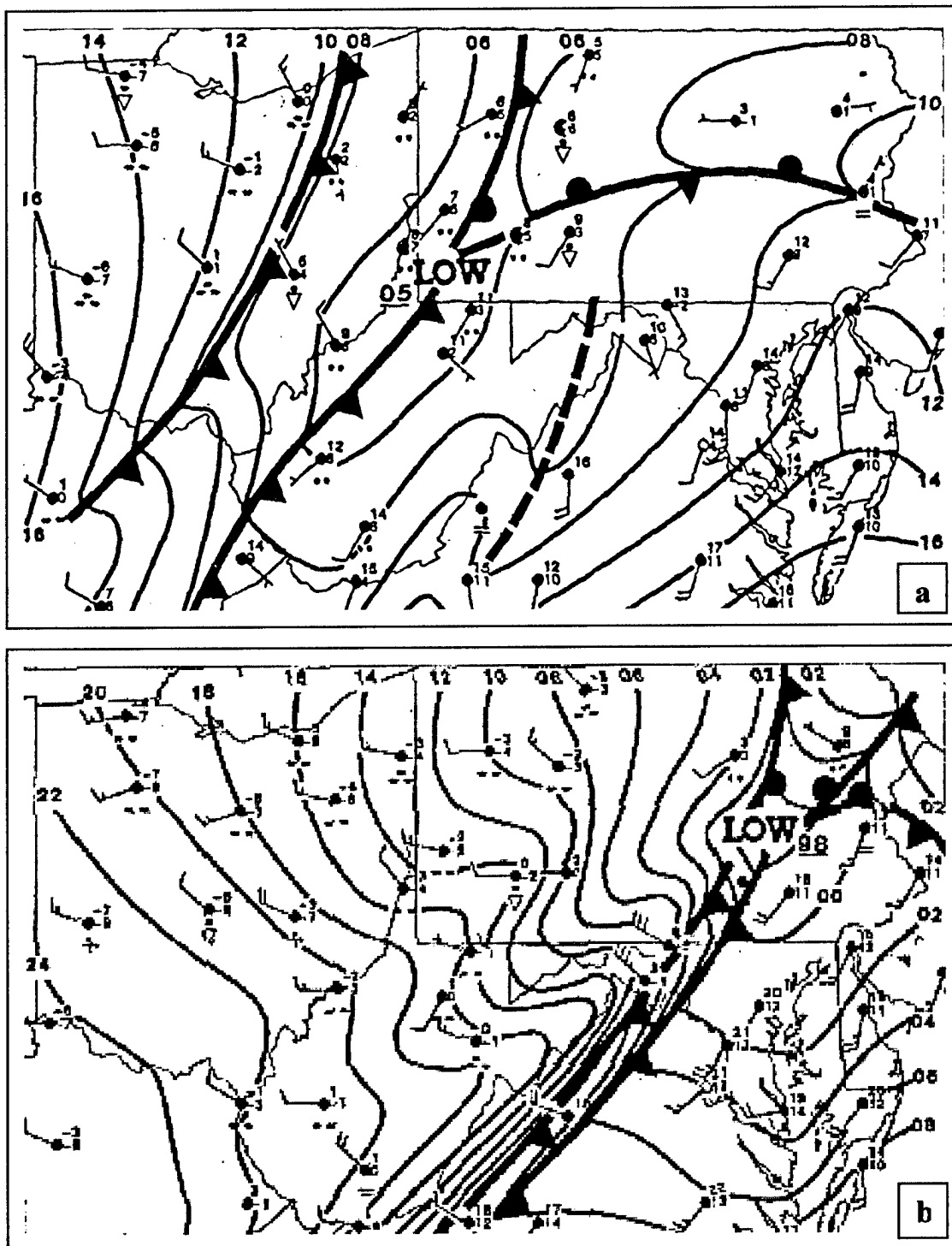
Figure 2. Subjective mesoanalysis of surface fronts, isobars (hPa), and winds (ms^{-1}) valid 28 Dec 1988, (a) 1400 UTC and (b) 1900 UTC (after Koch and Kocin 1991)
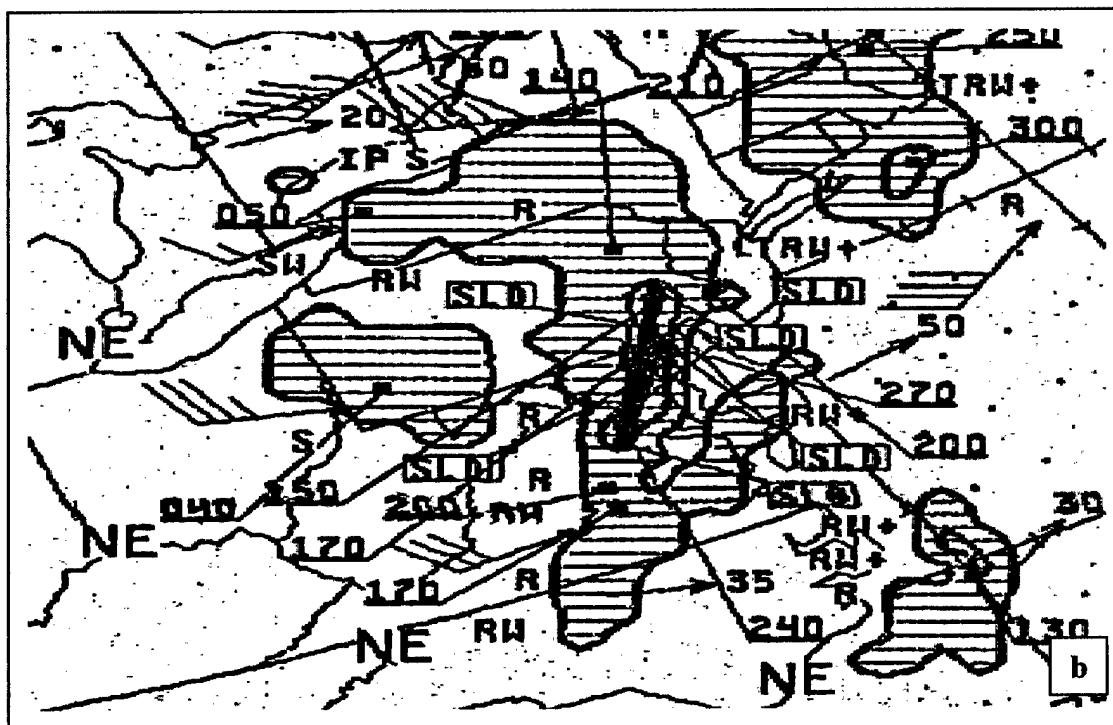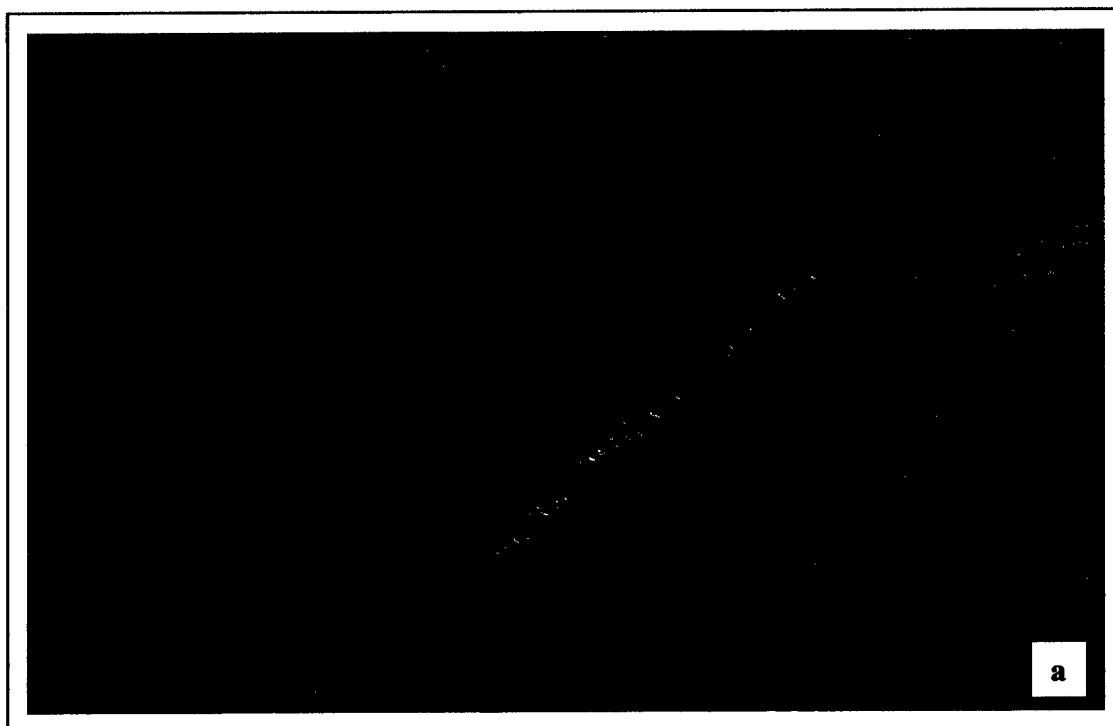
Figure 3. (a) GOES-7 Visible satellite imagery at 2003 UTC 28 December 1988 and
(b) RADAR summary valid 2030 UTC 28 December 1988

73

Figure 4. NWS 850 hPa analysis valid 1200 UTC 28 Dec 1988.

Figure 5. NWS 700 hPa analysis valid 1200 UTC 28 Dec 1988.
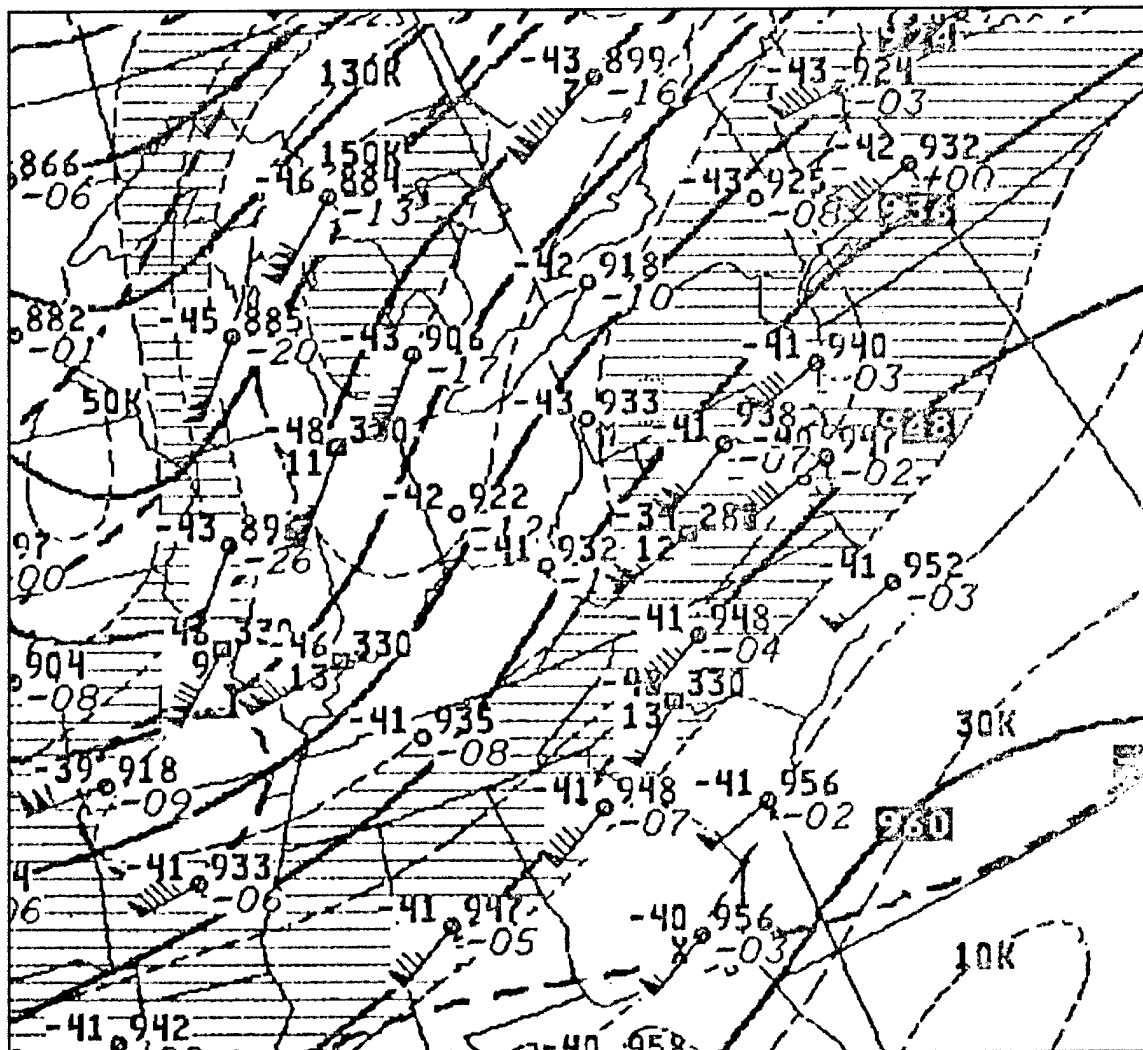
Figure 6. NWS 300 hPa analysis valid 12 UTC 28 Dec 1988.
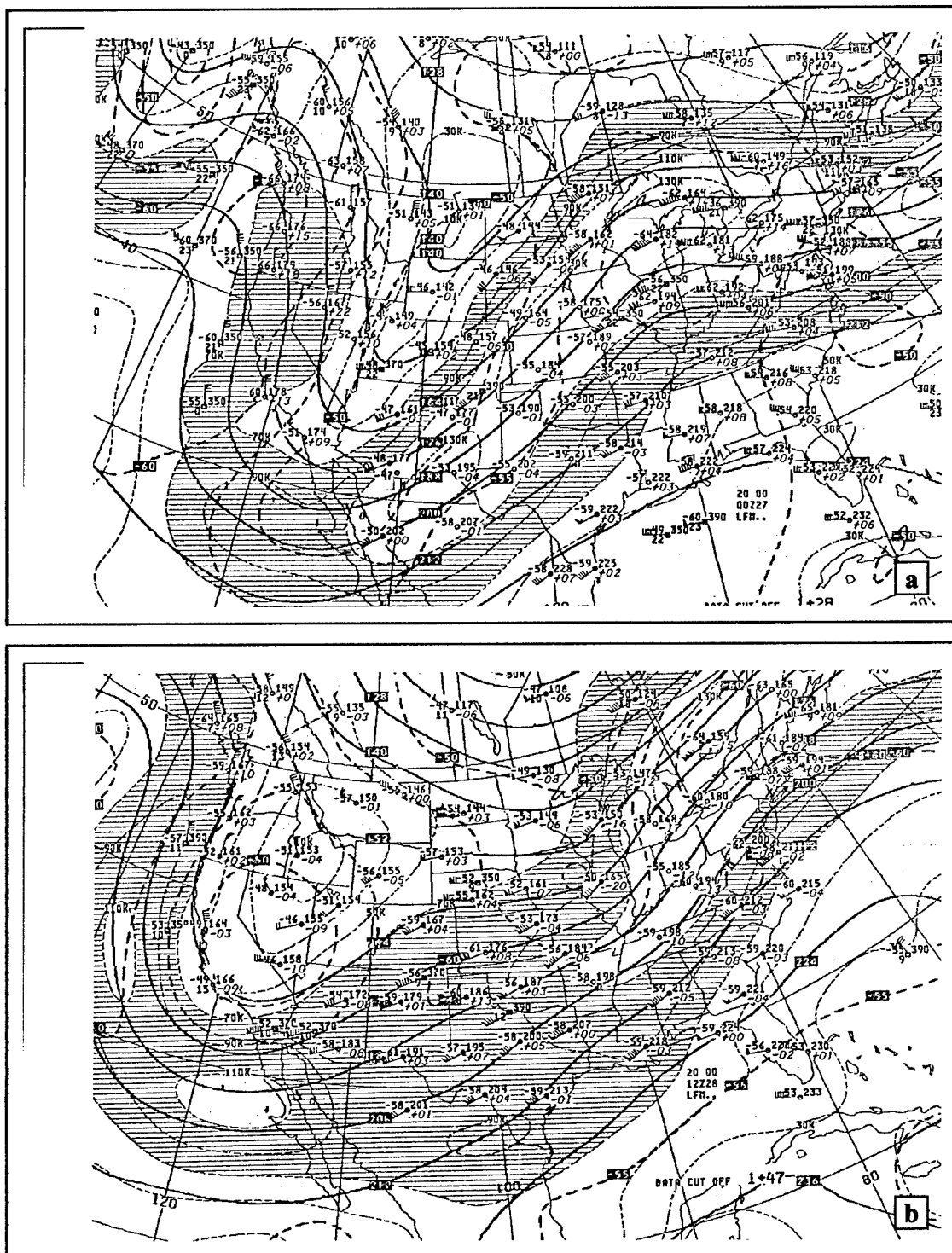
Figure 7. 200 hPa analysis valid (a) 00 UTC 27 Dec 1988, (b) 12 UTC 28 Dec 1988.
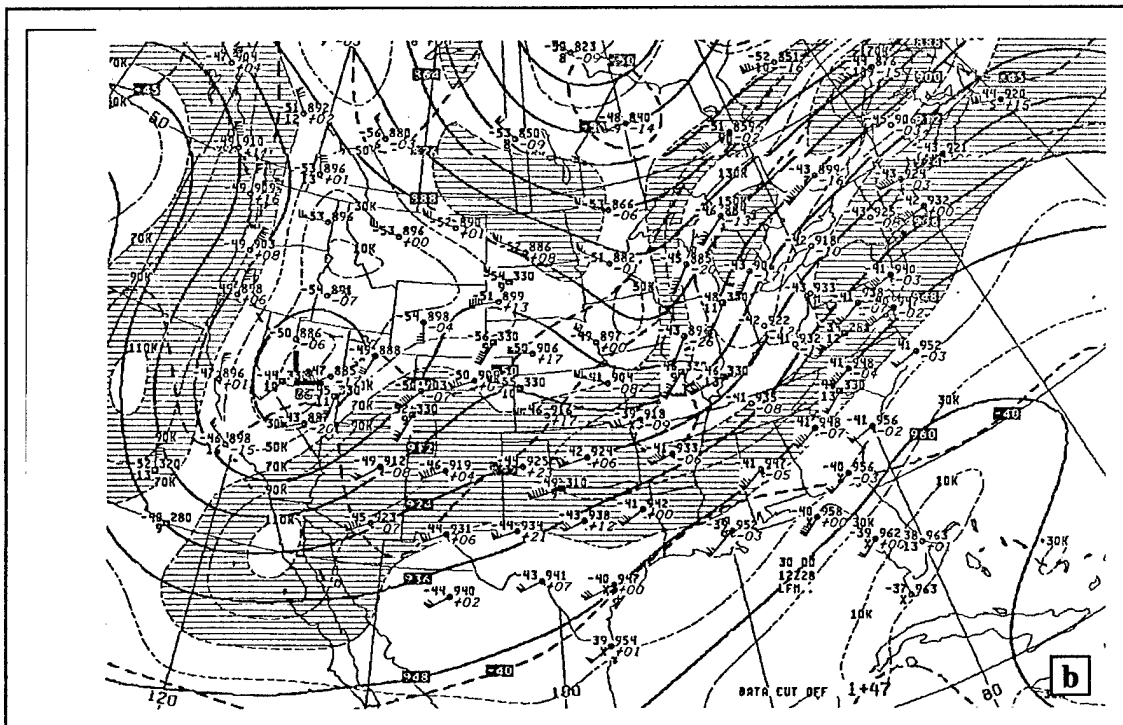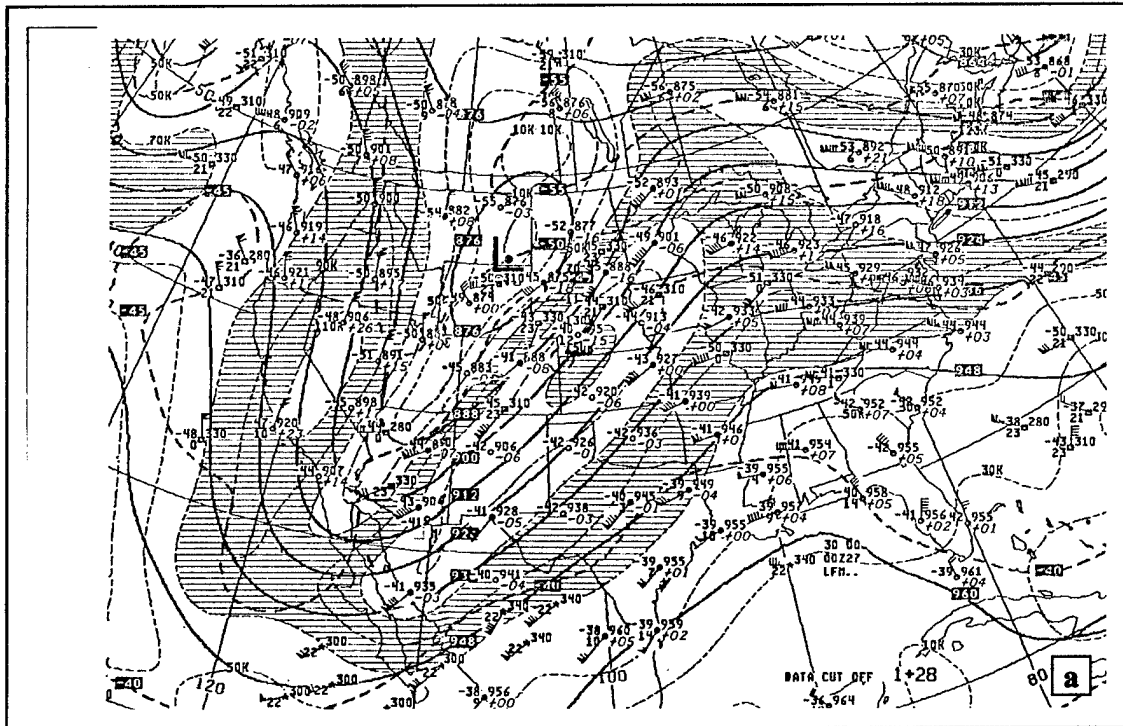
Figure 8. NWS 300 hPa analysis valid (a) 00 UTC 27 Dec 1988, (b) 12 UTC 28 Dec 1988.
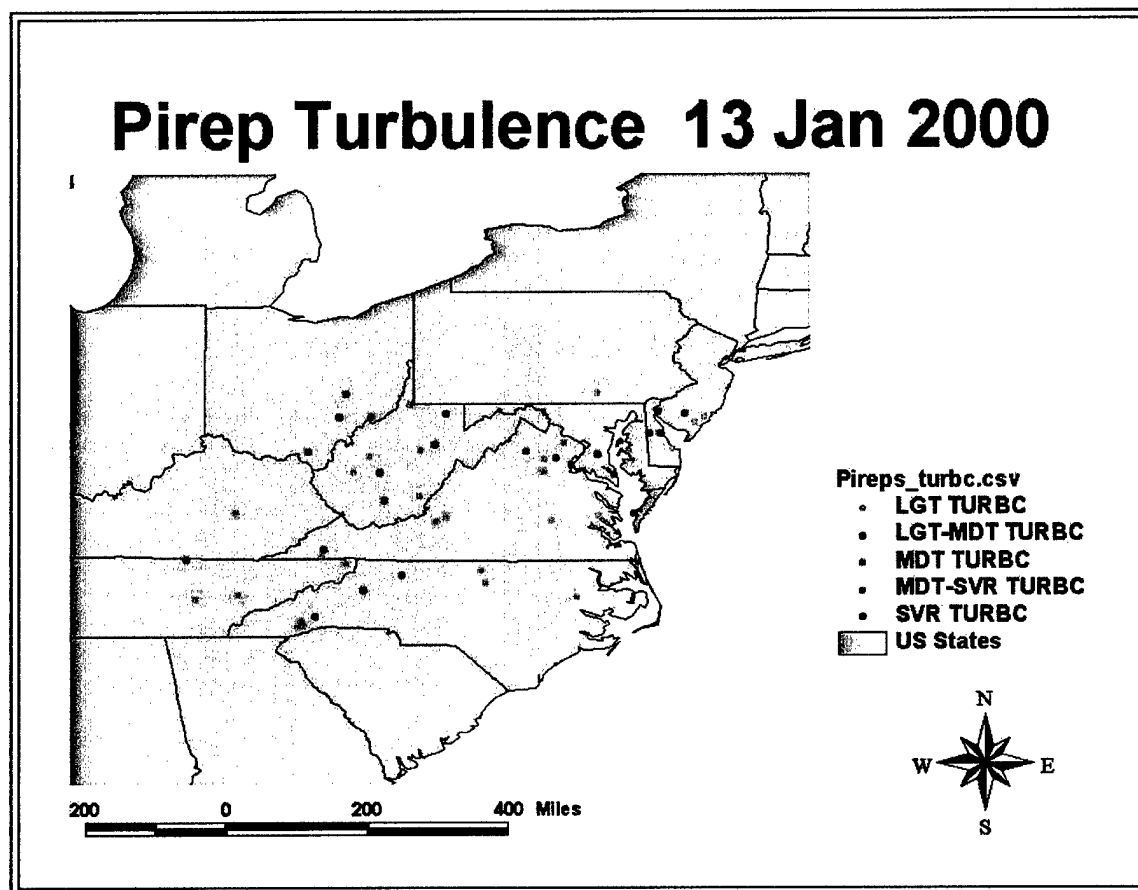
Figure 9. PIREP turbulence reports for 13 Jan 2000.
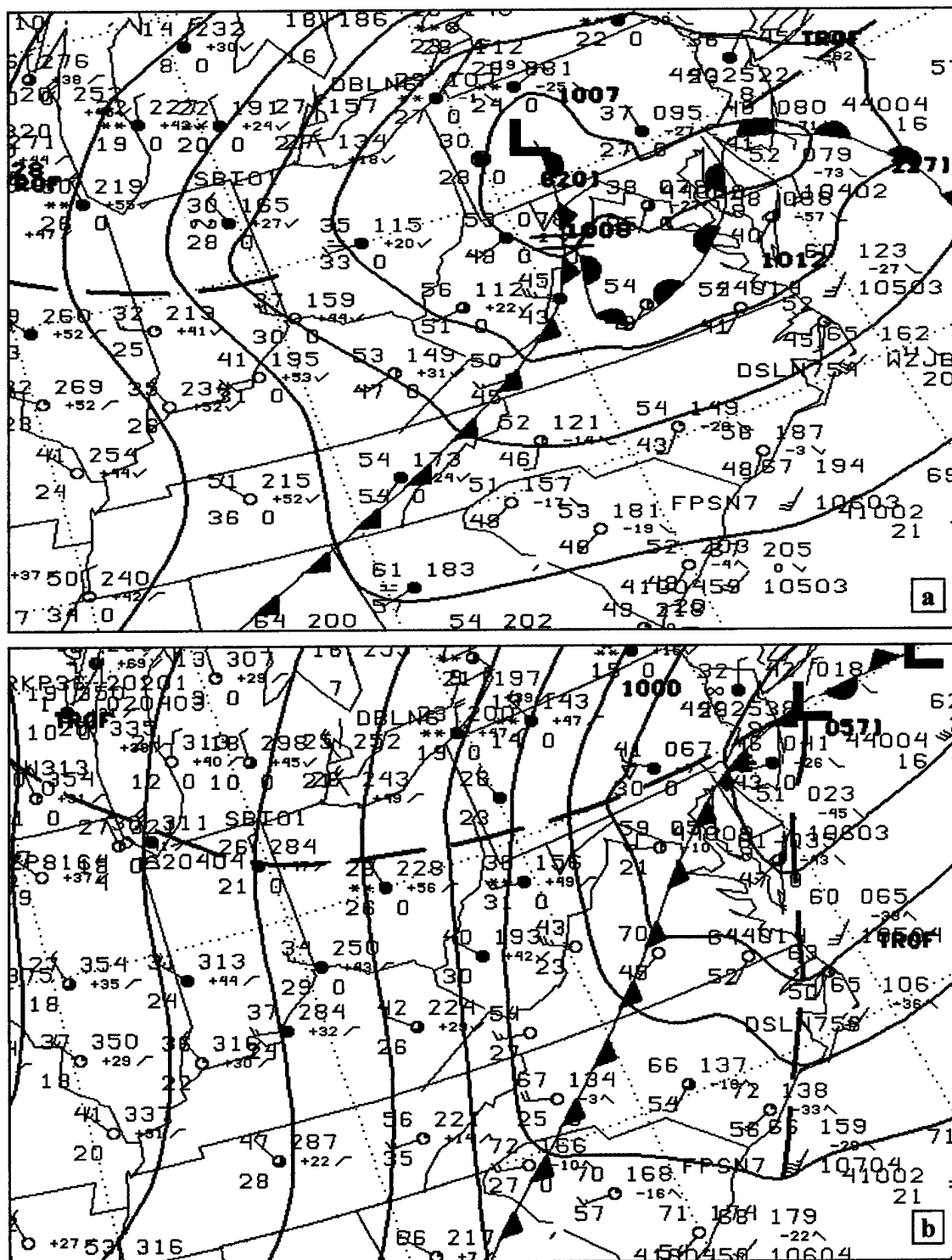
Figure 10. Surface analysis valid (a) 12 UTC, (b) 18 UTC for 13 January 2000.
Note: KILG is identified by red triangle in figure (b).

80
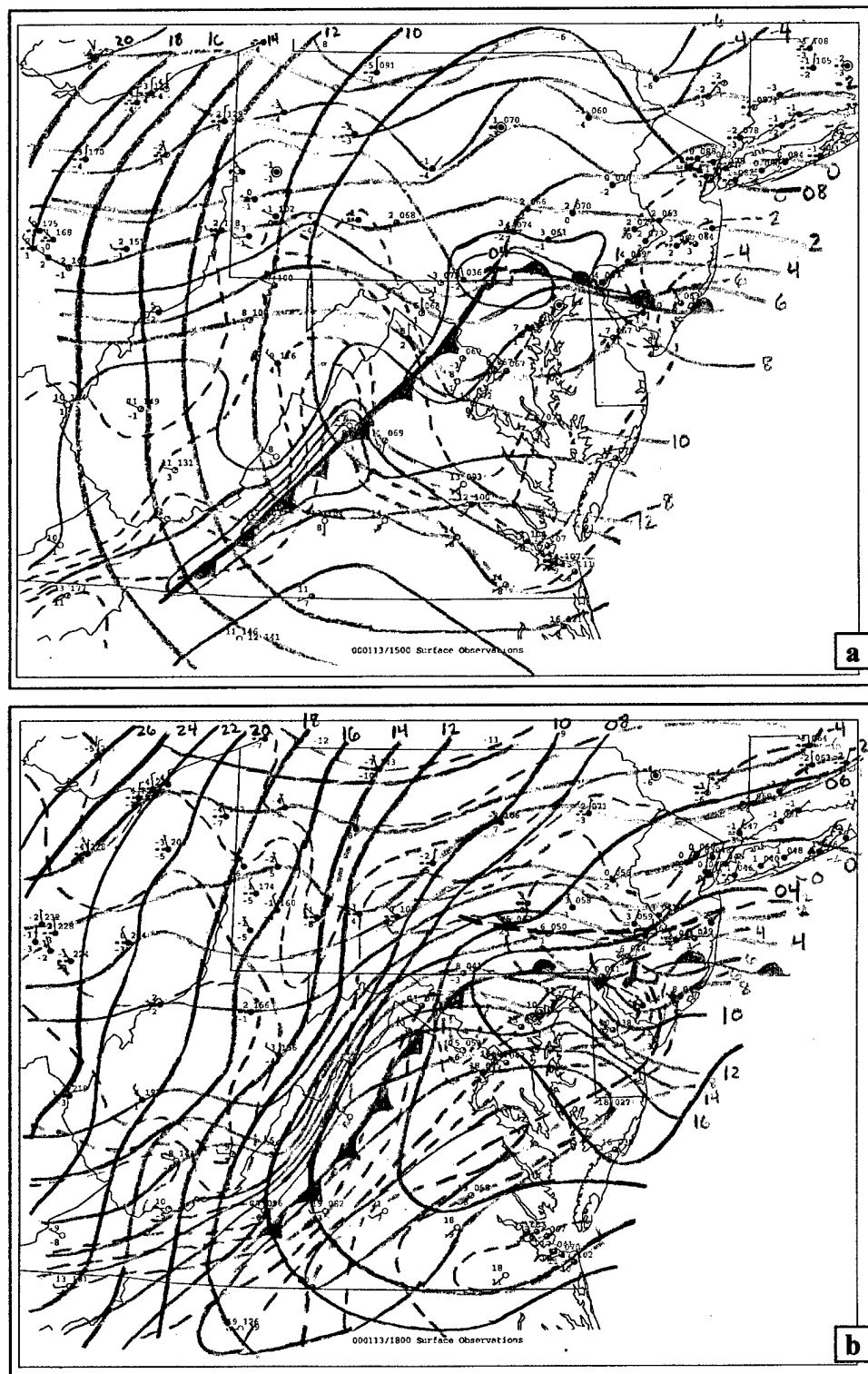
Figure 11. Surface mesoanalysis valid 13 Jan 2000 (a) 1500 UTC, (b)
1800 UTC. Pressure is contoured every 2 hPa (black), temperature is
contoured every 2 ^{0}C (red), and dewpoint is contoured every 2 ^{0}C (green).

81
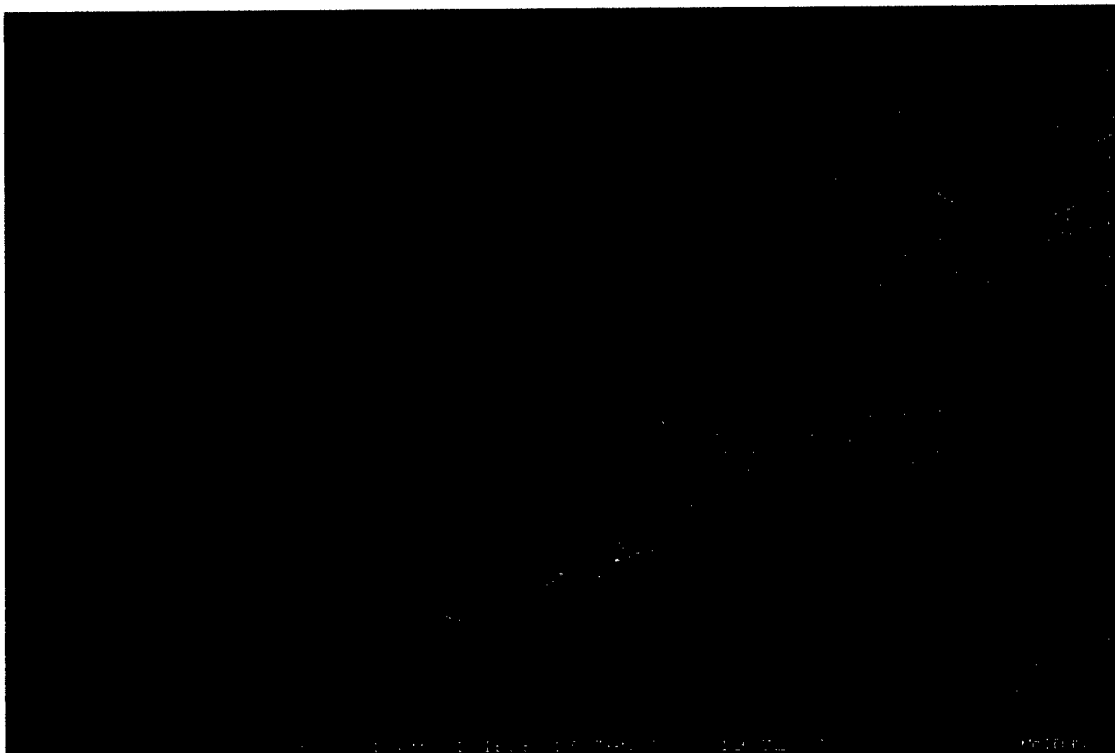
Figure 12. GOES 1-km visible satellite imagery valid 1932 UTC 13 Jan 2000.

KILG PRESSURE TRACE 13 JAN 2000
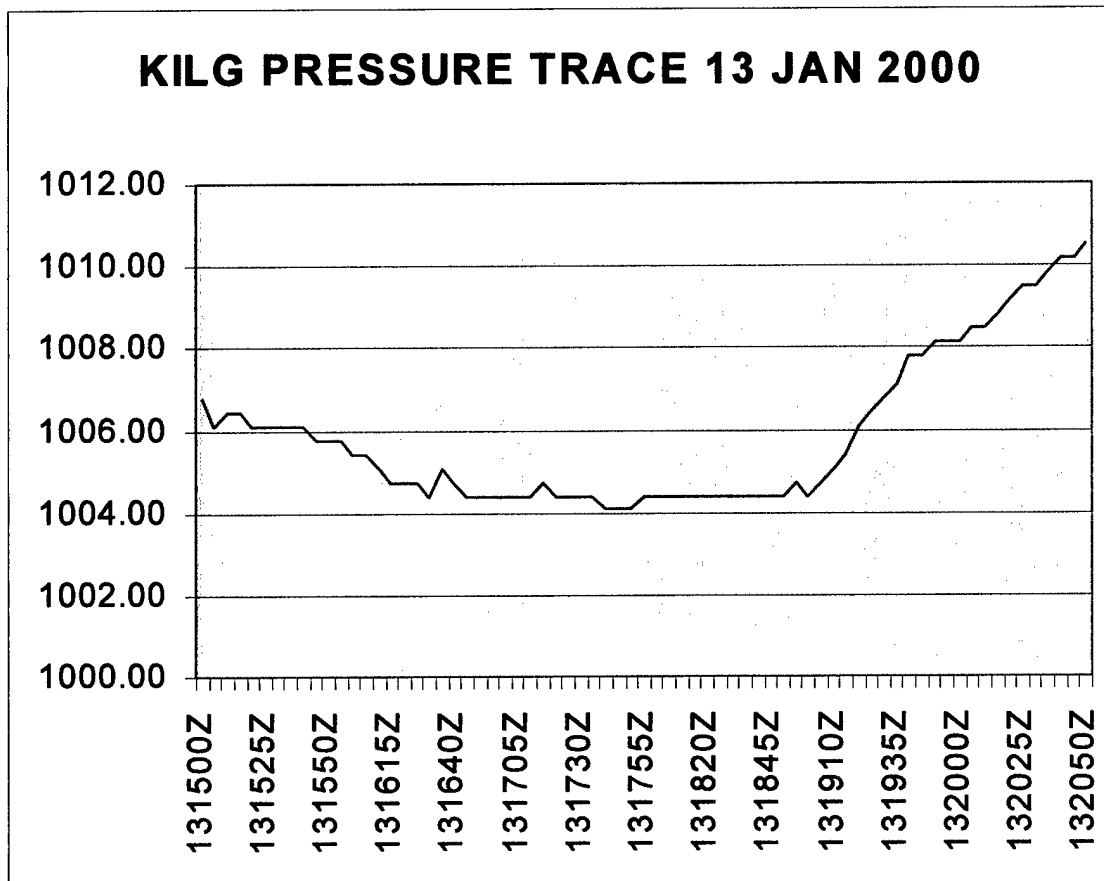
Figure 13. ASOS pressure trace valid 13 Jan 2000.
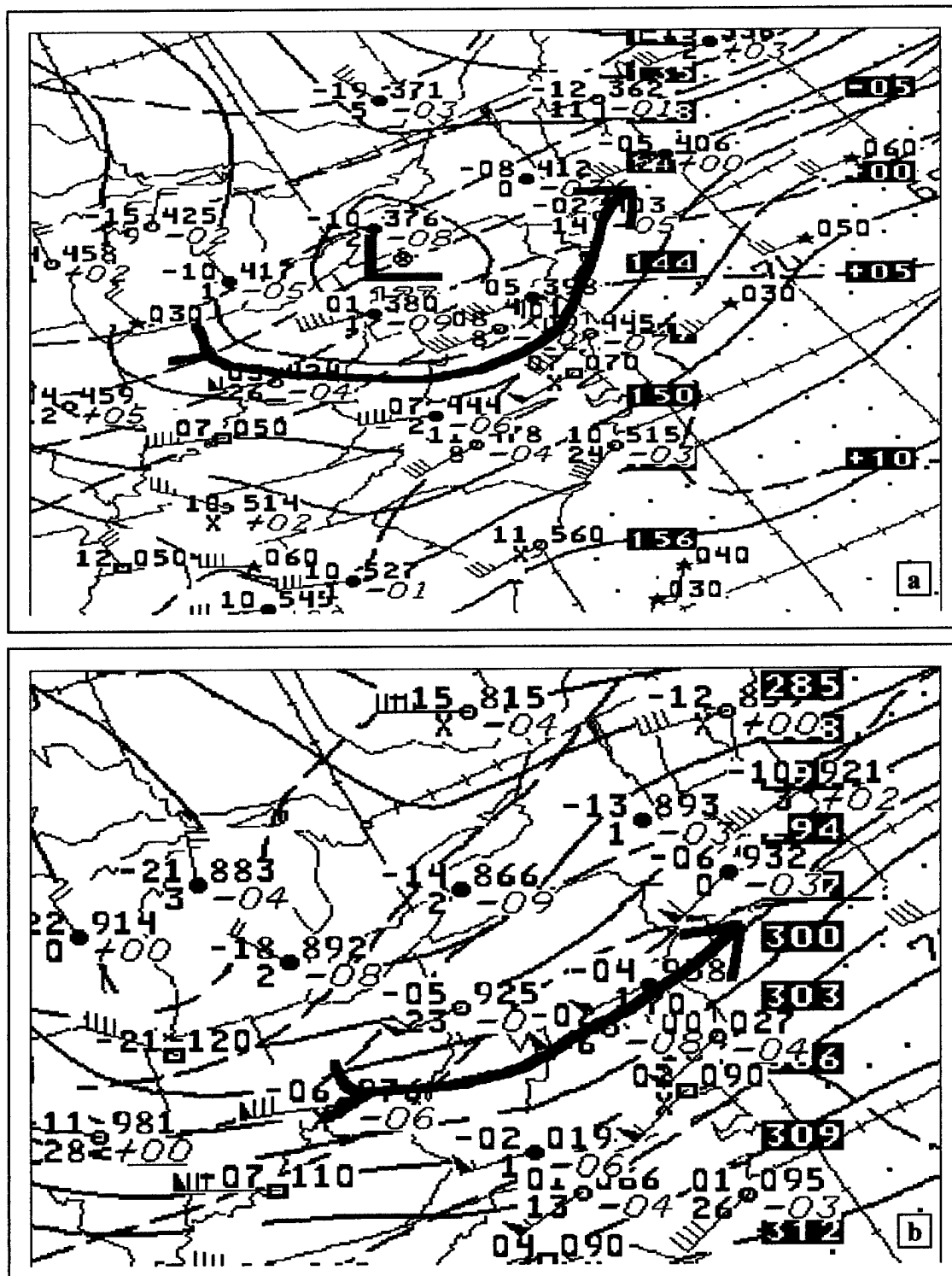
Figure 14. (a) 850 hPa analysis valid 12 UTC 13 Jan 2000, (b) 700 hPa analysis
valid 12 UTC 13 Jan 2000. Wind speeds are in knots.
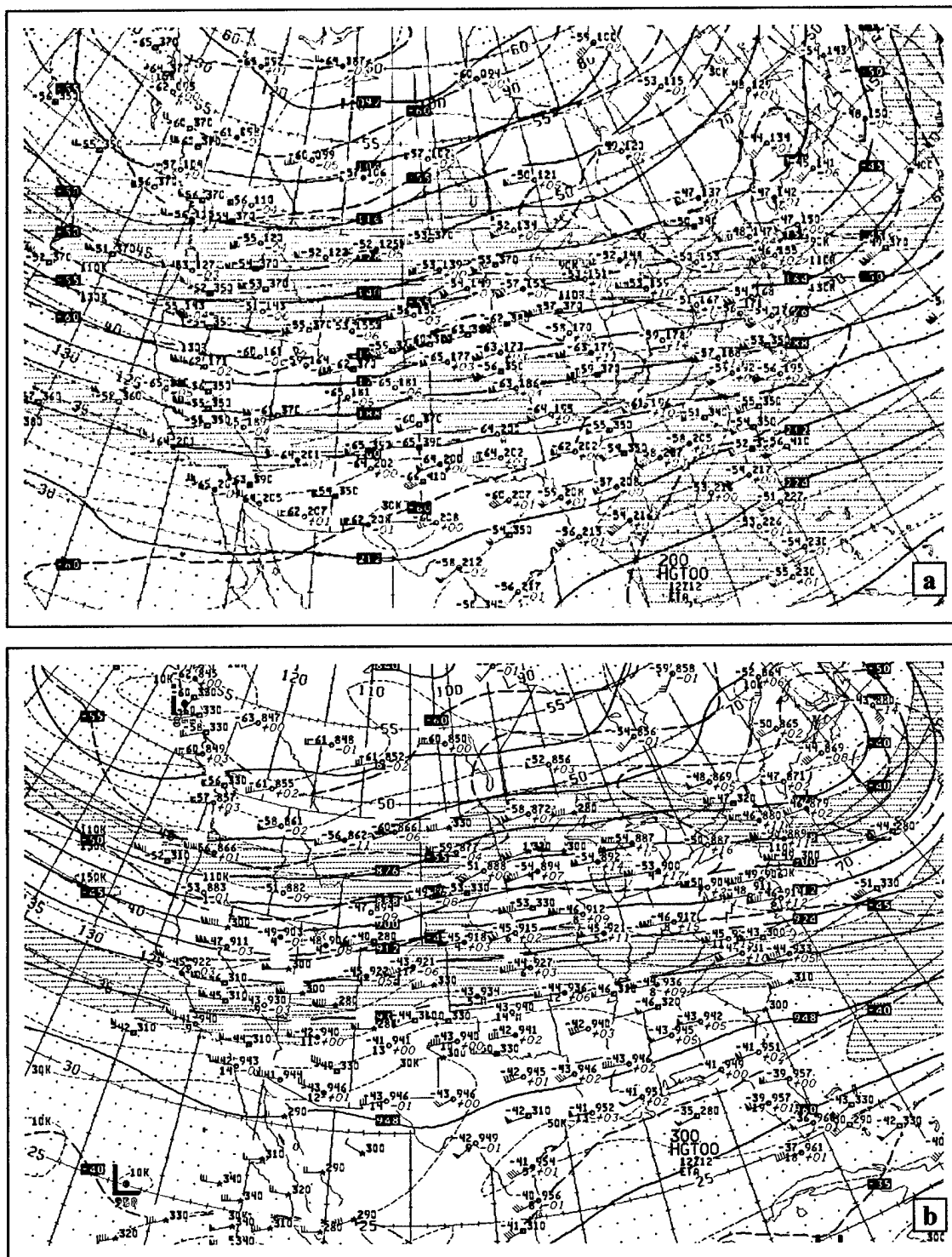
Figure 15. (a) 200 hPa analysis valid 12 UTC 12 Jan 2000, (b) 300 hPa analysis valid 12 UTC 12 Jan 2000.
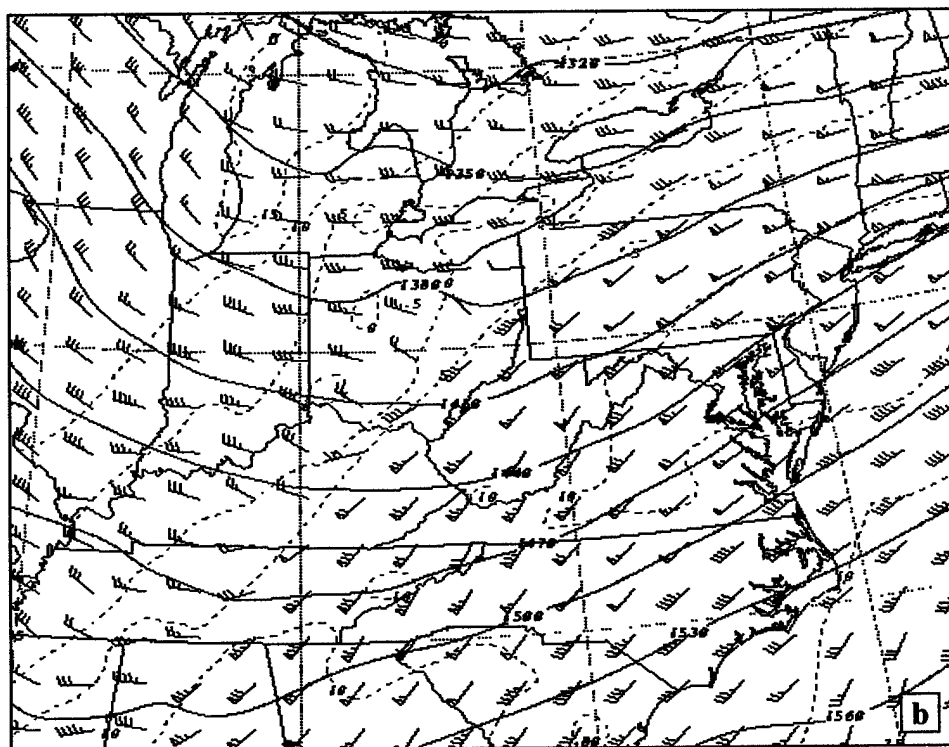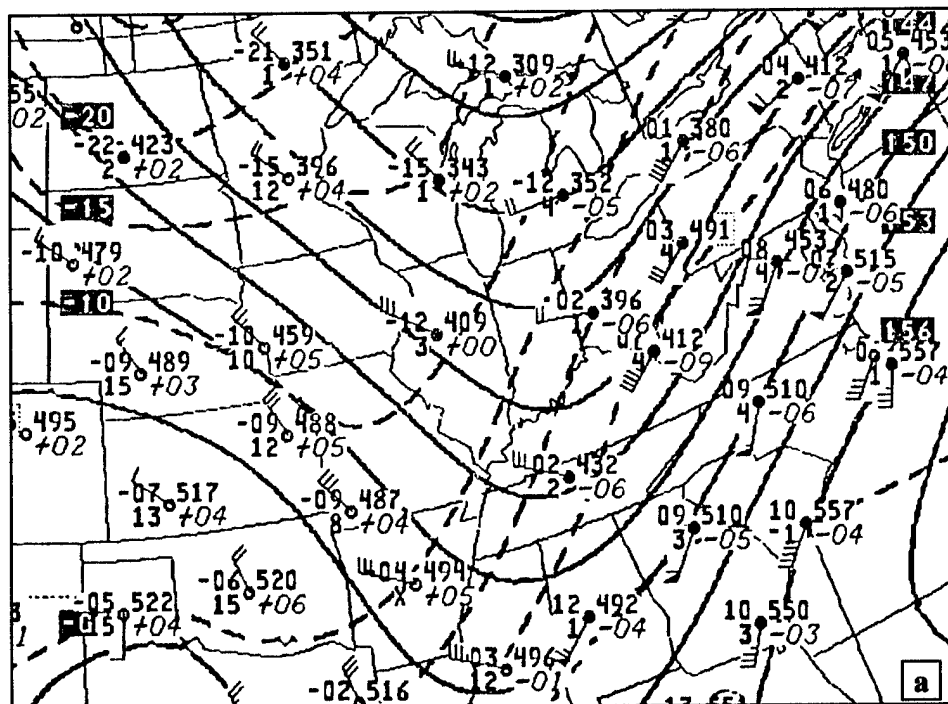
Figure 16. 850 hPa height (m), temperature (^{0}C), and wind (kt) valid 1200
UTC 28 Dec 1988. (a) NWS analysis, (b) 30-km control simulation.
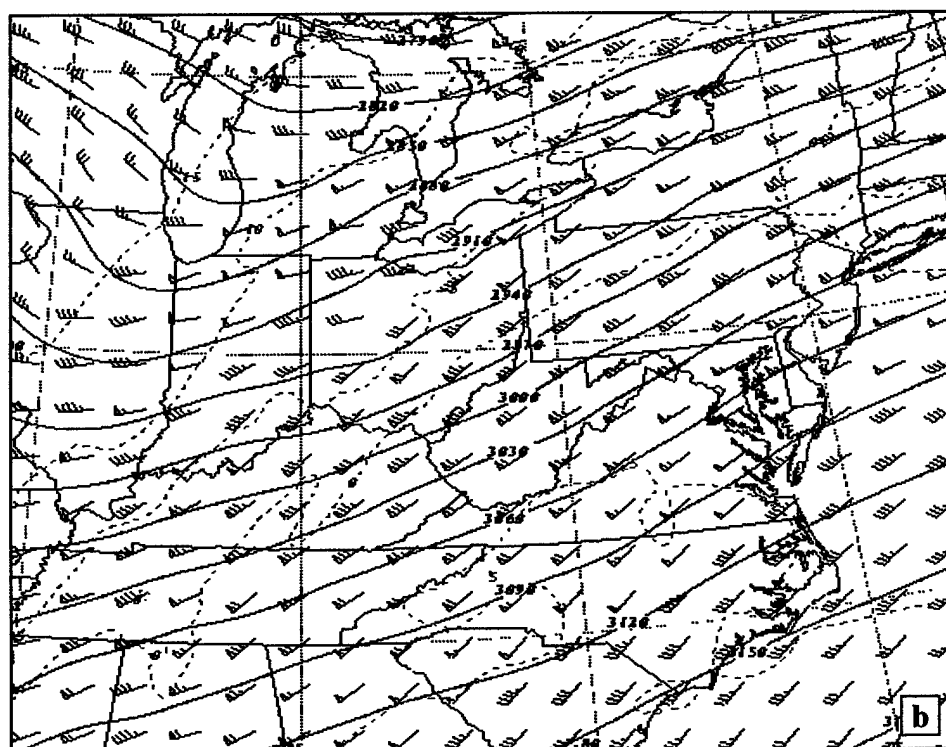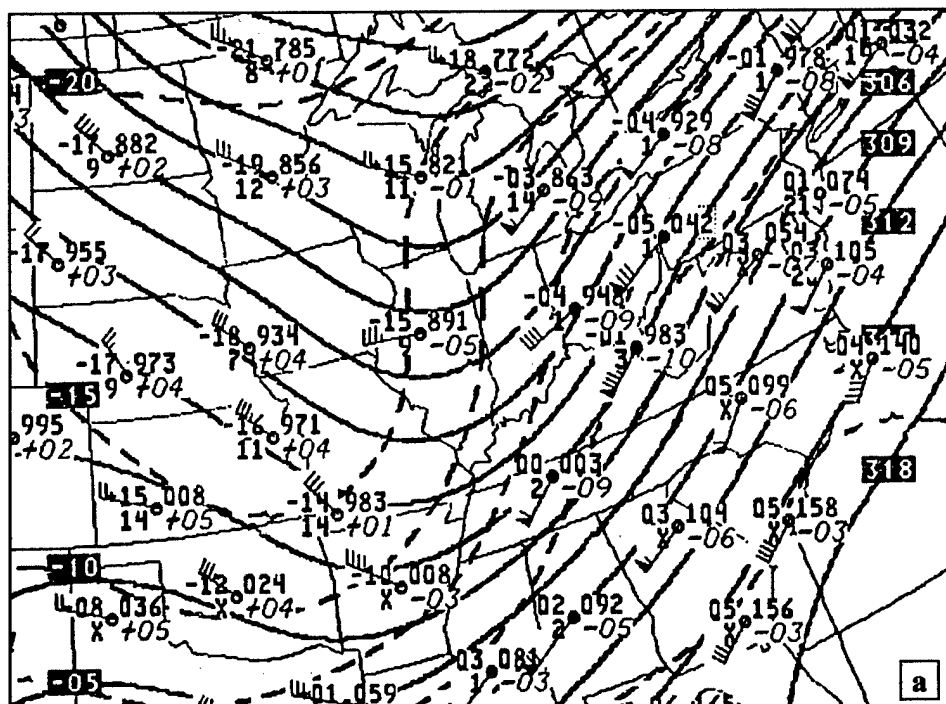
Figure 17. 700 hPa height (m), temperature (^{0}C), and wind (kt) valid 1200 UTC 28 Dec 1988. (a) NWS analysis, (b) 30-km control simulation.
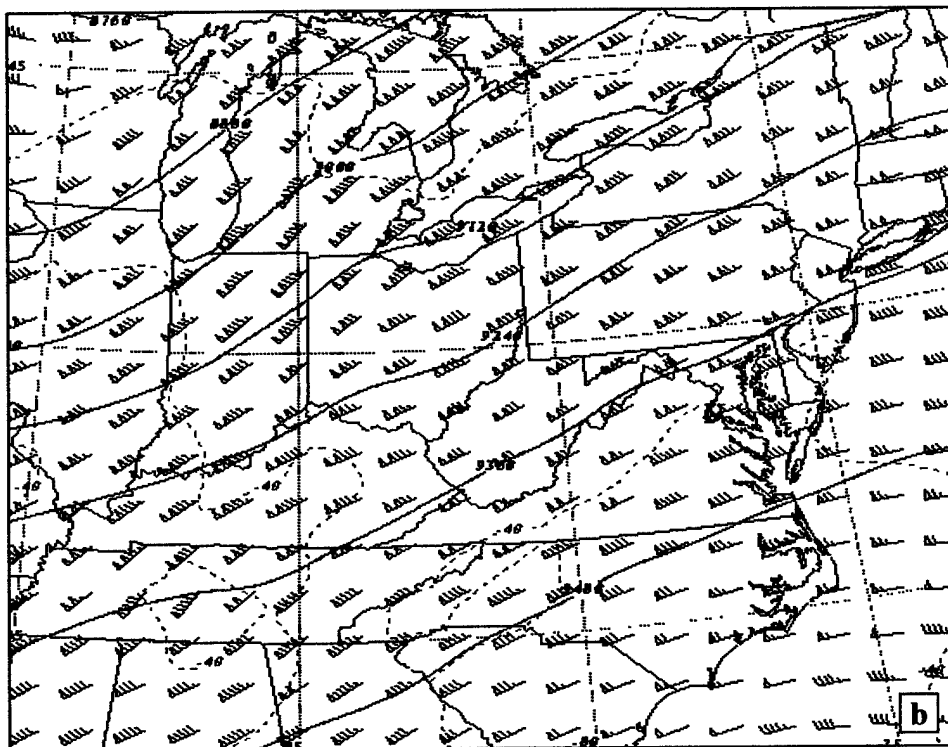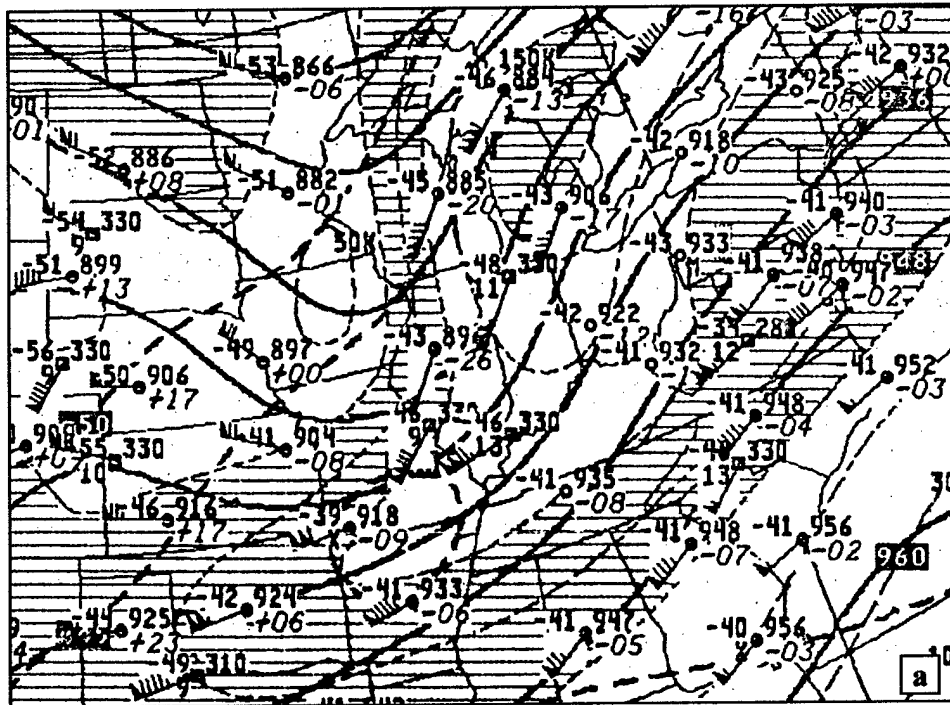
Figure 18. 300 hPa height (m), temperature (^{0}C), and wind (kt) valid 1200 UTC 28 Dec 1988. (a) NWS analysis, (b) 30-km control simulation.
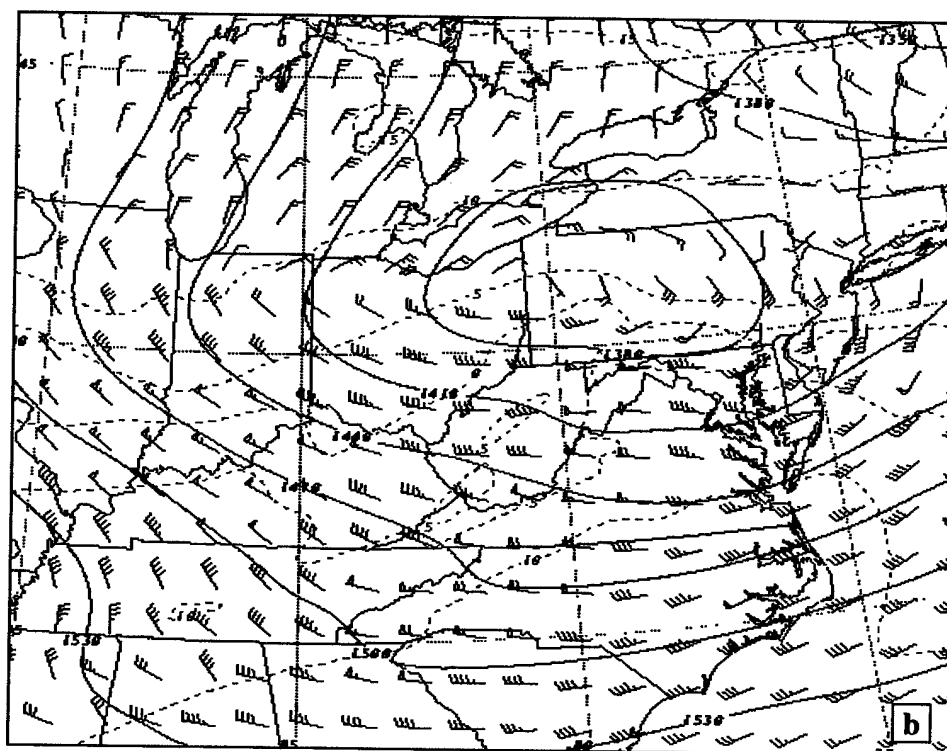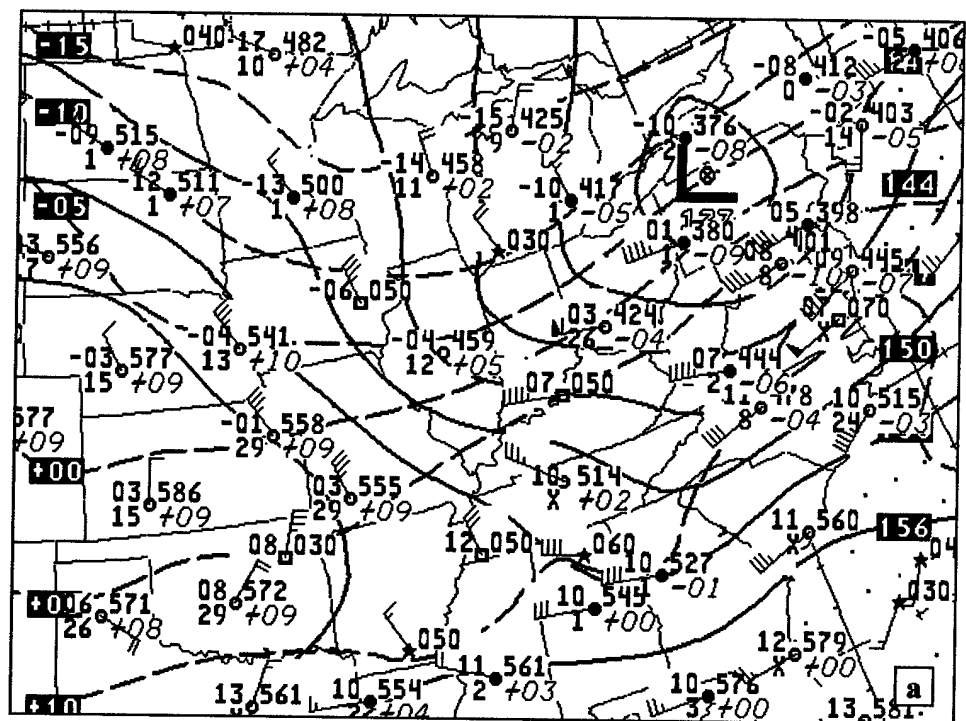
Figure 19. 850 hPa height (m), temperature (^{0}C), and wind (kt) valid 1200
UTC 13 Jan 2000. (a) NWS analysis, (b) 30-km control simulation.
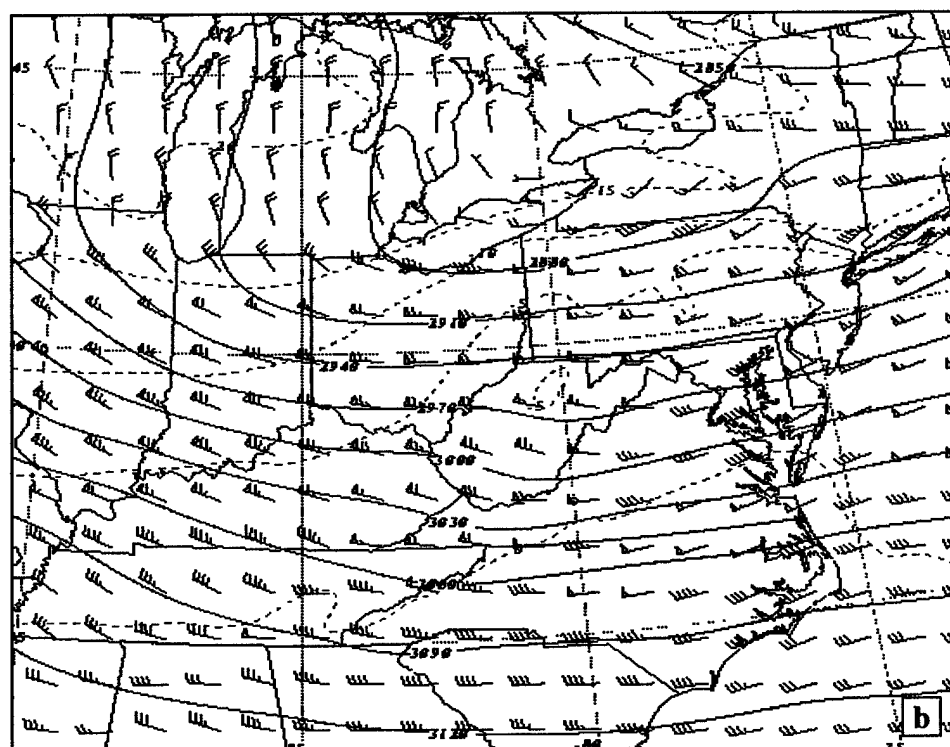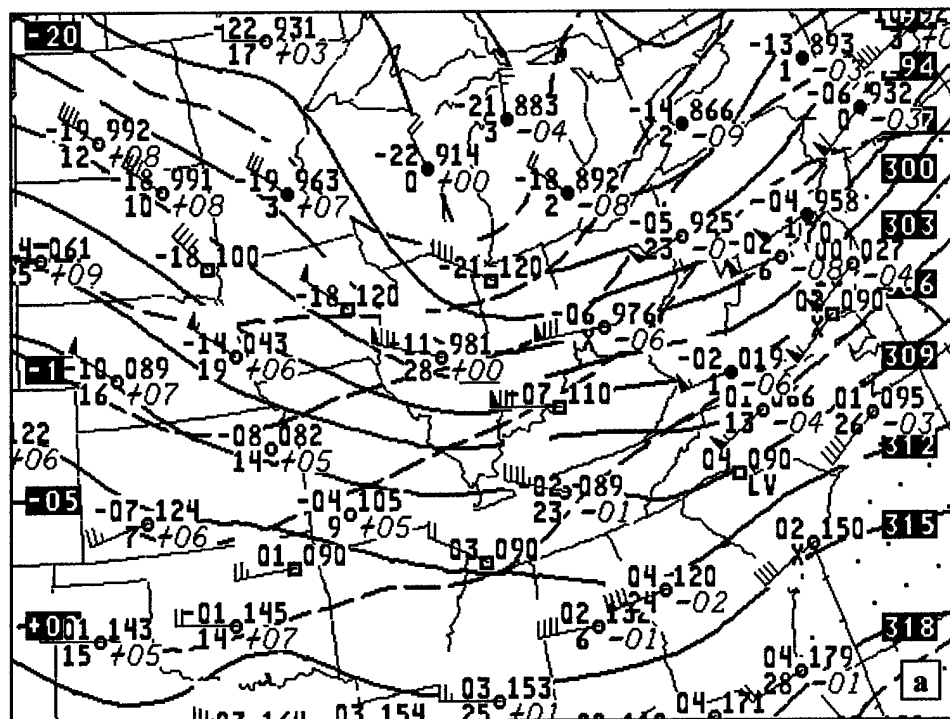
Figure 20. 700 hPa height (m), temperature (^{0}C), and wind (kt) valid 1200
UTC 13 Jan 2000. (a) NWS analysis, (b) 30-km control simulation.
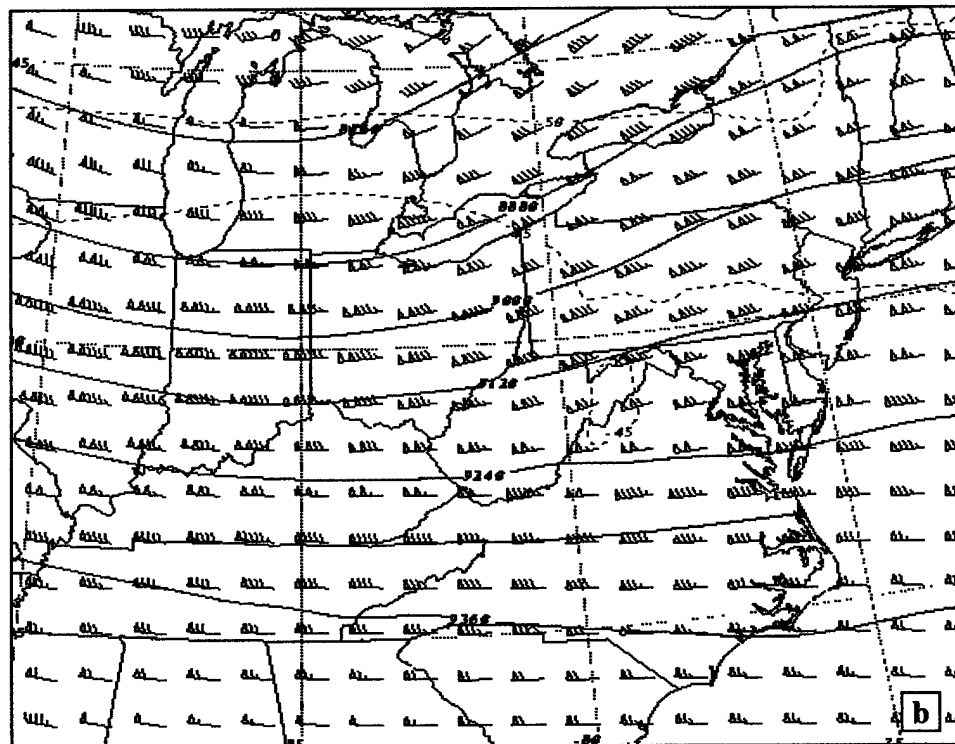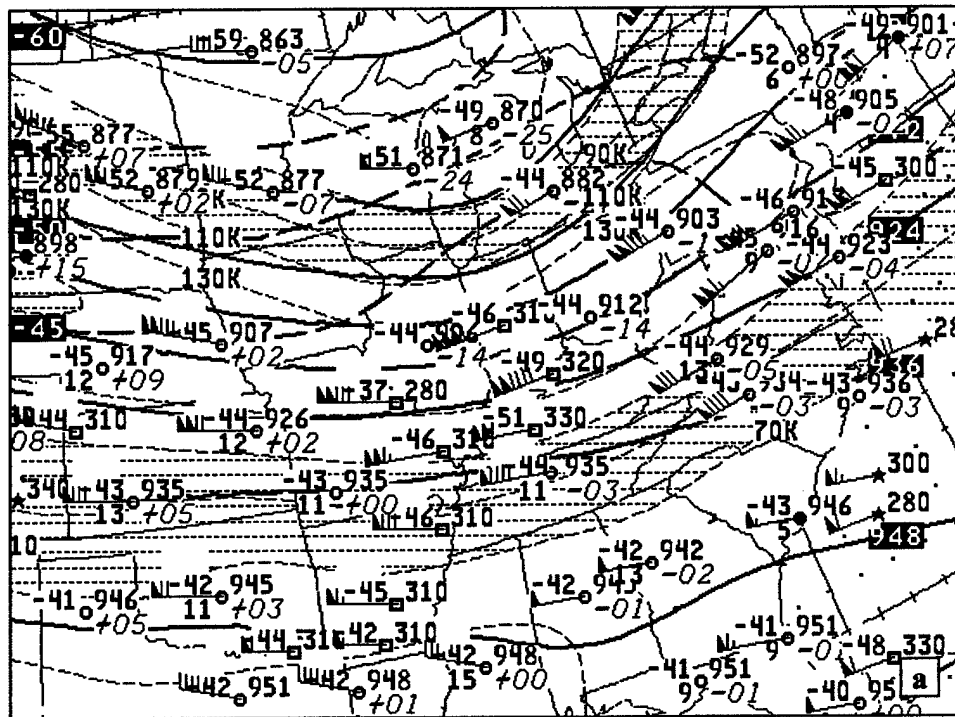
Figure 21. 300 hPa height (m), temperature (^{0}C), and wind (kt) valid 1200
UTC 13 Jan 2000. (a) NWS analysis, (b) 30-km control simulation.
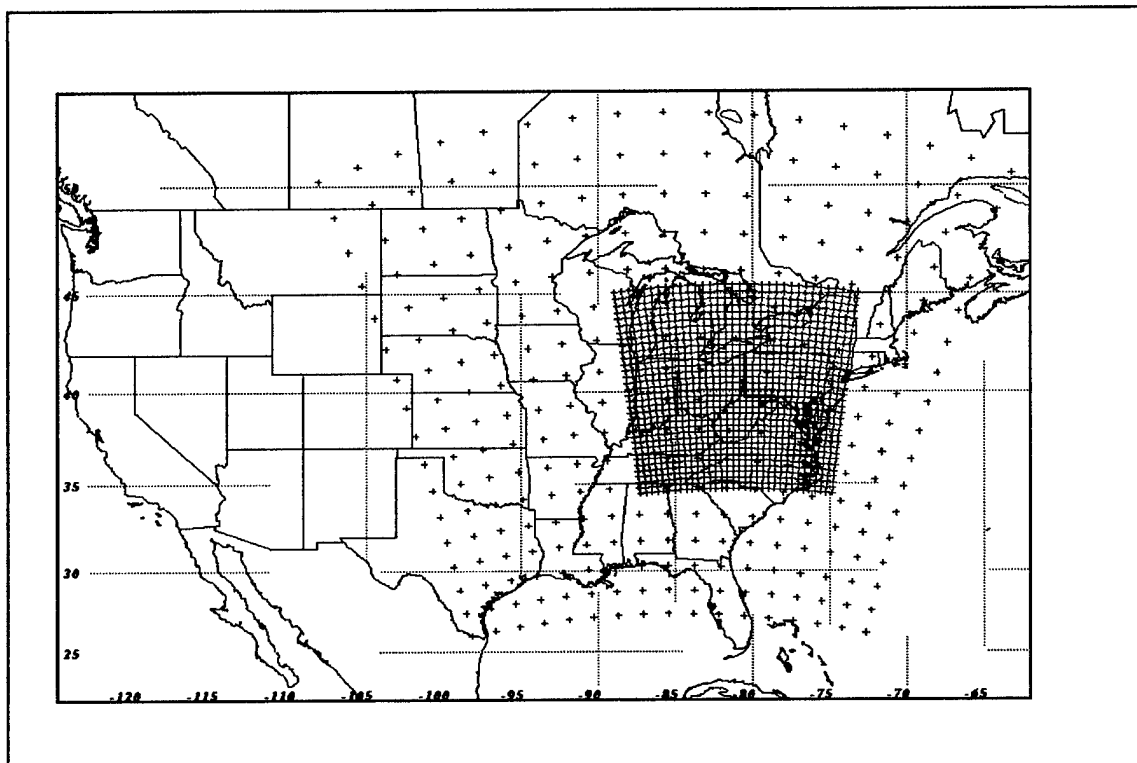
Figure 22. 30-km and 6-km grid meshes used for both J00 and D88 model simulations.
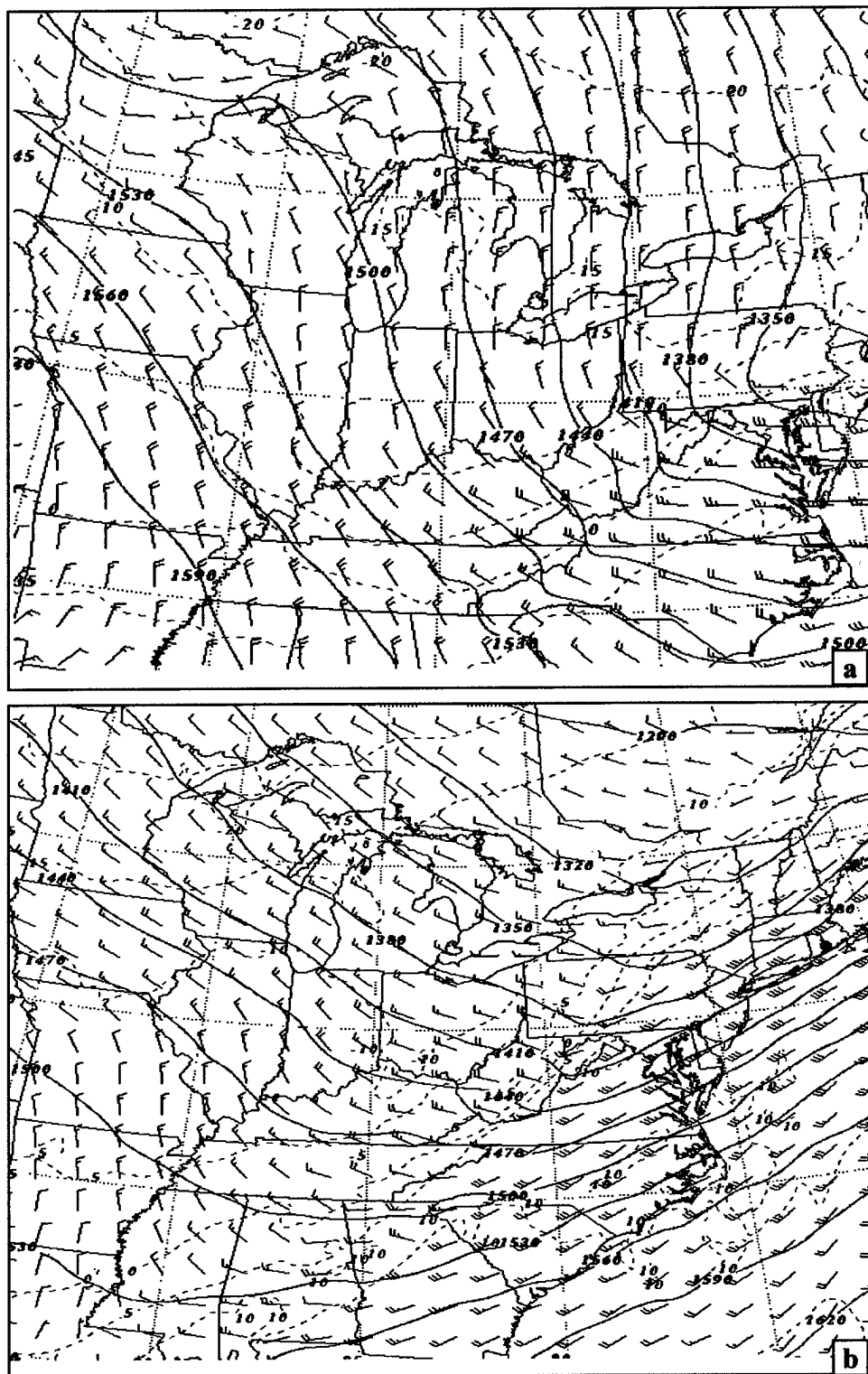
Figure 23. Simulated 850hPa winds (ms^{-1}), temperature (^{0}C), and heights (m) valid (a) 18 UTC 13 Jan 2000, (b) 18 UTC 28 Dec 1988.
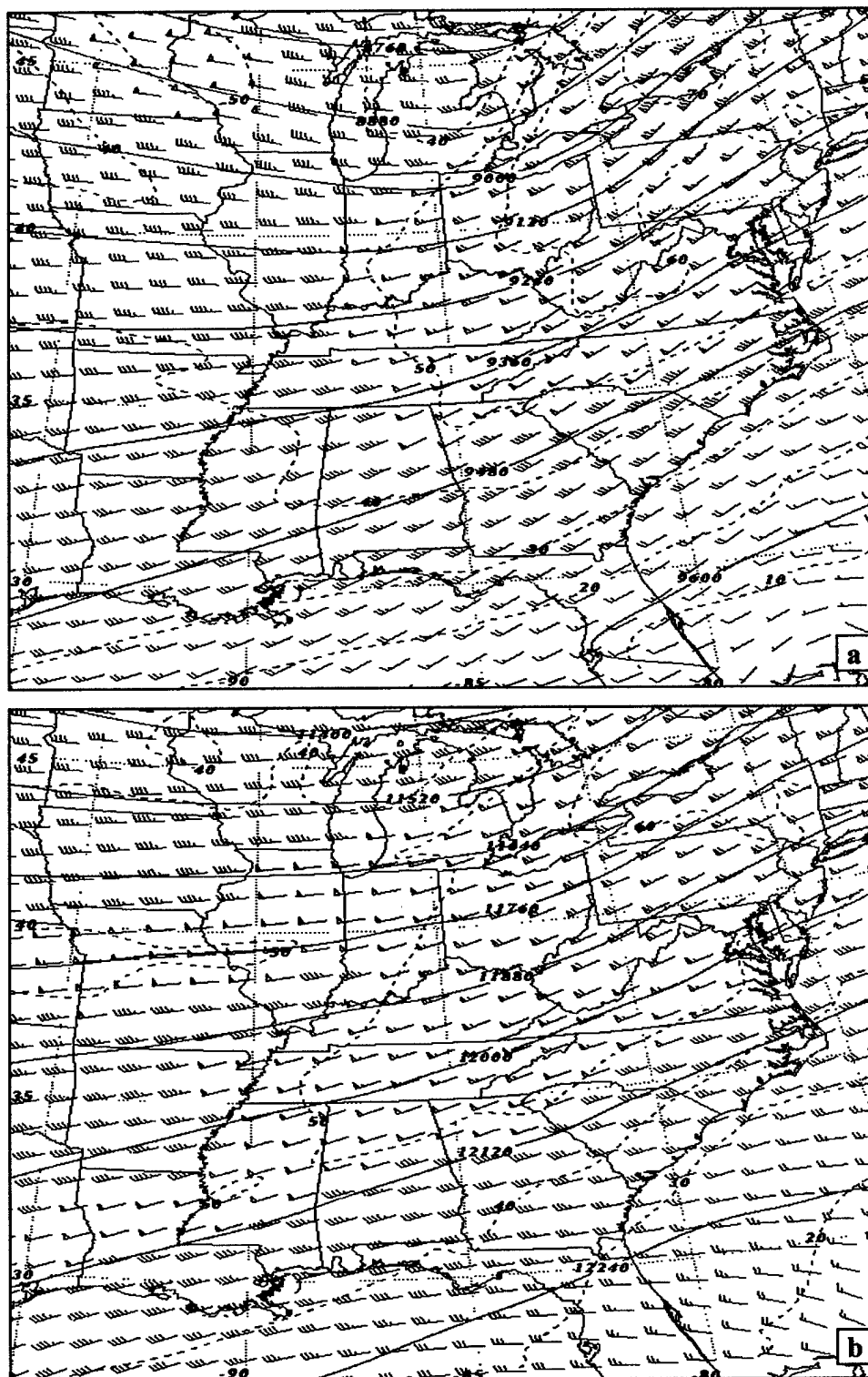
Figure 24. Simulated winds (ms^{-1}) and heights (m) valid 18 UTC 28 Dec
1988 (a) 300 hPa, (b) 200 hPa. Heights are contoured every 120 m.
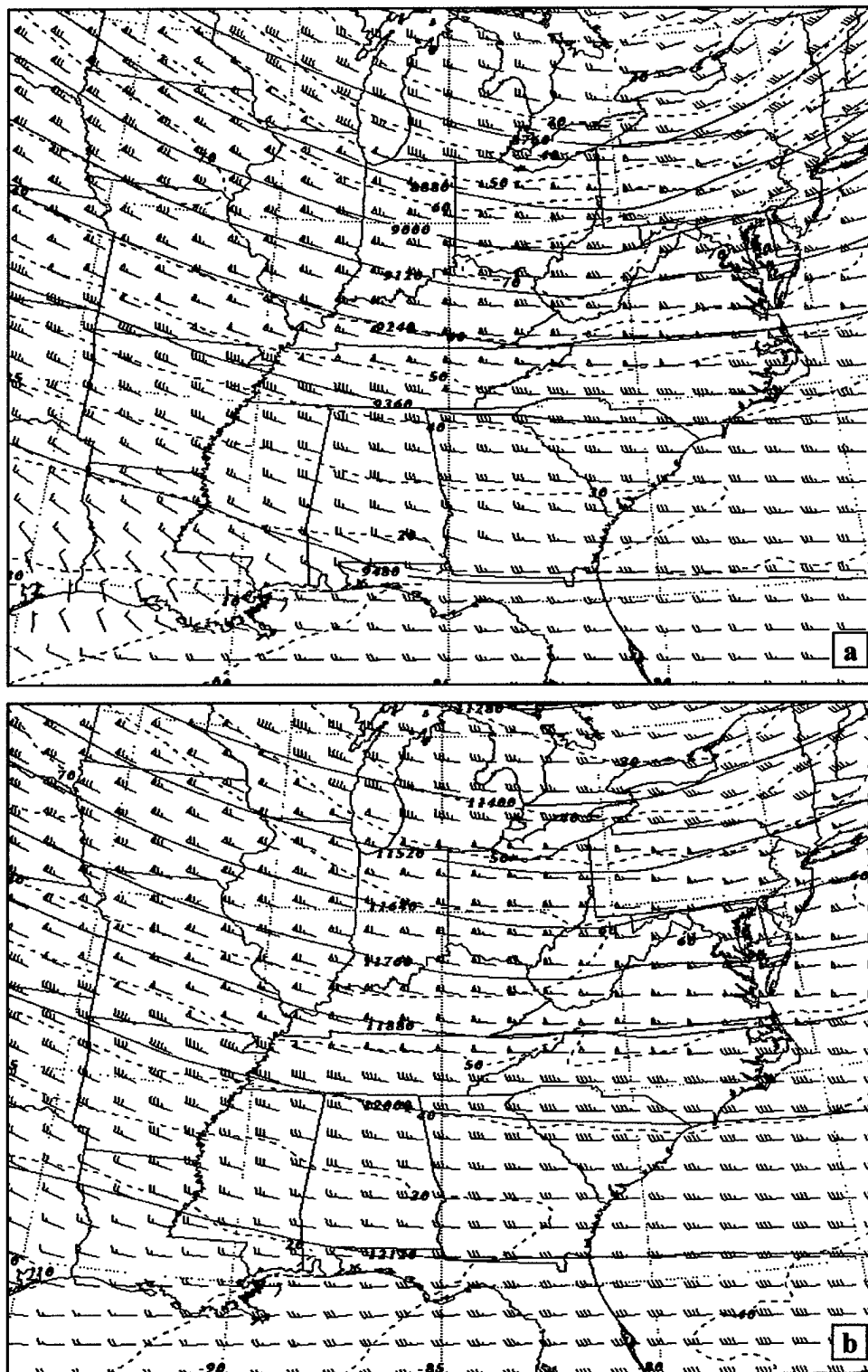
Figure 25. Simulated winds (ms^{-1}) and heights (m) valid 18 UTC 13 Jan 2000 (a) 300 hPa, (b) 200 hPa. Heights are contoured every 120 m.
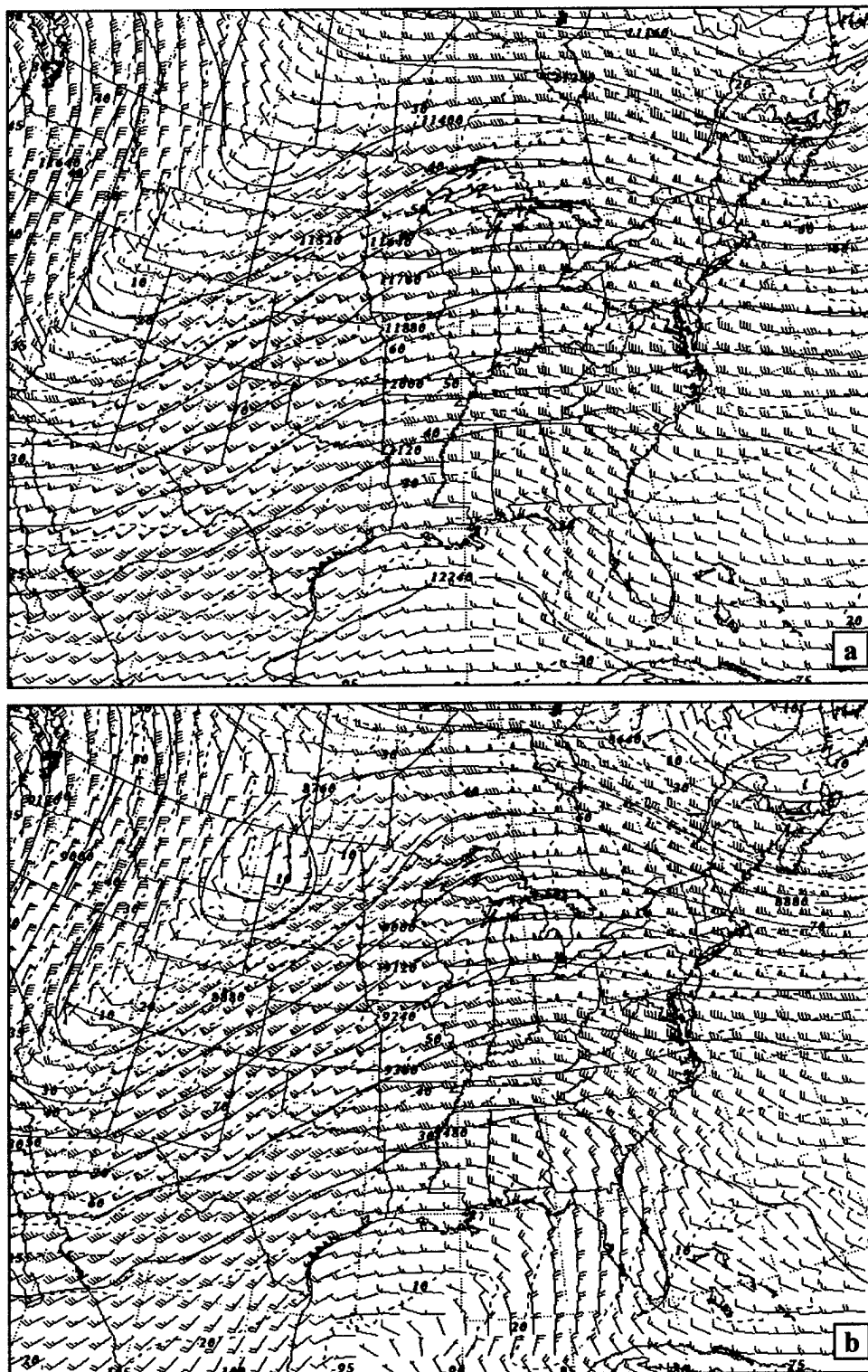
Figure 26. Simulated winds (ms^{-1}) and heights (m) valid 00 UTC 27 Dec 1988 (a) 200 hPa, (b) 300 hPa. Heights are contoured every 120 m.
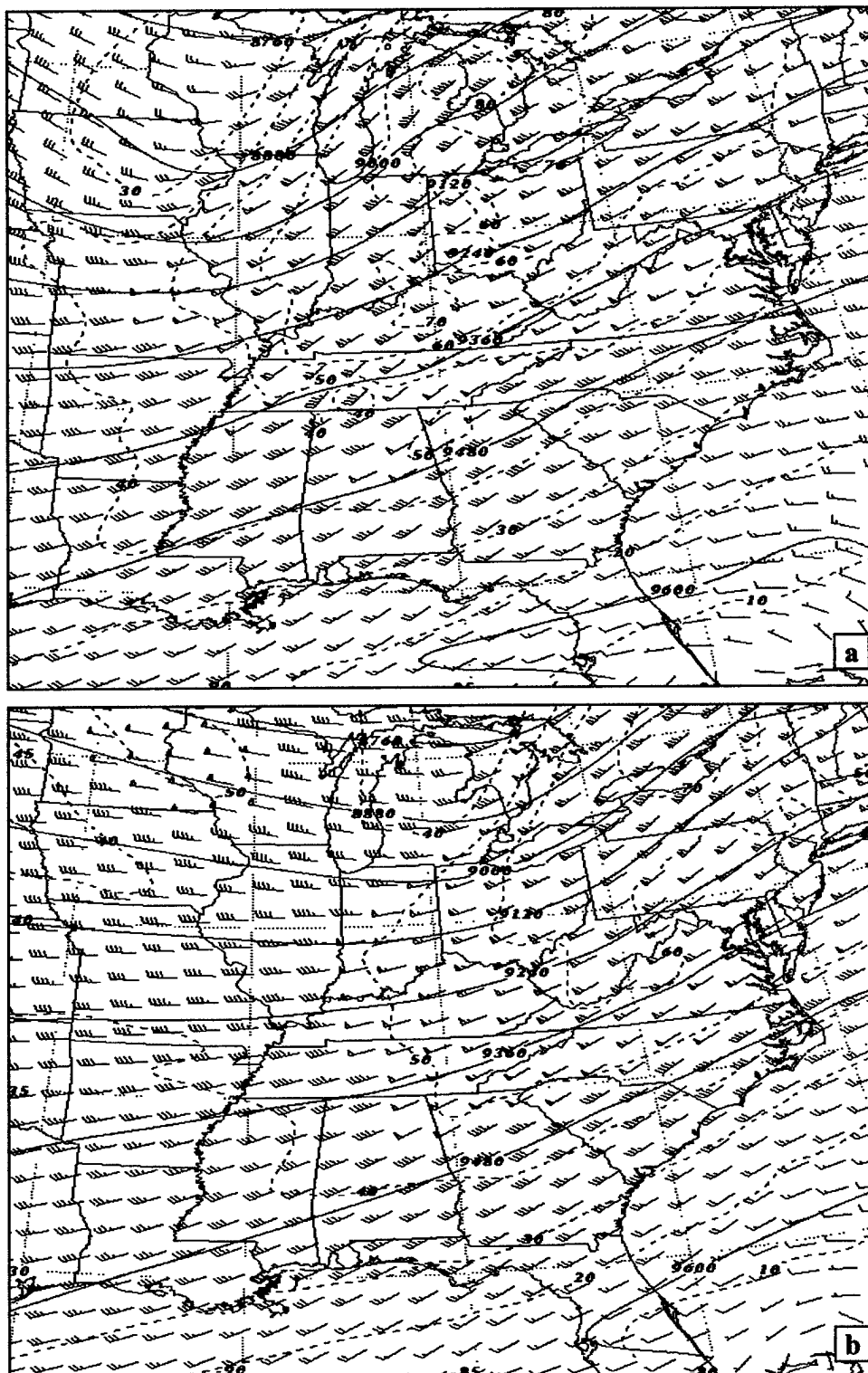
Figure 27. Simulated 300 hPa winds (ms^{-1}) and heights (m) valid (a) 12 UTC 28 Dec 1988, (b) 18 UTC 28 Dec 1988. Heights are contoured every 120 m.
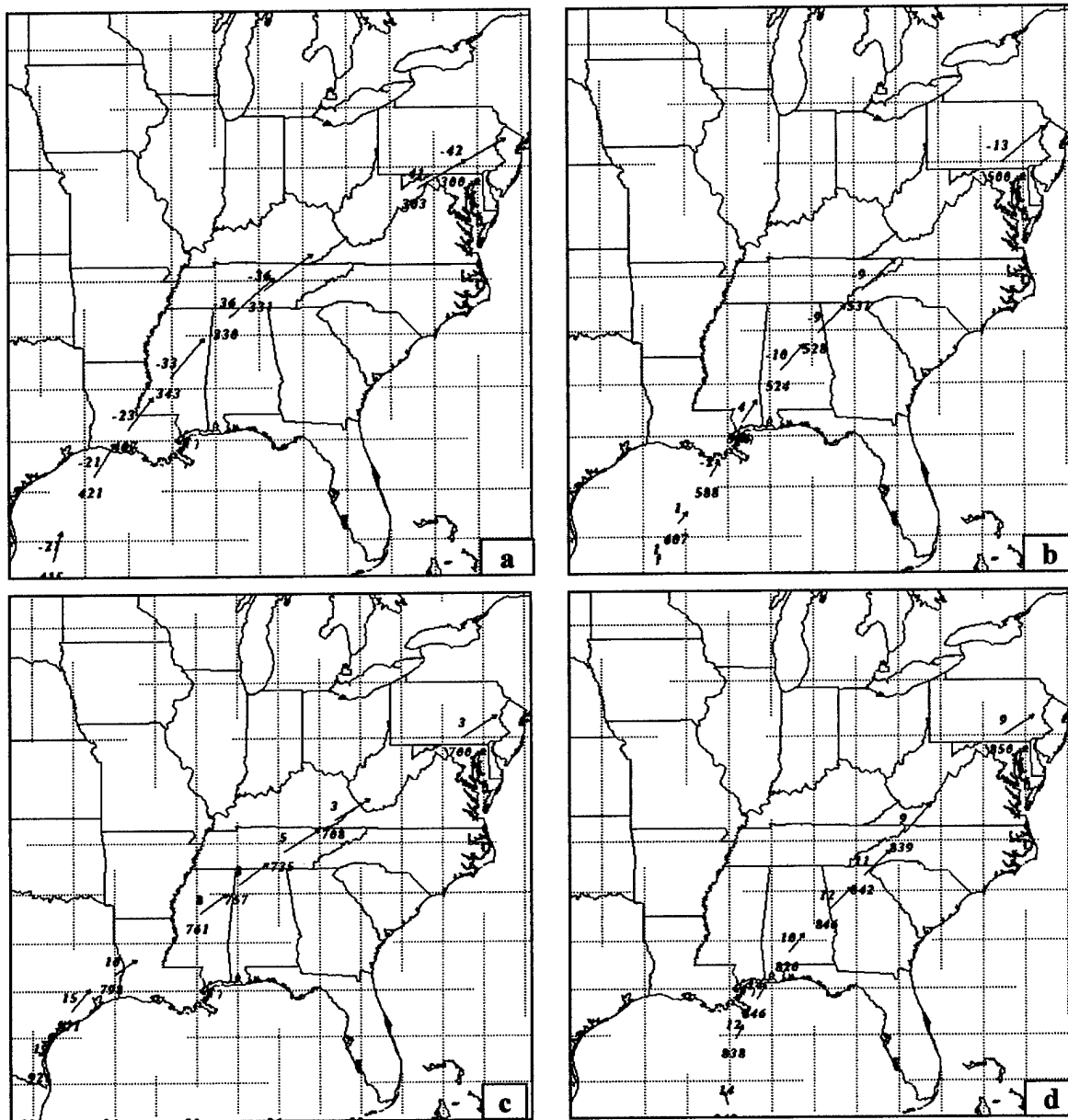
Figure 28. Simulated backward trajectories valid 12 UTC 28 Dec 1988 – 00 UTC 26 Dec 1988 (a) 300 hPa, (b) 500 hPa, (c) 700 hPa, (d) 850 hPa.
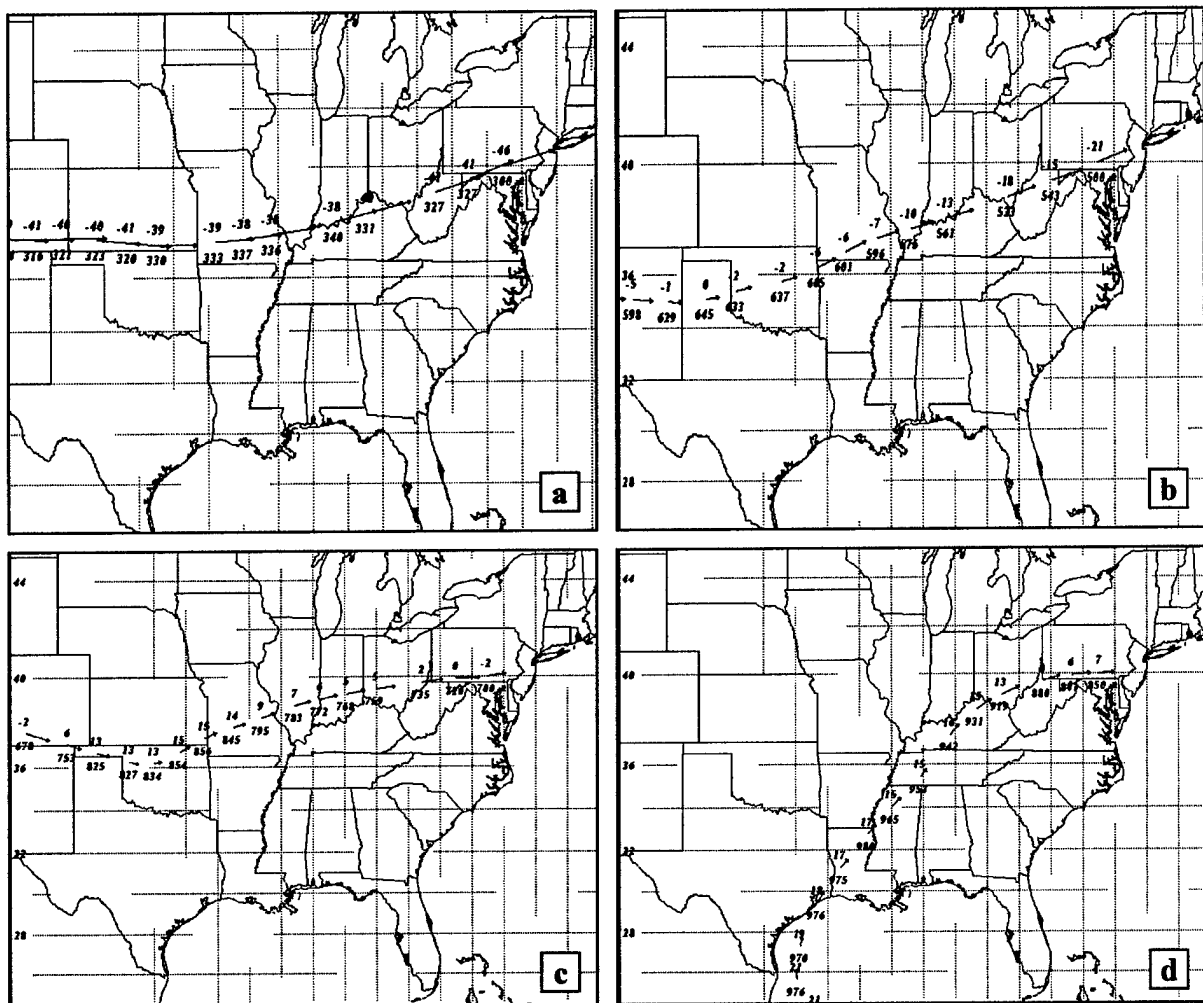
Figure 29. Simulated backward trajectories valid 12 UTC 13 Jan 2000 – 00 UTC 21 Jan 2000 (a) 300 hPa, (b) 500 hPa, (c) 700 hPa, (d) 850 hPa.
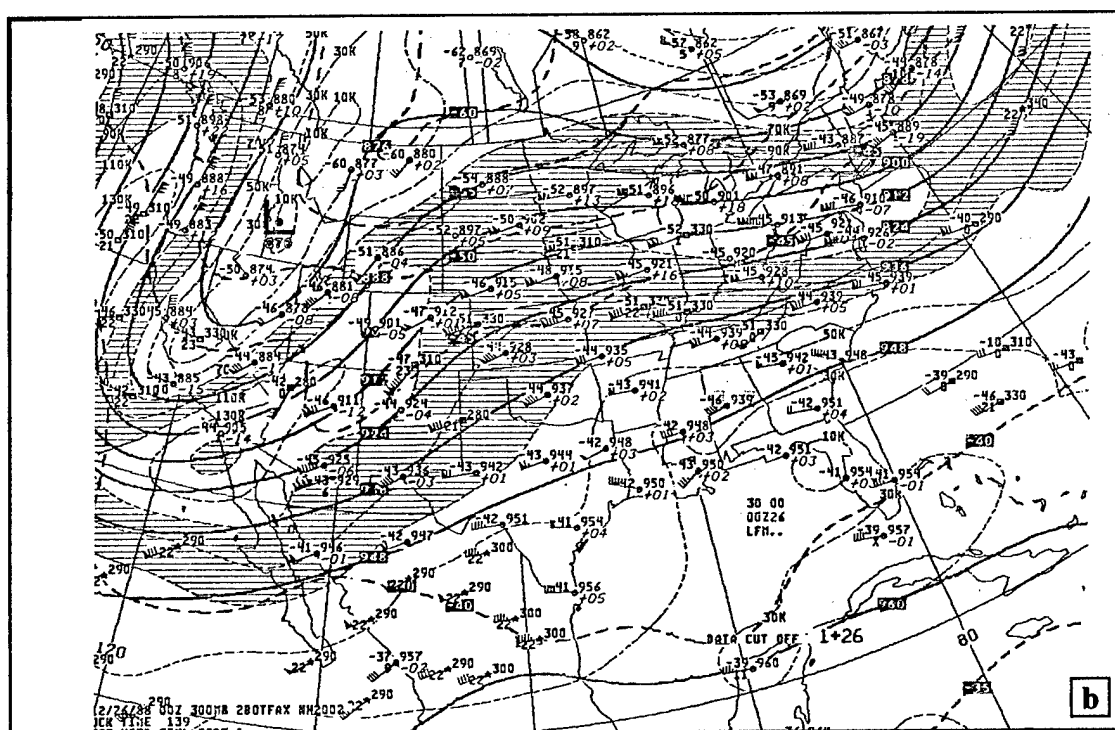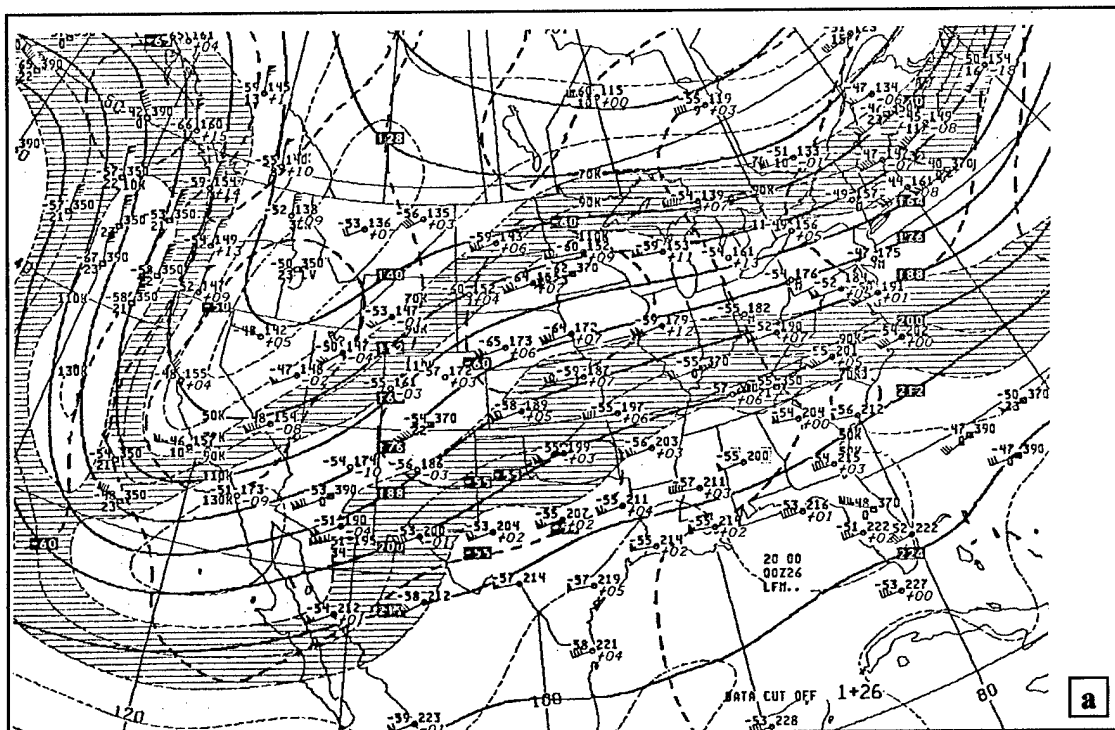
Figure 30. NWS analysis valid 00 UTC 26 December 1988, (a) 200 hPa, (b) 300 hPa
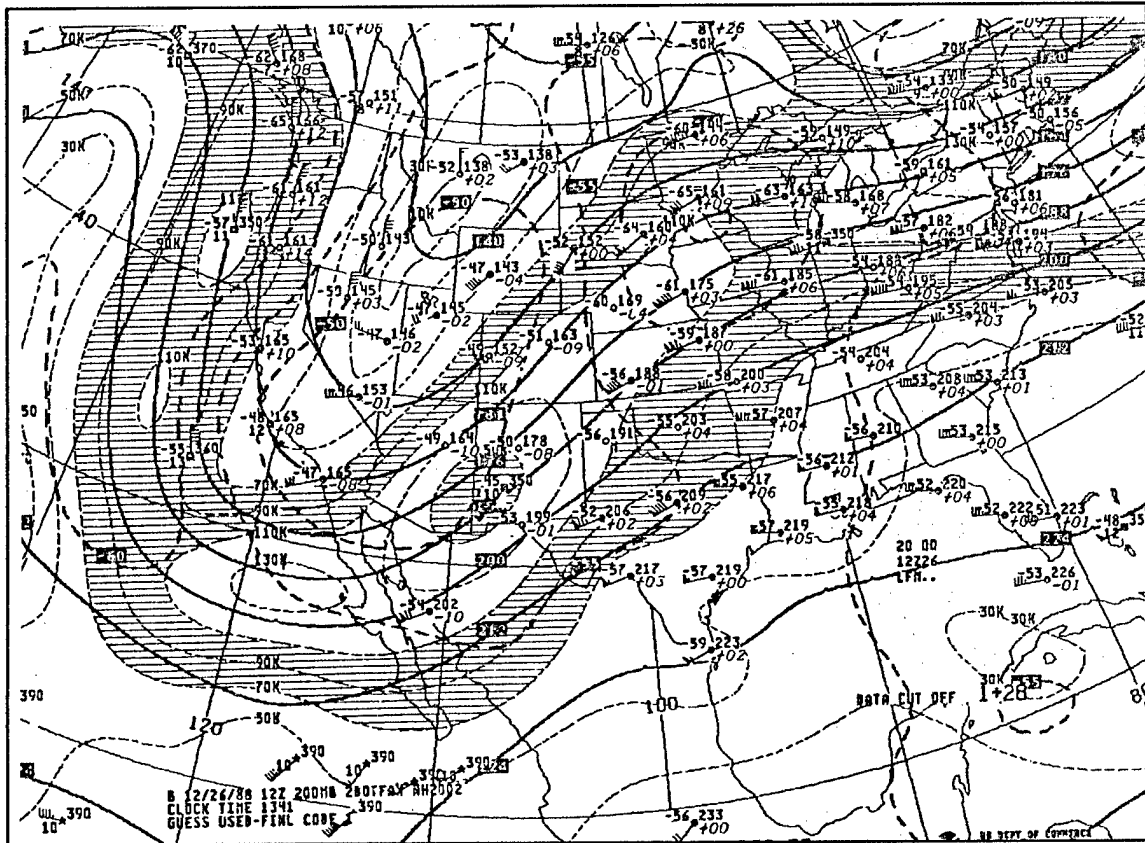
Figure 31. NWS 200 hPa analysis valid 12 UTC 26 December 1988.
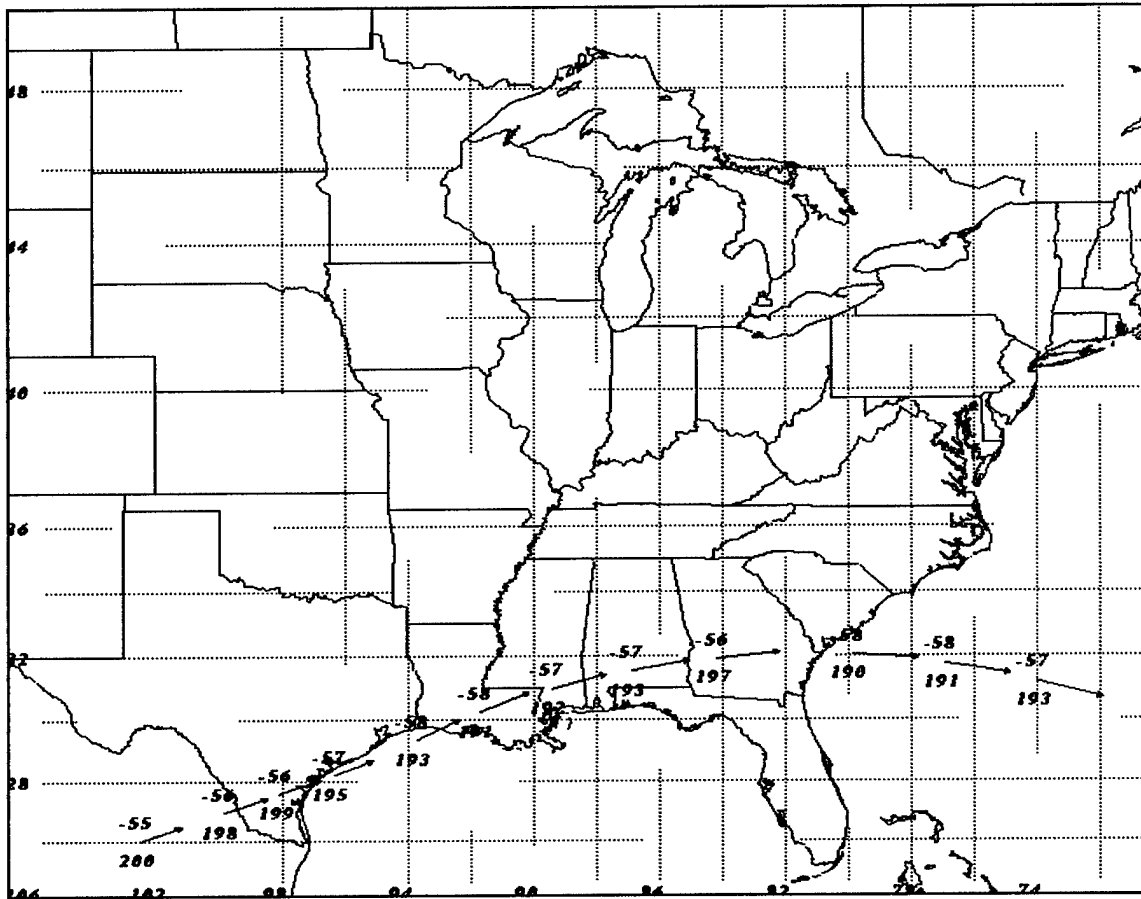
Figure 32. 200 hPa forward trajectory valid from 06 UTC 11 Jan 2000 to 18 UTC 13 Jan 2000. Note leftward turning in STJ entrance region (near 94 ^{0}W) and rightward turning in STJ exit region (near 80 ^{0}W).
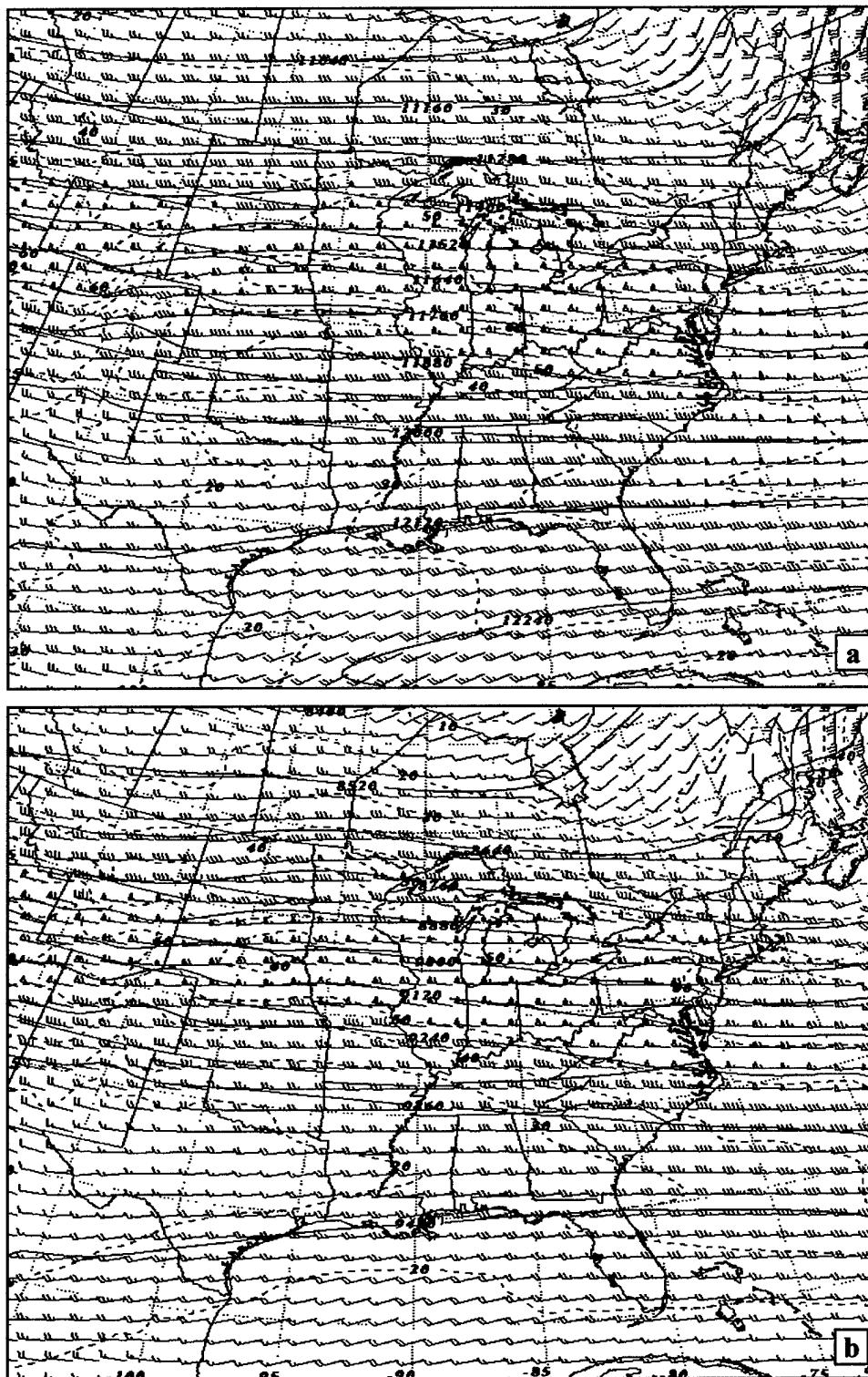
Figure 33. Simulated winds (ms^{-1}) and heights (m) valid 12 UTC 12 Jan 2000 (a) 200 hPa, (b) 300 hPa. Heights are contoured every 120 m.
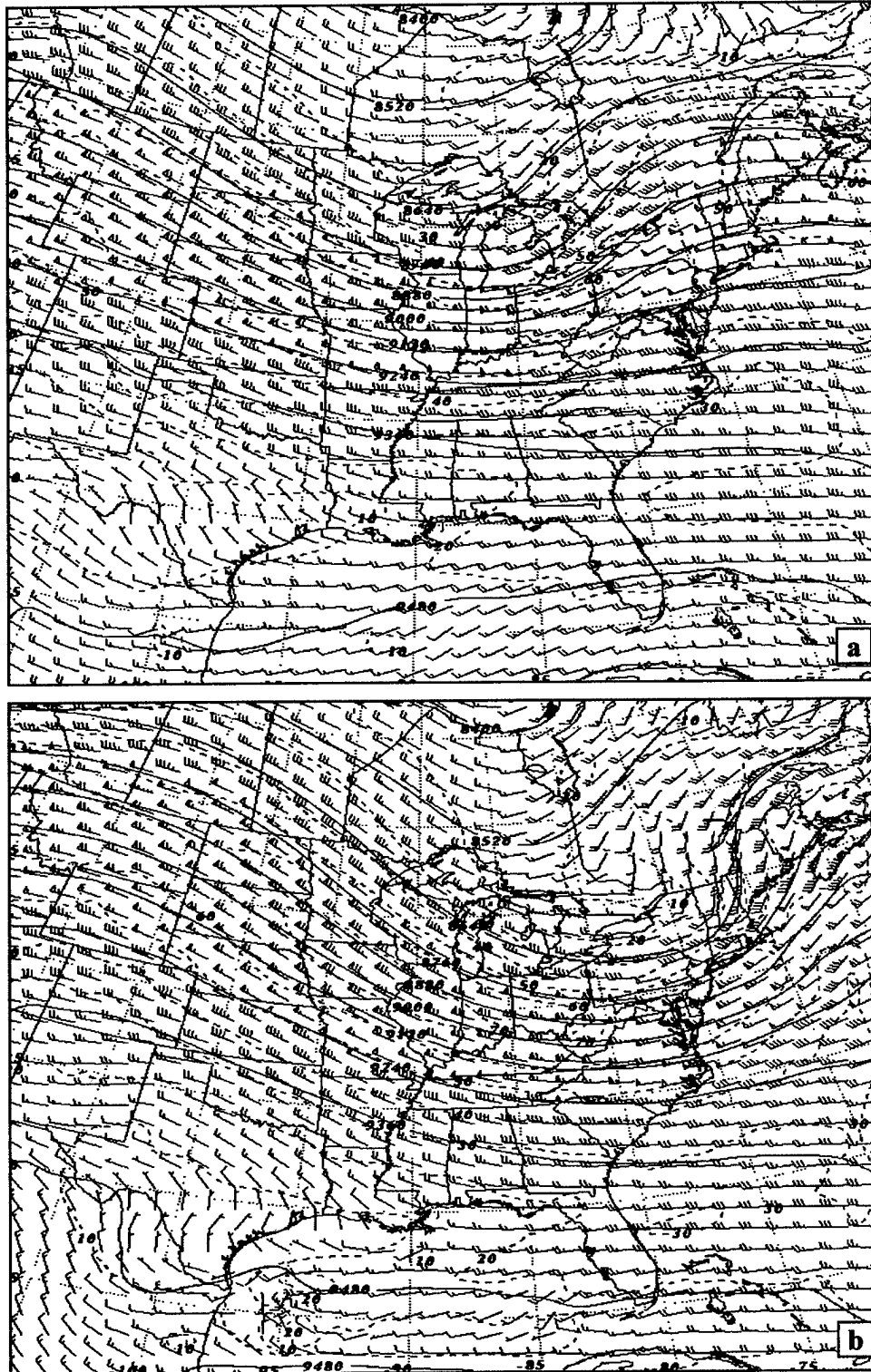
Figure 34. 300 hPa simulated winds (ms^{-1}) and heights (m) valid (a) 12 UTC 13 Jan 2000, (b) 00 UTC 14 Jan 2000. Heights are contoured every 120 m.
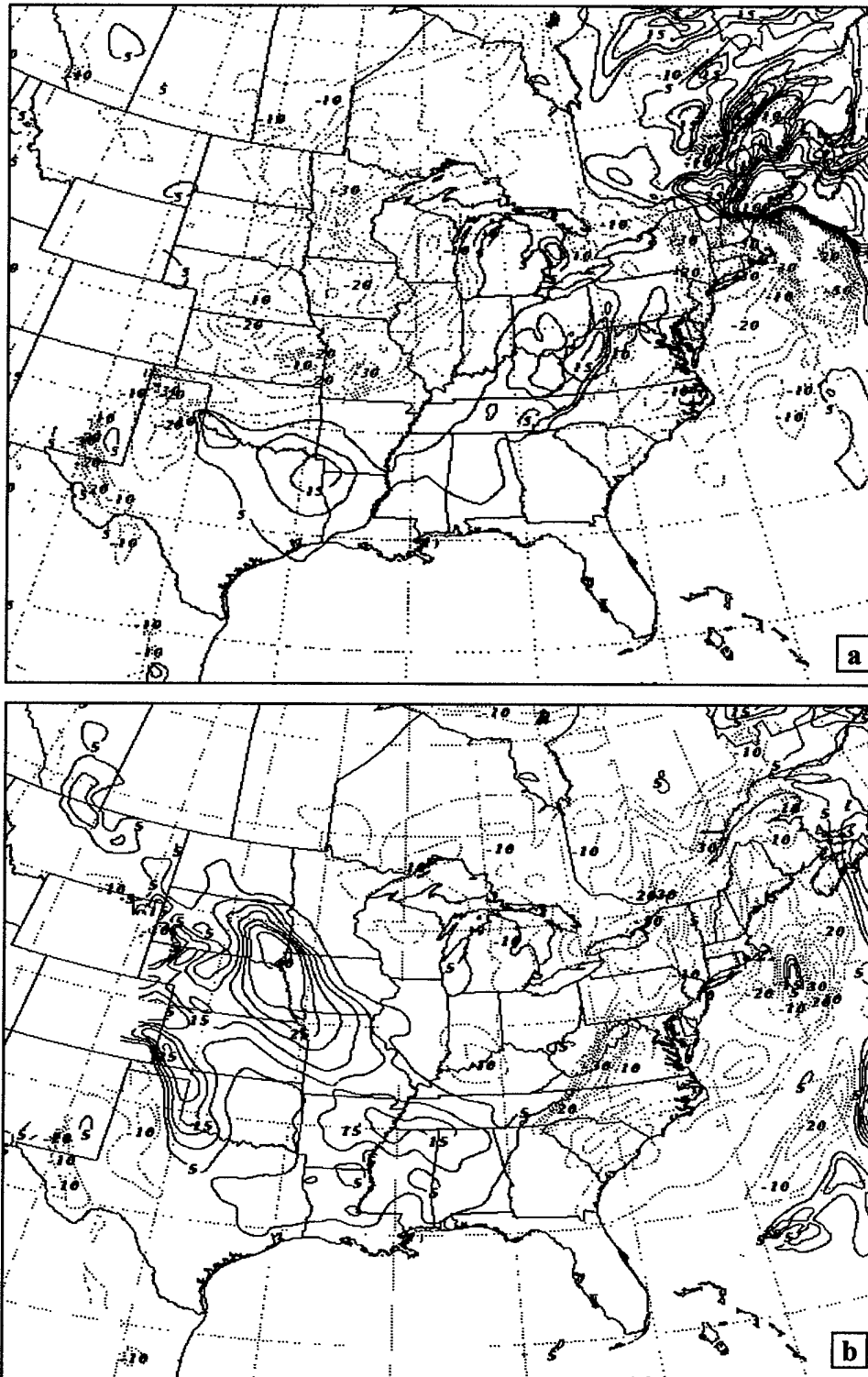
Figure 35. Simulated 940-750 hPa hourly thickness change (m). Height
rises are indicated by solid contours and height falls by dashed contours.
Valid (a) 0400 UTC 11 Jan 2000, (b) 0000 UTC 12 Jan 2000.

105
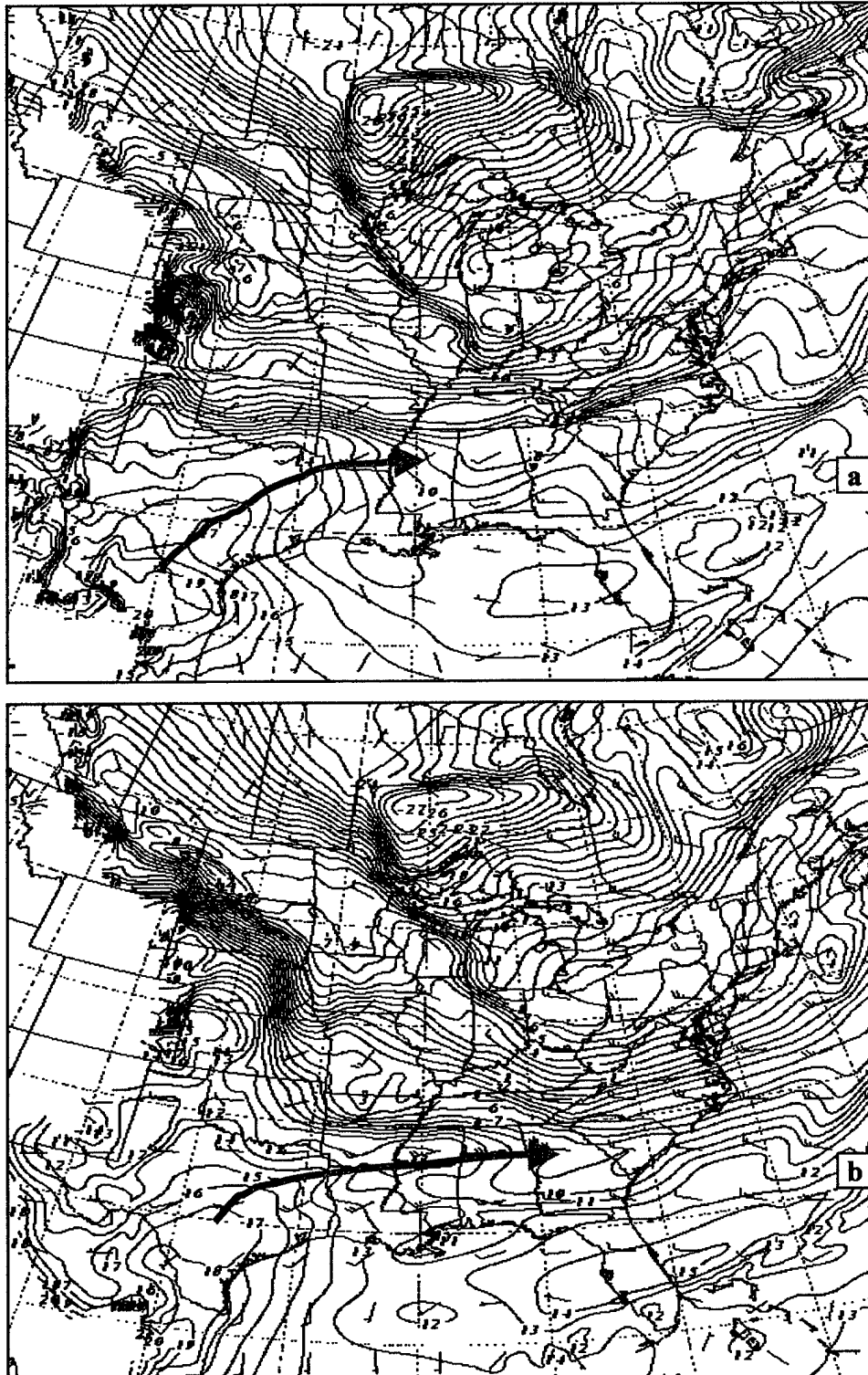
Figure 36. Simulated 850 hPa temperature (^{0}C) and wind (ms^{-1}). Red arrow depicts low-level warm advection pattern. Valid (a) 1600 UTC 11 Jan 2000, (b) 0000 UTC 12 Jan 2000.
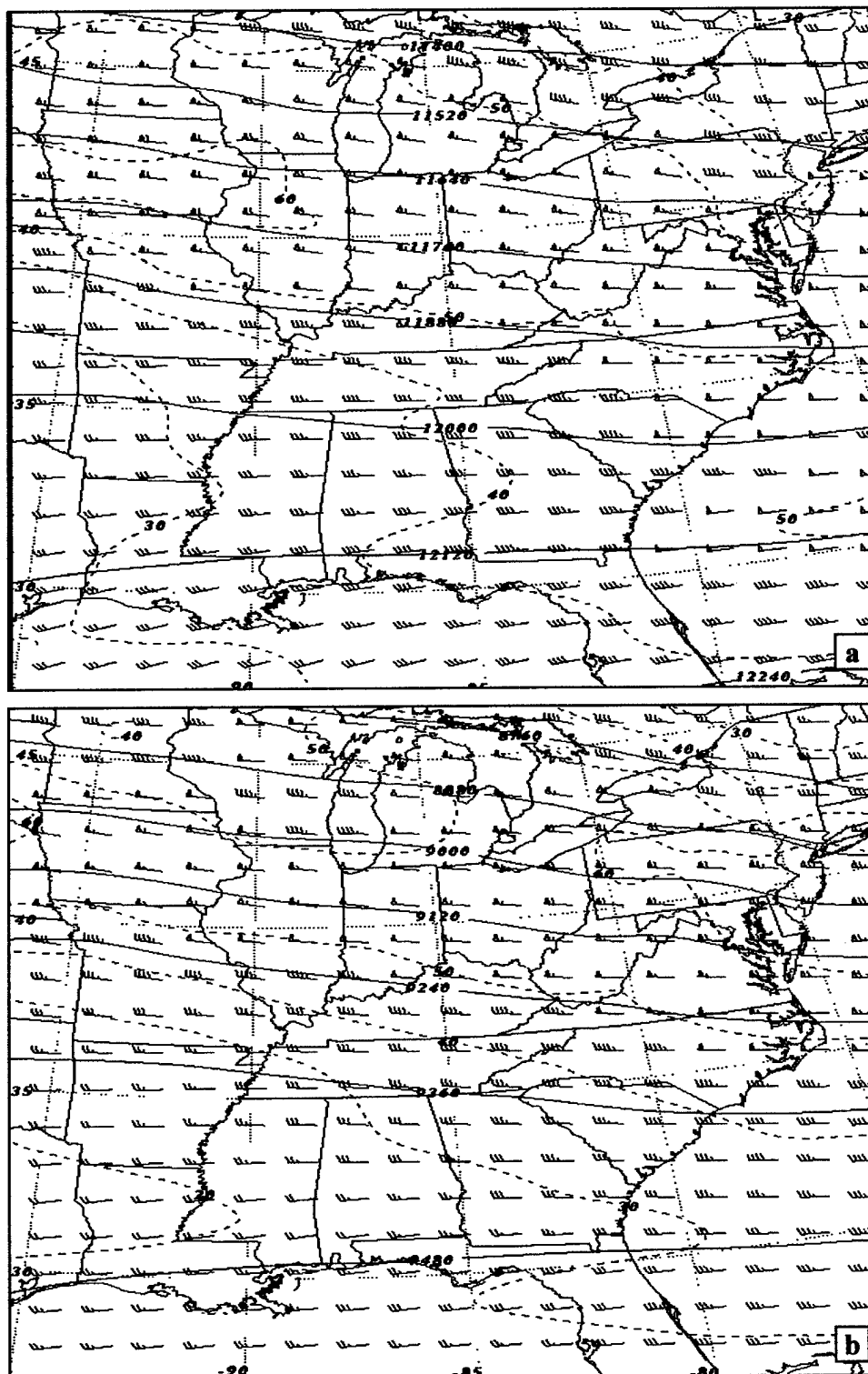
Figure 37. Simulated winds (ms^{-1}) and heights (m) valid 09 UTC 12 Jan 2000 (a) 200 hPa, (b) 300 hPa. Heights are contoured every 120 m.

107
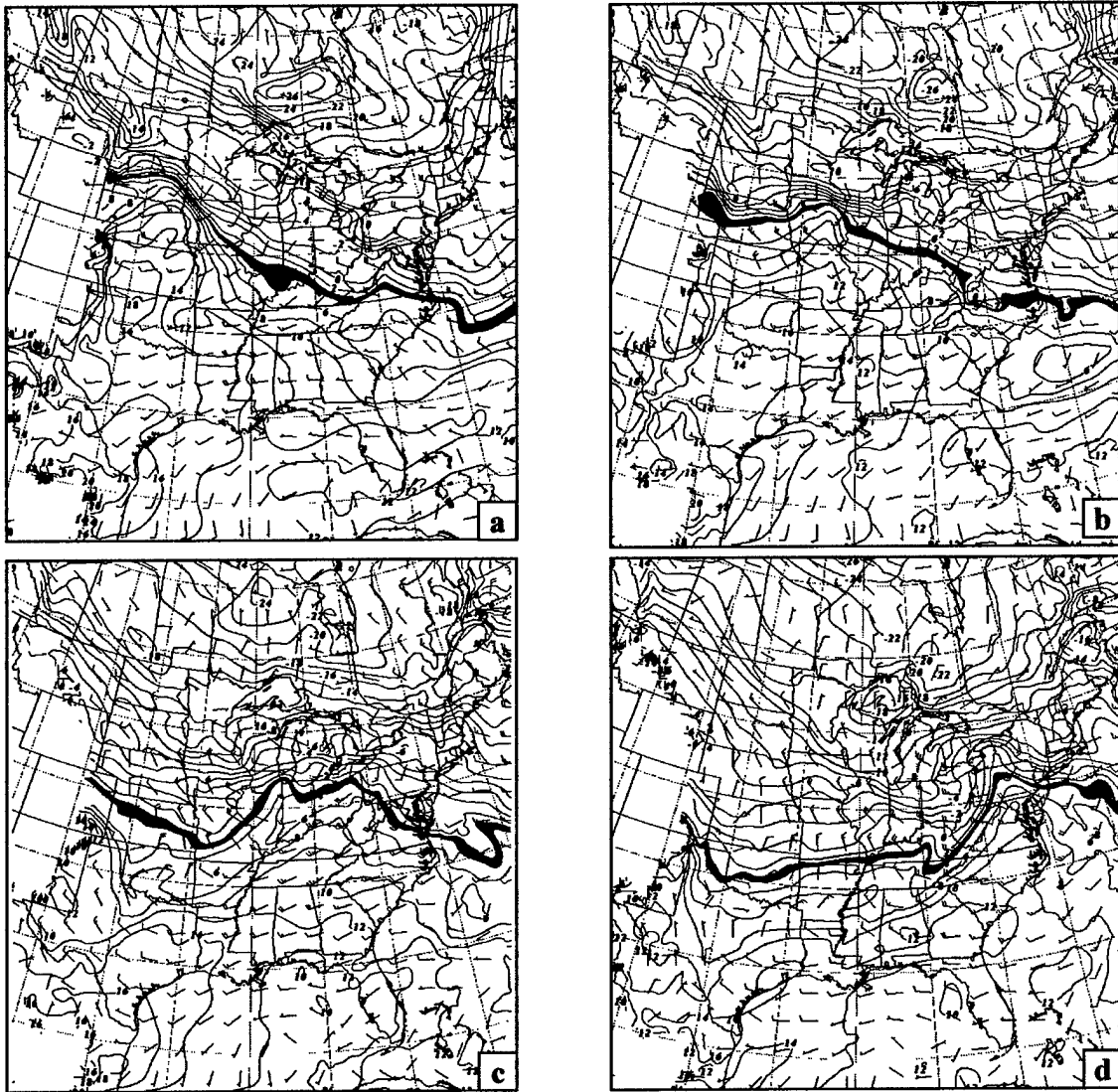
Figure 38. Simulated 850 hPa temperature (^{0}C) and wind (ms^{-1}). The 3-4 ^{0}C isotherm interval is highlighted. Valid times (a) 09 UTC 12 Jan 2000, (b) 18 UTC 12 Jan 2000, (c) 03 UTC 13 Jan 2000, (d) 12 UTC 13 Jan 2000.
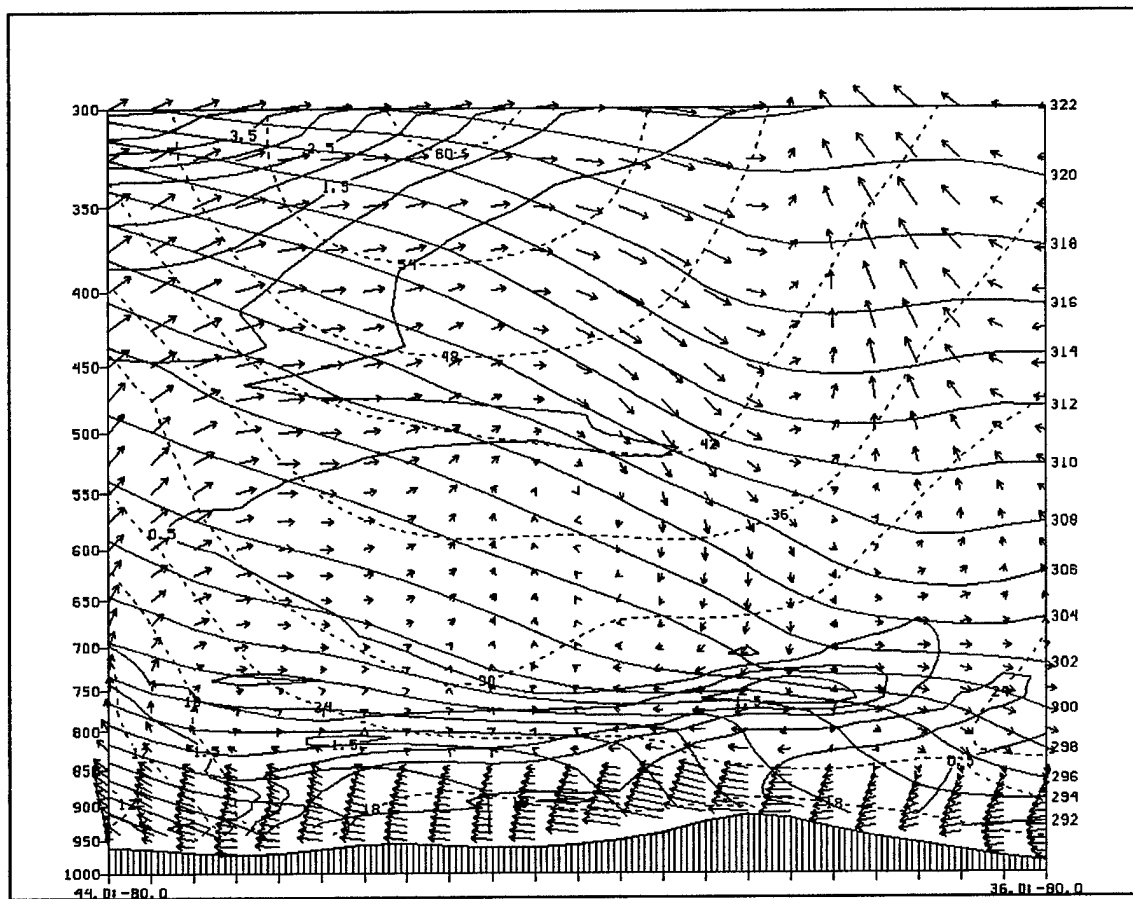
Figure 39. Simulated north to south cross section (latitude and longitude listed across the lower horizontal axis, hatch marks beneath terrain are spaced at 40 km) depicting potential temperature (solid line), isotachs (ms^{-1}, dashed line), potential vorticity (1 PVU and greater shaded), and ageostrophic circulation (arrows). Valid 1200 UTC 13 Jan 2000.

109
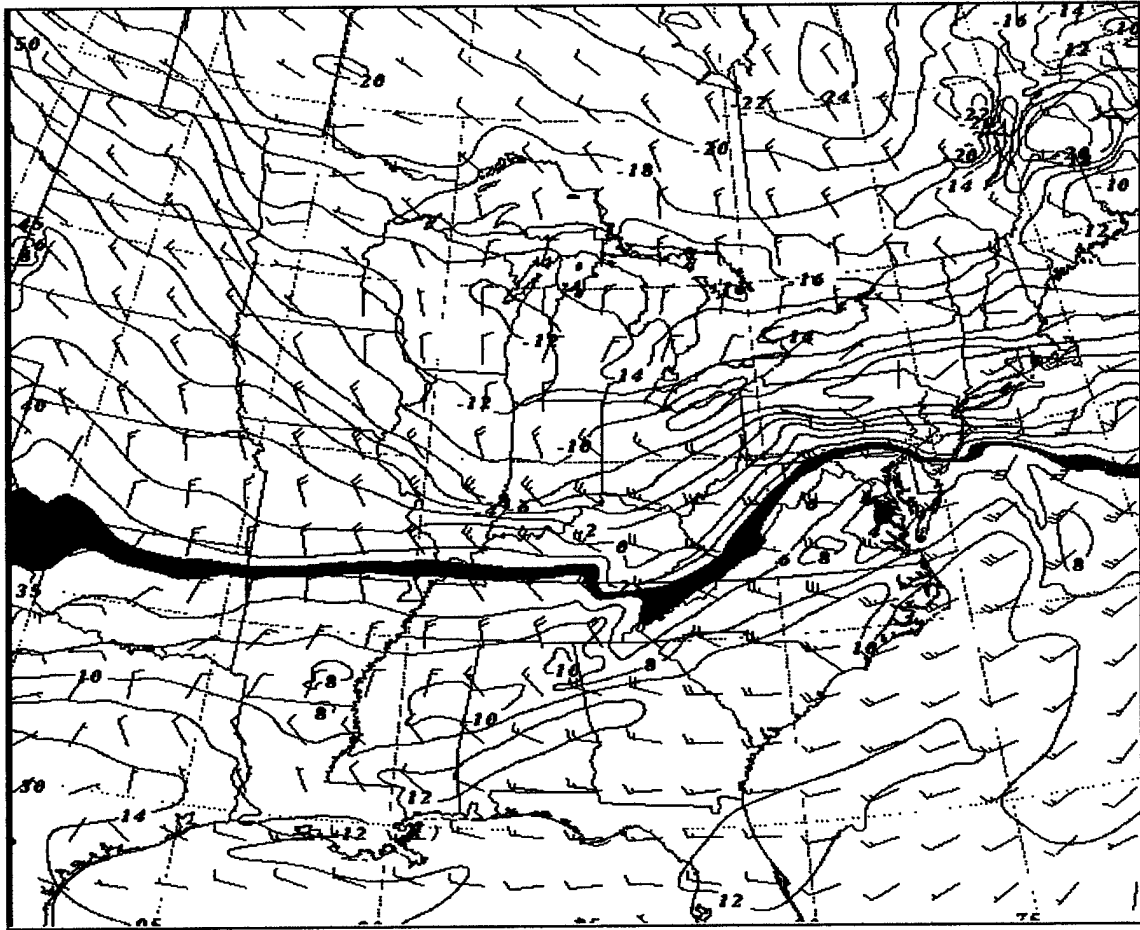
Figure 40. Simulated 850 hPa wind (ms^{-1}) and temperature (^{0}C) analysis valid 1400 UTC 13 Jan 2000. Red shading highlights the 3-4^0 temperature range.

Figure 41. Nashville, TN Skew-T (KBNA) Valid 00 UTC 13 Jan 2000.
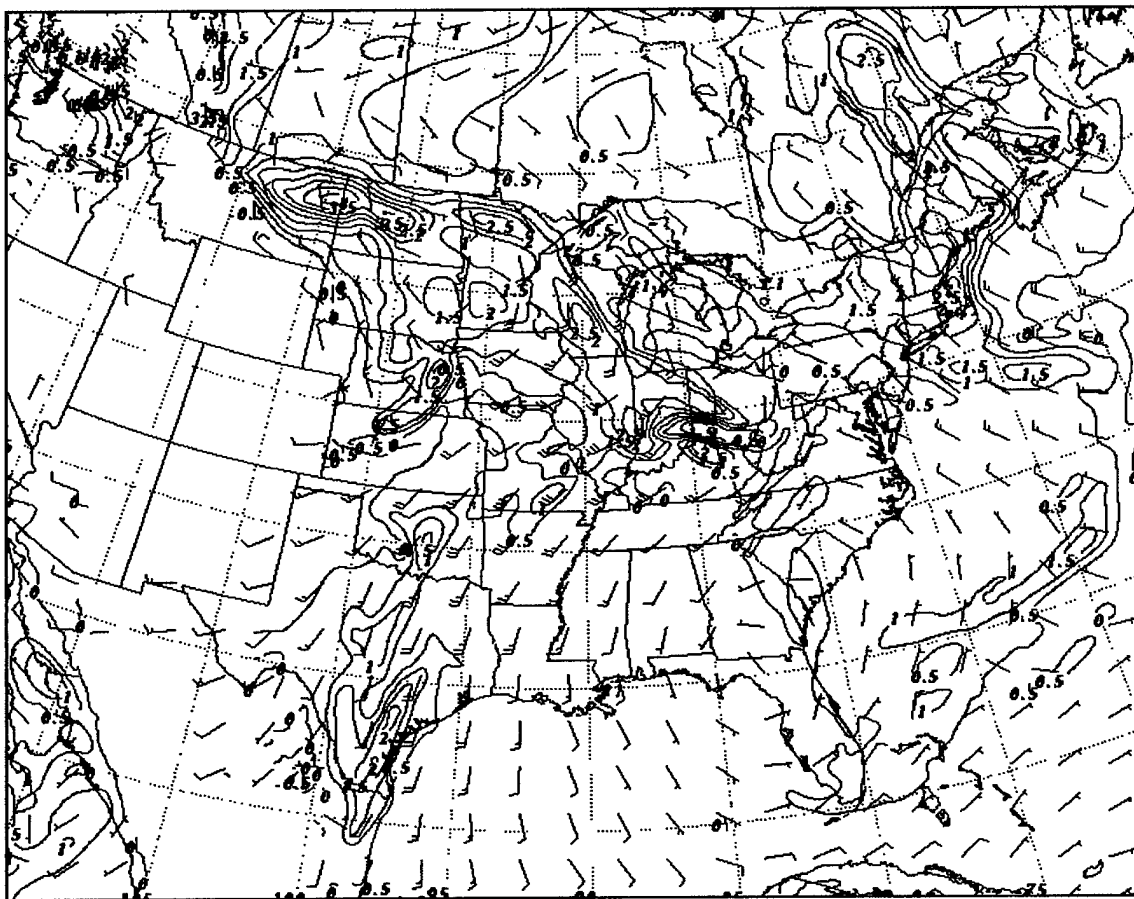
Figure 42. Simulated 850 hPa wind (ms^{-1}) and potential vorticity (contoured every 0.5 PVU) valid 00 UTC 27 Dec 1988.
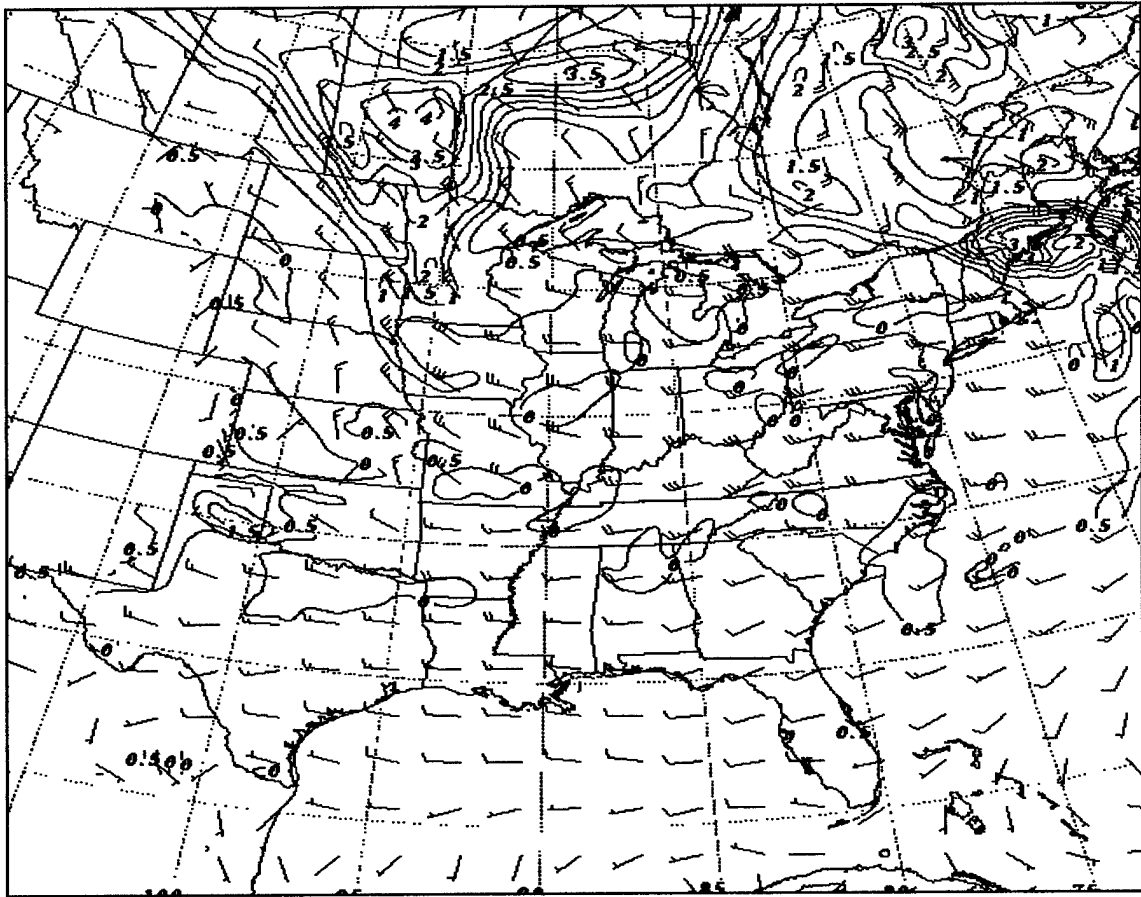
Figure 43. Simulated 850 hPa wind (ms^{-1}) and potential vorticity (contoured every 0.5 PVU) valid 06 UTC 11 Jan 2000.
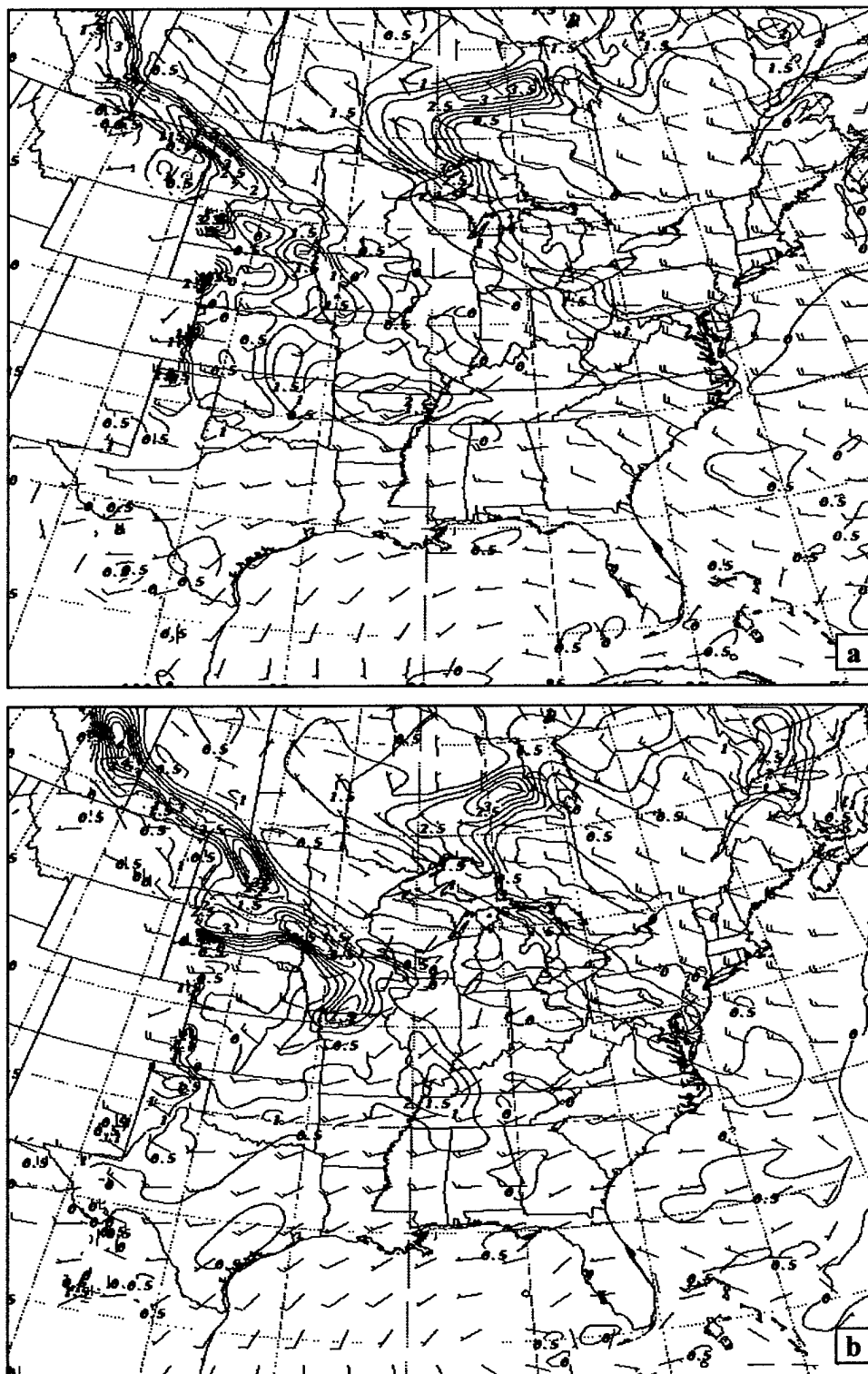
Figure 44. Simulated 850 hPa wind (ms^{-1}) and potential vorticity
(contoured every 0.5 PVU) valid (a) 05 UTC 12 Jan 2000, (b) 12 UTC 12
Jan 2000.

CHAPTER 3

MESOSCALE SIMULATIONS OF DYNAMICS AND STRUCTURE FOR TWO DIFFERING LOW-LEVEL TURBULENCE EVENTS EAST OF THE APPALACHIAN MOUNTAINS. PART II: TERRAIN INTERACTION AND DOWNSTREAM MESO-α AND MESO-β RESPONSE

3.1 Introduction

Atmospheric turbulence is the leading cause of non-fatal injuries to airline passengers and aircrew. Low-level turbulence is of particular concern as aircraft take-off and landing are considered the most dangerous stages of flight and there is much less room to react or compensate for unexpected turbulent motions. Accurate forecasts of moderate or greater turbulence would significantly benefit the aviation field. Unfortunately, the very fine scale nature of turbulence combined with the rather coarse observational network make this difficult. Precursors at the larger scale (i.e., observable) must be identified and related to the various scale-interactive processes leading to the turbulence in order to adequately identify regions prone to this dangerous phenomenon.

Numerous explanations and expected locations for turbulence have been provided in the literature (see review in Chapter 1). These include entrance regions of jet streaks (Reiter and Nania 1964; Mancuso and Endlich 1966; Roach 1970; Reed and Hardy 1972; Shapiro 1976; Gidel and Shapiro 1979; Uccellini et al. 1986; Keller 1990; Ellrod and Knapp 1992), shear zones above and below jet streaks (Kennedy and Shapiro 1975, 1980), undercutting jet features (Uccellini et al. 1986), vertical shear of the horizontal wind (Knox 1997), Kelvin-Helmholtz Instabilities (Hopkins 1977; Keller 1990; Fairall et al. 1991; Ellrod and Knapp 1992; Jingliang and Jianzhong 1996), large-scale atmospheric imbalance (McCann 1998), and gravity waves (Fairall et al. 1991; McCann 1998, 1999). Conditions crucial for

115

turbulence formation and subsistence include large variations in the vertical and horizontal wind vectors, vertical motions, and often the existence of a stably stratified layer. These conditions tend to occur more often for curved flow than for straight flow (Endlich 1964; Ellrod 1985). Recently, Kaplan et al. (2003a) utilized 40 accident reports and four in-depth severe turbulence case studies to determine that turbulence should be forecast in regions with the following synoptic signatures: jet stream entrance region, upstream curvature, cold advection, and nearby convection. Their study focused primarily on upper-level turbulence where the effects of terrain were minimal. The introduction of elevated terrain complicates matters somewhat.

The presence of terrain can significantly impact both upstream and downstream weather. Various authors have demonstrated that the movement of a deep front approaching a mountain range is altered and that the front advances irregularly when compared to the expected propagation absent the mountain range (Buzzi and Tibaldi 1978; Smith 1982a; Davies 1984; Blumen and Gross 1986; Schumann 1987; Zehnder and Bannon 1988; Egger and Hoika 1992; Gross 1994; Steenburgh and Blazek 2001). The environment surrounding the mountains also plays an important role in the terrain's ability to block (or retard) flow as it encroaches upon the mountain.

Durran (1986) noted that the presence of an upstream inversion enhanced the existence of tropospheric waves as well as the pressure drag due to terrain and that increased mountain height greatly increased terrain drag—in a similar manner to that predicted in hydraulic theory as the height of a mountain becomes sufficient to force a transition from subcritical to supercritical flow at the crest. This transition from subcritical to supercritical flow has been associated with a sharp increase in leeside wind speeds. Results from

116

numerical modeling studies suggest that mountain-induced frontal distortions are most pronounced when the Froude number is much less than one (Schumann 1987; Gross 1994). Froude number is generally defined as Fr=U/Nh, where U is the upstream velocity, N the Brunt-Väisälä frequency, and h the mountain height. Low Froude number favors low-level blocking. This blocking is enhanced by increased mountain height and static stability and decreased cross-mountain winds. Additionally, weaker fronts (those with smaller temperature, density, and pressure gradients) tend to be more frequently blocked than stronger fronts with faster propagation (Gross 1994).

Smith (1982b), Gross (1994), and others found that the presence of terrain effectively slowed incoming flow near the surface while the cold air aloft was unimpeded resulting in "differential advection" and mountain-induced vertical shear. As the cold air aloft overrides the relatively warmer air at low levels, instability results downstream from the mountains. Although infrequently presented in the literature, scale interaction effects due to terrain interference can play an important role in weather downstream from mountains. Karyampudi et al. (1995a) noted that interaction of the Rocky Mountains with specific larger-scale flow patterns and the vertical structure of the atmosphere produced a scale-interactive process from large-scale baroclinic to mesoscale to microscale downstream.

In this chapter we investigate two cases of low-level turbulence (between 800 and 700 hPa) east of the Appalachian Mountains in detail and identify the meso-α and meso-β signals that play a role in generating this turbulence and the scale-interactive processes immanent in these signals. The first case occurred on 28 December 1988 and has been studied previously in the literature (Koch and Kocin 1991; Chen et al. 1997) as an event where a strong narrow cold frontal rainband (NCFR) formed east of the Appalachians. The

117

amount of low-level turbulence for this event was significant, but the majority of reports were of moderate or lighter intensity. The second case investigated is from 13 January 2000 in the same region. This case also involved a multitude of low-level turbulence reports, but the vast majority of reports were of severe intensity. Although these two cases were similar in many respects, there are some significant differences with decreasing scale that play a role in determining the eventual convective structures and resultant downstream turbulence.

Large-scale (synoptic and meso-α) similarities and differences between these cases were detailed in the previous chapter. Both events occurred during winter months, at the same time of day, and at similar altitudes. Surface analyses were similar as both cases featured a cold front along the Appalachians that moved through the region of reported turbulence between 1700 and 2100 UTC. Additionally, both cases possess many of the large-scale turbulence precursors detailed in Kaplan et al. (2003a,b,c) as favorable for turbulence formation (i.e., nearby jet entrance region, upstream curvature, strong cold advection, and nearby convection). In spite of these early similarities, some crucial differences prior to turbulence formation exist and are likely responsible for the different atmospheric responses and different turbulence intensities reported for these cases.

Large-scale differences between these two cases in the hours prior to turbulence formation have a direct effect on subsequent atmospheric response along and downstream of the Appalachian Mountains. To begin, the events display different large-scale wave patterns. The 28 December 1988 case (henceforth D88) exhibits a meridional wave pattern with ridging over the East Coast while the 13 January 2000 case (henceforth J00) possesses a more zonal wave pattern with a vortex over Quebec and a distinct southern jet stream which combine to enhance convergence east of the Appalachians. Additionally, flow in D88 is less

118

perpendicular to the terrain in advance of the cold front and is essentially uni-directional at all levels. Flow for J00 is more orthogonal to terrain and multi-directional in the vertical. Essentially, the 28 December 1988 pattern does not favor frontogenesis east of the Appalachians and the 13 January 2000 pattern does. Perhaps more significantly, these two cases display different jet-front structures in the 72 hours prior to the turbulence events and these differences have a significant impact on the low-level environment downstream of the Appalachian Mountains on the dates in question.

As discussed in Chapter 2, the presence of a subtropical jet (STJ) and its associated transverse ageostrophic circulations distinguishes J00 from D88 and ultimately plays an important role in the advection of low-level warm air (as well as PV) along and east of the Appalachians. As detailed in Chapter 2, the interaction between the STJ and PJ (and their concomitant ageostrophic circulations) prior to the 13 Jan 2000 event enabled warm air from the Mexican Plateau to move east and northeast where it is transported over the colder surface air east of the Alleghenies, thus increasing the static stability and (as will be shown) played a significant role in the blocking of flow over the elevated terrain. This advection pattern resulted in the increase in the subsequent strength of the isentropic upfold elemental to the low-level frontogenesis, convection, and turbulence as described in the following hypothesis.

It is hypothesized that the orography of the East Coast of the United States in combination with identifiable meteorological signals of decreasing scale can combine in the following, logical scenario resulting in convection and the generation of severe low-level turbulence:

(1) Strong flow orthogonal to the Appalachian Mountains results in large-amplitude

119

hydrostatic mountain wave formation.

(2) Mountain-wave induced vertical motions produce a downstream isentropic upfold (i.e., a mid-level cold pool) oriented northeast-southwest as a reflection of the Appalachian Mountains. This cold pool is deformed by the large-scale background jet and its concomitant ageostrophic motions (to include an indirect circulation that enhances the cold pool). This process is similar to that described by Kaplan and Karyampudi (1992a) except applied on the Appalachians.

(3) Intensification of the cold pool aloft and mass flux convergence results in a leeside pressure ridge and a building edgewave that propagates to the south-southeast in a manner previously described by Tilley (1990) and Colle and Mass (1995). This Kelvin-wave response leads to increased surface convergence and frontogenesis as the front at the surface becomes oriented ENE-WSW.

(4) Leeside warming due to downslope adiabatic effects results in a temperature ridge (leeside trough) east of the Appalachians.

(5) These features (leeside trough, cold pool aloft, surface cold surge) coalesce to form a system somewhat similar to a cold occlusion and results in a lapse rate much greater than moist adiabatic as cold air resides over low-level warm air in a region of tightening surface temperature gradient and convergence east of the Appalachian Mountains.

(6) This combination in the vertical results in convection, cold downdrafts, formation of a density current-like feature, and ultimately breaking vortices (as discussed in Chapter 4). These microscale features are believed to result in a helicity-rich low-level environment highly predisposed to strong low-level turbulence near their level of interaction (i.e., 800 – 700 hPa).

120

The downstream effects of mountain-induced cold pools and their interaction with other terrain-induced features have been largely ignored in the literature. It is believed these interactions along the US East Coast (and likely other regions) can play an important role in the development of convection, scale contraction, and low-level turbulence generation. The synoptic and meso-α scale signals and precursors were detailed in the previous chapter. This chapter will bridge the transition from the meso-α signals to the meso-β signals detailed in the first five stages of the hypothesis. It is highly likely that a combination of inter-scale signals, to include differences in jet-front signatures and pre- and post-mountain stability structures, along with different frontal structures (anafront versus katafront) and resultant convection (lineal versus cellular), delineate the difference in turbulence intensities reported for these two events. These differences and how well each case fits the first five stages of the hypothesis presented will be the focus of this chapter. The finer, meso-γ and microscale signals leading to the final stage of the hypothesis will be presented in Chapter 4. The remainder of this chapter is set up as follows: Section 2 provides a brief summary of the numerical model utilized in this study. Section 3 details the pre-mountain wave environment for both events. Section 4 discusses the hydrostatic mountain wave formation and subsequent isentropic upfold (mid-level cold pool). Section 5 details the deformation of the mid-level cold pool and the surface response and Section 6 provides a summary of results.

3.2 Numerical Model Description

In order to increase the spatial (both horizontal and vertical) and temporal coverage necessary to adequately diagnose the multi-scale phenomena involved in the two low-level turbulence events studied in this research, a mesoscale model is utilized. The non-hydrostatic Mesoscale Analysis and Simulation System (NHMASS) model version 6.0 (Kaplan et al. 2000) produces the simulations used in this study. The numerical experiments, model specifics, grid resolution and coverage are detailed in Chapter 2. Three dimensional parcel trajectories are plotted and analyzed in order to ascertain parcel origination and flow patterns. The Mesoscale Atmospheric Simulation System Trajectory (MASSTRAJ) software package (Rozumalski 1997) is used to accomplish this.

3.3 Pre-Mountain Wave Meso-β Environment

Synoptic-scale differences in jet-front structure and Rossby wave configuration resulted in different environments in the vicinity of the Appalachian Mountains for the two cases studied in this research (for more details, see Chapter 2). The presence of a subtropical jet in the 13 Jan 2000 event, the overall large-scale wave pattern, wind orientation to terrain, and resultant stability and hydraulic structures both upstream and downstream of the Appalachians play a role in the subsequent atmospheric response and the degree of conformity these cases display in regards to the low-level turbulence hypothesis presented in Section 1. The differences in large-scale jet-front structure and Rossby wave orientation have a profound effect on the degree of damming/blocking present in these two cases and the atmospheric response to these differences ultimately affects the downstream frontal structure, convective geometry, and degree of helicity and low-level turbulence (as will be shown in Chapter 4).

The southern, subtropical jet (acting in tandem with the more northerly polar jet) and its concomitant elevated (warm) mixed layer on 13 Jan 2000 enables the transport of warm air from the Mexican Plateau to the leeside of the Alleghenies early on 13 January. This elevated warm layer helps set up a strong inversion on the leeside of the mountains and enables blocking of the windward front (and mass) and deflects the low-level flow around the Alleghenies and aloft downstream. On the other hand, flow on 28 December 1988 is driven by a single jet-front system with a strong polar jet-front only (i.e., no subtropical jet). Low-level continental air in this event arrives farther to the northwest as part of the transverse low-level return branch circulation of the more compact (traditional) polar jet-front system. Additionally, the Rossby wave structure is oriented differently in these two cases (more

details are provided in Chapter 2). The large-scale tilt in J00 is primarily NW-SE which enables the cold air east of the Alleghenies to be dammed and (when combined with the previously described transport of low to mid-level warm air above this cold surface) helps set up a flow transition across the Alleghenies that is essentially blocked (supercritical upstream and subcritical downstream) early on the 13th. The large-scale tilt in D88 is primarily NE-SW (and there exists only the single polar jet). This large-scale tilt results in a more partially-blocked hydraulic structure with transition from subcritical upstream to supercritical downstream. These different structures, in combination with overall wind profiles and hydrostatic mountain wave formation, significantly affect the downstream atmospheric response (as will be shown).

As a result of the large-scale differences previously discussed, the low-level temperature and stability structures upstream and downstream of the Appalachian Mountains are markedly different for 28 Dec 1988 and 13 Jan 2000. These differences have a profound impact on the atmosphere's hydraulic response in terms of frontal propagation (i.e., blocking effects) as well as the strength of the isentropic upfold and its associated cold pool which plays a critical role in the processes leading to turbulence formation—particularly in J00.

The presence of the subtropical jet (absent in D88) as well as the more west to east polar jet enables warm Mexican Plateau air to advect to the ENE where it ultimately resides over the colder surface air east of the Alleghenies early on 13 Jan 2000, essentially setting up a fairly strong low-level inversion on the leeside of the Alleghenies. A similar scenario does not occur on 28 Dec 1988 and no significant leeside inversion is present early on the 28th (or at any time prior to cold frontal passage). Between 1200 and 1400 UTC on 13 Jan 2000, a clear difference in temperature advection (and parcel origination) exists on both sides of the

Alleghenies, whereas on 28 Dec 1988 no significant temperature difference is apparent on either side of the mountains and the strongest inversion/stability is located upstream with the approaching Arctic front. Fig. 1 clearly depicts the simulated differences in low-level temperature patterns for these two events. This difference in low-level temperature advection and environment naturally results in a fairly distinct difference in the stability structures on both sides of the Alleghenies for these two cases. And these stability structures directly impact the progression of the large-scale frontal systems as they traverse the Alleghenies.

An examination of vertical cross sections bisecting the Alleghenies and generally orthogonal to frontal propagation highlights the differences in temperature and stability structure on both sides of the mountains as the cold fronts propagate to the east (Fig. 2). Clearly, the static stability is much stronger downstream of the Alleghenies (the primary peak in terrain elevation pictured in the cross section) for J00 than for D88 as depicted in the more tightly packed isentropes east of the mountains at low levels in J00 at 14 UTC (Fig. 2a). On the other hand, static stability is much greater upstream of the Alleghenies for D88 (Fig. 2b). In general, in the hours prior to the cold fronts completely traversing the mountains (i.e., prior to 18 UTC), reduced gravity ($g\frac{\Delta\theta}{\theta}$) for 28 Dec 1988 was more than twice that for 13 Jan 2000 upstream of the Allegheny Mountains indicative of the increased upstream static stability in D88. Additionally, model generated soundings plotted during the early morning hours (10-17 UTC) for both events evince these differences. These soundings—plotted on both sides of the Alleghenies—further highlight the difference in temperature and stability structure in the region of interest in advance and during mountain wave and subsequent mid-

125

level cold pool formation (discussed later in this chapter). Upstream and downstream skew-Ts for 16 UTC plainly depict the much lower and stronger downstream inversion on 13 Jan 2000 and the stronger upstream inversion on 28 Dec 1988 (Figs. 3 and 4). The upstream sounding is located at 40 ^{0}N, 80 ^{0}W and the downstream sounding at 40 ^{0}N, 77 ^{0}W (i.e., on either side of the Allegheny peak terrain elevation along 40 ^{0}N Latitude). These differences in upstream and downstream temperature and stability profiles (as well as ambient wind and propagation speed of the cold front as it traverses the region) affect the hydraulic flow regime and the downstream impact of the cold front as it propagates. Differences in stability are further highlighted in a comparison of Brunt-Väisälä frequencies throughout the region computed in the lower levels using output from the 6-km control runs.

The Brunt-Väisälä frequency is defined as $N = \left(\dfrac{g}{\theta} \dfrac{\partial \theta}{\partial z} \right)^{\frac{1}{2}}$, where g is the acceleration due to gravity, θ is a mean potential temperature over the layer, and $\dfrac{\partial \theta}{\partial z}$ is a measure of the lapse rate or static stability. Plots of N^2 (both prior to frontal transit and after) highlight the differences between these two cases (Fig. 5). For the 13 Jan 2000 event, the early (i.e., prior to 1700 UTC) streamwise variation of N (i.e., variation along the flow as opposed to across the flow where the stream is defined as the axis of strongest geostrophic wind) from low to high across central Maryland and south-central Pennsylvania is consistent with a low-level blocked flow regime that transitions into an unblocked (or partially-blocked) regime during the afternoon as surface heating and the isentropic upfold due to hydrostatic mountain wave formation (discussed in the following sub-section) eliminate the leeside inversion and reverse the streamwise N-gradient (note: $N^2 = 5.5 \times 10^{-4} s^{-2}$ at 13/12 UTC and $1.5 \times 10^{-4} s^{-2}$ at 13/18

126

UTC). In the 28 Dec 1988 event, the opposite scenario occurs (Fig. 6). Initially, there is a much larger windward-side N^2 (inverse) consistent with partial blocking and hydraulic jump phenomena ($N^2 = 1.0$ x10^{-4} s^{-2} at 28/12 UTC and 3.5 x10^{-4}s^{-2} at 28/18 UTC). In order to better quantify the differences in these regimes, internal Froude numbers are computed based on the technique described in Simpson (1997). The internal Froude number allows for the effects of both the upstream and downstream fluids on the motion of the obstacle (i.e., cold front).

Although these two dimensional Froude number and height/interface computations are somewhat idealized, they do enable a quantified comparison of the two flow regimes and the types of disturbance/regime likely to result in an environment similar to those observed in this study. The four types of disturbance which can be generated by a moving obstacle (i.e., the cold front) at the interface between two fluids can be inferred from Fig. 7 (Simpson 1997). Computations utilizing $F_0 = U / \sqrt{g'h_0}$ for internal Froude number, where U is the speed of the obstacle, g' is reduced gravity, and h_0 is the height of the fluid interface and $H = d_0 / h_0$, where d_0 is the height (or depth) of the obstacle, are made for various times for the two cases studied and compared to Fig. 7 in order to make a quantitative comparison between the 28 Dec 1988 and 13 Jan 2000 events. The height (or depth) of the obstacle (d_0) was estimated based on the height of the upstream inversion utilizing both cross sections (Fig. 8) and skew-Ts (Fig. 3) where upstream refers to the cold front (west of the terrain). The height of the fluid interface (h_0) was estimated based on the height of the downstream inversion utilizing both cross sections (Fig. 8) and skew-Ts (Fig. 4) where downstream refers to the environment in advance of the front (east of the terrain). Estimates for D88 (for 16-17 UTC) yield d_0 values of 870 m and 1220 m and h_0 values of 1320 m and 1400 m.

Computations result in H values between 0.66 and 0.87 and F_0 values of 1.35 and 1.13. These results identify flow for this case as falling in either regime A or B, i.e., partially blocked or supercritical flow. These results agree with the observed flow and behavior of the atmosphere as the rapidly moving arctic front crosses the mountains in a relatively unimpeded manner. Computations for J00 also mirrored observed and simulated frontal motion. Estimates for J00 yield d_0 values of 1690 m and 1610 m and h_0 values of 540 m and 550 m. Non-dimensional height (H) values were considerably higher (largely due to the downstream low-level inversion) and Froude numbers were somewhat smaller with H values between 2.95 and 3.11 and Froude numbers ranging from 0.54 to 0.90. These results indicate flow for J00 falls in regime B or C, i.e., partially blocked or completely blocked flow regimes based on Fig. 7. Additionally, the low internal Froude numbers in J00 indicate possible subcritical flow given a lower non-dimensional height. Based on these computations, low-level flow in J00 is more likely to be retarded than is flow in D88—and this is indeed observed and simulated. As a result, and as will be shown later in this (and the next) chapter, these differences suggest different downstream responses for these two cases with supercritical flow and hydraulic jumps expected as the arctic front moves to the east in D88, and blocked or subcritical flow with Kelvin modes or edgewaves expected for J00 (Tilley 1990). Clearly, these two cases represent a stark contrast in hydraulic theory and the role of the mountains on airflow. These differences have a significant effect on the downstream weather east of the Appalachians as well as the strength of any mountain-wave induced upfolds acting on these environments.

Based on the previous analysis, the 13 Jan 2000 regime is a highly blocked regime with little hydraulic forcing. As a result, the middle to upper tropospheric mass fields are

more likely to adjust downstream if the synoptic-scale cold front is to propagate over the blocking mountains. This alteration is not necessary for the 28 Dec 1988 case since the flow is only partially blocked or supercritical and the arctic front traverses the region essentially unimpeded. As a result, the terrain-induced katafront (detailed later in this chapter) is much better developed in J00, as is the critically important low-level leeside cold surge. This leeside cold surge allows the low-level front and its local mass field to discretely propagate downstream as the Kelvin/edgewave progresses to the south constrained by the Alleghenies to the north and west in a manner similar to that described by Tilley (1990) and Colle and Mass (1995). The low-level front on 28 Dec 1988 is simply accelerated through the mountainous region by the hydraulic feature and downstream-directed pressure gradient force. The leeside cold surge (and upfold) is strong on 13 Jan 2000, but much weaker (and difficult to discern) on 28 Dec 1988 as a result of the differences in structure on both sides of the Alleghenies (initially set up by the early processes detailed in Chapter 2). It is probable that the depth and strength of the resultant frontogenesis aloft is collocated with these structures as the initial surface front propagates away from the mountains. Similarly, it is likely these differences play a role in the downstream convective environment, i.e., whether the storms are more supercellular/helical (J00) or lineal (D88). As discussed earlier, a stronger low-level inversion exists on 13 Jan 2000 downstream of the Alleghenies. This low-level inversion results in a pressure gradient force acting against the downstream advance of the surface front as it traverses the terrain. This pressure gradient force retards the near-surface flow and combined with cross-mountain wind flow aloft results in an isentropic upfold (mid-level cold pool) and a lifting of the downstream inversion in order to enable the blocked mass field to propagate to the east. Simulated frontal propagation for 13 Jan 2000

was estimated at approximately 4-6 ms^{-1} during this time with a doubling in propagation speed after the upfold and diurnal PBL depth increase. On the other hand, the fields in the 28 Dec 1988 event tend to be more similar to that of a traditional downslope windstorm (Lilly and Zipser 1972; Lilly 1975) with the stronger inversion upstream of the terrain instead of downstream (with the pressure gradient force acting with the flow instead of against it). Simulated frontal propagation for this case was estimated between 16-20 ms^{-1} in agreement with the 19.4 ms^{-1} reported in KK91. Additionally, straight-line surface winds in excess of 40 ms^{-1} were observed from central Virginia eastward on 28 Dec 1988 (Koch and Kocin 1991). These different structures, as well as the wind orientation to the terrain have a substantial impact on the strength of the hydrostatic mountain wave formation and the resultant downstream isentropic upfolds (mid-level cold pools) present in these two events. This topic is treated in the next section.

3.4 Hydrostatic Mountain Wave and Isentropic Upfold

As will be shown in this section, hydrostatic mountain wave formation and the accompanying isentropic upfolds and downfolds (tied to the vertical motion field) play a vital role in determining the downstream response as the cross-mountain low-level winds impinge upon the Appalachians. The different intensities of these features also help to differentiate the mid- and low-level temperature, pressure, and density patterns as well as convection, frontogenesis, scale contraction, and low-level turbulence intensity in the two events studied in this research.

In the morning of both 28 Dec 1988 and 13 Jan 2000, strong cross-mountain flow leads to hydrostatic mountain wave formation and a sequence of upslope cooling, downslope warming, and a downstream isentropic upfold (Fig. 8). However, the cold pool intensity varies dramatically between the two case studies. This pattern is much more discernible in J00 (Fig. 8a) as the downstream upfold (located in south central Pennsylvania and encircled in the vertical cross section) is stronger, colder, and located further downstream than that of D88. Winds at the level of these terrain-induced upfolds are fairly strong ($> 30 \text{ ms}^{-1}$) and from the west (i.e., from left to right in the cross section). This orientation enables the large-scale jet stream to act on (and deform) the temperature variation along the stream as the air is differentially lifted. This scenario sets up an along-stream temperature gradient which leads to along-stream pressure variations and acceleration of the low- to mid-level jet due to the relatively higher pressure aloft accompanying the mid-level warm air and lower pressure with the cold upfold in a manner similar to that described by Kaplan and Karyampudi (1992a) in their study of mid-tropospheric frontogenesis east of the Rocky Mountains. This results in integrated mass flux convergence in this region (downstream of the larger-scale jet-

131

frontal system which is located west of the mountains) and relatively high pressure at the surface beneath the downstream cold pool. Additionally, since there is necessarily low- to mid-level divergence aloft with the downstream cold air and convergence with the downslope warming, an indirect circulation exists (cold air rising, warm air sinking) that acts to strengthen this along-stream mid-level cold front. This enhanced cold pool aloft (note Fig. 10) is continually deformed and enhanced by the large-scale jet acting upon it (particularly when curvature is imbedded with the jet streak entrance region). Eventually, this mid-level (850 – 700 hPa) cold pool becomes oriented NE – SW as a reflection of both the mountain topography and jet deformation. The curved jet entrance region acting on this cold pool ultimately results in high pressure at the surface which is trapped by terrain to the north and west and surges toward the south and east with time over south central Pennsylvania. More details of these individual processes are provided later in this Chapter as is the degree to which each case conforms to this scenario (and the early stages of the hypothesis laid out in the introduction). As would be expected given the differences in hydraulic structure presented in the previous section, the 28 Dec 1988 and 13 Jan 2000 events have very different responses (and intensities) to the terrain-induced wave pattern.

The differences in hydraulic and stability structures previously described will have a distinct impact on the strength of the downstream cold upfold. The leeside planetary boundary layer is more shallow for D88 (and convective activity begins earlier in the day) and the strength of the downstream low-level inversion (and necessarily larger vertical temperature gradient) is significantly stronger for J00 (as evident in the cross sections shown in Fig. 8). The earlier onset time and the weaker cross-mountain flow on 28 Dec 1988 (note Fig. 9) allows the inversion layer to be closer to the upstream side of the Alleghenies thereby

132

allowing a transition from sub- to supercritical flow for the 28 Dec 1988 event while the slightly later onset time, reduced cloud cover, and stronger cross-mountain flow in the 13 Jan 2000 event results in a deeper leeside planetary boundary layer and a transition from super- to subcritical flow. A comparison of the mean boundary layer cross-mountain winds impinging upon the Alleghenies at 12 UTC for these two cases (see Fig. 9) nicely highlights another difference between these two cases: Cross-mountain (i.e., orthogonal) flow for 13 Jan 2000 is consistently more than twice that for 28 Dec 1988 (17.5 ms^{-1} compared to 6.8 ms^{-1}) all along the Appalachians throughout the morning hours. This stronger upstream cross-mountain flow in J00 leads to greater mountain-wave induced ascent in regards to the thermodynamic fields for this case than in D88, where the upstream cross-mountain flow is weaker prior to cold frontal passage (Attié et al. 1997). This stronger cross-mountain flow, in combination with the differences in PBL and stability, indicates J00 will have a deep downstream cold pool and D88 a shallow downstream cold pool more indicative of a propagating undular bore (as shown previously in Fig. 8 and consistent with the blocking regimes in Fig. 7). Additionally, the stronger downstream cold pool on 13 Jan 2000 will result in a deeper katafront and stronger, downstream surface pressure rises (in advance of the larger-scale QG frontal system). The difference in strength of the cold upfolds is readily apparent in a comparison of the 700 hPa temperature fields through Pennsylvania in the vicinity of the Alleghenies (see Figs. 10 and 11) for both 13 Jan 2000 and 28 Dec 1988. Even though surface temperatures were comparable with frontal passage, the 700 hPa temperatures associated with the mountain-induced cold upfold were more than 12 ^{0}C colder on 13 Jan 2000 than 28 Dec 1988. Note in Fig. 10d that the cold pool in J00 is denoted by the closed −16 ^{0}C isotherm at 1830 UTC along the Pennsylvania-Maryland border. No such

cold pool exists in D88 as the temperature pattern for this case is elongated and temperatures throughout the Pennsylvania-Maryland region are $-2+^0C$ and warmer at 1800 UTC. Additionally, the cold pool in J00 is clearly downstream of the larger-scale cold advection (delineated by the packed isotherms in western Pennsylvania). There is no significant downstream cold pool evident in advance of the larger-scale cold advection in D88. These features and their relation to deformation by the large-scale system and jet stream will be discussed in more detail in the next section. Most importantly, however, they clearly demonstrate the terrain-induced downstream cold front aloft formation in J00 and absent in D88.

Essentially, the overall concept (induced by the hydrostatic mountain wave) of a windward cold pool (upslope), leeside warming (downslope), and downstream cold upfold (mid-level cold pool) can be summarized as follows: Cross-mountain flow produces a downslope warm pool at low levels immediately on the lee slope and an isentropic upfold just downstream and aloft. This scenario creates a streamwise warm-cold pattern that tilts up at an angle, downstream from the leeside (as is typical of large-amplitude mountain waves). There is also an upslope low-level cold pool on the windward slope (see Fig. 8). This upslope cold pool enables a tilted ring of cold air to envelop the mountain range with the leeside warm air sandwiched in between. Kaplan and Karyampudi (1992a) described a similar process east of the Rocky Mountains in their study of "Meso-β Scale Simulations of Terrain Drag-Induced Along-stream Circulations". They described the process as follows: (1) Vertical wind shear in the along-stream plane increases and results in the enhanced non-uniform variation of horizontal temperature advection in the vertical as the ageostrophic wind component increases downstream of the mesoscale terrain-induced adiabatic heating

134

(isentropic downfold). (2) Increasing streamwise differential vertical motions (via an along-stream thermally-indirect circulation) tilt the vertical gradient of potential temperature into the horizontal as the vertical temperature gradient increases (due to vertical wind shear) in close proximity to the horizontal gradients in the along-stream component of the ageostrophic wind. (3) Lastly, as tilting motions act to increase the streamwise horizontal temperature gradient, the along-stream confluence (with the large-scale jet entrance region) acts to non-uniformly increase the streamwise frontal temperature gradient which increases the streamwise pressure gradient force and results in further accelerations, ageostrophy, and frontal steepening as part of a scale contraction process. As the large-scale background flow becomes more confluent, the frontogenetical jet entrance region stretches and deforms the cold pool and tightens and modifies the background front along the stream—increasing the downstream leeside mass flux convergence and ultimately resulting in leeside surface pressure pulses/rises. The difference in the mid-level cold pool strength between J00 and D88 will have a direct bearing on subsequent atmospheric responses.

3.5 Deformation of the Mid-level Cold Pool and Surface Response

A particularly interesting facet of this research and the events studied involves the interaction of the terrain-induced mid-level cold pool with the larger-scale jet-front system previously described in an earlier chapter. When the dynamic cold upfold forms, the mid-level cold air becomes available for advection.

3.5.1 Mid-level Cold Pool – 13 Jan 2000 Case

Fig. 12 depicts cross sectional analyses from the J00 6-km control simulation. The top figure (Fig. 12a), valid 13 Jan 2000 at 1200 UTC indicates the incipient isentropic upfold-downfold-upfold pattern windward and downstream from the Allegheny peak (approximately in the center of the cross section) throughout much of the troposphere. An examination of mid-level winds at this time indicates the westerly jet entrance region is upstream of the terrain peak with the jet stream axis essentially in the west (i.e., upper left quadrant of the cross section) to central portion of the cross section. By 13/1700 UTC (Fig. 12b), the slightly curved, convergent entrance region of the jet is acting on the mid-level cold pool along and downstream of the Alleghenies. Note the significantly enhanced baroclinicity associated with the mid-level cold pool in the region at 700 hPa downstream from the maximum terrain heights. This cold air can be deformed by the larger-scale jet entrance region resulting in enhanced streamwise frontogenesis and mass flux convergence. In addition to the increased baroclinicity apparent in Fig. 12b, a brief examination of the wind and temperature patterns at 700 hPa for the times depicted in Fig. 12 demonstrates the eastern progression of the jet entrance region, the location and ageostrophic stretching deformation accompanying the mid-level cold pool, and the distinct, separate nature of the upfolded (downstream) mid-level cold

136

pool from the larger scale cold advection aloft and upper-level trough (Fig. 13).

An examination of the 700 hPa winds at 13/1200 UTC indicates the jet stream entrance region is upstream as diagnosed in the cross section (essentially located along the 40 ^{0}N latitude line (the first latitude line north of the Pennsylvania-Maryland border in Fig. 13)). The larger scale trough and associated cold advection (at this level) are located outside the plotted domain at this time (to the northwest). An analysis of temperatures at 13/1200 UTC indicates the cold-warm-cold pattern associated (represented by K-W-K in Fig. 13a) with the terrain-induced upfold in the cross section for the region in south central Pennsylvania (essentially between 39.7 and 40 ^{0}N latitude). A comparison with terrain clearly indicates this temperature pattern coincides with the Allegheny peak (note: for reference purposes, Fig. 14 depicts the surface terrain used for the simulation depicted in Figs. 12 and 13) and is an early signal in the mid-levels of the cold pool depicted in the cross section (Fig. 12a). By 13/1700 UTC (Fig. 13b), significant changes in the wind and temperature patterns are apparent. The terrain-induced mid-level cold pool is now being stretched (and, hence, deformed at the regions identified by the boxed "K"s in the figure) by the convergent curved jet entrance region (i.e., between the west-northwesterly and west-southwesterly flow) as it traverses the Alleghenies into south central Pennsylvania. Baroclinicity is significantly stronger than before—note the tightly packed isotherms and strong along-stream temperature gradient downstream of the Alleghenies in southern Pennsylvania and western Maryland as the mid-level cold pool is becoming elongated in a NE-SW sense. The specifics of this cold pool and that of D88 will be discussed in more detail later in this chapter.

This deformation of the mid-level cold pool by the jet is occurring downstream from the integrated mass flux convergence associated with the large-scale cold front (and the

137

subsidence in the left entrance region of the large-scale jet). In the 13/1700 UTC 700 hPa plot (Fig. 13b), the terrain-induced, downstream mid-level cold pool is demarcated by the –12.5 ^{0}C isotherm (light blue contour) embedded in the westerly flow east of the elevated terrain in the region. The larger-scale cold advection is located upstream over northwestern Pennsylvania with the 700 hPa trough and associated wind shift from primarily westerly flow to northerly flow and is demarcated by the –16.5 ^{0}C isotherm (plum contour in the northwest corner of the plot). As a result, a secondary integrated cold advection and mass flux convergence region is created over the Alleghenies in advance (i.e., downstream) of the large-scale QG front location resulting in a downstream region of integrated mass flux convergence. In essence, this downstream tilt due to the mid-level cold pool and subsequent surface response (detailed later in this chapter) acts to discretely advance the surface front (and frontogenesis) from its upper-level QG location west of the mountains as the surface pressure rises downstream (east of the mountains). Essentially, the downstream terrain-induced mid-level cold pool and jet-deformed mid-level front result in a forward-tilted cold frontal structure (i.e., katafront) as detailed later in this chapter and depicted in Fig. 15. This cross section valid 1930 UTC on 13 Jan 2000, clearly depicts the forward tilt to the cold front at this time (surface cold front position denoted by triangle on x-axis) as reflected in the isentropes. This forward tilt is consistent with the cold upfold downstream from the mountains as the new surface mesohigh forms in response to this downstream terrain-induced cold pool which has been further deformed by the confluent mid-level jet. Normally, this upper-level jet streak would be tilted upstream in relation to the surface front, but as previously discussed (and particularly on 13 Jan 2000) the terrain effectively slows the progression of the surface front and the upper-level winds propagate in advance of the

138

normal relation to the mass field, thus allowing the jet to interact with the terrain-modified cold pool downstream from the jet's typical close association with the QG baroclinic zone. In order to better visualize this process and delineate distinctions between the 13 Jan 2000 and 28 Dec 1988 events, each case (and its conformity to the above) will be looked at in more detail. To begin, surface pressure rises will be identified in relation to the mid-level cold pool as well as the QG jet-front system through the use of observations, satellite imagery, and numerical simulations.

The primary inception time of jet interaction with the nascent low- to mid-level (800 – 700 hPa) cold pool for the 13 Jan 2000 event is between 1700 and 1800 UTC. The meridional shear in the confluent jet entrance region approaches and deforms the cold pool along and downstream of the Alleghenies, initially through south central Pennsylvania and central Maryland (as shown earlier). This deformation forces a NE – SW frontal structure aloft with the bulk of the coldest mid-tropospheric air located just north of Virginia where the confluent jet entrance region shear is strongest. A series of 700 hPa temperatures from the 6-km simulation (see Figs. 16 and 17) clearly demonstrates this evolution and the distinctly separate nature of this system from the upstream cold air associated with the larger-scale jet-front system. The two figures provided show the initial cold pool at 700 hPa for J00 along and east of the Alleghenies through central and south Pennsylvania in the vicinity of Bedford County (40^0N, 78-79^{0}W—denoted by gray box in Fig. 16) beginning at 13/1700 UTC through 13/1845 UTC. This pool of cold air (initially at a temperature of nearly $-15\ ^0$C) is clearly distinguishable from the upstream cold air (demarcated by the NE to SW $-16\ ^0$C isotherm in the northwest corner of the plots) associated with the large-scale trough located to the northwest of the deforming downstream cold pool. In time, this upfolded cold pool is

139

stretched by the convergent curved jet into a streamwise cold front aloft primarily oriented west to east (Fig. 17a) and propagating to the SSE from southern Pennsylvania to northern Virginia and western Delaware near the approximate accident location in space and time (see Figs. 18 and 19 for the 13/1900 UTC – 13/2045 UTC evolution of this mid-level cold pool). The progression of this cold pool closely mirrors the propagation of the cellular convection that traverses the accident location (as will be shown in the next chapter)—both in satellite and the 500 m simulation.

3.5.2 Mid-level Cold Pool – 28 Dec 1988 Case

In contrast to the 13 Jan 2000 low-level turbulence event, a similar low- to mid-level downstream cold pool (850 – 700 hPa) fails to develop or play a significant role in the 28 Dec 1988 event. While the impact of terrain forcing is more prevalent in the 13 Jan 2000 case and the initial response occurs downstream in the mid-levels (near 700 hPa) in the form of an isentropic upfold, the 28 Dec 1988 event is influenced by the terrain much closer to the surface and much farther upstream. Additionally, the lack of a strong downstream inversion (present in the 13 Jan 2000 case) restricts the strength of any downstream isentropic upfold (i.e., there is less of a vertical temperature gradient to work with—the gradient over the same depth was 13 ^{0}C for the 13 Jan 2000 case and only 5 ^{0}C on 28 Dec 1988) and the weaker cross-mountain flow results in any upfold being located much closer to the lee slope (and the large-scale trough) than further downstream as in the 13 Jan 2000 case (see Fig. 8). A detailed temperature analysis (850 – 700 hPa) from 28/12 UTC indicates a fairly weak cold pool forms along the mountains over West Virginia and western Virginia (Fig. 20). A second weak cold pool appears between 28/1600 – 1630 UTC in the western Bedford County

140

region of Pennsylvania and is 12 ^{0}C warmer (and farther west) than the mid-level cold pool that formed in the 13 Jan 2000 case. These relatively weak cold pools are stretched by the strong WSW jet (40+ ms^{-1} at this level) into a NE – SW band of cool temperatures along the Appalachians and Alleghenies immediately preceding the larger-scale QG system. The primary inception time of jet interaction with the weaker mid-level cold pool in D88 is between 16 and 17 UTC. Temperature loops from the 6-km control simulation at both 775 hPa and 700 hPa throughout this period reveal an absence of any significant cold pool at these levels in advance of the mid-level trough (or primary surface cold front) and indicate the mild downstream cold air is essentially collocated with the strong large-scale QG cold air associated with the surface front (see Fig. 20). These plots are in stark contrast to those of J00. There is little indication of any significant cold pool in advance of the larger-scale cold advection (located in the extreme NW quadrant of the plots) in D88 and the pools of cold air that exist are not organized or of a significant magnitude when compared to the surrounding temperatures. Additionally, the jet stream and temperatures are oriented parallel to each other indicating an across-stream temperature gradient and little if any along-stream cold advection or frontogenesis as was apparent in J00 (cf. Figs. 16-17). A comparison of deformation for J00 and D88 further illustrates key differences between these events.

Analysis of the total deformation fields for J00 clearly demonstrates the effect of the confluent jet entrance region on the mid-level cold pool (upfold) from south central Pennsylvania to the SSE near the accident location as time progresses. An analysis of the 700 hPa total deformation (with wind and temperature overlaid) through the period of interest for this case (Fig. 21) demonstrates the relationship between the north-to-south and west-to-east shear in the u- and v- components of the confluent, slightly curved jet entrance

141

region and the mid-level cold pool for the 13 Jan 2000 event. The 6-km simulated output at 13/1730 UTC depicts two primary regions of deformation through Pennsylvania—one aligned from southwest to northeast associated with the large-scale trough (collocated with the upstream cold air), and the other through south central and eastern Pennsylvania (collocated with the downstream cold pool (upfold)). These two patterns persist and propagate to the south and east with time (as shown in Figs. 21 and 22) as the deformation acting on the mid-level cold pool advances into central Maryland and northern Delaware by 13/1830 UTC and, as with the cold pool itself, is located in proximity to the 13 Jan 2000 accident location as it bisects north central Delaware/southern New Jersey between 13/2000 and 13/2030 UTC. This separate downstream deformation maximum coupled to the mid-level cold pool in J00 is of similar magnitude and remains downstream of the deformation maximum associated with the large-scale trough. This coupling is much less apparent in D88.

An analysis of total deformation in the low to mid levels (850 to 700 hPa) for 1600 – 1900 UTC on 28 Dec 1988 indicates two primary regions of deformation (Fig. 23) – one associated with the prefrontal, weak cold pool stretching from northeast Pennsylvania through central Virginia, and another deformation maximum just upstream attached to the larger-scale jet-front system. Unlike in J00, where the cold pool is of significant strength and clearly separate from the larger-scale jet-front system, the weak, elongated cold pool in D88 is essentially indistinguishable from and overwhelmed by the larger-scale system. Not only is the mid-level response to terrain different in these two events, adjustment at the surface and the sources of surface pressure rises/surges differ substantially. This difference is closely related to the relative absence of a deformed mid-level cold pool (downstream isentropic

142

upfold) combined with the presence of a very strong meridional QG jet-front system in D88 that is essentially unimpeded by topography as it moves through the region of interest.

The relationship between the confluent jet entrance region and the cold upfold in J00 has a simultaneous effect on the surface pressure tendencies due to the increased mass flux convergence in the column associated with the convergent jet stream entrance region deforming the mid-level cold pool. As the deformed mid-level cold pool moves to the south-southeast, it outpaces the upstream (larger-scale) cold air and the surface frontal system (which is slowed by terrain-induced hydraulic effects as discussed earlier) and, as a result, reduces the static stability as the cold air aloft overruns the warmer air at the surface. This cold pool aloft induces a region of smaller scale mass flux convergence. Additionally, the confluent jet entrance region further enhances upper-level mass flux convergence resulting in necessary divergence at the surface (high pressure surges) by Dines compensation. An examination of surface pressure tendencies throughout the time of interest leading up the severe turbulence report on 13 Jan 2000 highlights this process in Figs. 24 – 30.

3.5.3 Low-level Response and Comparison

The surface response to the mid-level cold pool in J00 (located downstream of the larger-scale cold advection and QG trough), caused by the enhanced mass flux convergence through the column, indicates low-level pressure increases to the lee of the Alleghenies (Fig. 24). This zone of pressure increase and its surface pressure surge and concomitant wind increase ultimately moves to the ESE in tandem with the mid-level cold pool and its deformation. Cross sectional analyses bisecting the mid-level cold pool (in the horizontal and vertical) for J00 verify that integrated mass flux convergence is present in the vertical

143

column encompassing the cold pool (Fig. 25). This figure, valid at 1900 UTC on 13 Jan 2000, depicts two primary regions of mass flux convergence east of the Alleghenies along the west to east cross section (the zones of convergence are denoted by the shaded, dashed contours). The easternmost region of mass flux convergence (along and east of the second, smaller terrain peak in the cross section) is associated with the downstream mid-level cold pool and mass flux convergence along and east of the Alleghenies (the taller terrain peak in the cross section) is associated with the larger-scale frontal system. Additionally, this columnar convergence is clearly reflected in the simulated surface pressure change at 15-minute, 30-minute, and 60-minute intervals between 13/1600 UTC and 13/2100 UTC utilizing output from the 6-km, 2-km, and 1-km simulations. These surface pressure increases are consistent with observations (not shown) within the region of interest east of the Allegheny and Blue Ridge Mountains (i.e., Pennsylvania, Maryland, Delaware, and Virginia). Output from the 6-km J00 simulation indicates a double pressure surge as early as 1730 UTC (30-minute pressure change is plotted in Fig. 26) with the southern- and easternmost surge (i.e., the small 1.5 hPa per half-hour closed contour in south central Pennsylvania) coupled with the cold pool and its deformation maximum and the northern surge linked to the larger, QG system to the northwest. As time progresses, the distinction between these two surges becomes even more evident as depicted in the 4-panel plot of the 30-minute pressure change from 13/1830 UTC – 13/2030 UTC (Fig. 27). These plots clearly indicate the dual nature of the surface pressure tendency in J00. By 13/1830 UTC (Fig. 27a), there are two relative maxima in the half-hourly pressure change with the surface response to the mid-level cold pool (and convergent jet entrance region and deformation) located near the Maryland-Pennsylvania border east and south of the pressure rises associated with the larger-

scale system near south central Pennsylvania. By 13/2000 UTC (Fig. 27c) this separation is even more distinct as the surface pressure surge moves to the ESE into eastern Maryland. The strength of this pressure surge and its proximity to the cold pool, deformation maximum, and accident location is even more impressive in the higher resolution output. Fig. 28 depicts the 30-minute pressure changes from 13/2000 UTC – 13/2100 UTC from the 2-km control simulation for J00. The nearly 5 hPa/hr pressure pulse for this time period is essentially coincident with the cold pool and deformation maximum shown earlier (in Figs. 19 and 21). Additionally, as will be shown in detail in the next chapter, these features are in proximity to resultant cellular convection, maxima in vorticity (vertical and horizontal) accompanying three-dimensional curvature, and the accident location. In addition to numerical output, all available observations within the region were plotted and the hourly pressure change (the highest temporal resolution available) was analyzed between 13/1800 UTC – 13/1900 UTC and 13/1900 – 13/2000 UTC (Fig. 29). The relatively coarse observed surface pressure tendency compared extremely favorably with the 6-km control simulation output as both observations and simulations indicate the double pressure surge (at the surface) with identical maxima of 3.5 hPa/hr attributed to both surges and located just west and north of the accident location. Additionally, these observed pressure changes were overlaid on the corresponding 1-km visible satellite imagery and appear to line up consistently with the clear region over south central Pennsylvania at 13/1900 UTC most likely associated with mass flux convergence and divergence at the surface (Fig. 30). There is also some indication of an outflow boundary, density current-like feature emanating to the south-southeast and approaching central Maryland and northern Delaware at this time (particularly visible in a loop of imagery through this time period). The downstream (in relation to the larger-scale

145

signal) surface pressure surge in J00 has been demonstratively linked to the downstream mid-level cold pool caused by the atmospheric response to hydraulic structure and terrain. As demonstrated earlier in this chapter and in a previous chapter, the atmospheric response near and downstream from the Appalachian Mountains in the 28 Dec 1988 event differs from that of the 13 Jan 2000 event. These differences continue downscale and are apparent in the surface pressure tendencies for D88 as well.

As detailed in the previous chapter, the large-scale jet structure and orientation for the two cases studied differed in several ways. The 13 Jan 2000 event was essentially a dual-jet system featuring both a subtropical jet and a polar jet. On the other hand, the 28 Dec 1988 event was a single-jet system driven by a strong polar jet and its circulations. Additionally, polar jet orientation on 13 Jan 2000 was primarily west to east resulting in a more north to south moving surface front while polar jet orientation on 28 Dec 1988 was more southwest to northeast resulting in a northwest to southeast propagating cold front. The strong $(75+ \text{ ms}^{-1})$ polar jet on 28 Dec 1988 is from the WSW with its confluent jet entrance region over south central Kentucky at 1200 UTC, northeast Kentucky at 1500 UTC, and West Virginia at 1800 UTC (as noted in observations, simulations, and KK91 (cf. their Fig. 5)). This orientation results in a transverse ageostrophic thermally direct circulation with low-level flow and frontal propagation from northwest to southeast. Additionally, this circulation enhances mass flux convergence and consequently low-level pressure rises behind the primary cold front as detailed by KK91 and as can be seen in the surface mesoridge and tightening surface pressure gradient through eastern Kentucky and West Virginia at 28/1700 UTC and through eastern West Virginia, Virginia, and Maryland at 28/1900 UTC in the 6-km simulation (Fig. 31). These features were also identified by KK91 in their mesoanalysis of surface

146

observations. The important distinction here is that the surface pressure rises in the 28 Dec 1988 event are behind the large-scale surface cold front and not downstream as in the 13 Jan 2000 case. Additionally, they are essentially associated with the large-scale jet-front system and not a downstream terrain-induced isentropic upfold as in J00. Cross sectional analyses bisecting frontal propagation indicate a tropopause fold to approximately 650 hPa (see Fig. 32) in agreement with the finding in KK91 that a strong tropopause fold and concomitant polar jet left-entrance subsidence (and necessary mass flux convergence) accompanying a thermally direct ageostrophic circulation were instrumental in the formation of the sub-synoptic pressure ridges behind the arctic front. This circulation provided additional mass and momentum in support of the rapidly moving cold front as it traversed the Appalachians. KK91 noted an observed pressure jump in excess of 8 hPa/hr at BWI following formation of a microscale pressure ridge in central Maryland/Virginia. The 2-km control simulation produced several pressure jumps near 8 hPa/hr and a 5+ hPa/hr jump at MRB and a 6+ hPa/hr jump at BWI at the same time as those noted by KK91 (i.e., immediately prior to NCFR formation). It is evident that these surface pressure surges are the result of a different mechanism than those in the 13 Jan 2000 case. The primary (or at least comparable) surface pressure surge in J00 was the result of mass flux convergence associated with the downstream mid-level cold pool (isentropic upfold tied to the hydrostatic mountain wave) which acted in advance of the larger-scale primary QG frontal system, not upstream and indirectly coupled with the large-scale system as in D88. The pressure surges in D88 are directly coupled with the larger-scale system and its polar jet entrance region and downfold and in this case acted to accelerate, strengthen, and contract the primary surface cold front as it traversed the region.

147

An analysis of surface pressure tendencies utilizing output from the 6-km and 2-km control simulations indicates a fairly long meridional band of increasing pressure coincident with the primary surface cold front in D88 (Fig. 33). Hourly surface pressure change analyses indicate that a few secondary pressure pulses are nearly collocated with the large-scale jet-front system and are coupled to the maximum subsidence with the jet entrance region. This feature moves from southwest to northeast with the maximum range of pressure increase between 5 and 8 hPa/hr as the polar jet and frontal system translates and the overall intensity of the surface pressure surge weakens in close agreement with KK91 in location, intensity, and timing. Higher resolution analysis of these fields indicates a split in the pressure field as the front traverses the elevated terrain and convection develops at approximately 28/1700 UTC in West Virginia. Plots from the 2-km simulation indicate a secondary, post-frontal pressure surge (essentially a split in the pressure field as the front crosses the Appalachian Mountains between 39.2 and 39.9 ^{0}N latitude between 1700–1715 UTC (Fig. 34)). This pressure surge coincides with the development of precipitation, a surface cold pool, and several 8 hPa/hr pressure change maxima along the frontal boundary through western Maryland and West Virginia (Fig. 35). Note the incipient precipitation in eastern West Virginia (along the Maryland and Virginia borders) as well as the 4 ^{0}C cool pool in the surface temperature plot. A cross sectional analysis along a line bisecting these features indicates the likelihood of terrain interaction with these features. In the time preceding the bifurcation of the pressure change field (i.e., prior to 28/1715 UTC), several terrain-induced features are observed and are readily apparent in cross sections plotted through this region (Figs. 36-38). The cross sections depicted run along a line at 39.7 ^{0}N from 76.9 ^{0}W – 79.2^{0}W (see inset with Fig. 36 for location). These cross sections, running

from west to east, capture three relative peaks in terrain elevation through the Appalachians. The most significant (both in width and height) is the westernmost peak (i.e., to the left, facing the cross section) located near 39.7 ^{0}N, 79.0 ^{0}W and part of the Allegheny Mountains. The next peak is just east of the middle of the cross section and is part of the Shenandoah Mountain Range (refer to Fig. 3, Chapter 1). The last peak is slightly higher and is part of the Blue Ridge Mountains, and is the final mountain range upstream from the Washington, D.C. metropolitan area (essentially, the Catoctin Mountain Range in Thurman, Maryland— near Frederick, Maryland).

Analysis at 28/1615 UTC (Fig. 36) indicates a weak leeside mountain wave closely aligned with the Allegheny Mountains and evidence of the weak, slow moving first cold front identified by KK91 located upstream of the Shenandoah Mountains at this time. A comparison with simulated wind, precipitation, vorticity, and convergence indicates there is no significant activity associated with this weak front and the only indication of its presence is a weak temperature gradient. The vertical motion field is depicted in the cross sections with blue shading representing upward motion and red shading representing downward motion. By 28/1645 UTC, the strong, rapidly progressing primary cold front is visible as it begins to cross the Alleghenies (Fig. 37). As the kinetic energy associated with the cold front crosses the mountains, an apparent hydraulic jump forms to the lee of the Alleghenies. Note the upward vertical motion on the windward side of the Alleghenies and the strong terrain-forced subsidence on the lee slope (the simulation using smooth terrain is absent these features). As the momentum associated with the frontal system traverses the Allegheny peak, an apparent hydraulic jump forms (as hypothesized in KK91) and shortly thereafter (by 1700 UTC) the rapidly moving cold front catches up to the downstream jump and the

enhanced vertical motion with this combined jump-front (Fig. 38) results in convection to the lee of the Alleghenies. This convection is inherently tied to the convergence associated with the primary cold front as its momentum is maintained (and actually increased) east of the Alleghenies due to the deep tropopause fold and ageostrophic (direct) circulation in the left entrance region of the southwesterly polar jet, with the greatest intensification occurring after 28/1900 UTC. As this frontal system traverses the remaining two peaks (Shenandoah and Blue Ridge) on its way east, a similar response occurs with a jump-front merger and enhanced vertical motion and precipitation along the Shenandoah between 28/1745 – 1800 UTC (Fig. 39) and along the Catoctin Mountains between 28/1830 –1845 UTC (Fig. 40). The enhanced upward vertical motion and increased precipitation evident in these plots does not occur between terrain peaks or during the intermittent times when the front is not crossing elevated terrain (i.e., it appears the enhanced vertical motions and increased precipitation are a byproduct of the front-terrain interaction). It should be noted that this frontal system is not significantly slowed by the terrain during its progression although upward vertical motion is enhanced downstream from the various mountain peaks with the jump-front mergers. A comparison with the sensitivity simulation utilizing coarse, smoothed terrain (see Chapter 2 for details) indicates vertical velocities at least an order of magnitude smaller than those in the control simulation. The adiabatic cooling on the upslope combined with the cold front and jump and downslope warming (along with convective heating and probable evaporative cooling behind the anafront) act to reinforce and strengthen the streamwise front as it interacts with and traverses the elevated terrain. In spite of these interactions with terrain for the 28 Dec 1988 event, the convection, frontal contraction, density current-like feature, vorticity maxima, and low-level turbulence (discussed in the

150

next chapter) are all primarily tied to the dominant rearward-sloping cold front which is bolstered by the isallobaric signal associated with the strong direct circulation (and tropopause fold) in the polar jet entrance region. The finer details of this process as the front contracts to a density current-like feature and low-level turbulence will be discussed in detail in the next chapter. It is important to note that at this stage, the differences between D88 and J00 (and their conformity to the hypothesis presented earlier in this chapter) are rather distinct and will become more so as the scale of phenomena contract. As shown, the 28 Dec 1988 event features a much weaker, barely discernible downstream cold upfold. The upfold in the 13 Jan 2000 event is much stronger (for reasons previously discussed) and is located further downstream from the terrain that forced it. Additionally, the surface response for these two events is markedly different. As shown, D88 features surface pressure surges that are coupled with the strong large-scale jet-front system and occurred with or behind the primary surge. On the other hand, the stronger downstream cold pool and different hydraulic structure in J00 results in a significantly different low-level response with a downstream mid-level, streamwise front created by jet deformation of the upfold (mid-level cold pool) and surface pressure rises in advance (downstream) of and only indirectly coupled to the larger-scale jet-front system.

An analysis of low-level temperatures, pressure, and winds during the time period encompassing the mid-level cold pool deformation, mass flux convergence, and associated surface pressure surges leading up to the severe turbulence report in J00 depicts the surface response. This response is ultimately coupled to enhanced frontogenesis, frontal contraction, convection, vorticity, and the low-level turbulence and helicity observed in J00 and serves as a contrast to the surface scenario presented for D88 (Note: meso-γ and microscale features

151

are discussed in the next chapter). A sequence of the 940 hPa temperature plots from 13/1700 UTC – 13/2100 UTC is indicative of the low-level (near surface) temperature pattern and response to the Bedford County pressure surge in this case. Modeled temperatures from the 6-km simulation at 13/1700 UTC clearly indicate a leeside trough just east of the mountains (Fig. 41) as well as another warm tongue (boundary layer warmed air, advected warm air previously described in Chapter 2). This leeside warm air is reflected in a weak cyclonic circulation (mesolow) in this region at the surface. As the surface pressure builds to the north in south central Pennsylvania (as described earlier), this warm air and its weak circulation are gradually forced to the east and south by the isallobaric response (i.e., increased WNW winds due to pressure rises) as can be seen in the low-level temperature plots for 13/1800-2100 UTC (Fig. 42) as well as the surface winds and pressures (Fig. 43). Meanwhile, the mid-level cold pool continues to track to the ESE. An important aspect of this leeside pressure rise due to the jet-deformed mid-level cold pool is the resultant surface cold pool initially located in Pennsylvania and constrained by the terrain. The high pressure pulse at the surface (due to the enhanced mass flux convergence in the column) is essentially trapped by the terrain to the north and west. As depicted in Tilley (1990, cf. Fig. 2-2), the mass build-up in the region results in a low-level cold surge that resembles a Kelvin-shelf hybrid (edge) wave and surges to the south and east. Bedford County, Pennsylvania is particularly well-suited for this type of surface cold surge generation. In this region (near 39.5 – 40 ^{0}N, 78.2 – 78.8 ^{0}W), the west to east downslope terrain gradient intersects the south to north downslope terrain gradient—aiding in the production of a low-level cold pool oriented perpendicular to the pressure gradient force. Additionally, the relatively low elevation over the southeastern quadrant (i.e., east and south Pennsylvania) allows the cold

air to flow downhill, unimpeded by terrain.

Tilley (1990) reviewed three low-level cold surge events in some detail. He found that the cold surges were always associated with an upslope wind component near elevated terrain, that the cold air making up the surge formed a dome with definite vertical and horizontal extent, and that the surges propagated with the terrain to the right (in relation to the surge itself) in the Northern Hemisphere. He concluded that vertically trapped edgewaves required blocked, upslope flow and mass build-up along the elevated terrain. The accumulation of mass near the mountain (barrier) results in a pressure perturbation that is enhanced hydrostatically by adiabatic (upslope) cooling. The excess mass is radiated off as gravity waves with the lower frequency waves forming a Kelvin or hybrid Kelvin-shelf wave which propagates parallel to the elevated terrain (north to south for a meridional mountain range such as the Appalachians). Tilley (1990) found that pressure rises, temperature falls, and northerly momentum increases with the cold surge and that these features were coincident as the surge progressed from north to south. Additionally, he noted the apparent ageostrophy of the surface flow in the surge region (winds crossing isobars at angles near 90^0 and greater) and concluded that a large isallobaric wind component was likely present in the region. He also noted that the vertical extent of the cold surge was roughly equivalent to that of the terrain height and that the extent of the cold surge's associated northerly momentum was generally confined to the lower levels as well.

All of these findings are consistent with the J00 simulations and available observations for the 13 Jan 2000 event. As previously discussed, no low-level cold surge is observed in the 28 Dec 1988 event due to the lack of a significant mid-level cold pool and the absence of upslope flow on the eastern side of the Allegheny Mountains. Figure 44 depicts

the near-surface flow overlaid on terrain elevation for 13 Jan 2000 valid at 1500 UTC. Simulated flow prior to the low-level cold surge traversing southern Pennsylvania into the Delmarva region remains upslope until the northerly shift occurs at approximately 13/1800 UTC. A cross section through southern Pennsylvania intersecting the elevated terrain indicates upslope flow with the vertical extent roughly equivalent to the Allegheny terrain height (Fig. 45). The region east of the Alleghenies below $\approx$930 hPa is dominated by upslope flow which is constrained to the height of the terrain. The cold pool is also visible in this figure approximately defined by the 276 ^{0}K isentrope in the lower right quadrant of the cross section. In order to determine the degree of terrain blocking present with this upslope flow east of the Alleghenies, Froude numbers were computed for 1200, 1400, and 1600 UTC on 13 Jan 2000. Smith (1979), Pierrehumbert (1984), and others have noted that a Fr < 1.0 is indicative of blocked flow. Computations for J00 indicate a high probability that the flow during these hours (13/1200–1600 UTC) was blocked by the terrain with Froude numbers of 0.31, 0.17, and 0.21 for 1200, 1400, and 1600 UTC respectively. Additionally, in agreement with Tilley's (1990) findings, low-level northerly flow is strongly ageostrophic and confined vertically (see Fig. 46) and the cold surge on 13 Jan 2000 clearly propagates from north to south (as will be shown). It should also be noted that the sensitivity simulations with coarse, smoothed terrain (see Ch. 2 for details) did not exhibit a low-level cold surge. No northerly momentum surge propagates through the Delmarva region (at anytime) as in the control simulations, nor does a surge of cold air and higher pressure move from north to south through the region. Instead, the cold advection progressed southeastward with the large-scale system. This absence of northerly momentum in the smooth terrain simulation is in agreement with the findings of Murakami and Nakamura (1983) and Sumi (1985) who found

154

that experiments without terrain failed to produce a cold surge and that the cold advection that occurred advanced eastward with the mid-tropospheric system. Similarly, in a sensitivity experiment utilizing 1% terrain height, Tilley (1990) found that no cold surge developed. Clearly, the Appalachian Mountains play a vital role in the development and propagation of the low-level cold surge that developed in J00.

As the low-level (surface) cold pool surges to the south parallel to the mountains (Fig. 47), it enhances surface convergence and tightens the temperature gradient as it approaches the relatively warm PBL air to the south. Additionally, the previously mentioned mid-level cold pool moves ESE during this period into the same region where it reduces static stability and enhances the atmosphere for convection. These thermally indirect frontogenetical circulations couple vertically and the combination of these features (mid-level cold upfold, leeside warm air, low-level cold surge) in space and time act to enhance low- and mid-level frontogenesis at a decreasing scale (i.e., scale contraction process) in this region and near the accident location.

An analysis of the 2-d frontogenesis equation (Miller 1948) utilizing output from the 6-km control simulation indicates surface frontogenesis as early as 13/1700 UTC coincident with the mid-level cold pool and surface pressure surge (and resultant convergence) in south central Pennsylvania. This relative maximum in frontogenesis forcing at the surface is distinct and separate from the upstream frontogenesis maximum associated with the larger-scale QG system that was retarded as it traversed the Alleghenies. A sequence of plots from 13/1730 – 13/2030 UTC depicts the increasing frontogenesis associated with the cold upfold, surface response, and tightening temperature gradient as the system moves toward and traverses the accident location at approximately 13/2030 UTC (Fig. 48). The feature of

155

significance in these plots is the maximum contoured in the eastern Bedford County region of southern Pennsylvania in Fig. 48a. This feature tracks to the south and east and is coupled with both the mid-level cold pool and the surface convergence associated with the low-level cold surge. This sequence is even more apparent as model resolution is increased and the scale of these features contracts (as traced in finer detail in the next chapter).

A sequence of fields from 13/1630 – 13/2130 UTC of 2-d surface frontogenesis utilizing output from the 2-km control simulation clearly shows frontogenesis collocated with the mid-level cold pool, surface pressure surge, and low-level cold surge beginning near Bedford County, Pennsylvania as early as 13/1700 UTC and particularly evident between 13/1930 and 2000 UTC (Fig. 49). The 2-d frontogenesis plot for 13/1930 UTC depicts a maximum along the Pennsylvania-Maryland border just west of Delaware. This maximum is coincident with the mid-level cold pool (denoted by the dark blue and light purple shading (-15 ^{0}C to -16 ^{0}C isotherm) in Fig. 49b), the low-level cold surge (denoted by the southernmost grey shading in Fig. 49c), and in the southern surface pressure tendency maximum. This pattern is even more evident by 13/2000 UTC as the frontogenesis associated with the low-level cold surge progresses into central Maryland and northern Delaware (Figs. 49e-h). This frontogenesis (clearly separate from the upstream QG frontogenesis—oriented NE-SW through east central Pennsylvania) strengthens and moves to the south (see Fig. 50) as the surface cold pool (edgewave) flows south and transits the accident location at approximately 13/2030 UTC. An interesting by-product of this downstream surface frontogenesis (i.e., downstream location of the mid-level cold pool/separation from the original QG forcing) is that the slope of this front becomes vertically forward (downstream) with time (i.e., has a katafront structure). Note the

156

downstream position (in relation to the surface cold surge and frontogenesis maximum) of the mid-level cold pool in Fig. 49.

The analyses of mid- and low-level temperatures (as well as internal Froude number calculations and frontal propagation speed estimates) indicate frontal propagation near the surface was slowed prior to 13/1600 – 1700 UTC while the jet at the mid-levels advanced unimpeded and helped deform a mid-level cold pool created by vertical motions forced by a hydrostatic mountain wave. As a result, this mid-level cold pool is located downstream of the Alleghenies and in advance of the slowed (retarded) surface cold front. As the large-scale cold front approached the Appalachians, it possessed classical rearward tilt (anafront). East of the mountains, frontal structure became more vertical and ultimately possessed forward tilt (Fig. 51). Surface cold frontal position is indicated by the open triangle in the figure with the forward-tilt (katafront) structure indicated by the dashed line. The surface front is along the eastern Pennsylvania-Maryland border at this time. This katafront structure is due to a combination of frontal drag (caused by friction, terrain, and hydraulic structure) and the creation of the downstream mid-level cold pool by a hydrostatic mountain wave—the mid-level cold pool subsequently transformed into a cold front aloft by the slightly curved advancing confluent mid-level jet entrance region. Steenburgh and Schultz (1997) identified surface friction and frontal retardation combined with a downstream cold front as the primary elements responsible for low-level kata-frontogenesis. Results from the 13 Jan 2000 case study indicate a downstream, mid-level terrain-induced cold pool could be another mechanism contributing to deeper kata-frontogenesis downstream from mountainous terrain. In the 13 Jan 2000 turbulence event, the combination of terrain drag, a mountain wave-induced, jet deformed cold pool aloft, and subsequent low-level pressure surge resulted in a

157

forward-tilted cold front (i.e., katafront) and quite possibly a discrete frontal jump east of the mountains. A close examination of cross section plots (from the 6-km and 2-km control simulations) bisecting frontal propagation indicates the cold front in J00 propagates discretely between 1600 – 1800 UTC below the cold upfold as the planetary boundary layer thickens due to surface sensible heat flux under the mid-level cold pool and momentum is mixed down to the surface. In essence, the surface cold front jumps eastward accompanying the cross-mountain momentum as a result of downward mixing adjacent to the new isallobarically-driven surface cold surge. As will be demonstrated in the next chapter, this forward-tilted cold front plays a strong supporting role in the generation of severe low-level turbulence east of the Appalachians in the 13 Jan 2000 case study.

3.6 Summary and Conclusions

The atmospheric environments prior to two cases of widespread low-level turbulence east of the Appalachian Mountains have been examined in this chapter. The large-scale similarities and differences between these two events were discussed in a previous chapter and clearly these differences—to include large-scale wave pattern, jet-front structure and orientation, and low-level temperature advection—affected the smaller scale atmospheric responses in the 28 Dec 1988 and 13 Jan 2000 cases studied. In this chapter, the meso-α and meso-β signals cascading from the larger scale signals (and differences) identified in Chapter 2 were studied in order to identify further differences (and similarities where they exist) between two cases of low-level turbulence of differing intensity. A hypothesis was presented and the level of conformity to the first five (of six) stages of this hypothesis was assessed for these events. Focus in this chapter was on the atmospheric response to and the impact of these differences on cold frontal propagation, hydrostatic mountain wave formation, isentropic upfold (mid-level cold pool) generation and deformation, and the surface response leading to convective initiation in two cases of differing low-level turbulence intensity east of the Appalachian Mountains.

The large-scale differences between these two events in the hours prior to turbulence formation have a direct effect on the subsequent atmospheric response along and downstream of the Appalachian Mountains. In the 13 Jan 2000 event, the southern subtropical jet (acting in tandem with the more northerly polar jet) enabled the transport of warm Mexican Plateau air to the leeside of the Alleghenies early on 13 Jan 2000. This elevated warm layer helped set up a strong inversion on the leeside of the mountains and enabled blocking of the windward front and deflection of the low-level flow around the Alleghenies and aloft

159

downstream. No such inversion sets up downstream of the Alleghenies on 28 Dec 1988 and frontal propagation is more or less unimpeded. Additionally, the large-scale wave structures are oriented differently in these two cases with a NW-SE structure for the 13 Jan 2000 event and a NE-SW structure for the 28 Dec 1988 event. These differences, combined with the different low-level temperature profiles, result in a more blocked/dammed regime for 13 Jan 2000 and a partially-blocked hydraulic structure for 28 Dec 1988. These different structures, in combination with overall wind profiles and hydrostatic mountain wave formation, significantly affect the downstream atmospheric response. Internal Froude number computations indicate that as the cold front approached the mountains, flow in the 28 Dec 1988 case was in the supercritical to partially-blocked regime. On the other hand, cold frontal propagation on 13 Jan 2000 was retarded as it crossed the mountains (prior to 1700 UTC) and internal Froude number computations placed this case near the junction of the subcritical, completely-blocked, to partially-blocked regime as noted in Simpson (1997). Observations and simulations agree with this assessment as the primary cold front on 28 Dec 1988 moved rapidly through the region (16-20 ms^{-1}) with little impact or retardation due to terrain drag while the cold front on 13 Jan 2000 was slowed considerably (4-6 ms^{-1}) as it moved through the region early on the 13th (prior to 1700 UTC). Additionally, the strength of the hydrostatic mountain waves formed and the resultant downstream isentropic upfolds generated in these two events vary substantially (in large part due to the large-scale differences in wind and temperature structure on both sides of the Alleghenies).

Hydrostatic mountain waves, observed on both days, were investigated. Cross-mountain flow on 28 Dec 1988 resulted in a mountain wave with the downstream upfold located fairly close to the lee slope due to the southwesterly flow at mountain level prior to

frontal passage. Relatively strong cross-mountain flow on 13 Jan 2000 resulted in a more vigorous mountain wave with concomitant upslope upfold, downslope downfold, and downstream isentropic upfold (mid-level cold pool). Consequently, and enhanced by the stronger downstream inversion, the mid-level (700 hPa) cold pool is more significant and located further downstream on 13 Jan 2000 than on 28 Dec 1988.

The stronger downstream mid-level cold pool results in a deeper katafront structure and stronger, downstream surface pressure rises in advance of the large-scale QG frontal system for the 13 Jan 2000 event. This isentropic upfold is deformed by the large-scale jet as it flows east above the Alleghenies and, on 13 Jan 2000, acts on the mid-level cold pool to create an upper-level cold front in advance (downstream) of the slowed surface cold front. An alternate explanation of this scenario involves the process of wave steepening (as opposed to the cold upfold-jet interaction) leading to hydraulic jump-like flow and downstream and downward propagation. In the future, researchers should consider running a simulation without the jet streak in order to assess its effect on any mid-level cold pool.

The mid-level cold pool on 13 Jan 2000 results in surface pressure rises to the lee of the Alleghenies—downstream from those associated with the large-scale system. As a result of this strong downstream mid-level cold pool and subsequent surface pressure rises, the low-level mass increase in the region (Bedford County, Pennsylvania) results in a low-level cold surge (edgewave-like feature) that surges to the south and east further tightening the surface temperature gradient and ultimately merging with the warm air from the south. This surface cold surge results in enhanced convergence, frontogenesis, and ultimately cellular convection near the Pennsylvania-Maryland border. No such north to south moving surface cold surge exists in the 28 Dec 1988 case as surface pressure rises are tied to the large-scale (west to

161

east) moving surface cold front and polar jet entrance region circulations (and the tropopause fold), behind the primary cold front and not downstream.

The combination of the mid-level cold upfold, leeside warm air, and low-level cold surge in space and time act to enhance frontogenesis in a scale contraction process near the accident location in the 13 Jan 2000 event. No such combination exists in the 28 Dec 1988 event as there is no discernible mid-level cold pool or surface cold surge in advance of the large-scale cold front. In other words, forcing in the 28 Dec 1988 case is tied to the large-scale QG frontal system and not intimately associated with a mountain-induced mid-level cold pool (and resultant surface response) as in the 13 Jan 200 case (and as presented in the hypothesis). Additionally, as a result of the downstream upfold on 13 Jan 2000, the frontal structure is essentially forward-sloping (i.e., a katafront) as opposed to the traditional anafront structure present in the 28 Dec 1988 event. In J00, the near-surface and mid-level mesoscale fronts become vertically juxtaposed. Although friction and terrain effects played an important role in retarding surface features and allowing the upper-level system to advance, the mid-level cold pool (isentropic upfold) clearly aids this frontal-slope process on 13 Jan 2000. The significance of frontal structure (i.e., katafront vs. anafront) as well as convection, and vorticity (vertical and horizontal) effects to include vortex tube formation result in low-level turbulence and will be the focus of the next chapter.
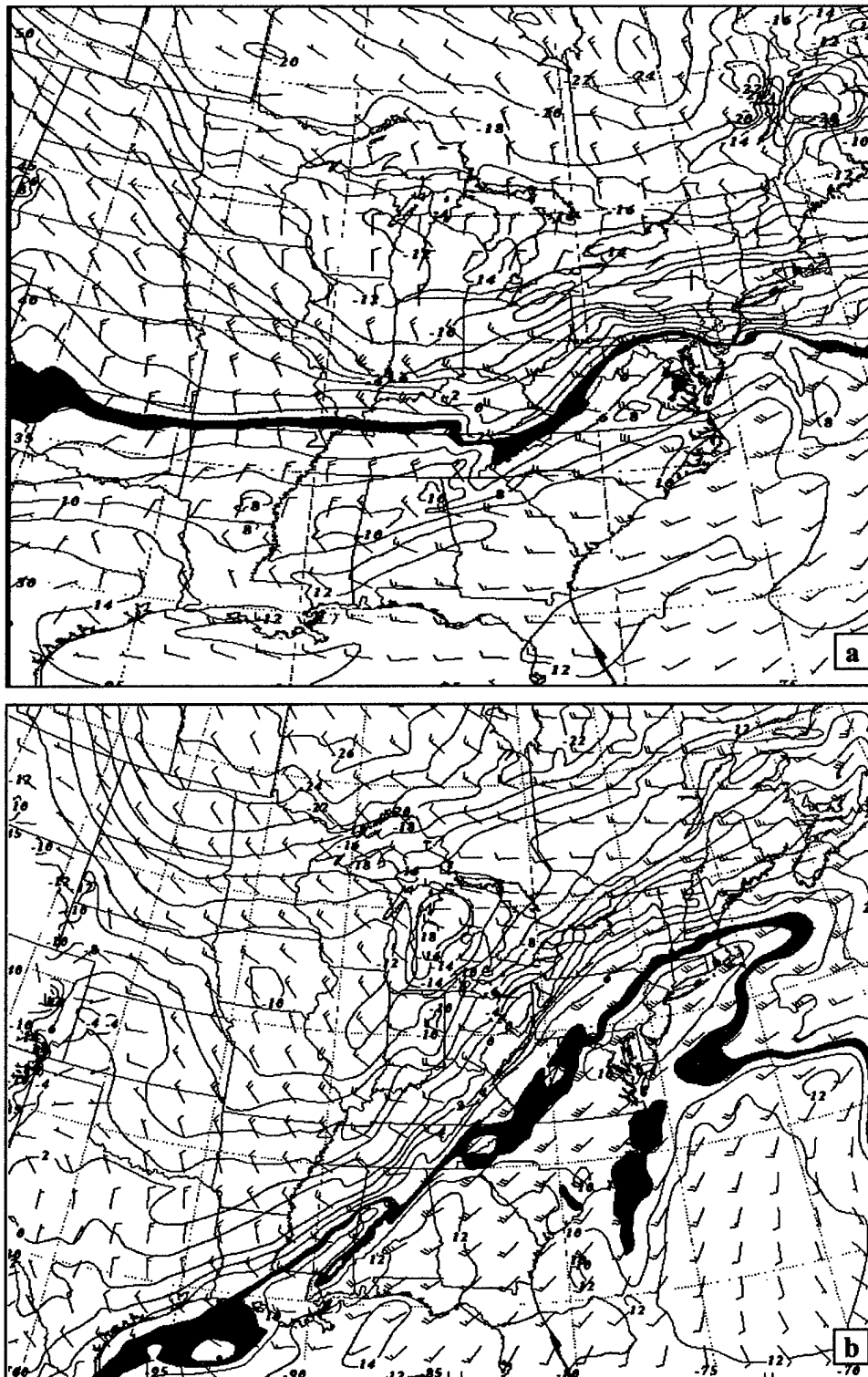
Figure 1. Simulated 850 hPa wind (ms^{-1}) and temperature (^{0}C) analysis valid (a) 14 UTC 13 Jan 2000, (b) 14 UTC 28 Dec 1988.
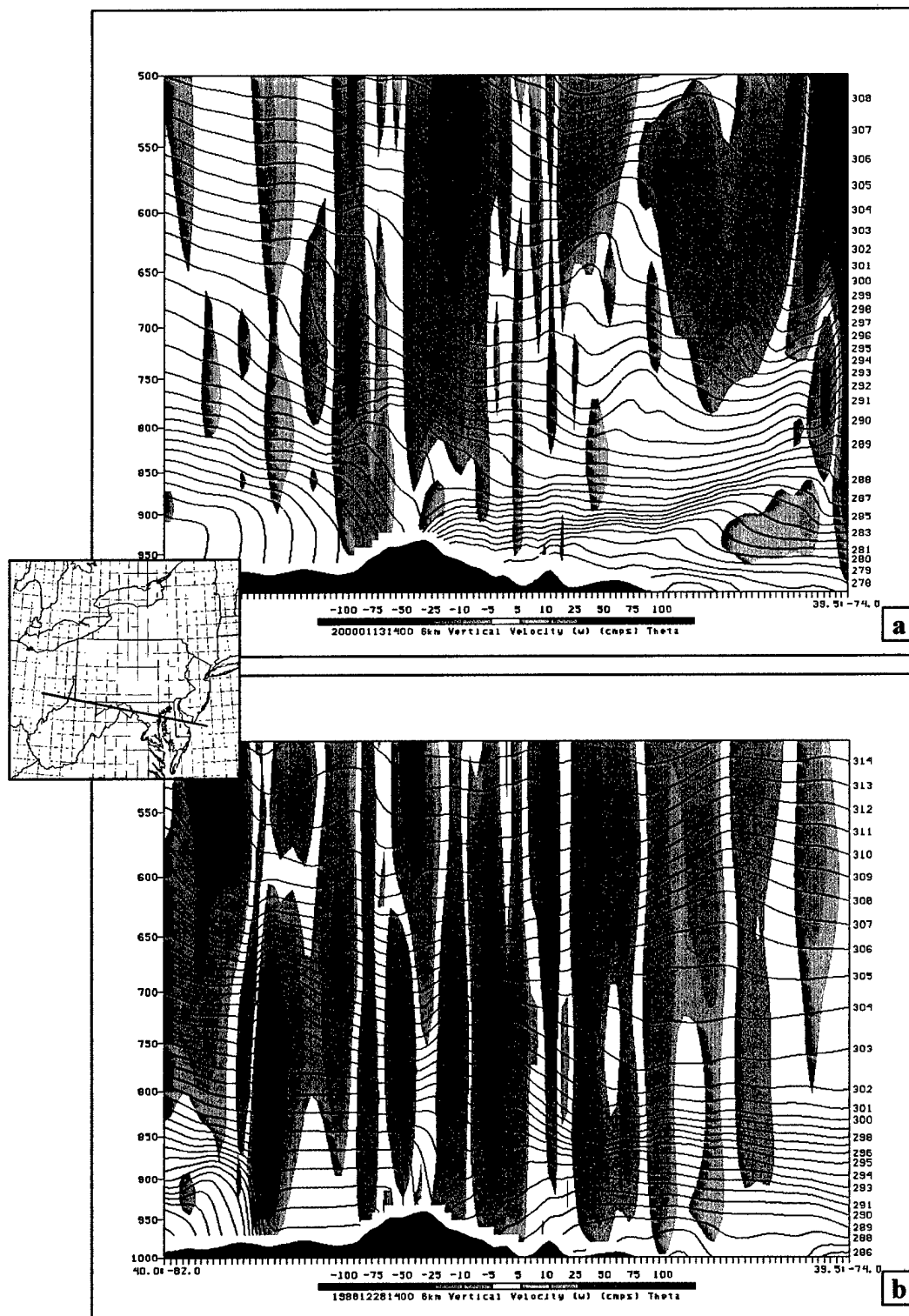
Figure 2. Simulated cross sections depicting vertical velocity (shaded, cms^{-1}) and potential temperature (K) along a line bisecting frontal propagation (see inset). Valid 14 UTC (a) 13 Jan 2000, (b) 28 Dec 1988.
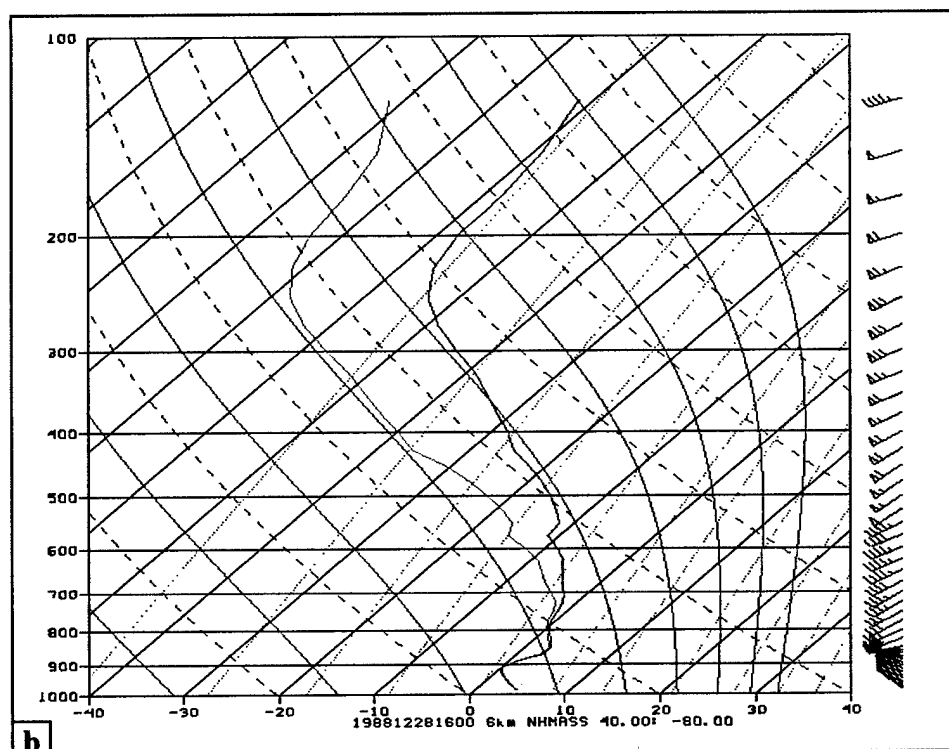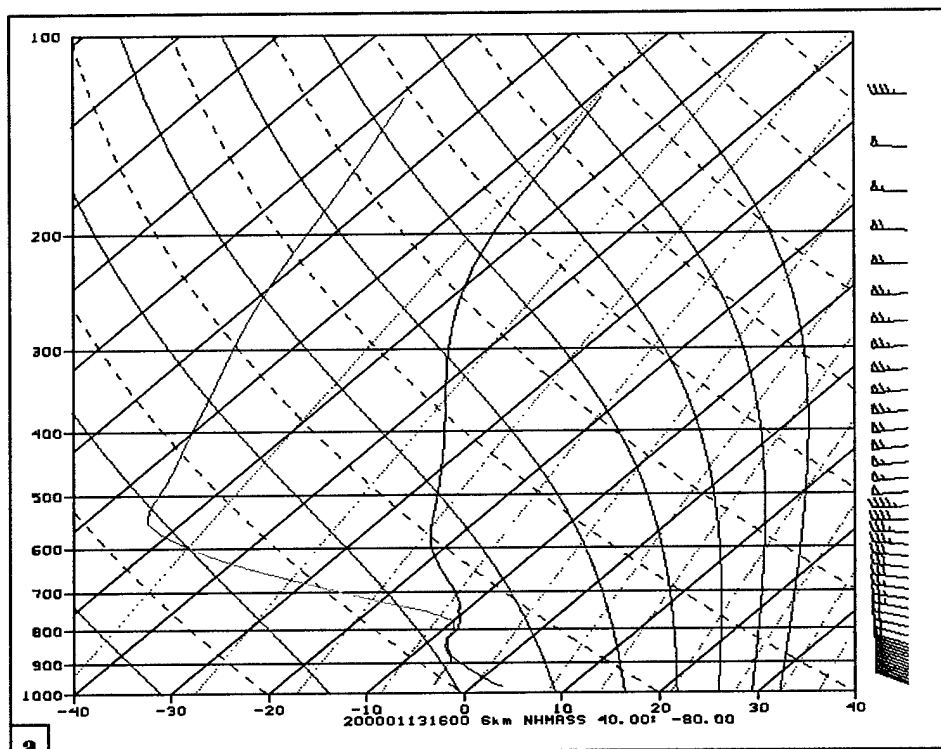
164

Figure 3. Simulated Skew-T soundings for 40 °N, 80 °W. Winds are in ms⁻¹ and temperature and dewpoint in deg C. Valid (a) 16 UTC 13 Jan 2000, (b) 16 UTC 28 Dec 1988.
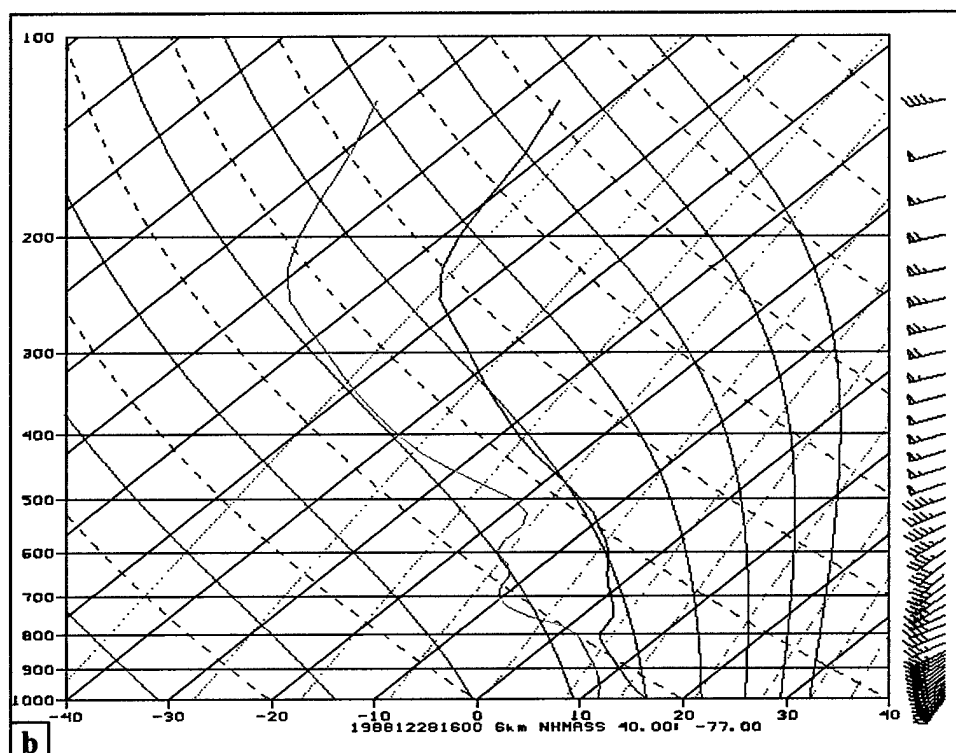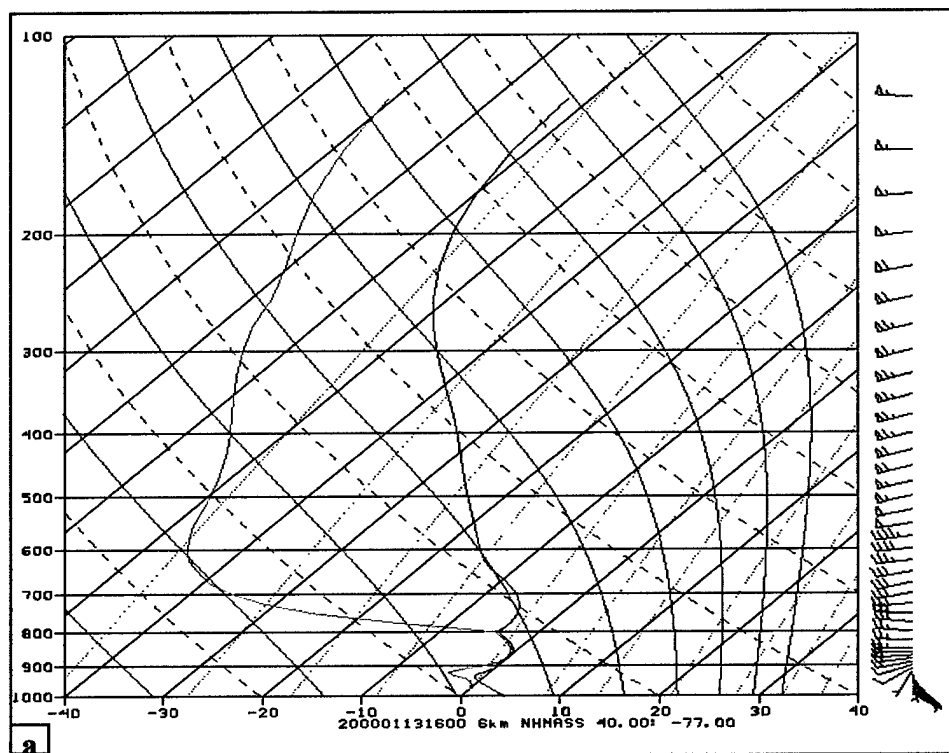
Figure 4. Simulated Skew-T soundings for 40 °N, 77 °W. Winds are in ms⁻¹ and temperature and dewpoint in deg C. Valid (a) 16 UTC 13 Jan 2000, (b) 16 UTC 28 Dec 1988.

166
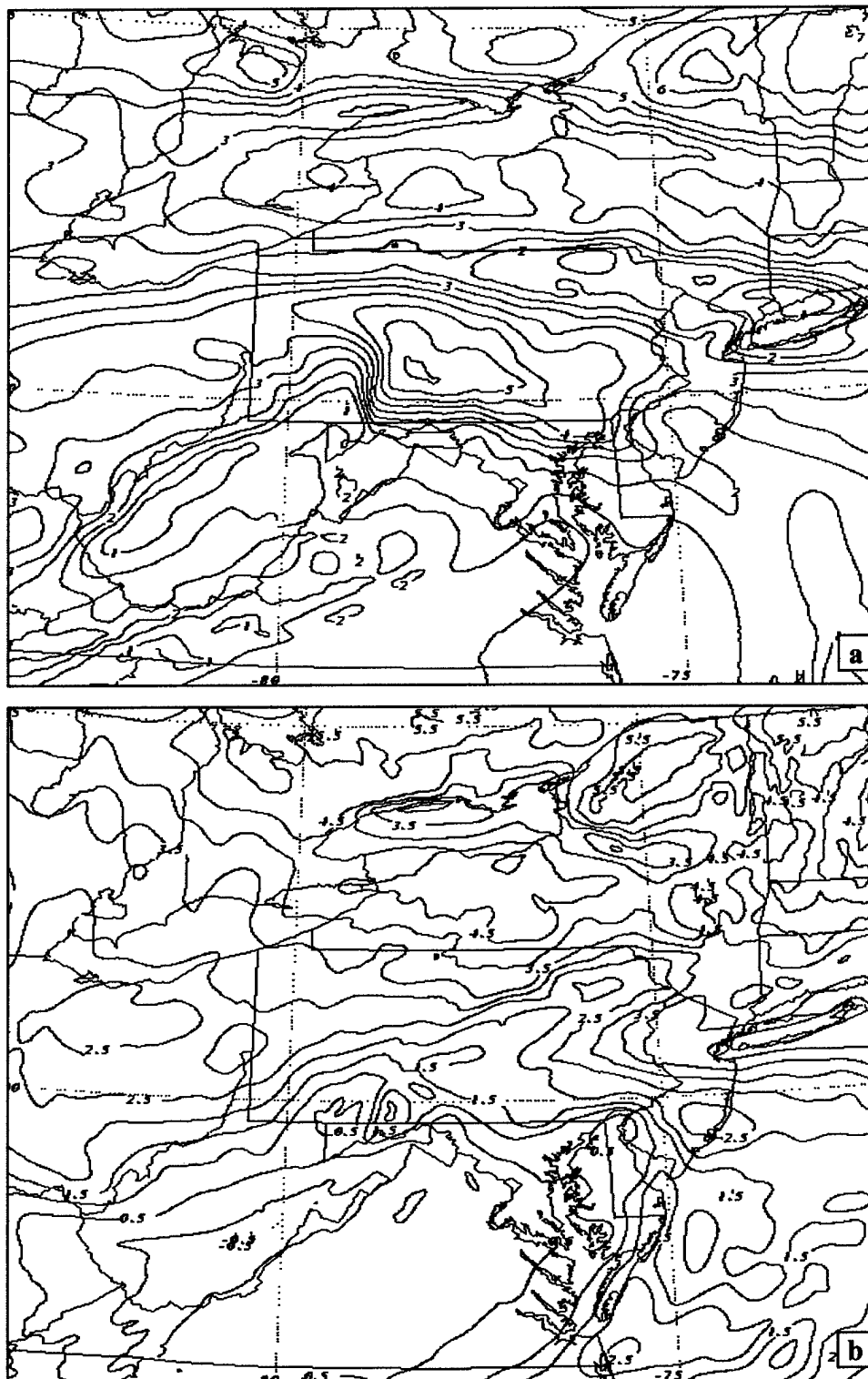
Figure 5. Simulated 900-800 hPa Brunt-Väisälä Frequency-Squared
(x 10^{-4} s^{-2}) valid (a) 12 UTC 13 Jan 2000, (b) 18 UTC 13 Jan 2000.
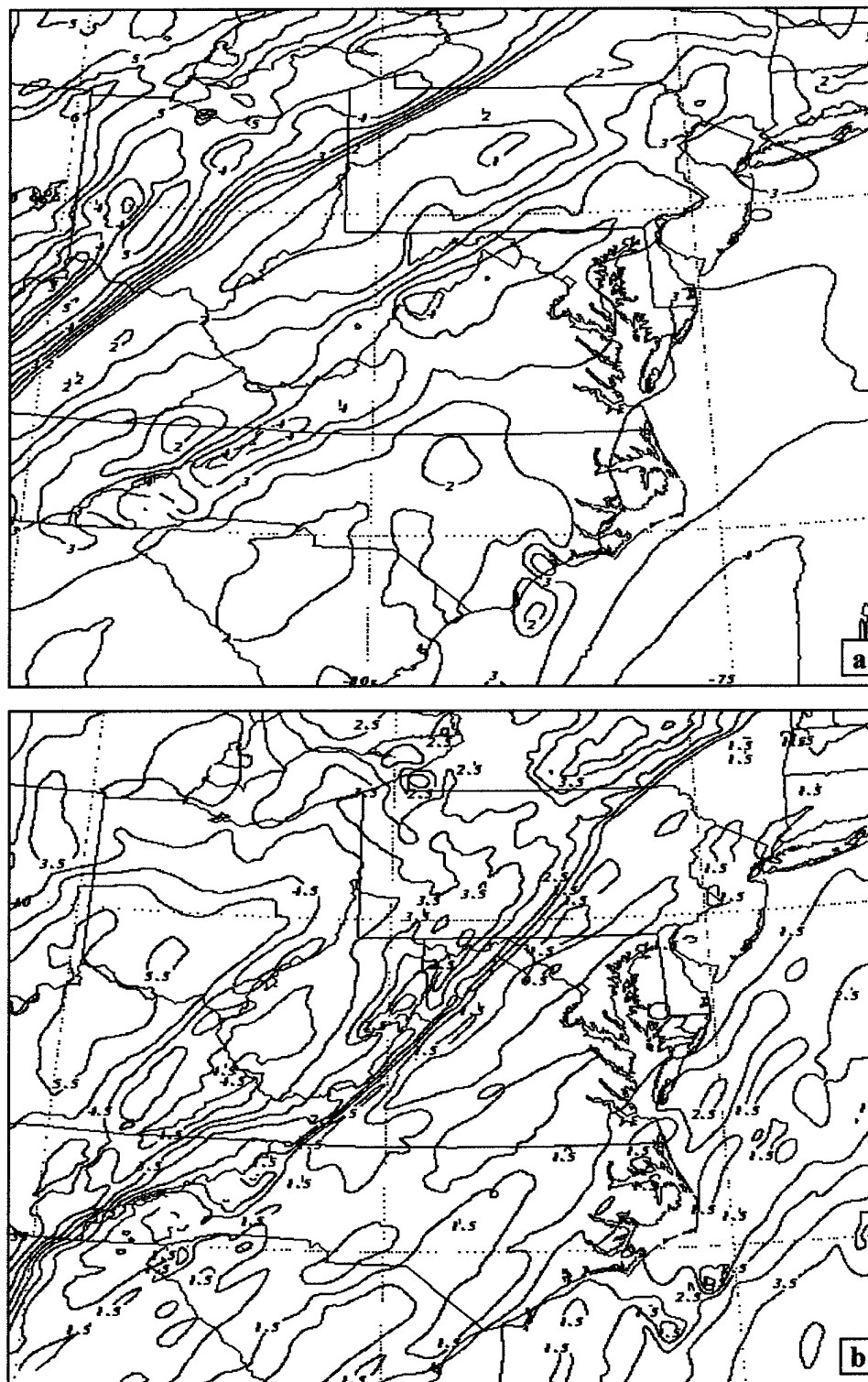
Figure 6. Simulated 900-800 hPa Brunt-Väisälä Frequency-Squared
($\times 10^{-4}$ s^{-2}) valid (a) 12 UTC 28 Dec 1988, (b) 18 UTC 28 Dec 1988.
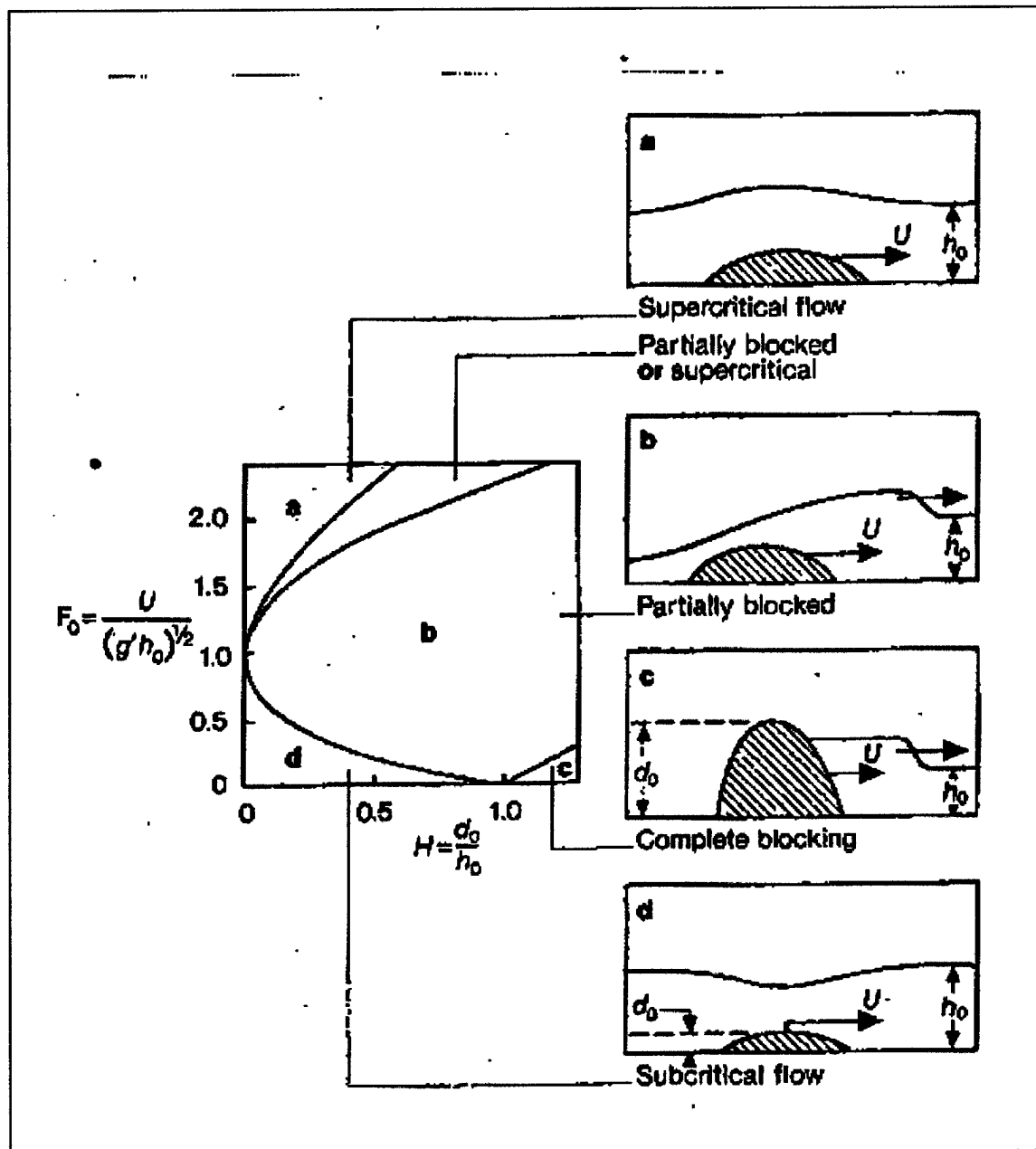
Figure 7. Four types of disturbance which can be generated by a moving obstacle at the interface between two fluids (after Simpson, 1997).
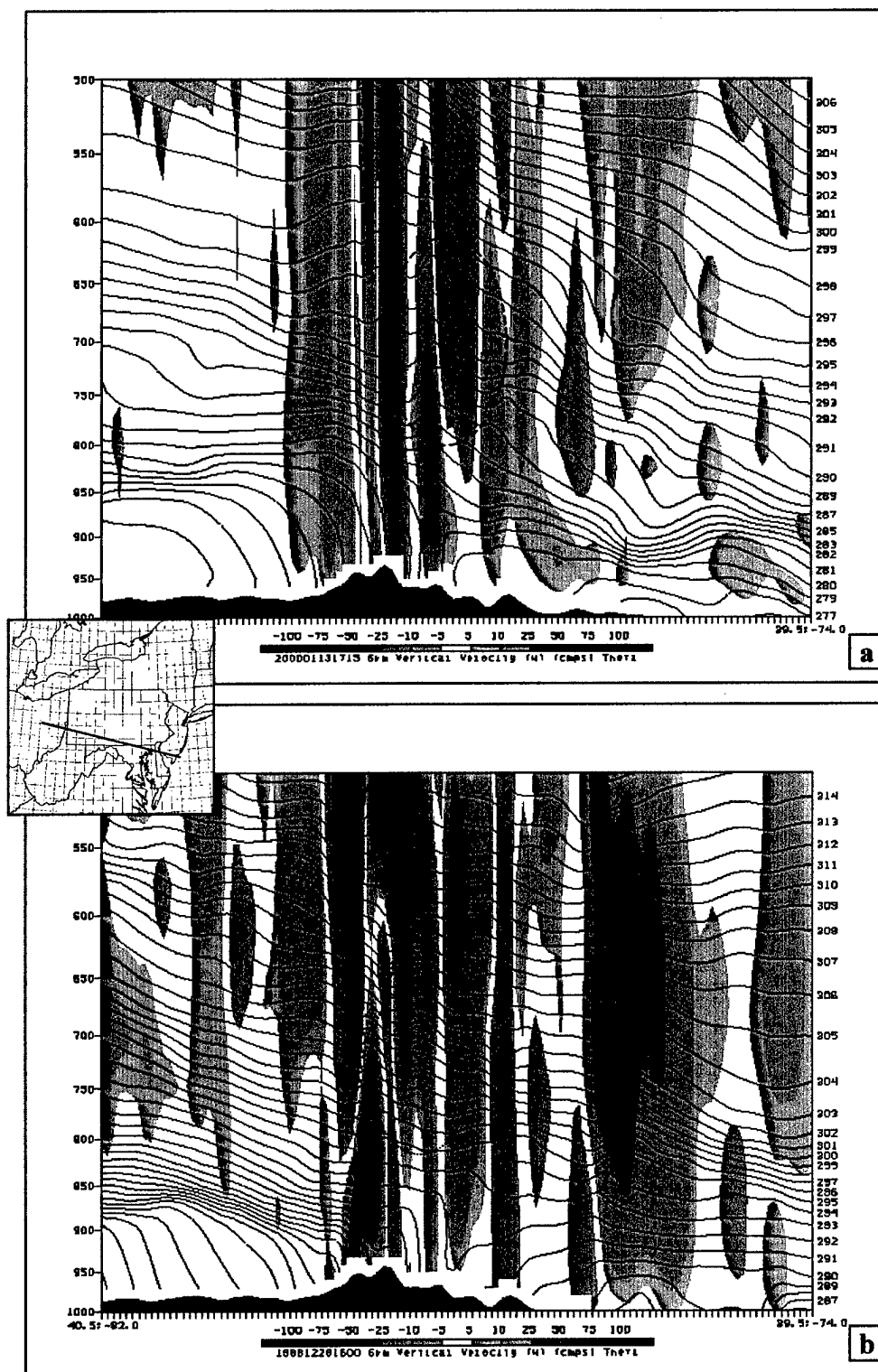
Figure 8. Simulated cross sections depicting vertical velocity (shaded, cms^{-1}) and potential temperature (K). The downstream cold upfold is encircled. Valid (a) 1715 UTC 13 Jan 2000, (b) 1600 UTC 28 Dec 1988.
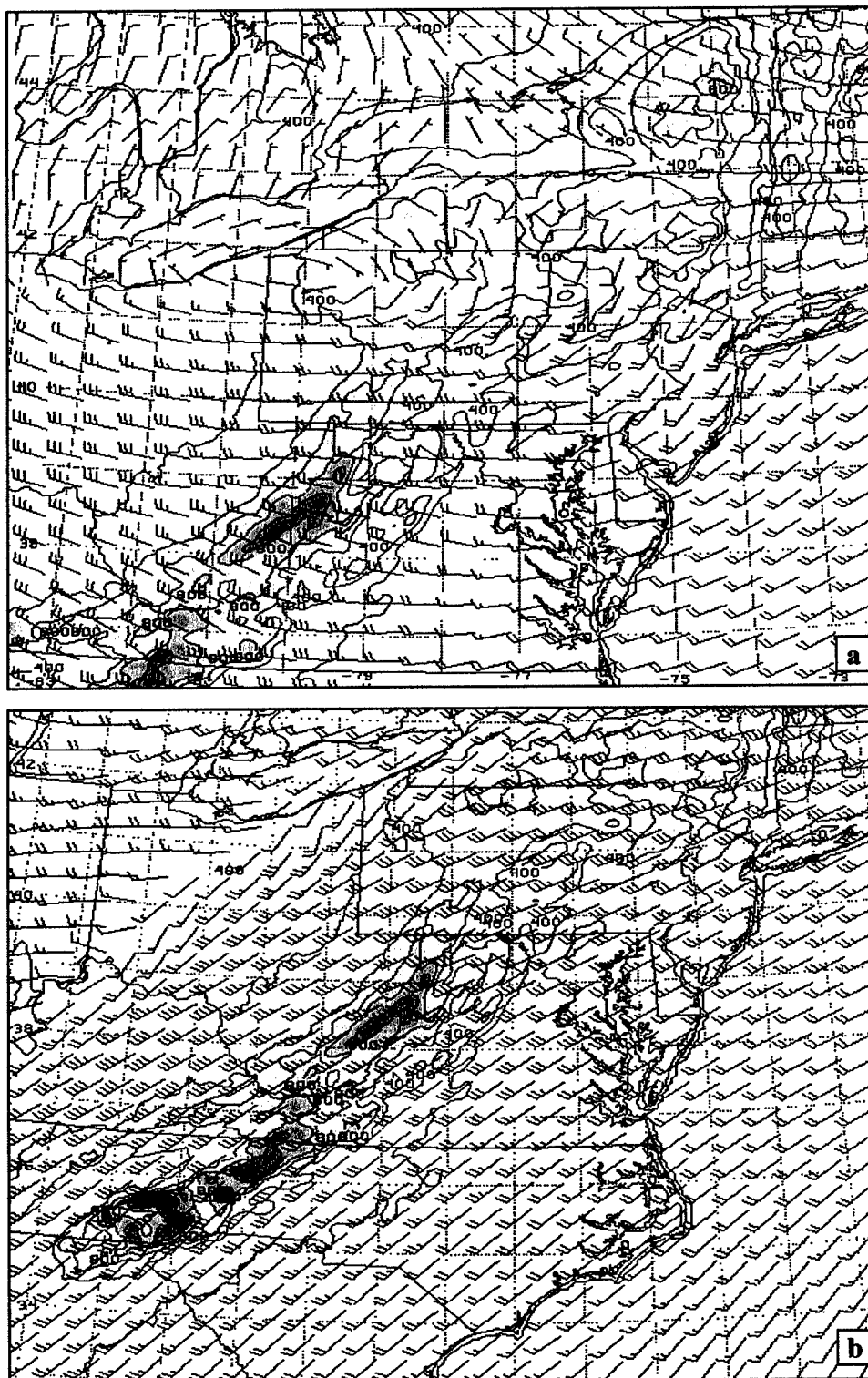
170

Figure 9. Simulated mean PBL wind (ms^{-1}) and NHMASS surface terrain contours (every 100 m) valid at 12 UTC (a) 13 Jan 2000, (b) 28 Dec 1988.
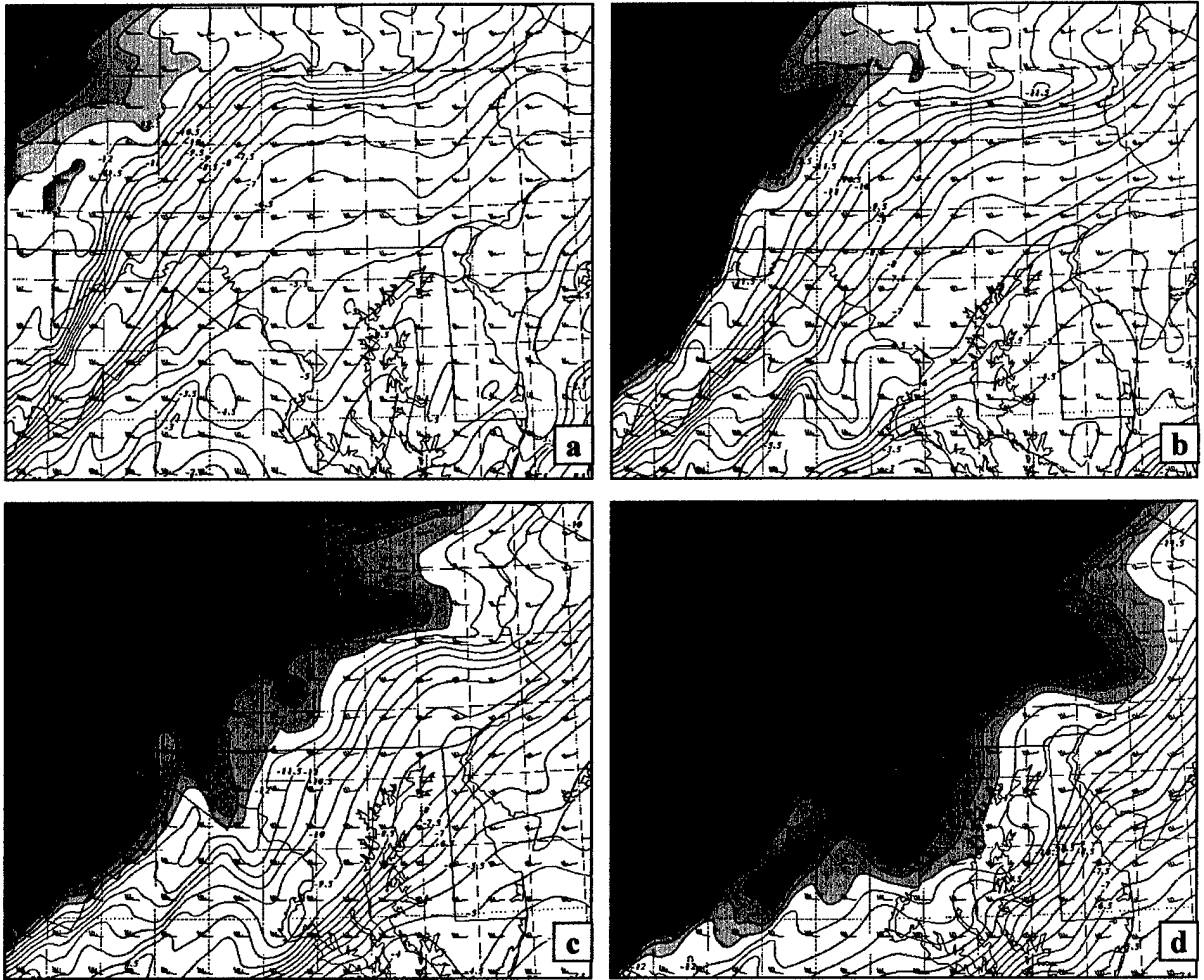
Figure 10. Simulated 700 hPa temperature (^{0}C) and wind (ms^{-1}). Temperatures of -12.5 ^{0}C and colder are shaded with those less than −16.5 ^{0}C the darkest shade. Plots are valid 13 Jan 2000 at (a) 1530 UTC, (b) 1630 UTC, (c) 1730 UTC, (d) 1830 UTC.
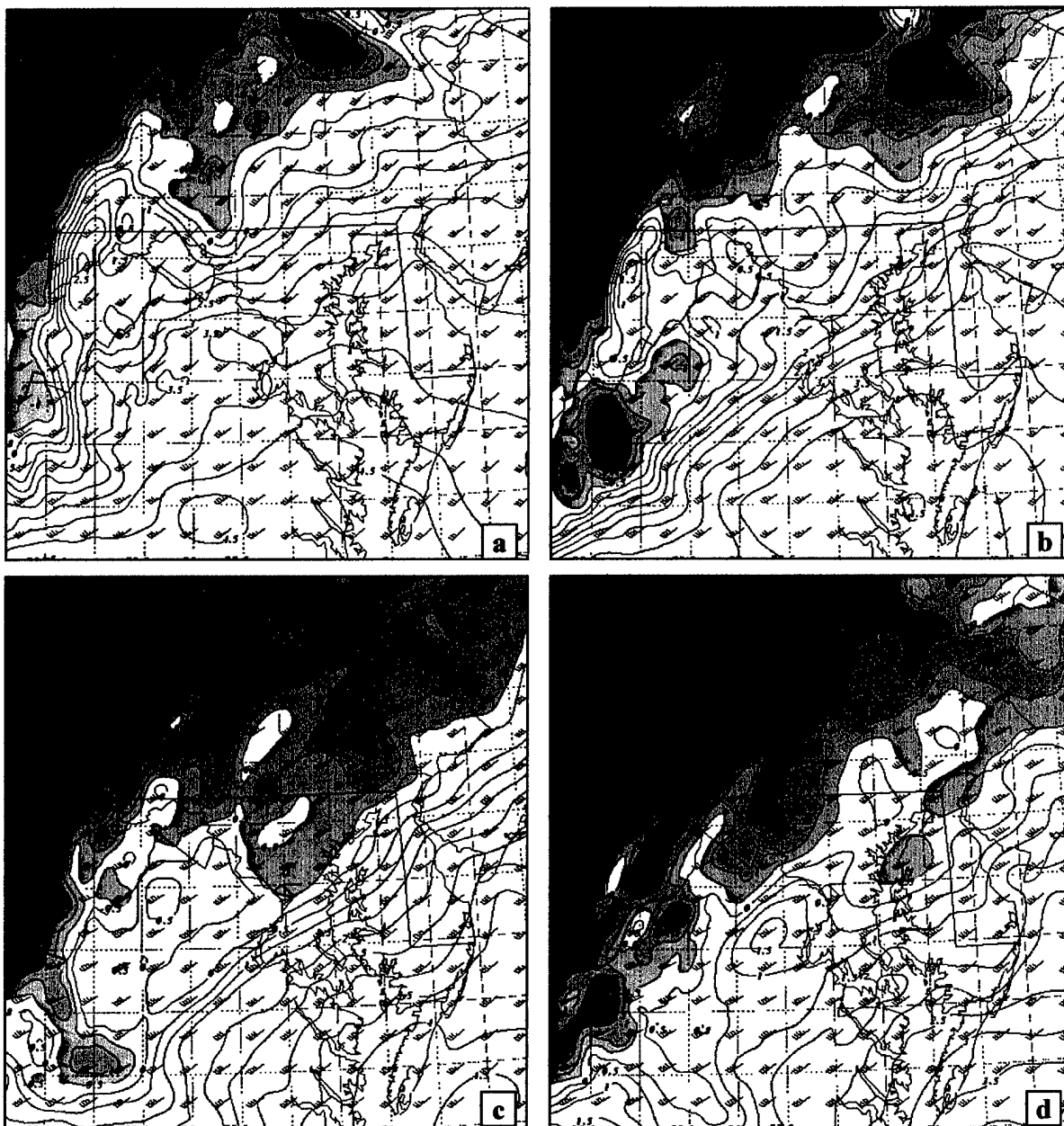
Figure 11. Simulated 700 hPa temperature (^{0}C) and wind (ms^{-1}). Temperatures of –0.5 ^{0}C and colder are shaded with those less than –4.5 ^{0}C the darkest shade. Plots are valid 28 Dec 1988 at (a) 1500 UTC, (b) 1600 UTC, (c) 1700 UTC, (d) 1800 UTC.
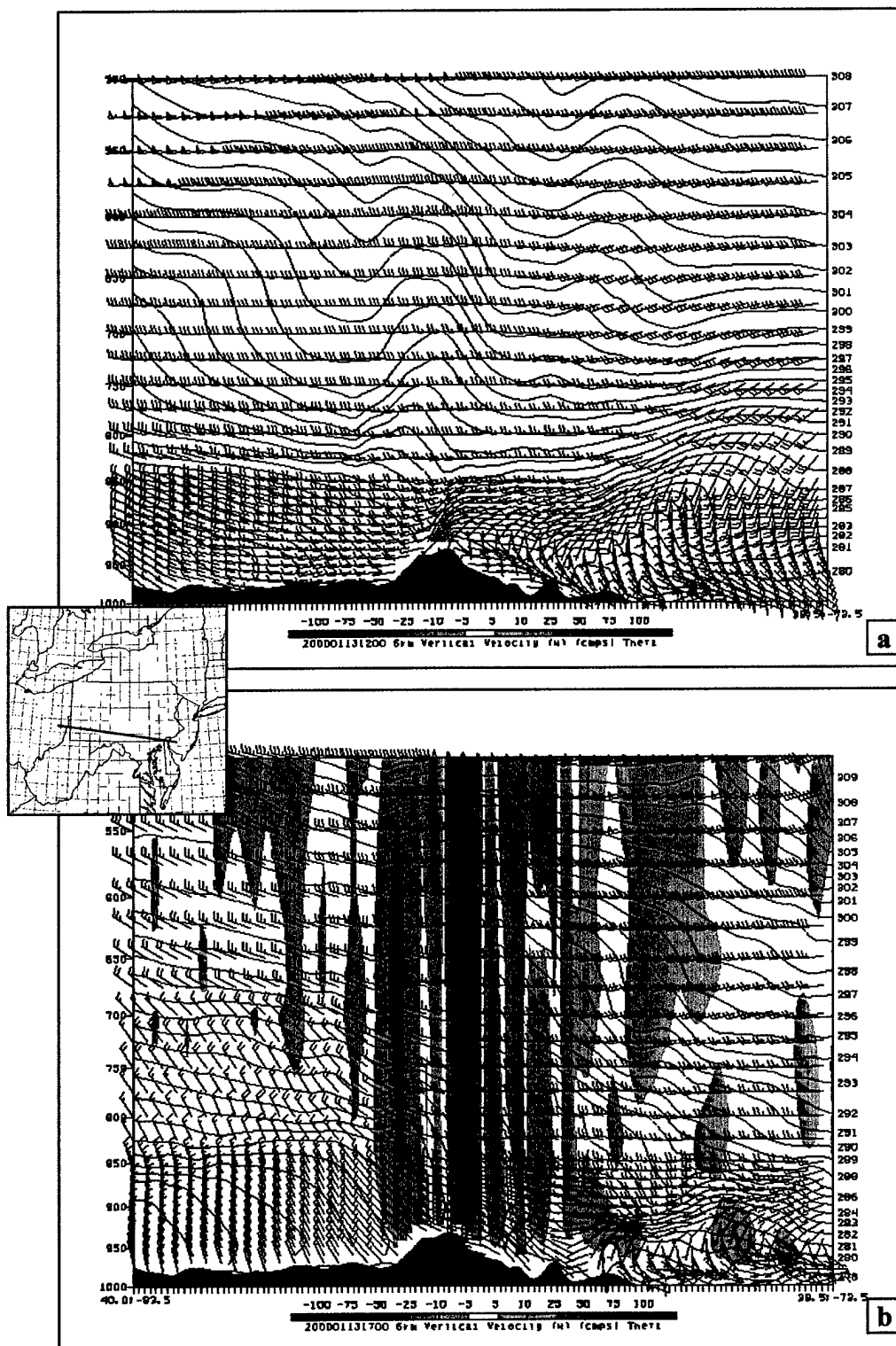
Figure 12. Simulated cross sections depicting potential temperature (K) and winds (ms⁻¹). Vertical velocity (cms⁻¹) is depicted in the bottom figure. Valid 13 Jan 2000 (a) 12 UTC, (b) 17 UTC.
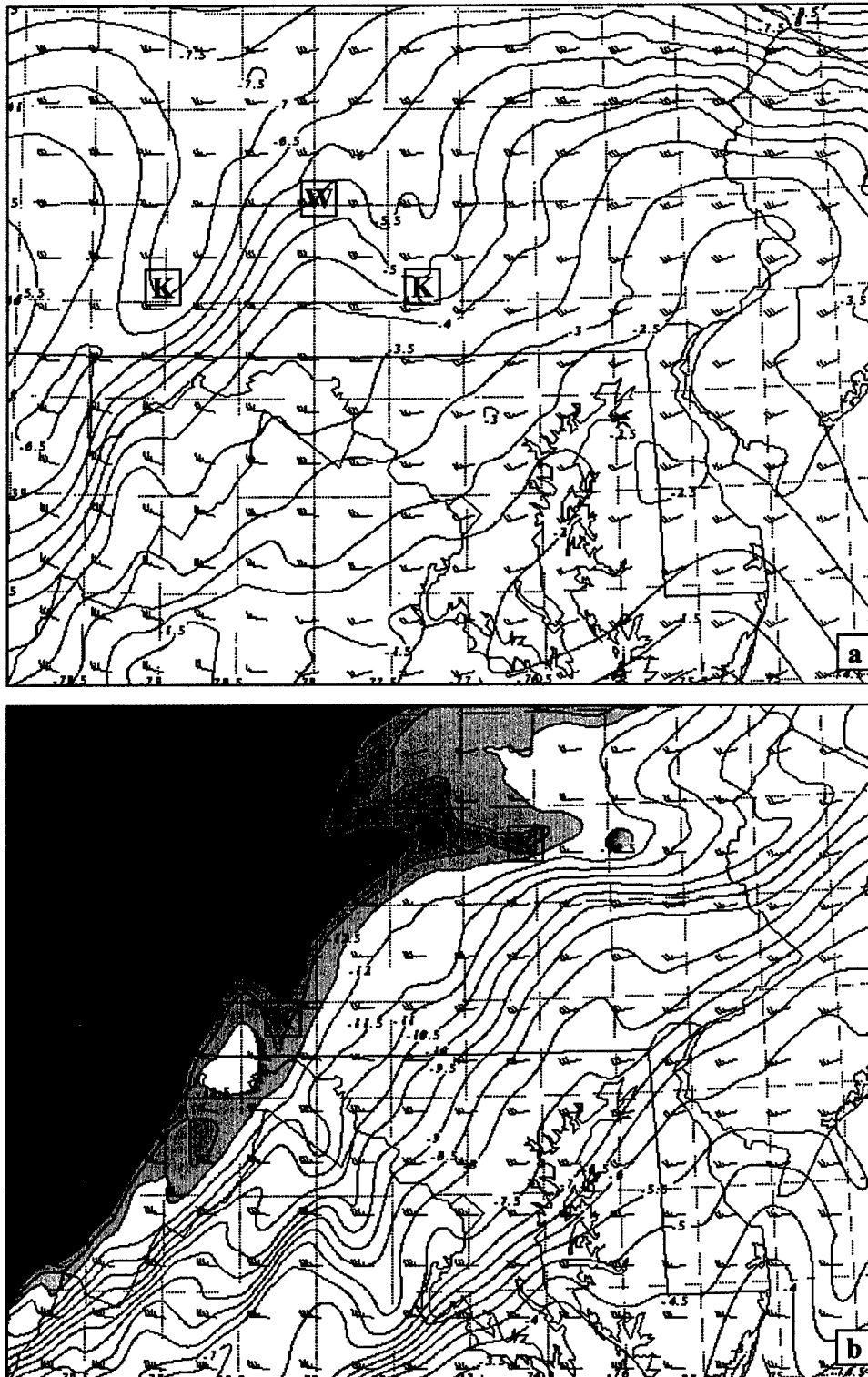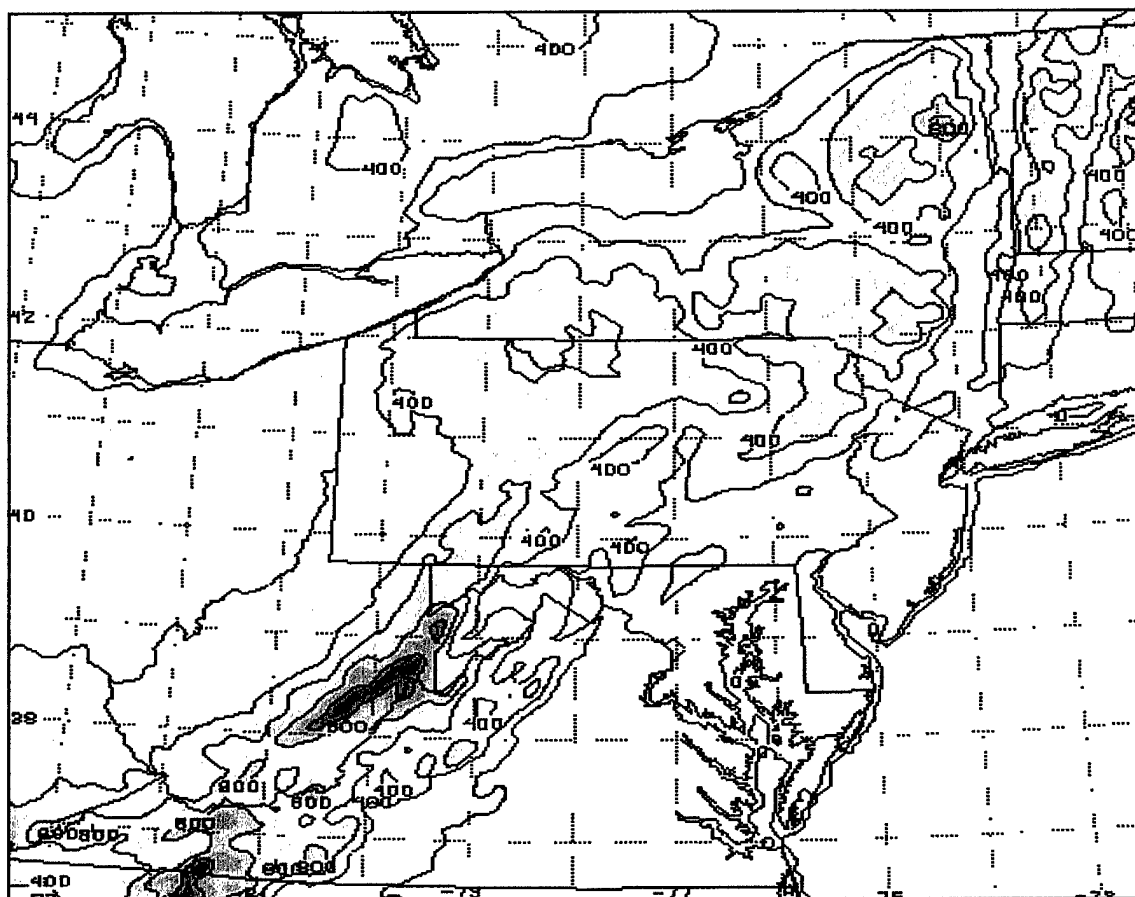
Figure 13. Simulated 700 hPa temperature (^{0}C) and wind (ms^{-1}) valid 13 Jan 2000 (a) 12 UTC, (b) 17 UTC. Boxed "K" points indicate cold air and boxed "W", warm. Note terrain in Fig. 14 (next page).
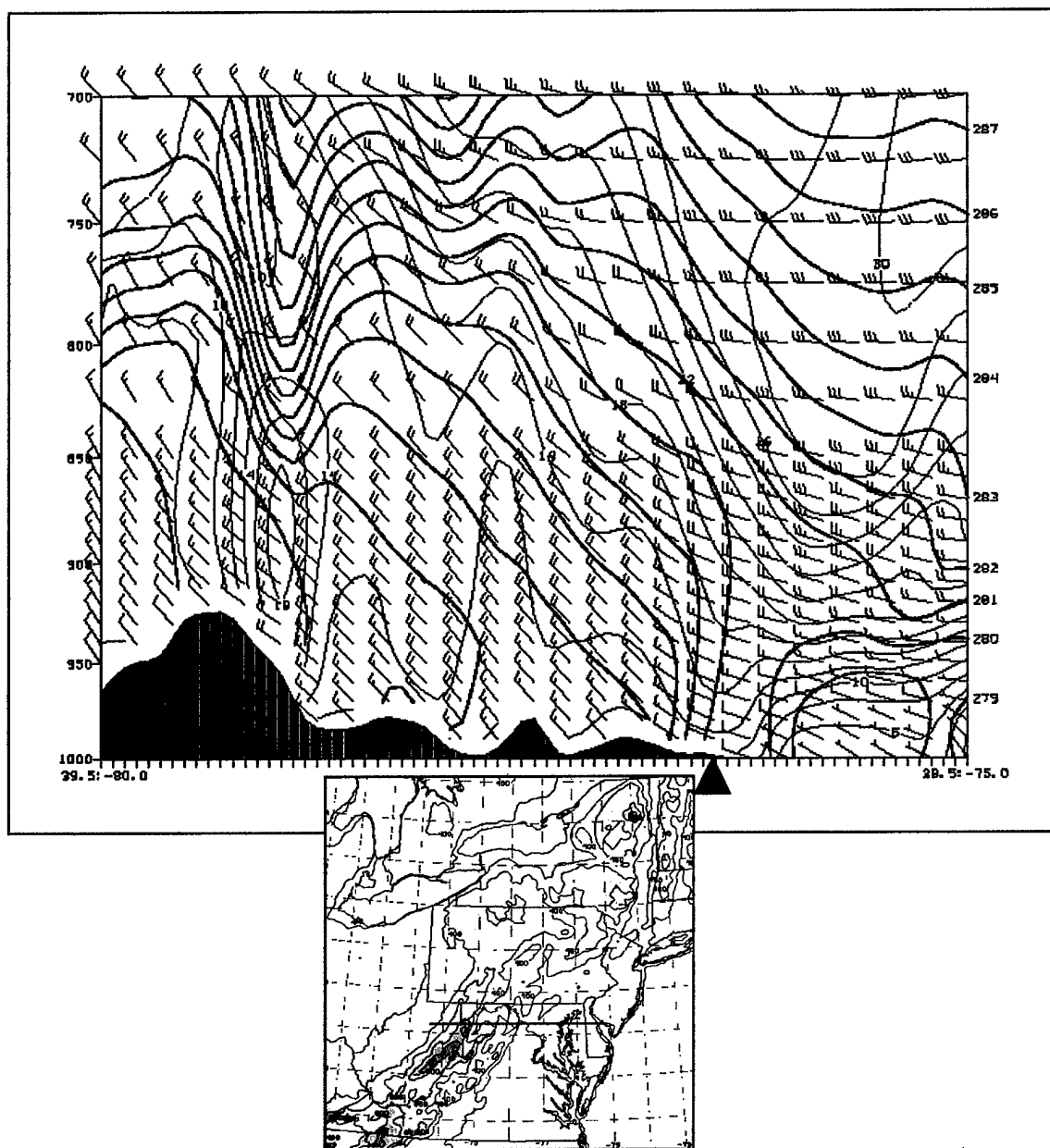
175

Figure 14. 6-km NHMASS terrain (m). Contours are 100m (filled) and 200m (lined).

Figure 15. Simulated cross section depicting wind (ms⁻¹), u-relative isotachs (ms⁻¹), and potential temperature (K, darker solid lines). Surface cold front position is denoted by filled triangle. Valid 13 Jan 2000/1930 UTC. Cross section location in inset above.

177
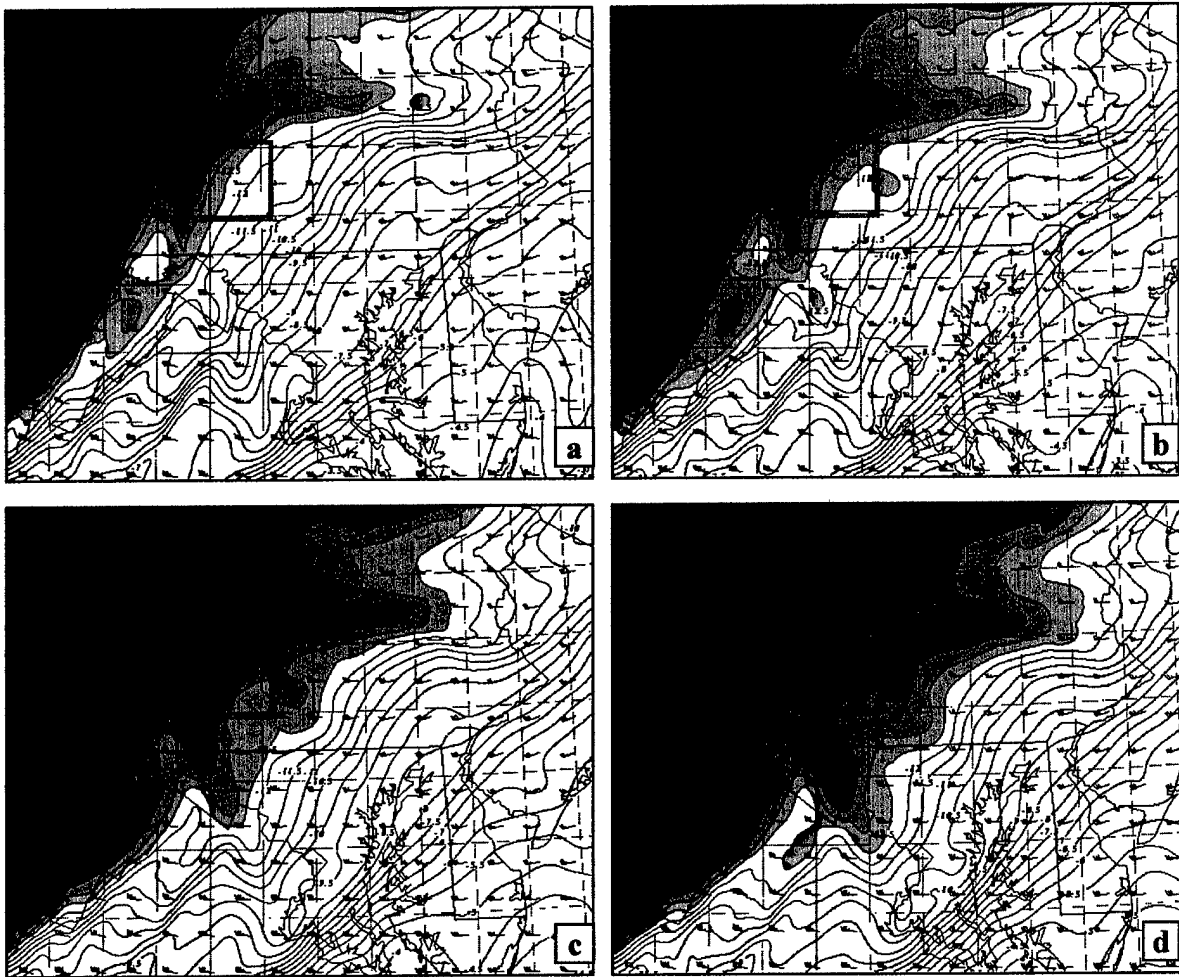
Figure 16. Simulated 700 hPa temperature (^{0}C) and wind (ms^{-1}). Temperatures of -12.5 ^{0}C and colder are shaded with those less than –16.5 ^{0}C the darkest shade. The grey box indicates the Bedford County region of Pennsylvania referred to in the text. Plots are valid 13 Jan 2000 at (a) 1700 UTC, (b) 1715 UTC, (c) 1730 UTC, (d) 1745 UTC.

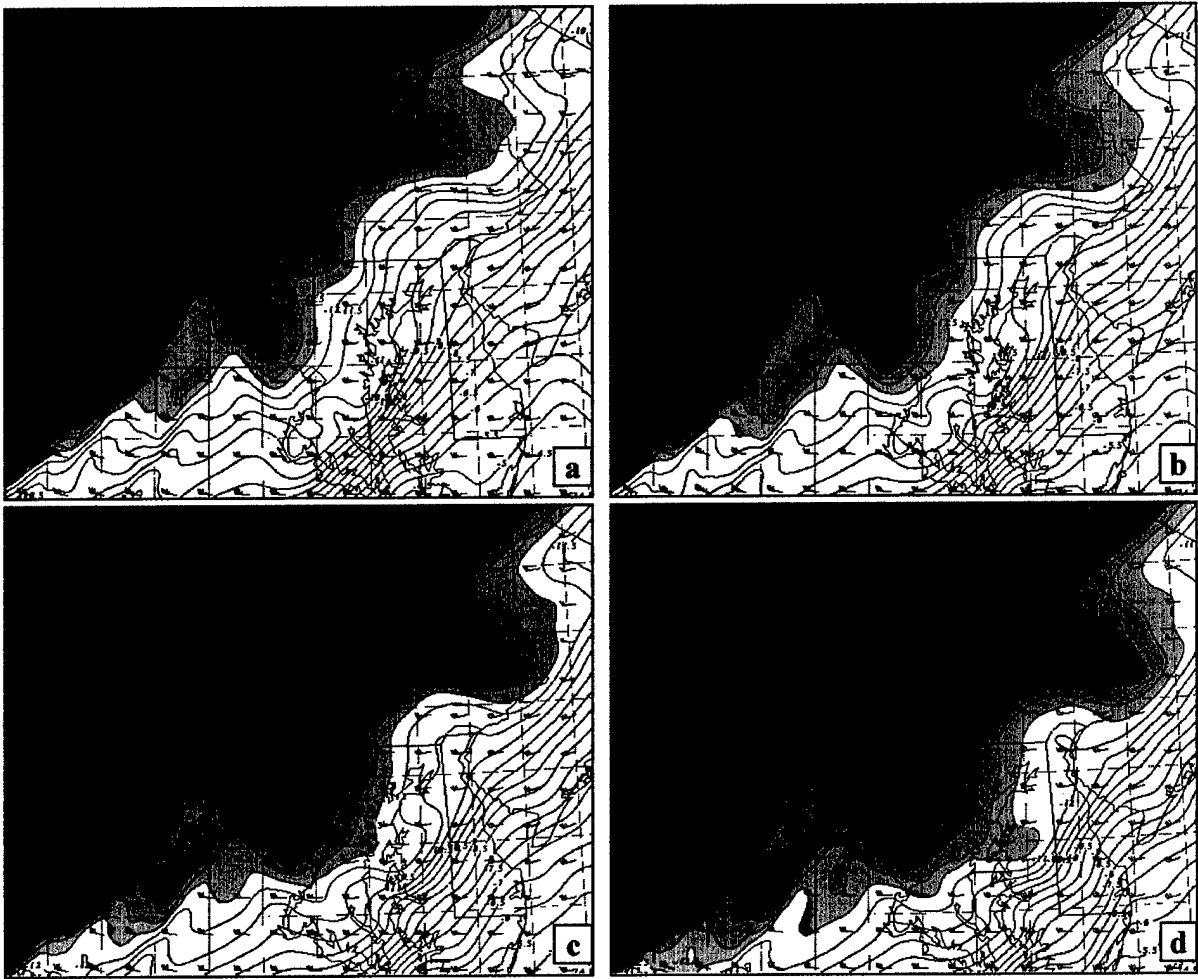Figure 17. Simulated 700 hPa temperature (^{0}C) and wind (ms^{-1}). Temperatures of -12.5 ^{0}C and colder are shaded with those less than −16.5 ^{0}C the darkest shade. Plots are valid 13 Jan 2000 at (a) 1800 UTC, (b) 1815 UTC, (c) 1830 UTC, (d) 1845 UTC.

Figure 18. Simulated 700 hPa temperature (^{0}C) and wind (ms^{-1}). Temperatures of -12.5 ^{0}C and colder are shaded with those less than –16.5 ^{0}C the darkest shade. Plots are valid 13 Jan 2000 at (a) 1900 UTC, (b) 1915 UTC, (c) 1930 UTC, (d) 1945 UTC.

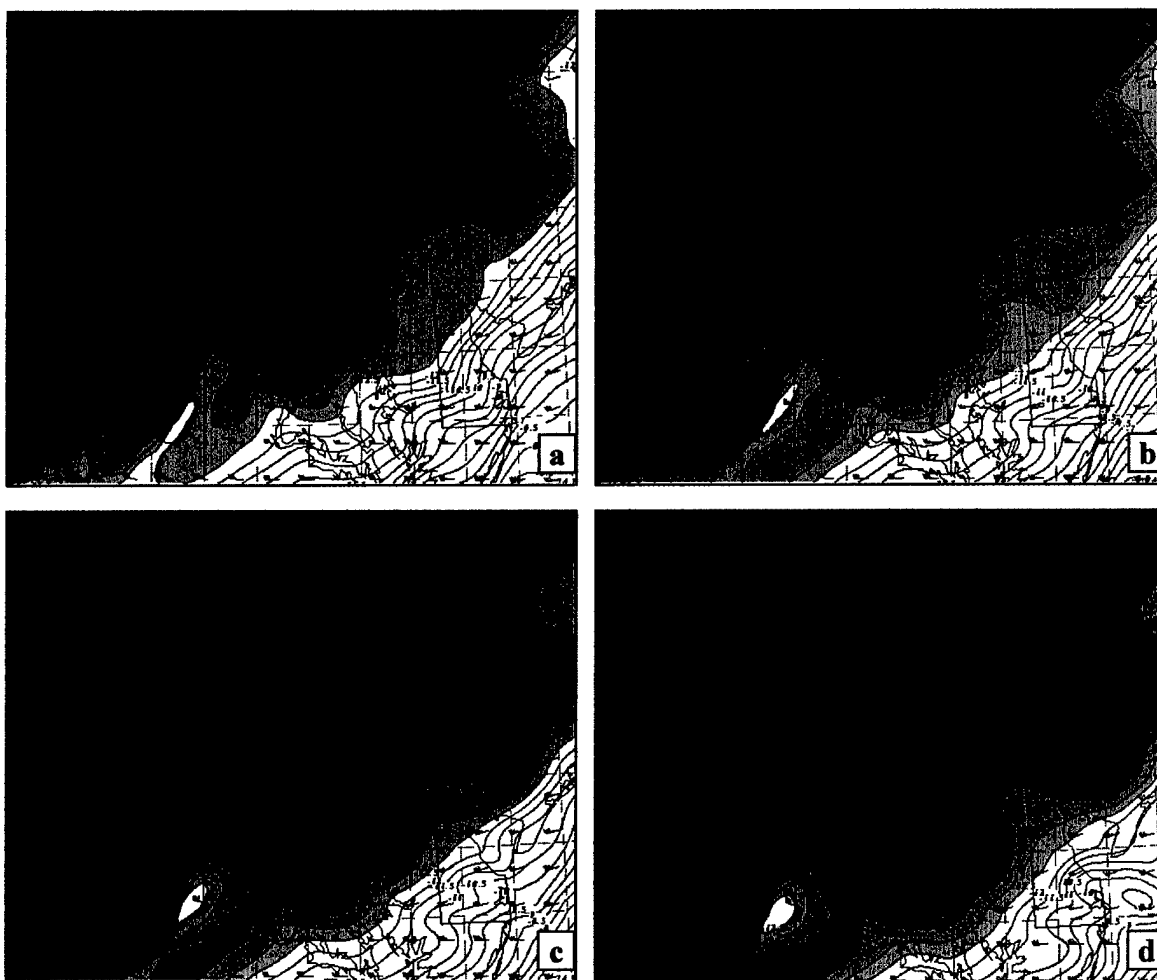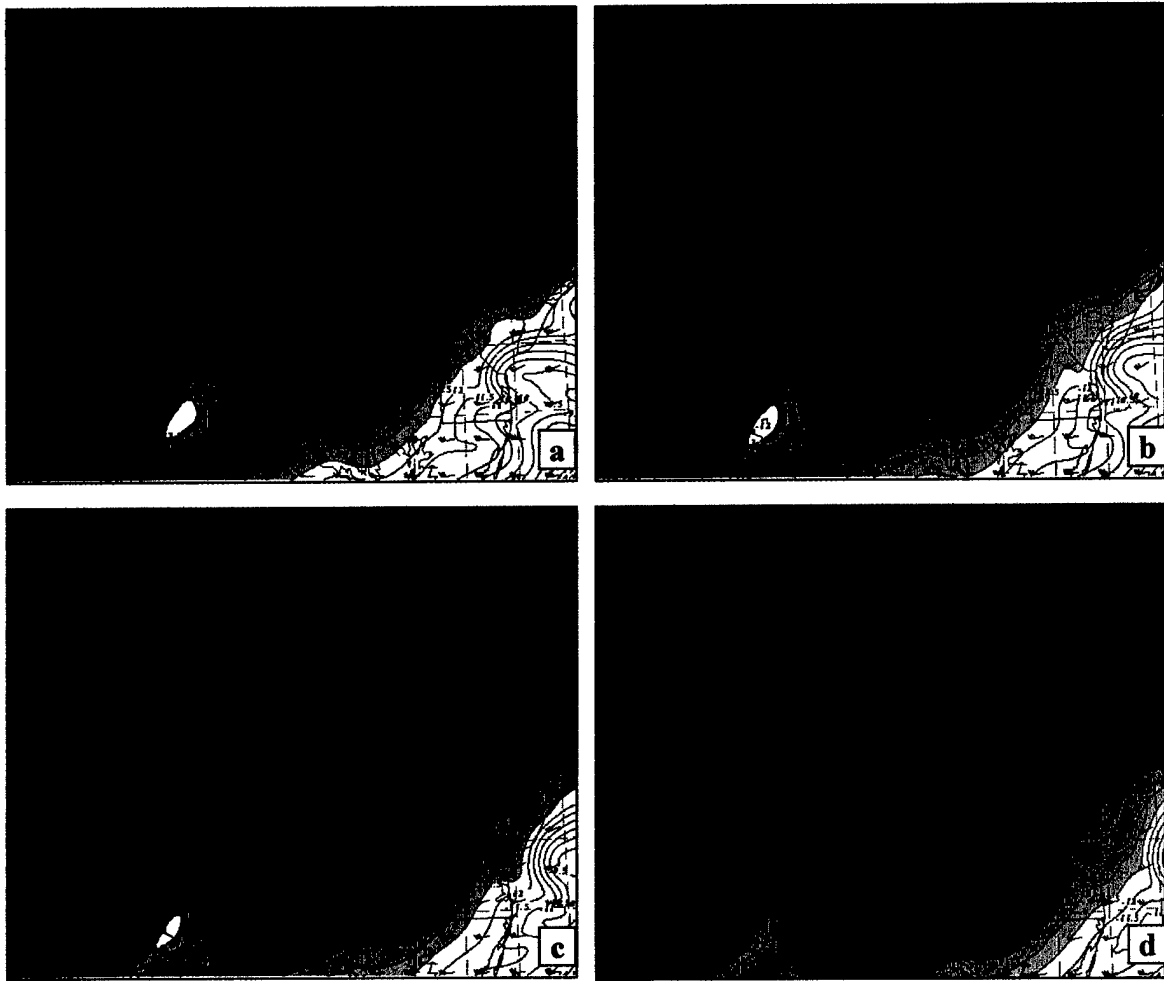Figure 19. Simulated 700 hPa temperature (^{0}C) and wind (ms^{-1}). Temperatures of -12.5 ^{0}C and colder are shaded with those less than −16.5 ^{0}C the darkest shade. Plots are valid 13 Jan 2000 at (a) 2000 UTC, (b) 2015 UTC, (c) 2030 UTC, (d) 2045 UTC.
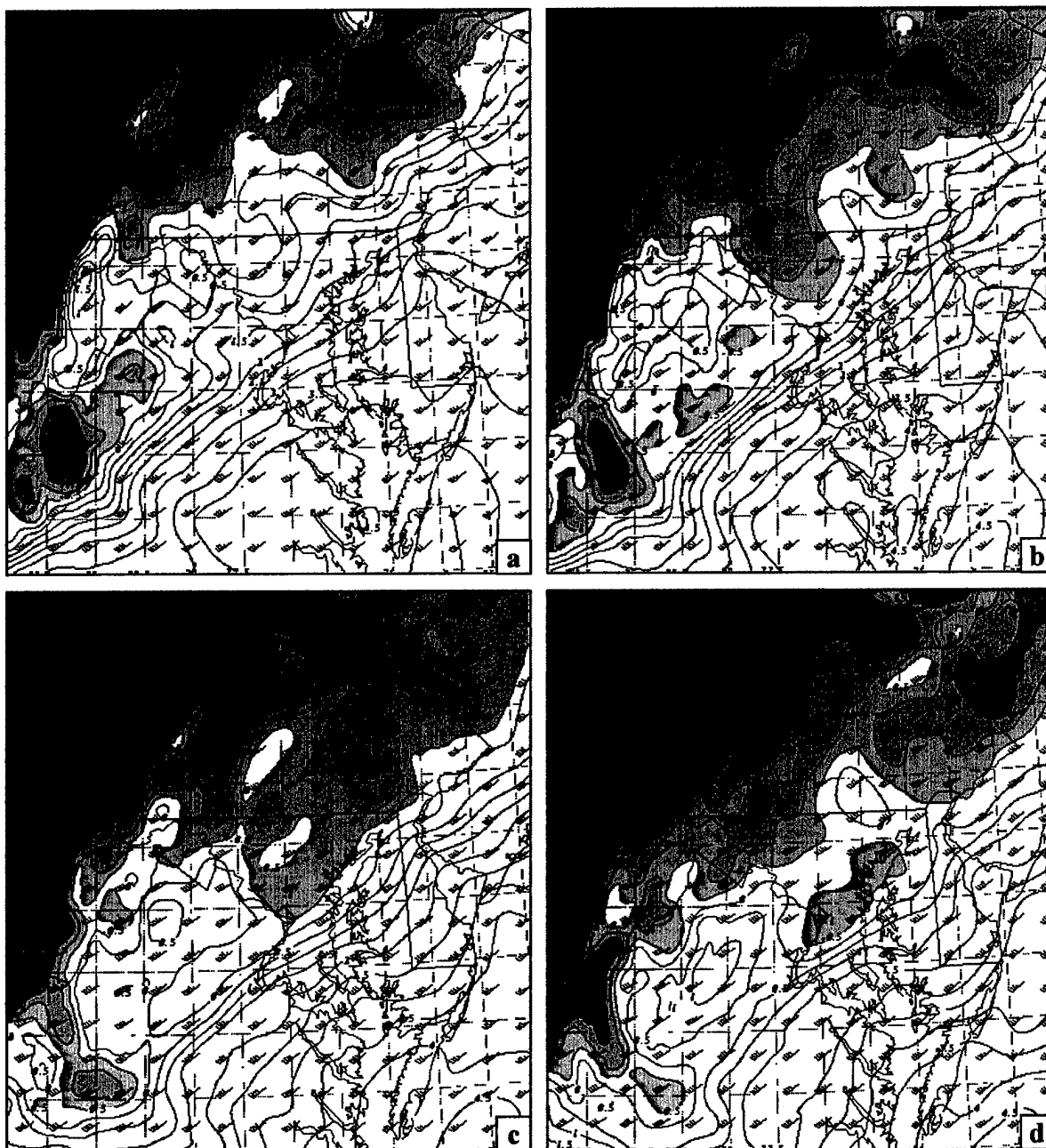
Figure 20. Simulated 700 hPa temperature (^{0}C) and wind (ms^{-1}). Temperatures of -0.5 ^{0}C and colder are shaded with those less than –4.5 ^{0}C the darkest shade. Plots are valid 28 Dec 1988 at (a) 1600 UTC, (b) 1630 UTC, (c) 1700 UTC, (d) 1730 UTC.
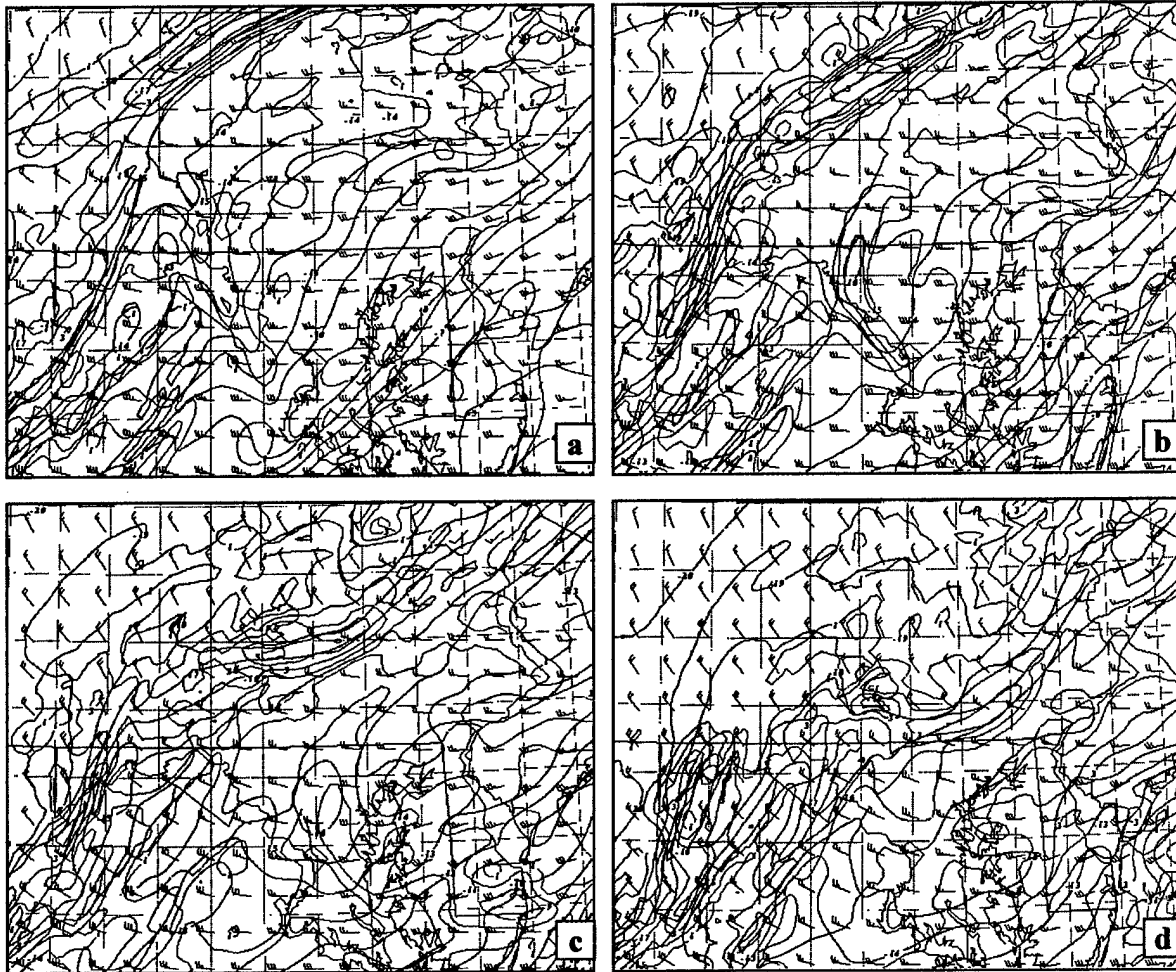
Figure 21. 700 hPa 6-km simulated total deformation (x10^{-4}s^{-1}) and temperature (^{0}C) for 13 Jan 2000 valid (a) 1730 UTC, (b) 1830 UTC, (c) 1930 UTC, (d) 2030 UTC. Deformation values larger than 1 x 10^{-4}s^{-1} are shaded.
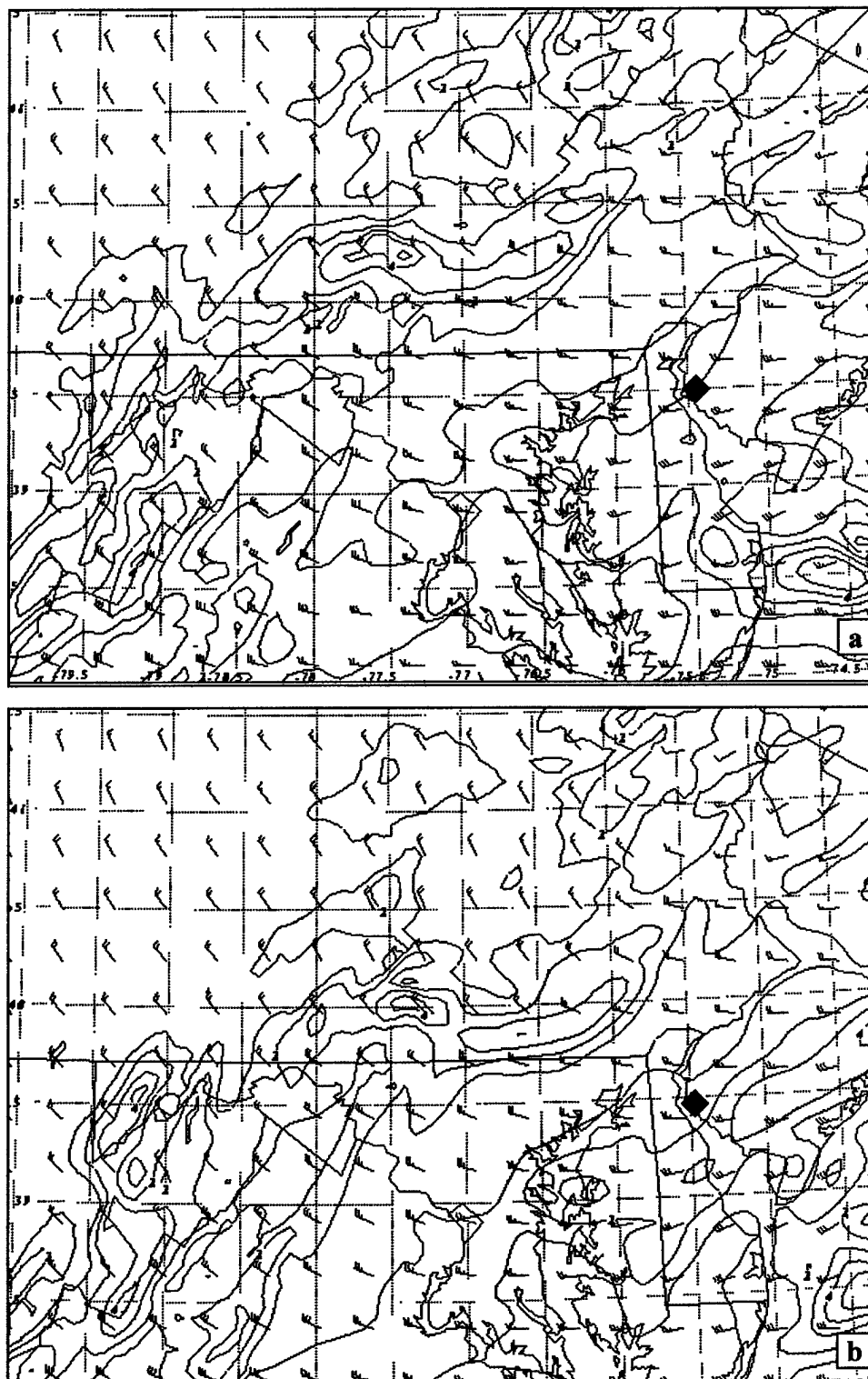
Figure 22. 700 hPa 6-km simulated total deformation ($\times 10^{-4} s^{-1}$) for 13 Jan 2000 valid (a) 2000 UTC, (b) 2030 UTC. The J00 accident location is denoted by a ◆.
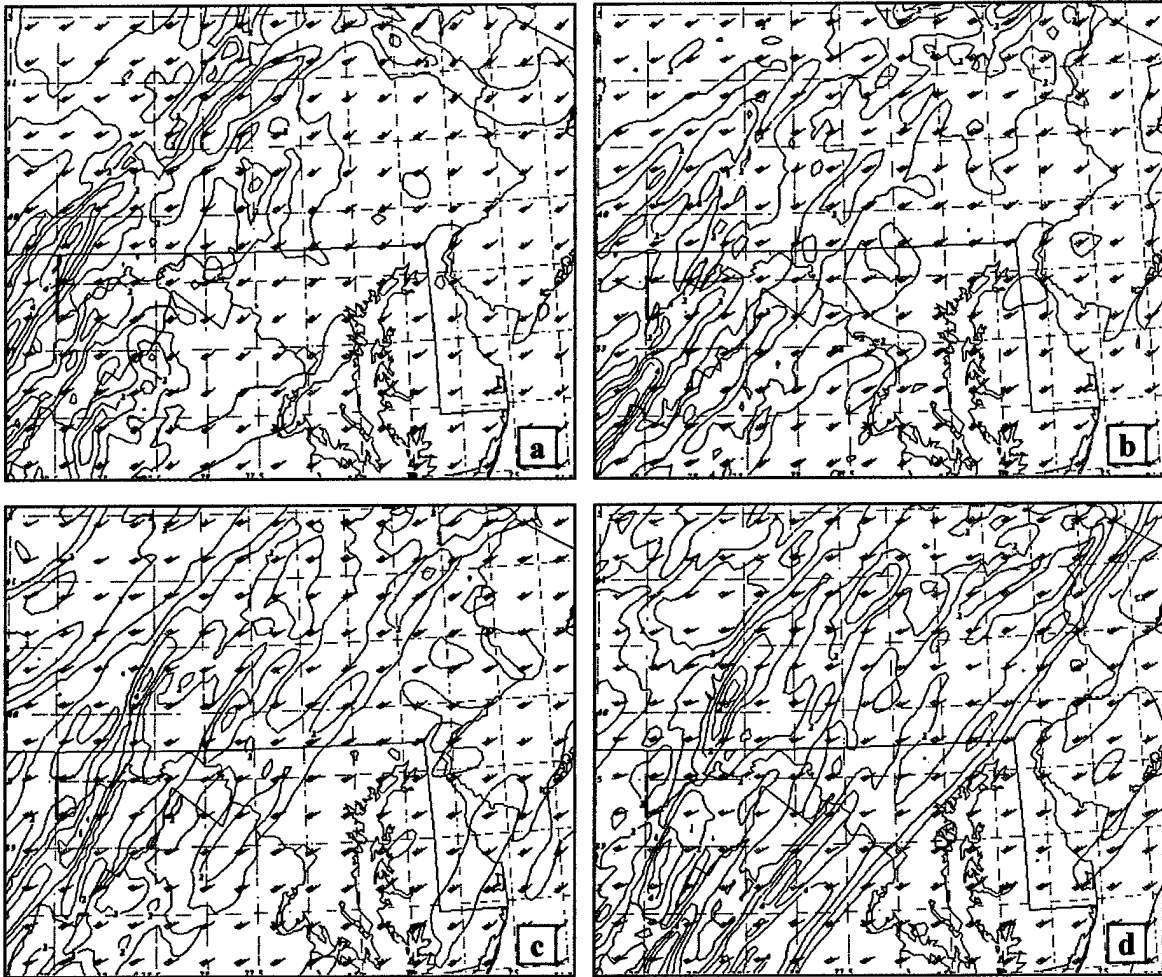
Figure 23. 700 hPa 6-km simulated total deformation $(\times 10^{-4} \text{s}^{-1})$ for 28 Dec 1988 valid (a) 1600 UTC, (b) 1700 UTC, (c) 1800 UTC, (d) 1900 UTC.
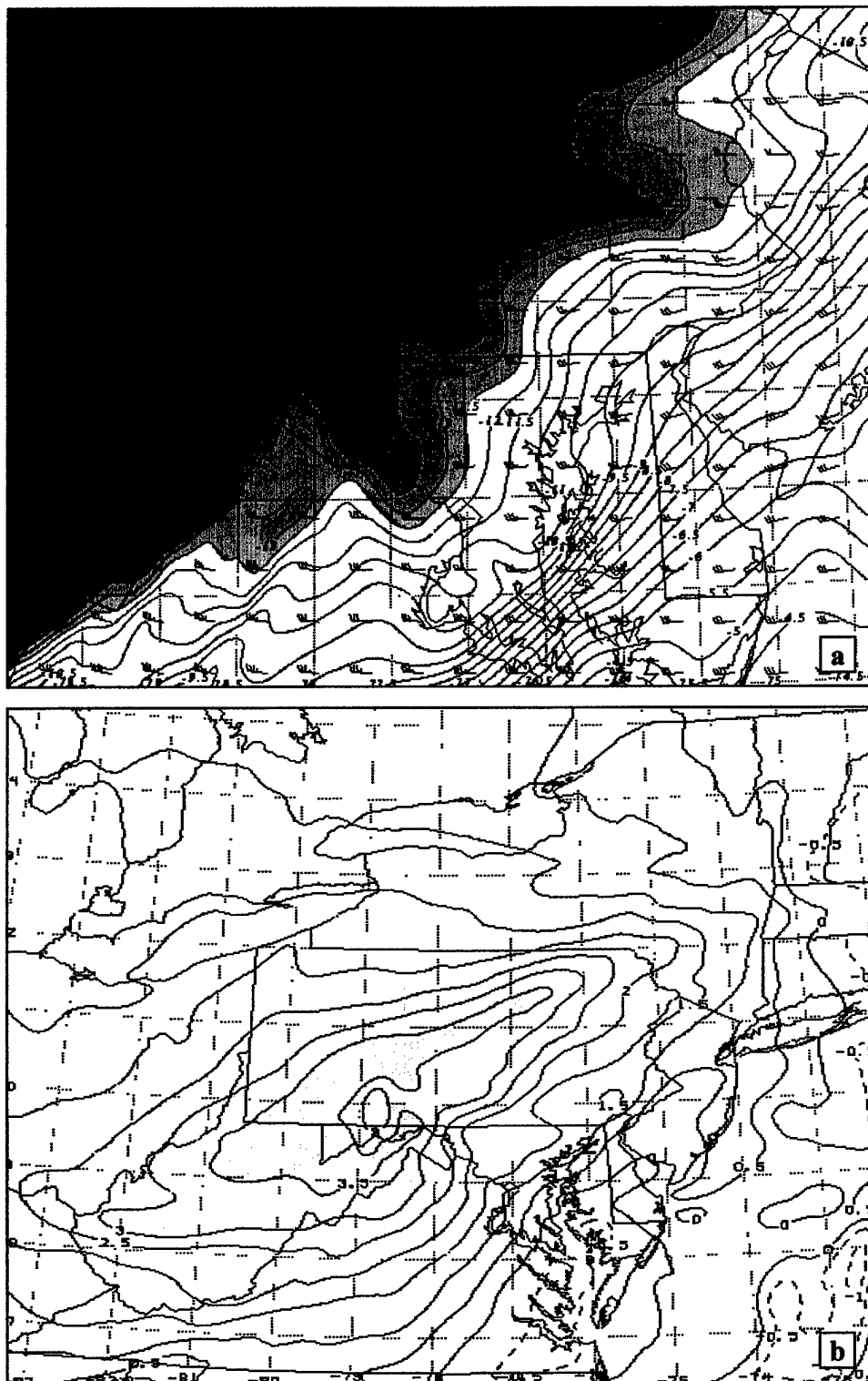
Figure 24. (a) Simulated 700 hPa temperature (^{0}C) and wind (ms^{-1}) valid
18 UTC 13 Jan 2000 and (b) Simulated hourly surface pressure change
(hPa) valid 1830 UTC 13 Jan 2000 contoured every 0.5 hPa.
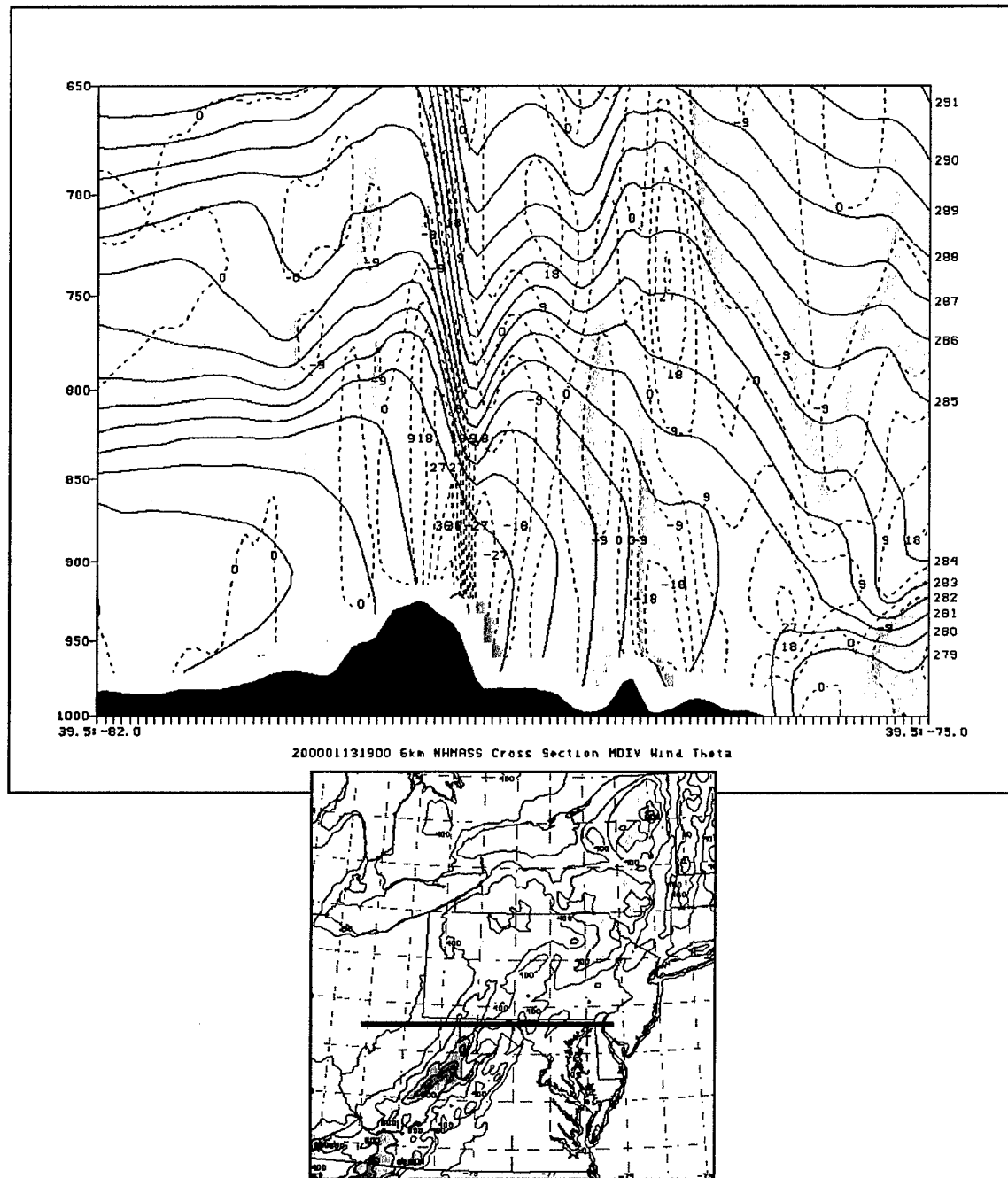
Figure 25. Simulated layer average mass divergence (kgs^{-1}). Shaded amounts indicate mass convergence in the column. Valid 19 UTC 13 Jan 2000. Location of cross section as depicted in lower figure.

187
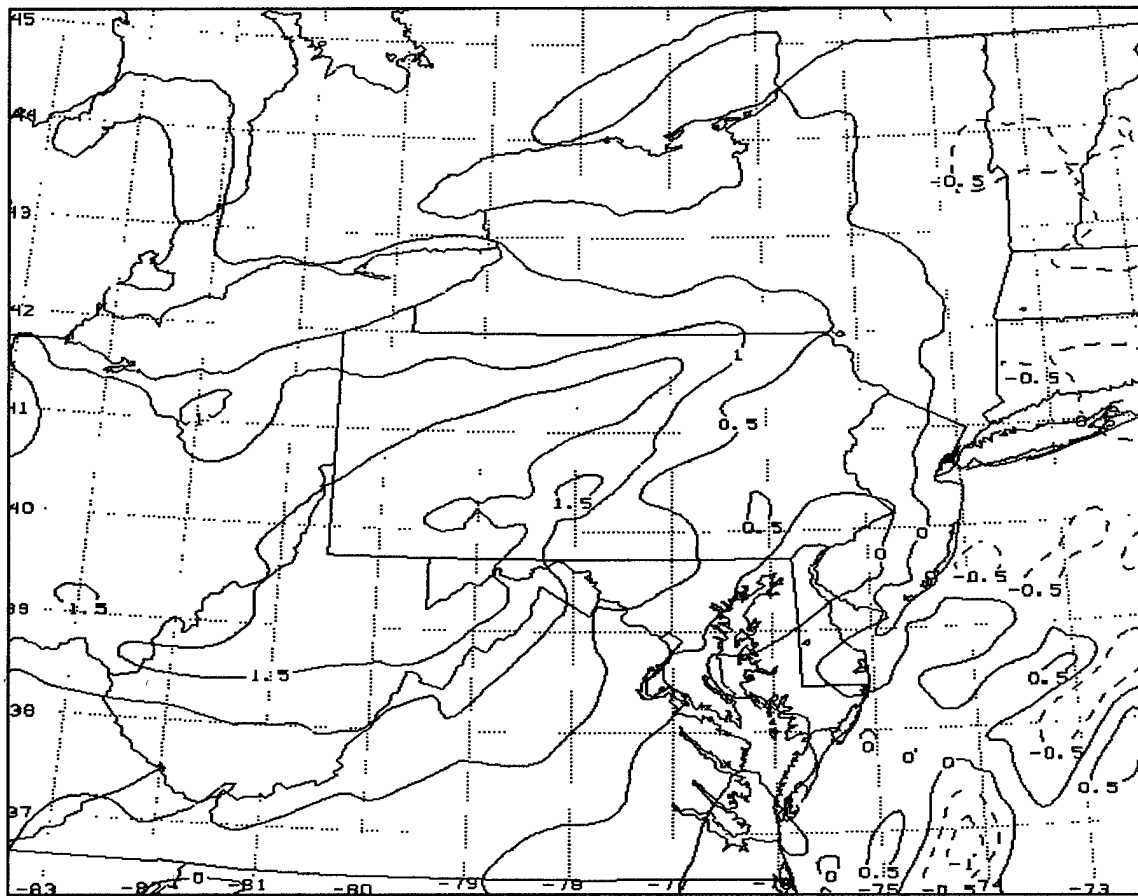
Figure 26. Simulated half-hour pressure change between 1700-1730 UTC on 13 Jan 2000.

Figure 27. Simulated half-hour pressure changes valid 13 Jan 2000 (a) 1800-1830 UTC, (b) 1900-1930 UTC, (c) 1930-2000 UTC, (d) 2000-2030 UTC.
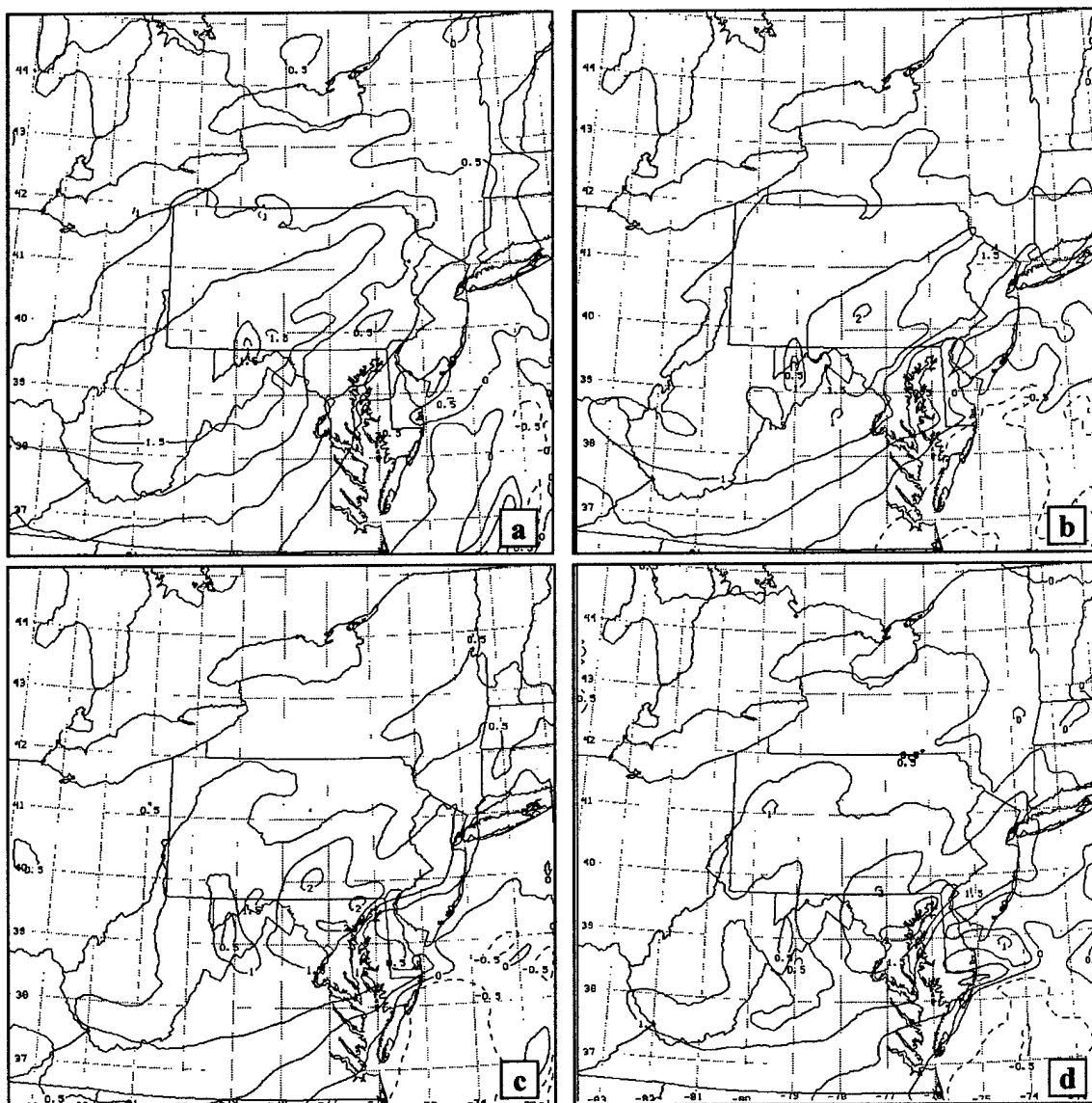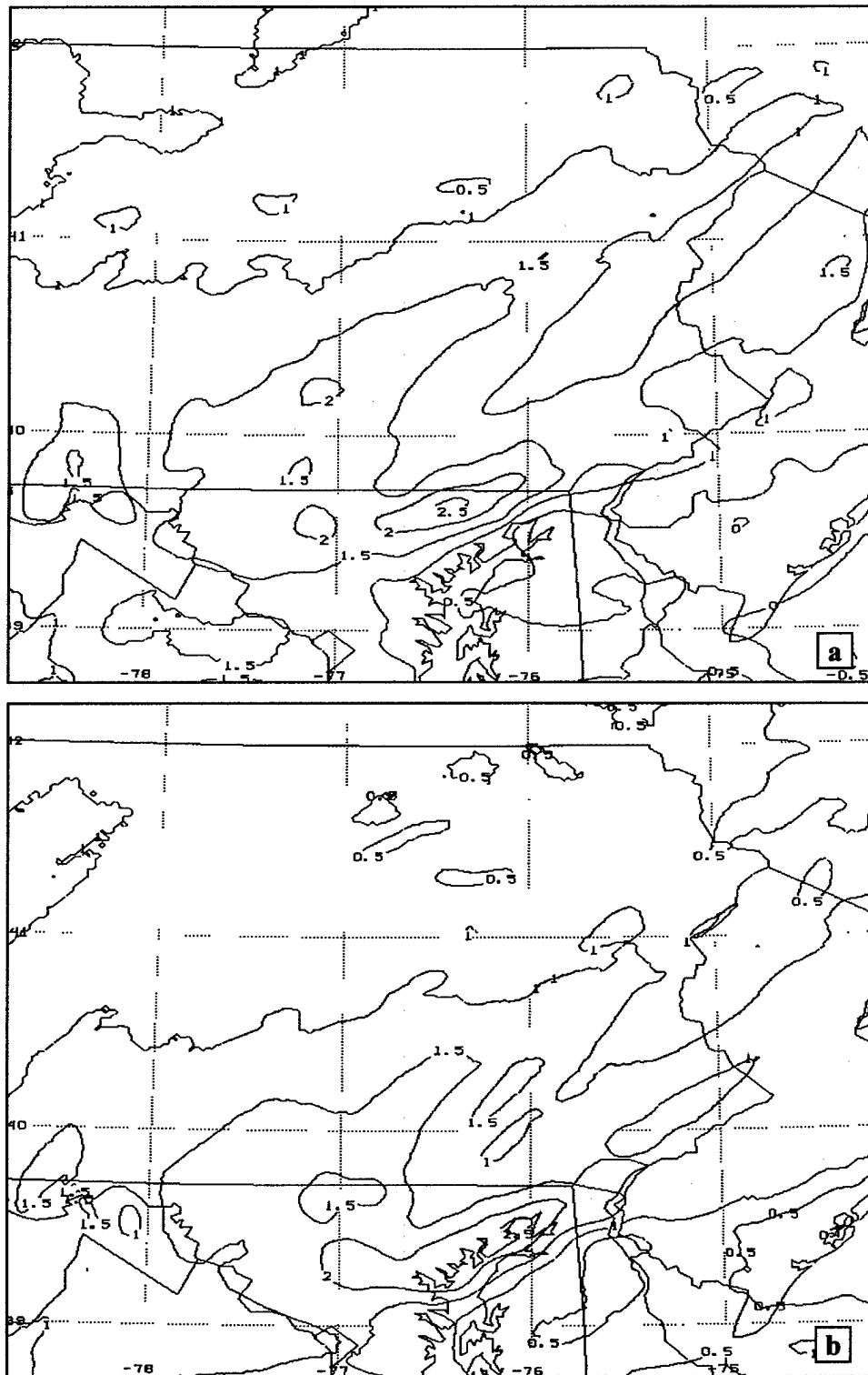
Figure 28. Simulated 2-km half-hour pressure changes valid 13 Jan 2000
(a) 1930-2000 UTC, (b) 2000-2030 UTC

Figure 29. Observed hourly pressure change (hPa/hr) valid 1900-2000 UTC 13 Jan 2000.
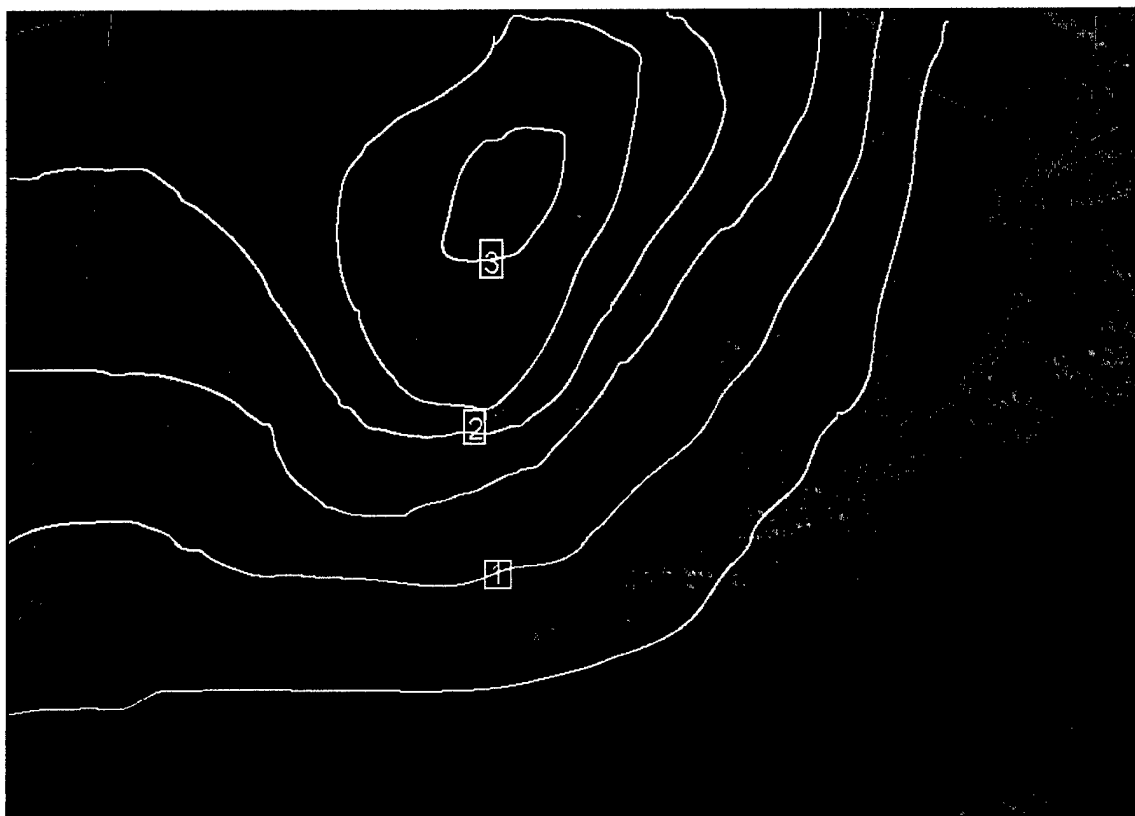
Figure 30. 1-km GOES-8 visible satellite imagery valid 1900 UTC 13 Jan 2000 with surface pressure tendency (hPa/hr) overlaid in white (valid 1800-1900 UTC).
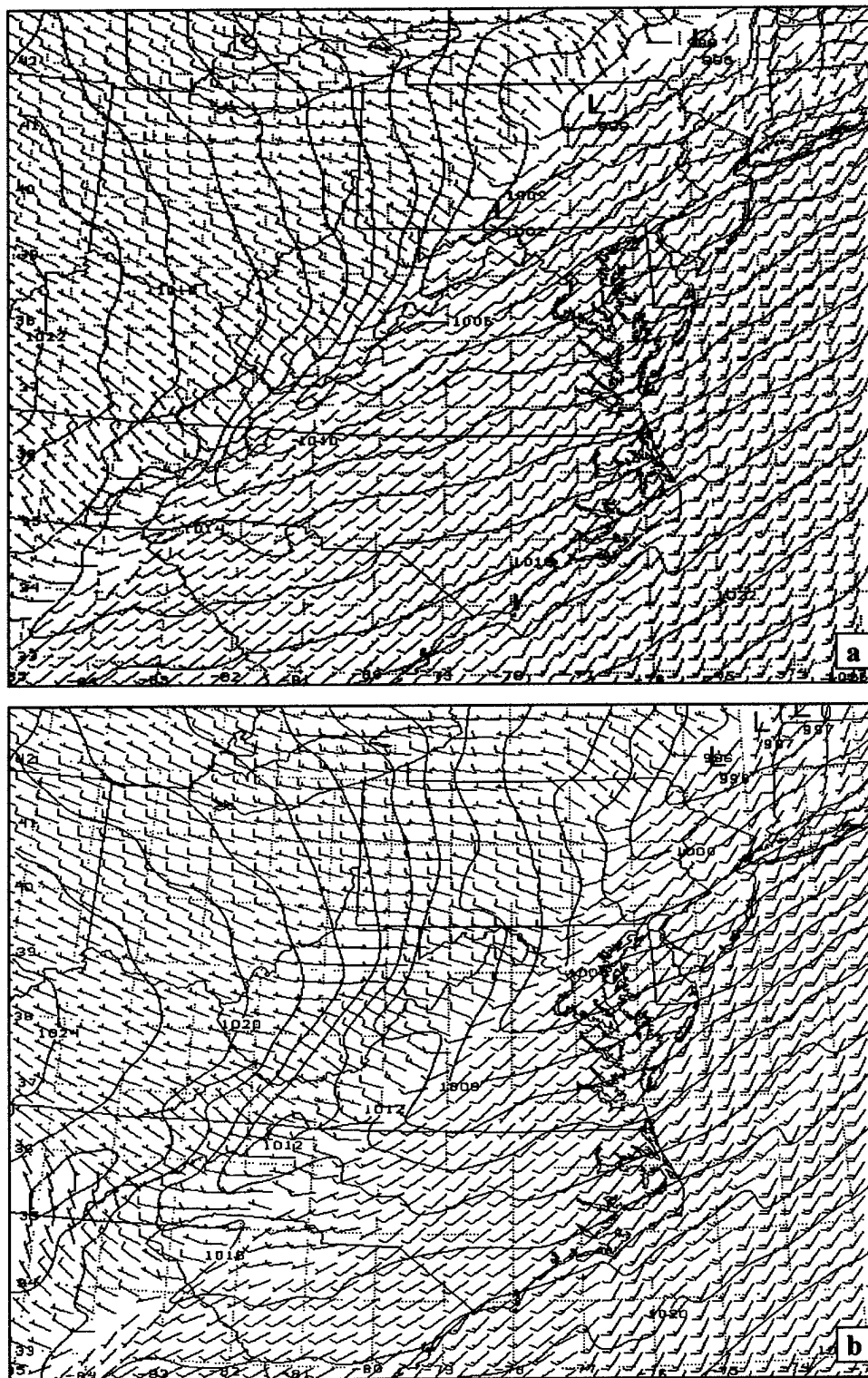
Figure 31. Simulated PMSL (hPa) and wind (ms^{-1}) valid 28 Dec 1988 (a) 1700 UTC, (b) 1900 UTC.

193
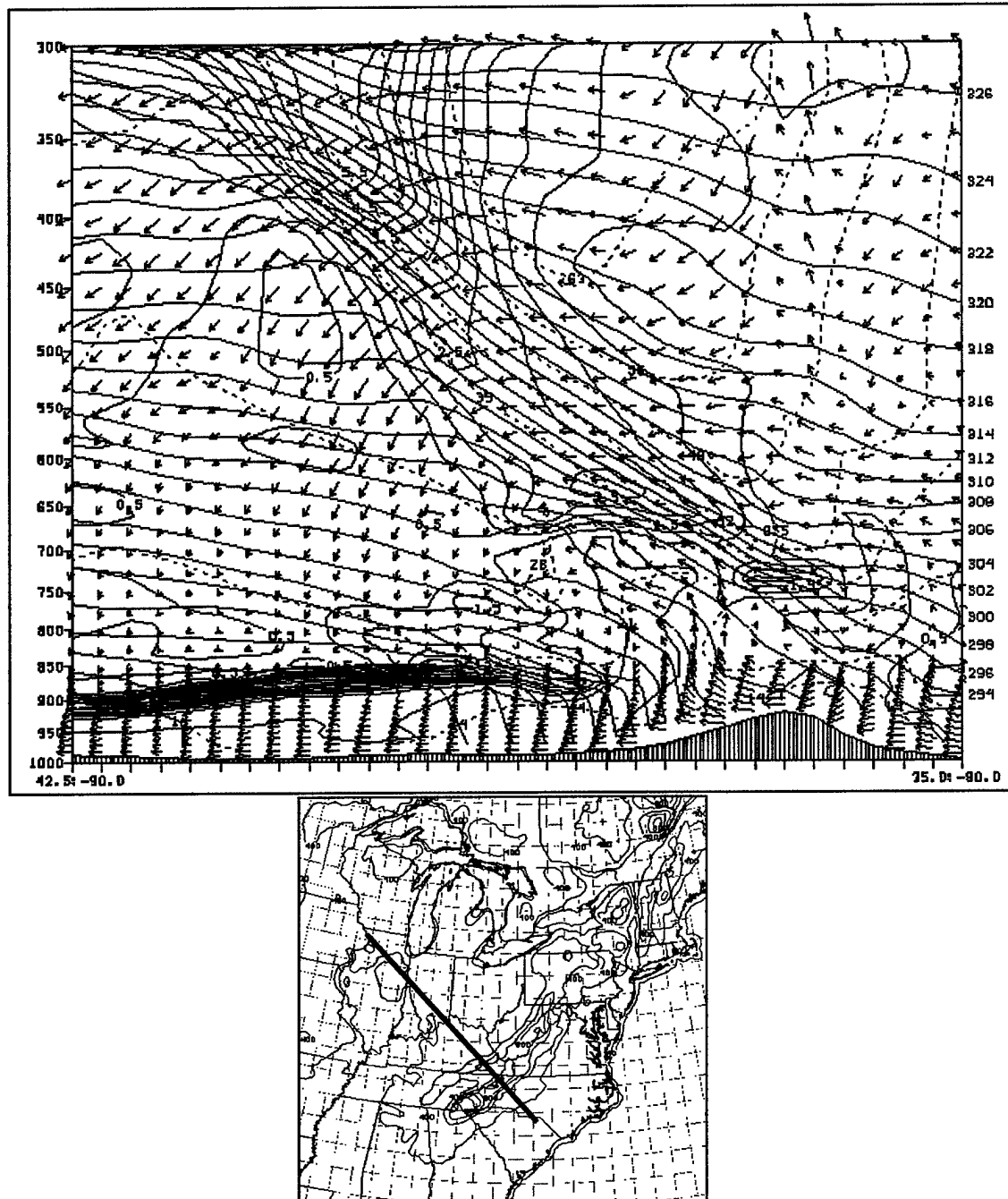
Figure 32. Simulated cross section bisecting the polar jet stream depicting ageostrophic circulation vectors, potential temperature (^{0}K), and potential vorticity (contoured every 0.5 PVU, with 1.0 PVU and greater shaded). Valid 1600 UTC 28 Dec 1988. Cross section located as depicted in lower inset.
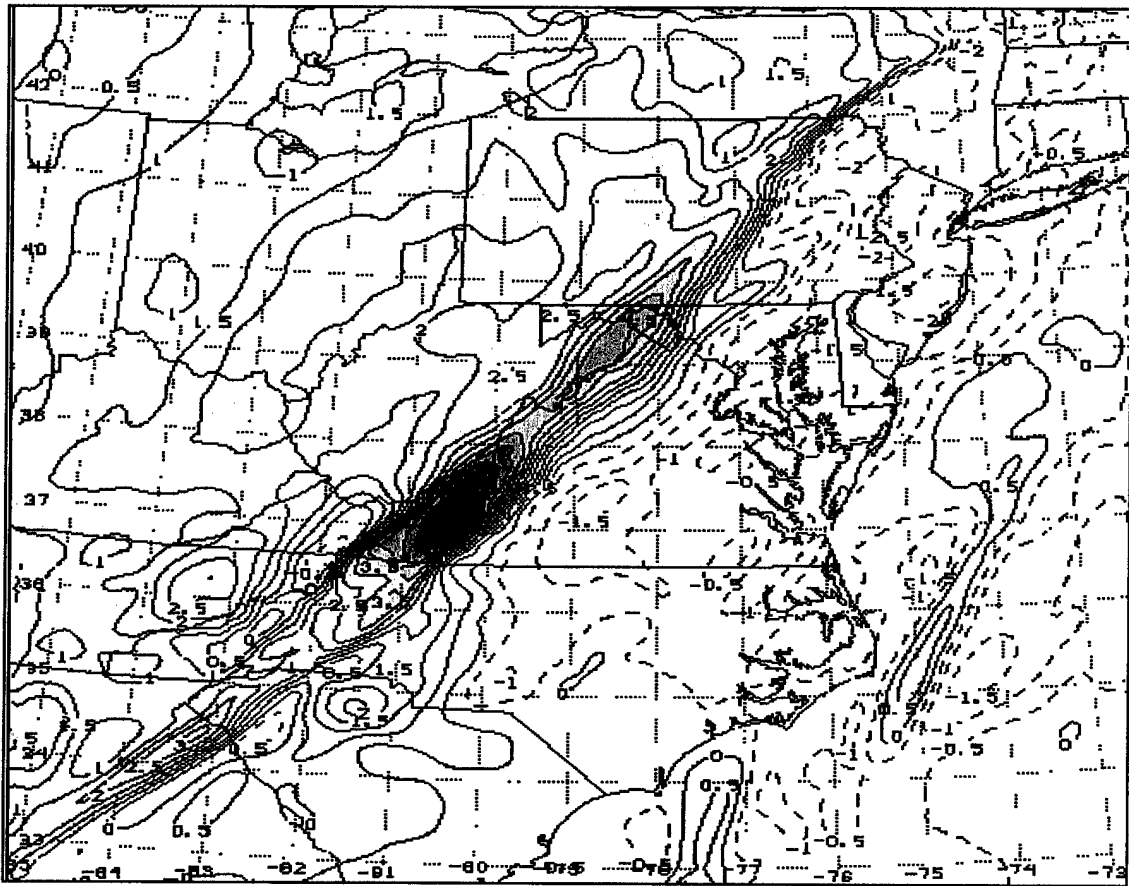
Figure 33. Simulated hourly pressure tendencies (hPa/hr). Valid 1830 UTC 28 Dec 1988.

195
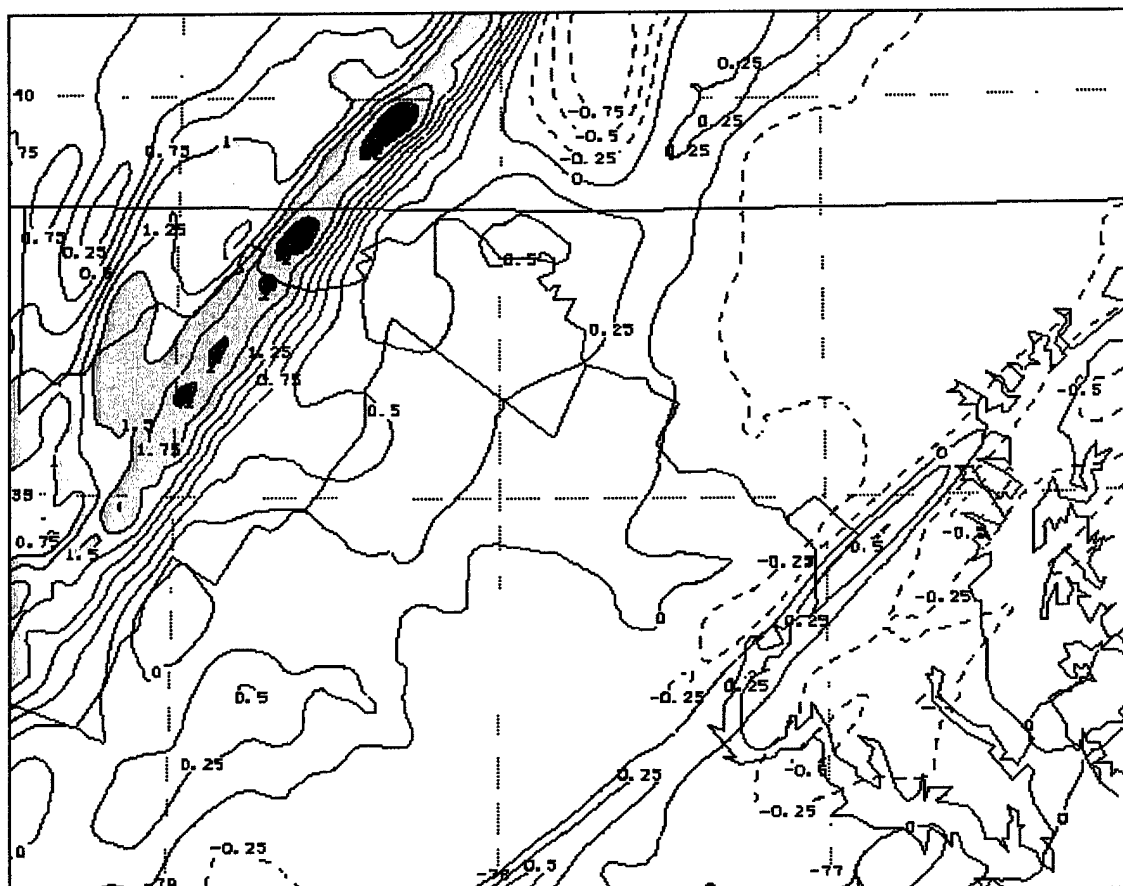
Figure 34. Simulated 15-min pressure tendency (hPa/.25 hr) valid 1715 UTC 28 Dec 1988.
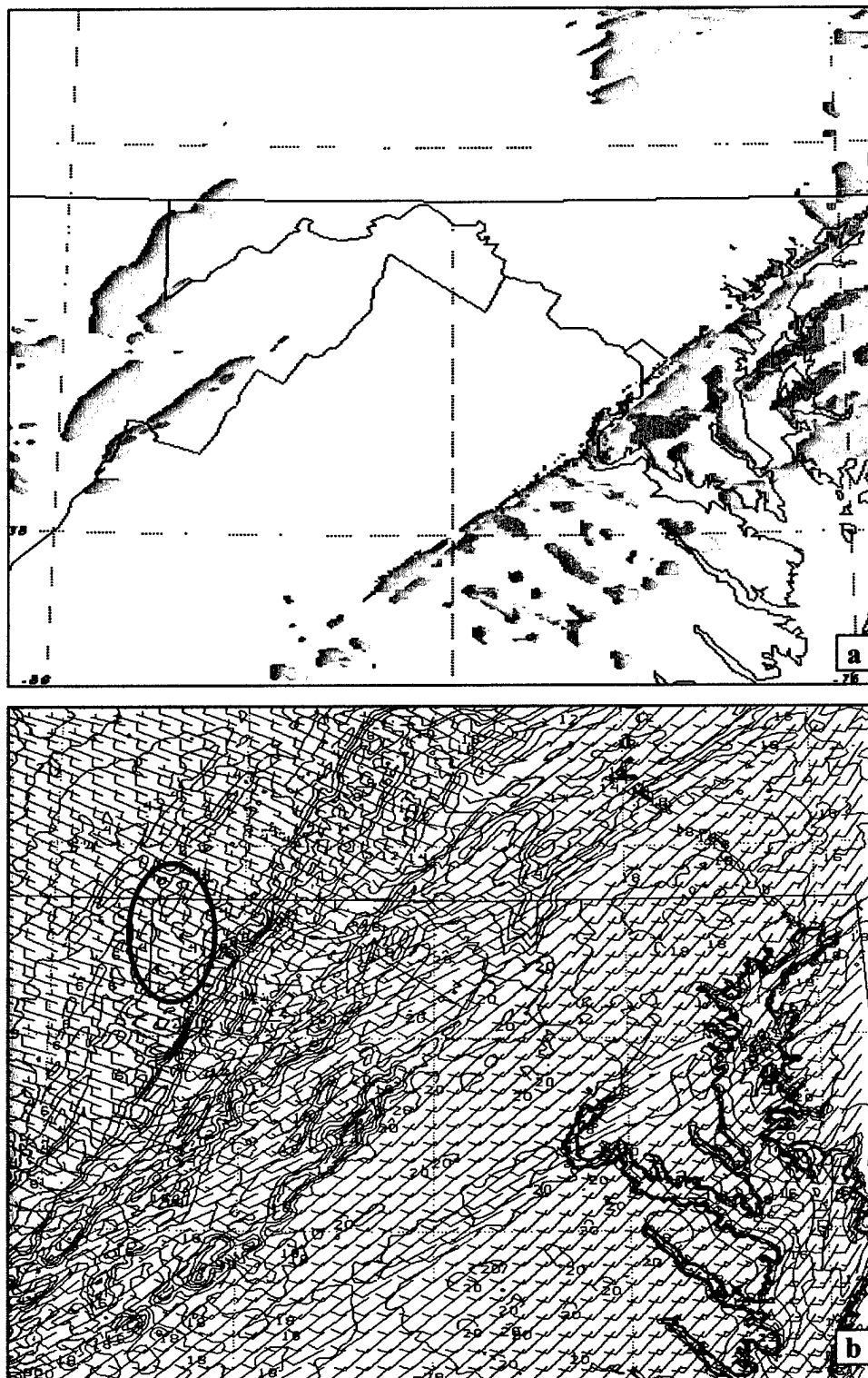
Figure 35. (a) Simulated precipitation (mm/hr) valid 1730 UTC 28 Dec 1988 and (b) simulated surface temperature (^{0}C) and wind (ms^{-1}) valid 1730 UTC 28 Dec 1988. The 4 ^{0}C cool pool is encircled.

197
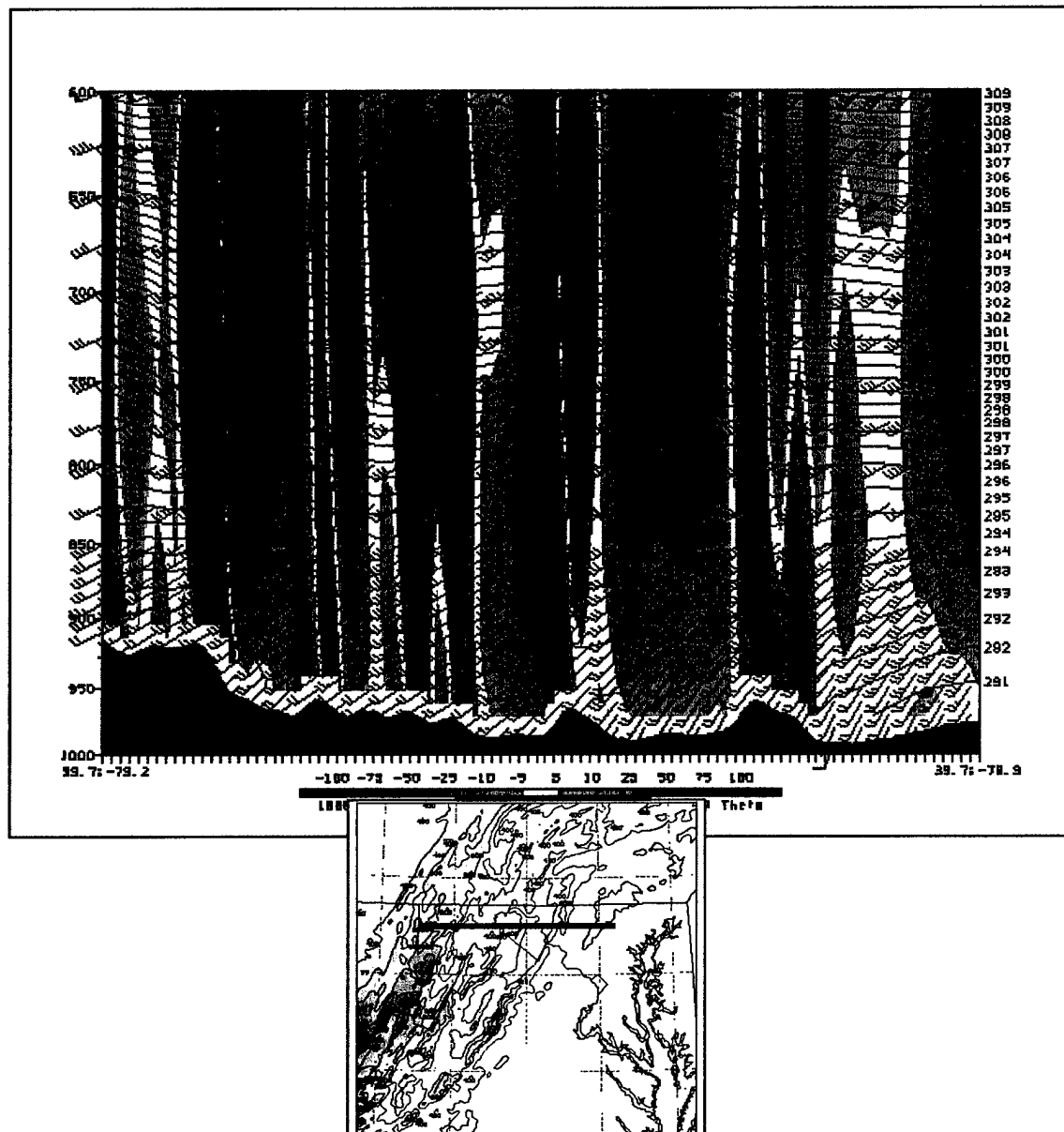
Figure 36. Simulated cross section depicting wind (ms^{-1}), potential temperature (K), vertical velocity (cms^{-1}), and terrain. Valid 1615 UTC 28 Dec 1988. Inset depicts horizontal domain of cross section.
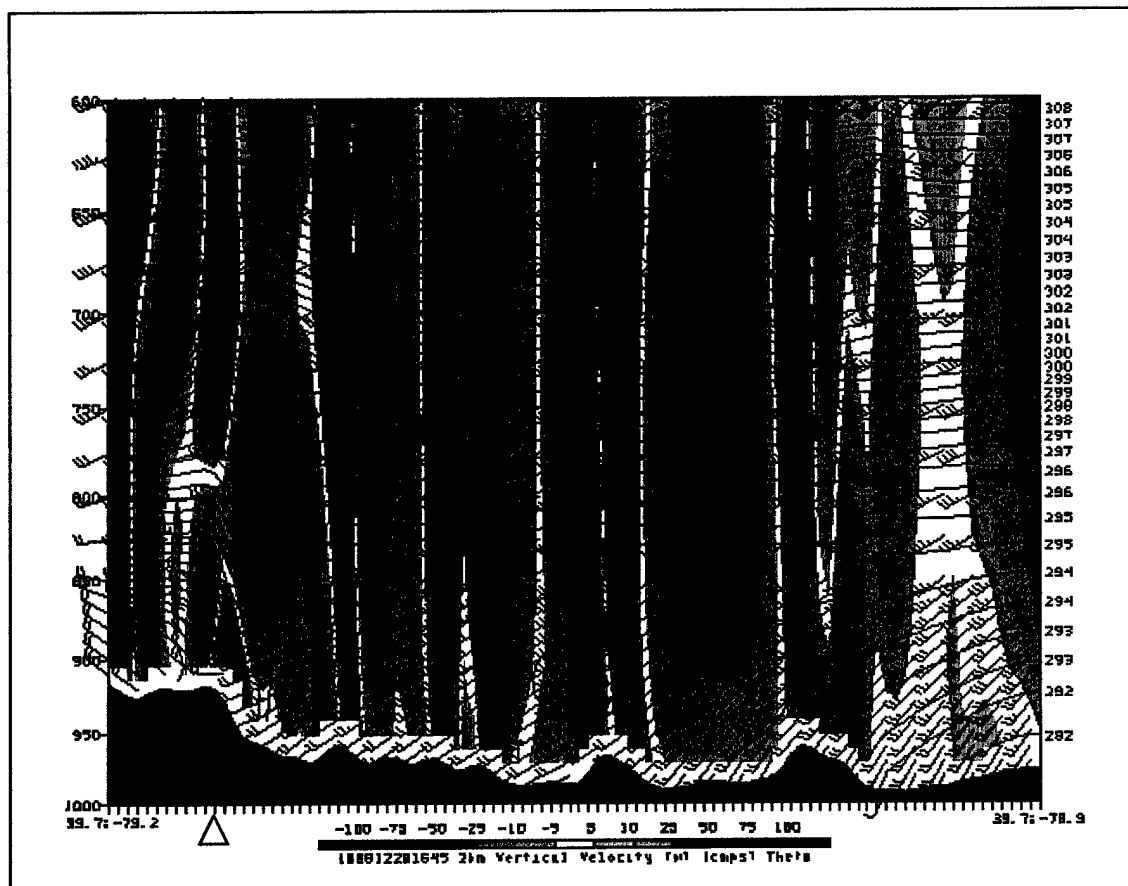
Figure 37. Simulated cross section depicting wind (ms^{-1}), potential temperature (K), vertical velocity (cms^{-1}), and terrain. Valid 1645 UTC 28 Dec 1988. Frontal position denoted by triangle. Cross section located as depicted in Fig. 36.
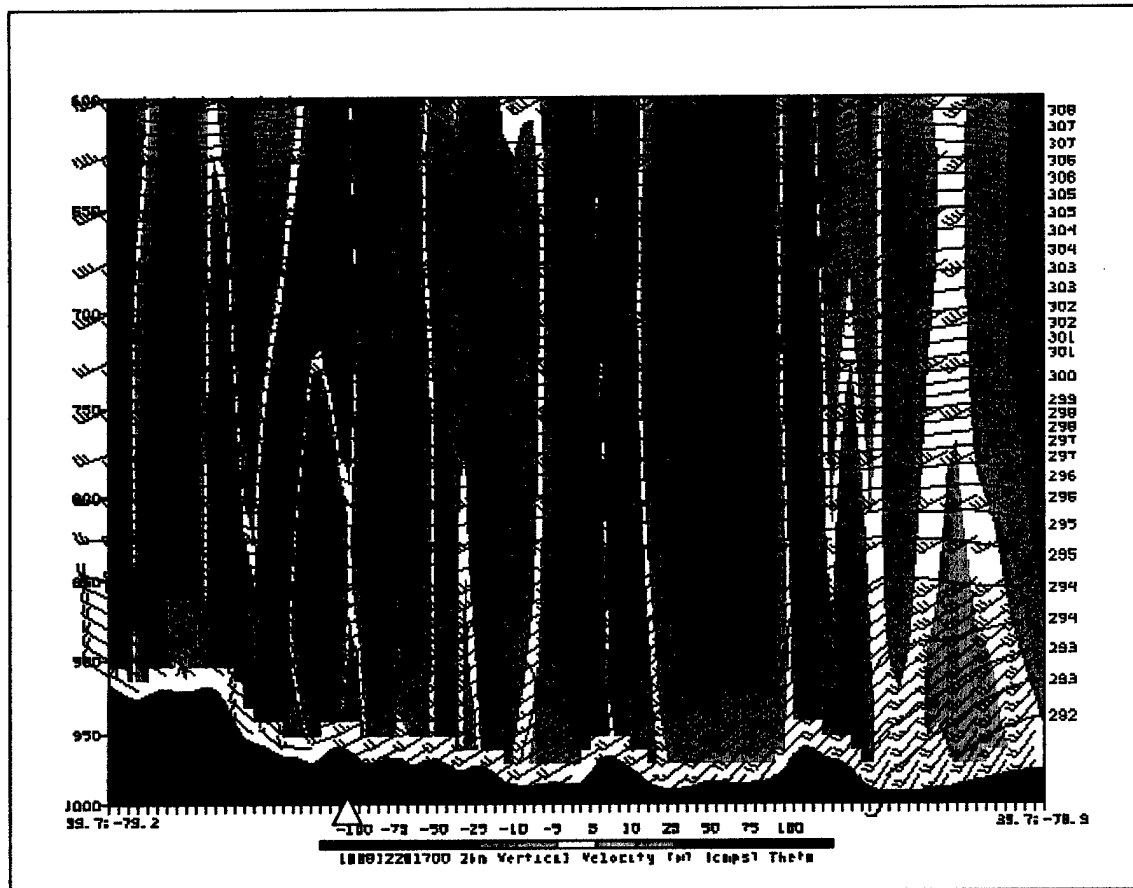
Figure 38. Simulated cross section depicting wind (ms^{-1}), potential temperature (^{0}K), vertical velocity (cms^{-1}), and terrain. Valid 1700 UTC 28 Dec 1988. Frontal position denoted by triangle. Cross section located as depicted in Fig. 36.
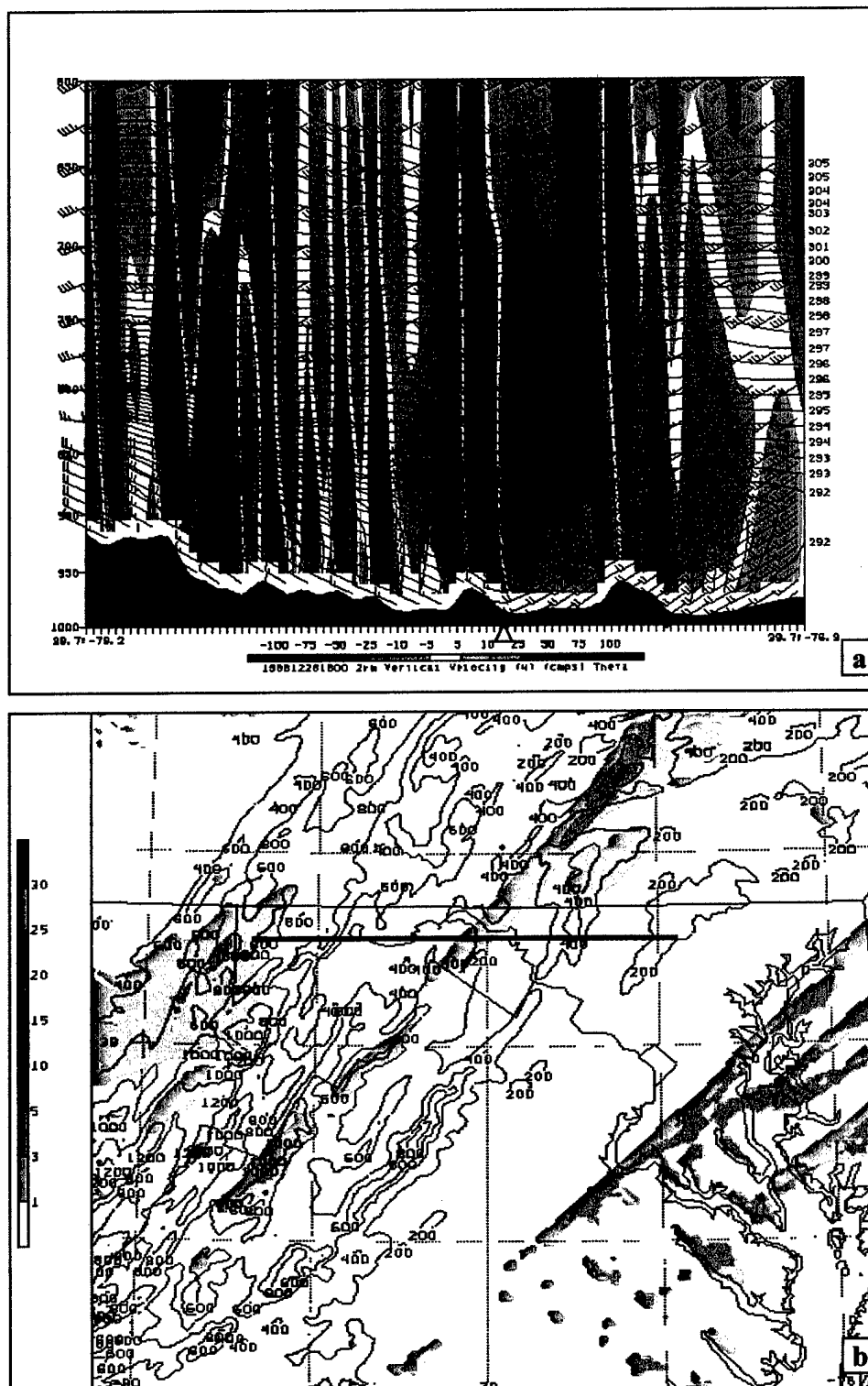
Figure 39. (a) Simulated cross section depicting wind (ms⁻¹), potential temperature (K), vertical velocity (cms⁻¹), and terrain. Frontal position denoted by triangle, (b) Simulated precipitation (mm/hr) and terrain elevation (m). Location of cross section denoted by heavy black line. Both plots Valid 1800 UTC 28 Dec 1988.

201
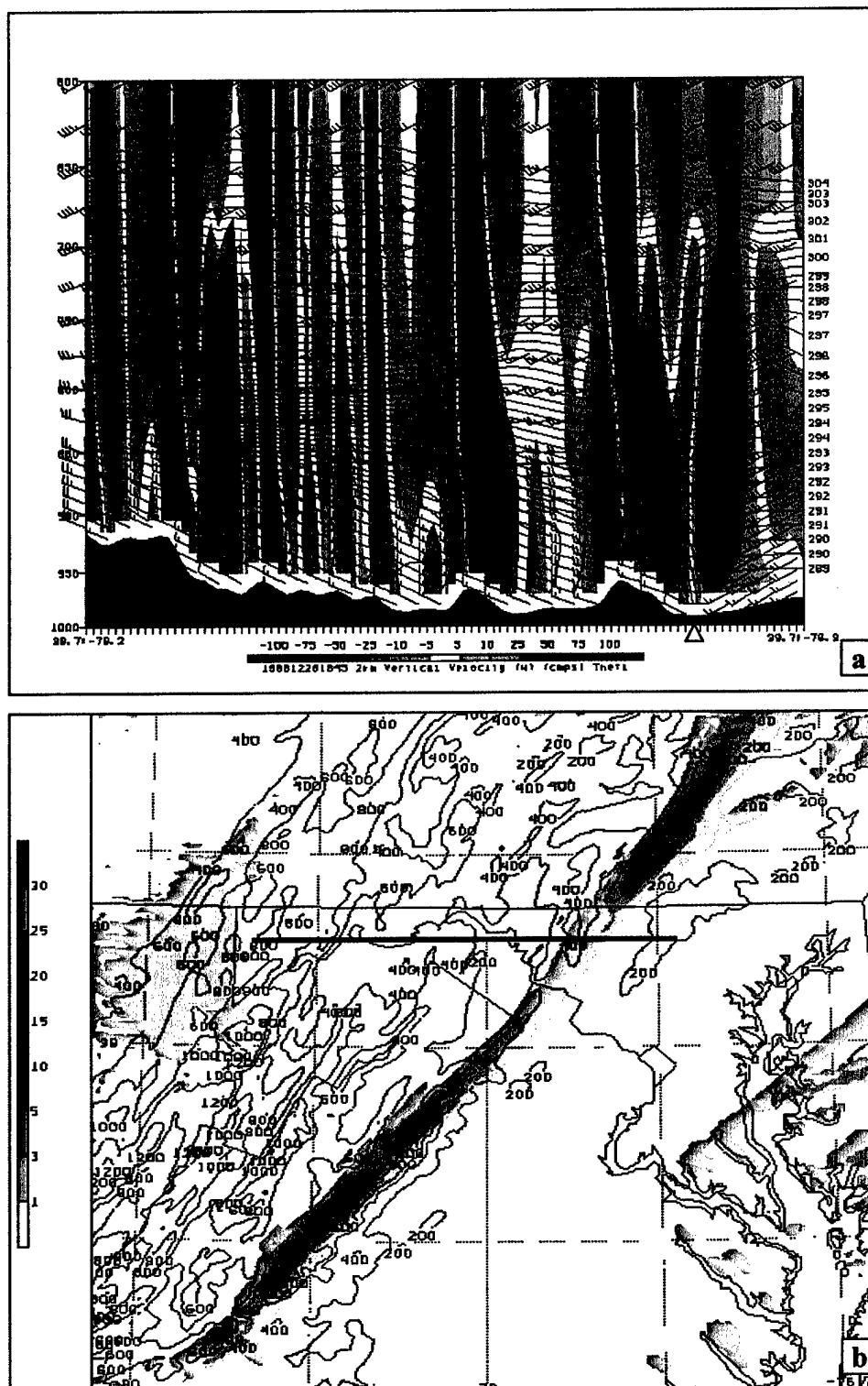
Figure 40. (a) Simulated cross section depicting wind (ms⁻¹), potential temperature (K), vertical velocity (cms⁻¹), and terrain. Frontal position denoted by triangle, (b) Simulated precipitation (mm/hr) and terrain elevation (m). Location of cross section denoted by heavy black line. Both plots Valid 1845 UTC 28 Dec 1988.
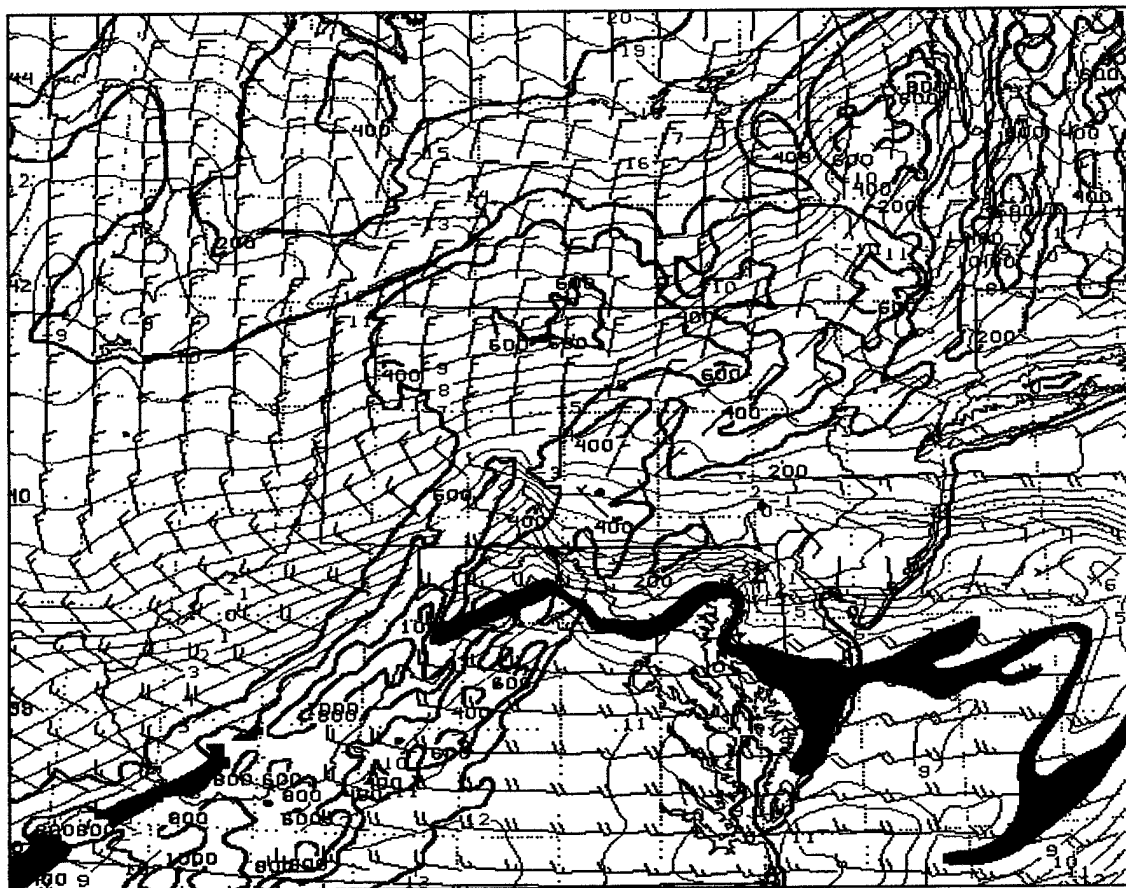
Figure 41. Simulated 940 hPa temperature (^{0}C) and surface terrain height (m) valid 1700 UTC 13 Jan 2000. The 7 ^{0}C isotherm is highlighted.
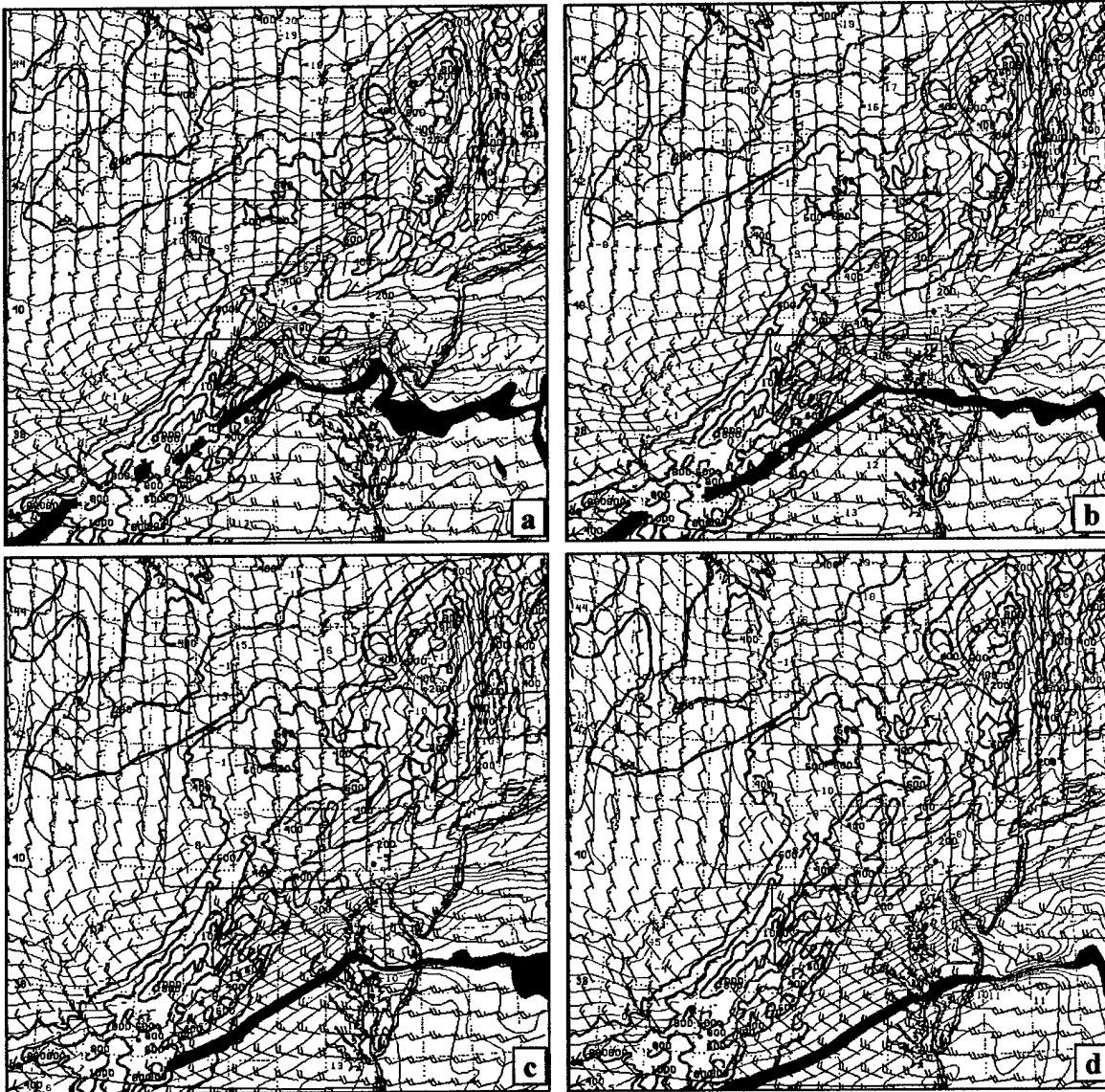
Figure 42. Simulated 940 hPa temperature (^{0}C) and surface terrain height (m). The 7 ^{0}C isotherm is highlighted. Valid 13 Jan 2000 (a) 1800 UTC, (b) 1900 UTC, (c) 2000 UTC, (d) 2100 UTC.

Figure 43. Simulated surface wind (ms^{-1}) and PMSL (hPa) valid 2000 UTC 13 Jan 2000.
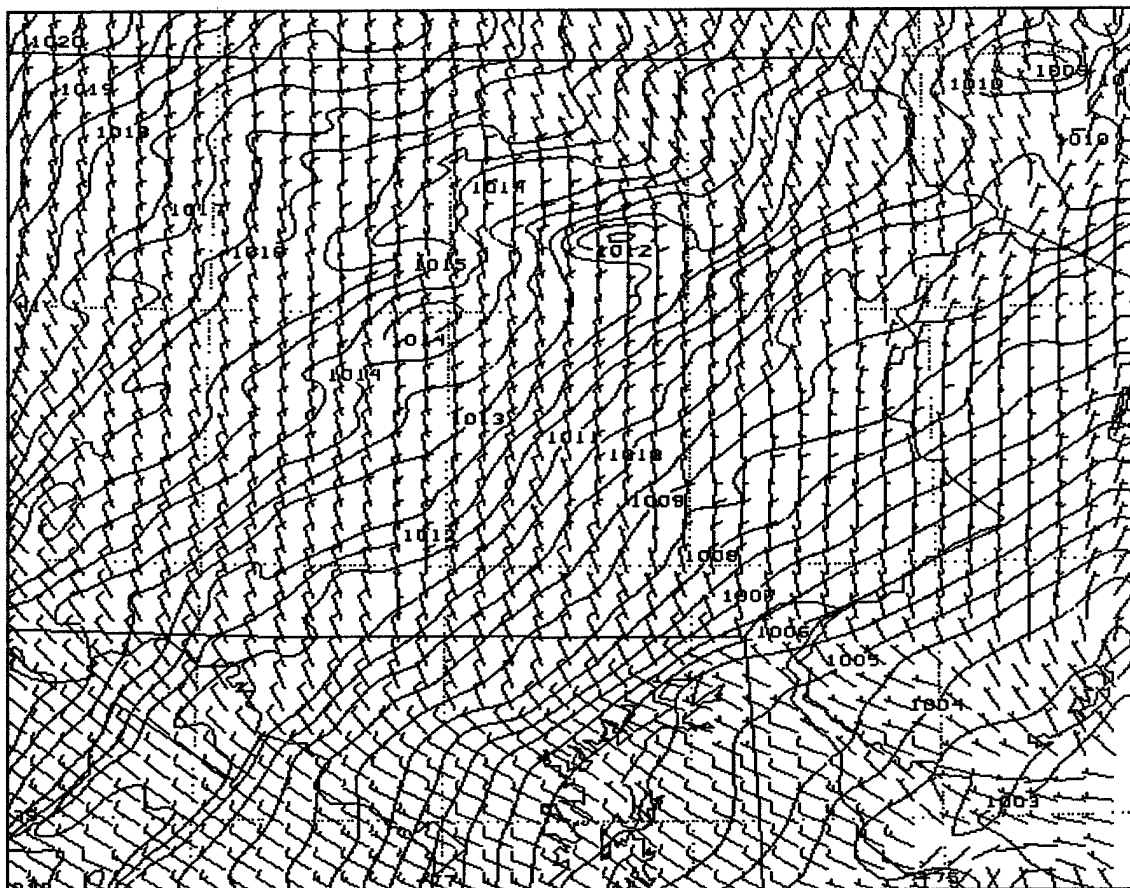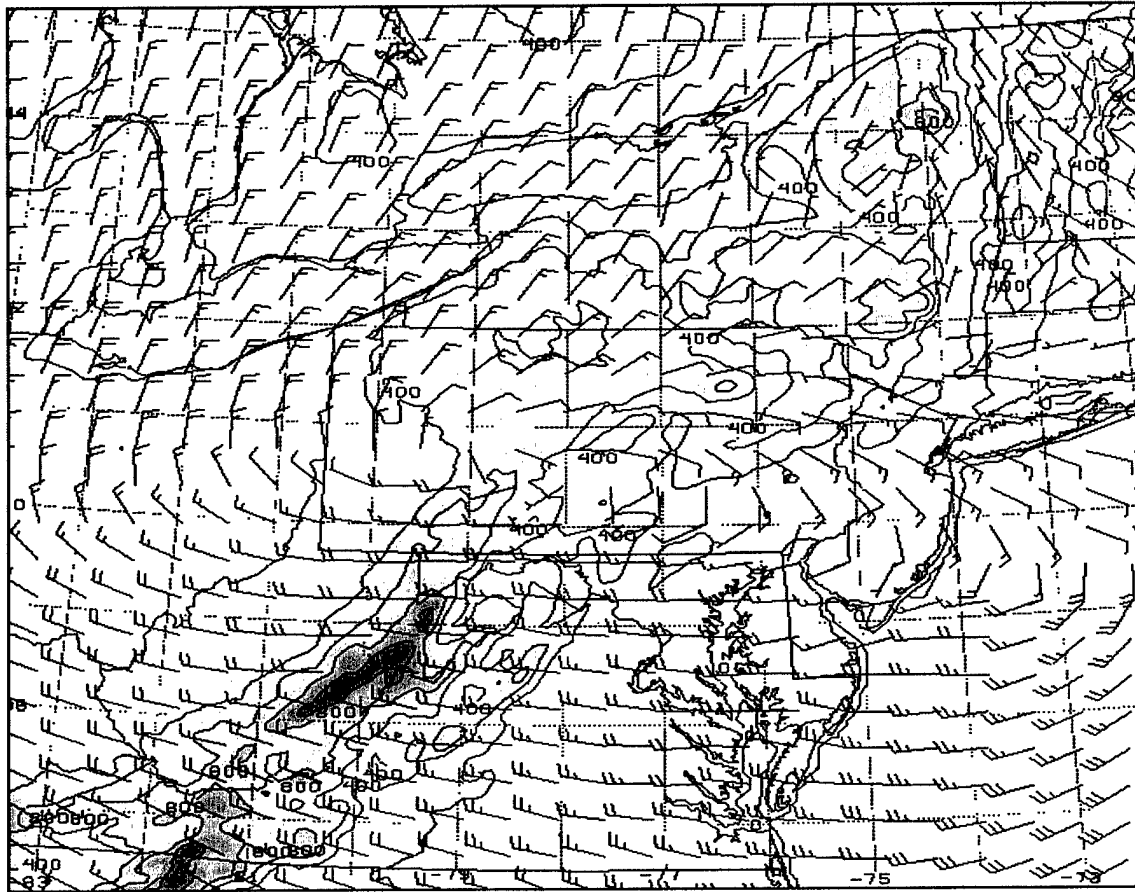
Figure 44. Simulated 900 hPa wind (ms^{-1}) and terrain elevation (m). Valid 1500 UTC 13 Jan 2000.
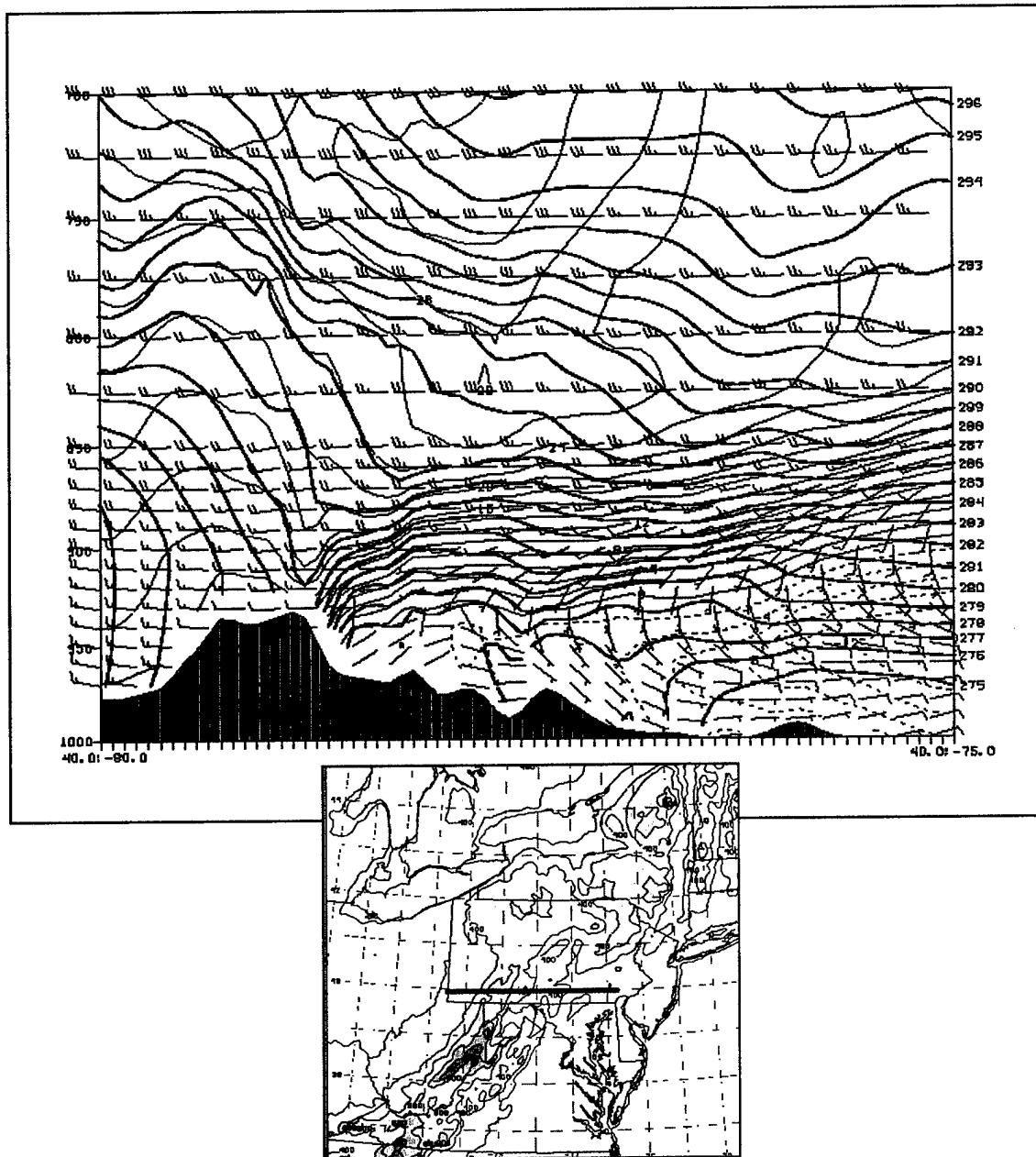
Figure 45. Simulated cross section along 40 °N latitude valid 1500 UTC 13 Jan 2000. Dark, thick lines depict potential temperature (K), thin lines are isotachs (ms⁻¹) with solid contours indicating westerly flow and dashed contours indicating easterly (upslope) flow. Grey shading indicates region upslope flow.
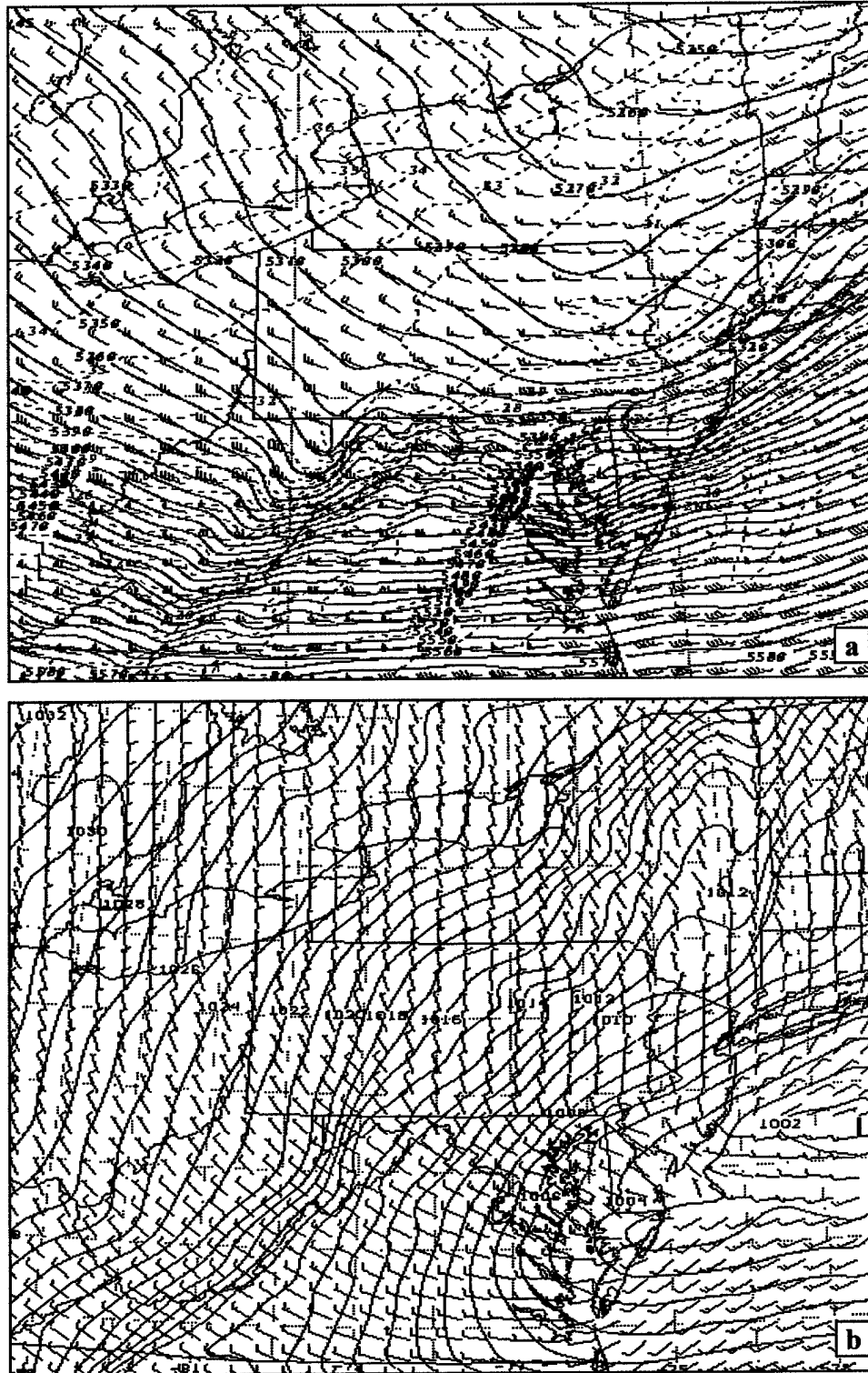
Figure 46. (a) Simulated 500 hPa heights (m) and wind (ms⁻¹) valid 2000 UTC 13 Jan 2000, (b) Simulated PMSL (hPa) and wind (ms⁻¹) valid 2000 UTC 13 Jan 2000.
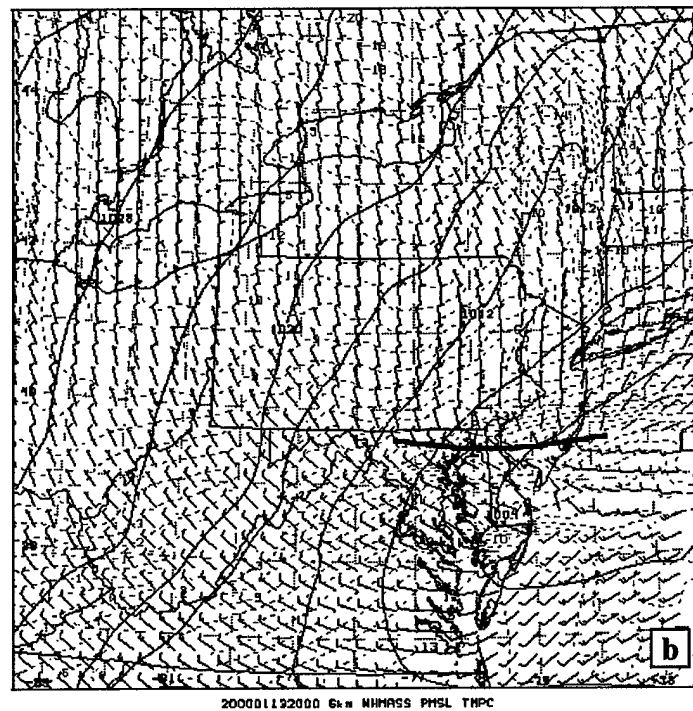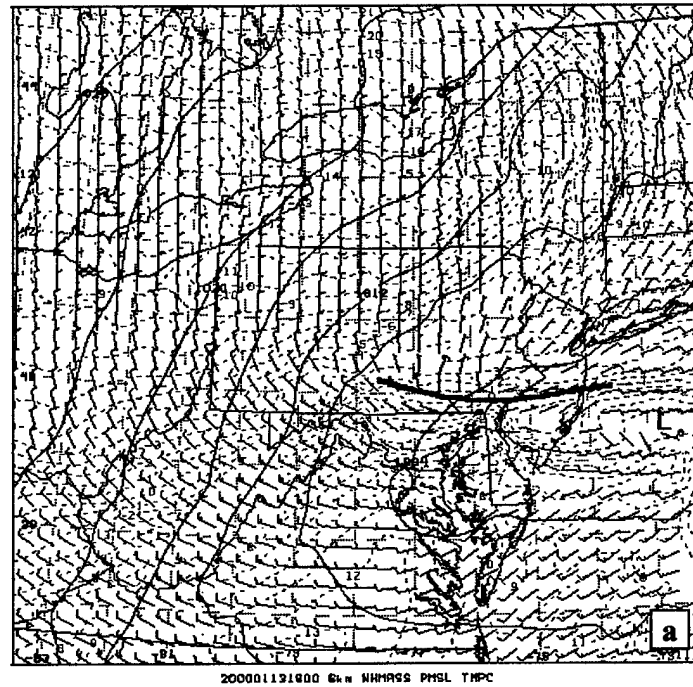
Figure 47. Simulated surface PMSL, wind (ms^{-1}), and
temperature (^{0}C) valid (a) 1800 UTC 13 Jan 2000 and
(b) 2000 UTC 13 Jan 2000. Low-level cold surge identified
by bold line.

209
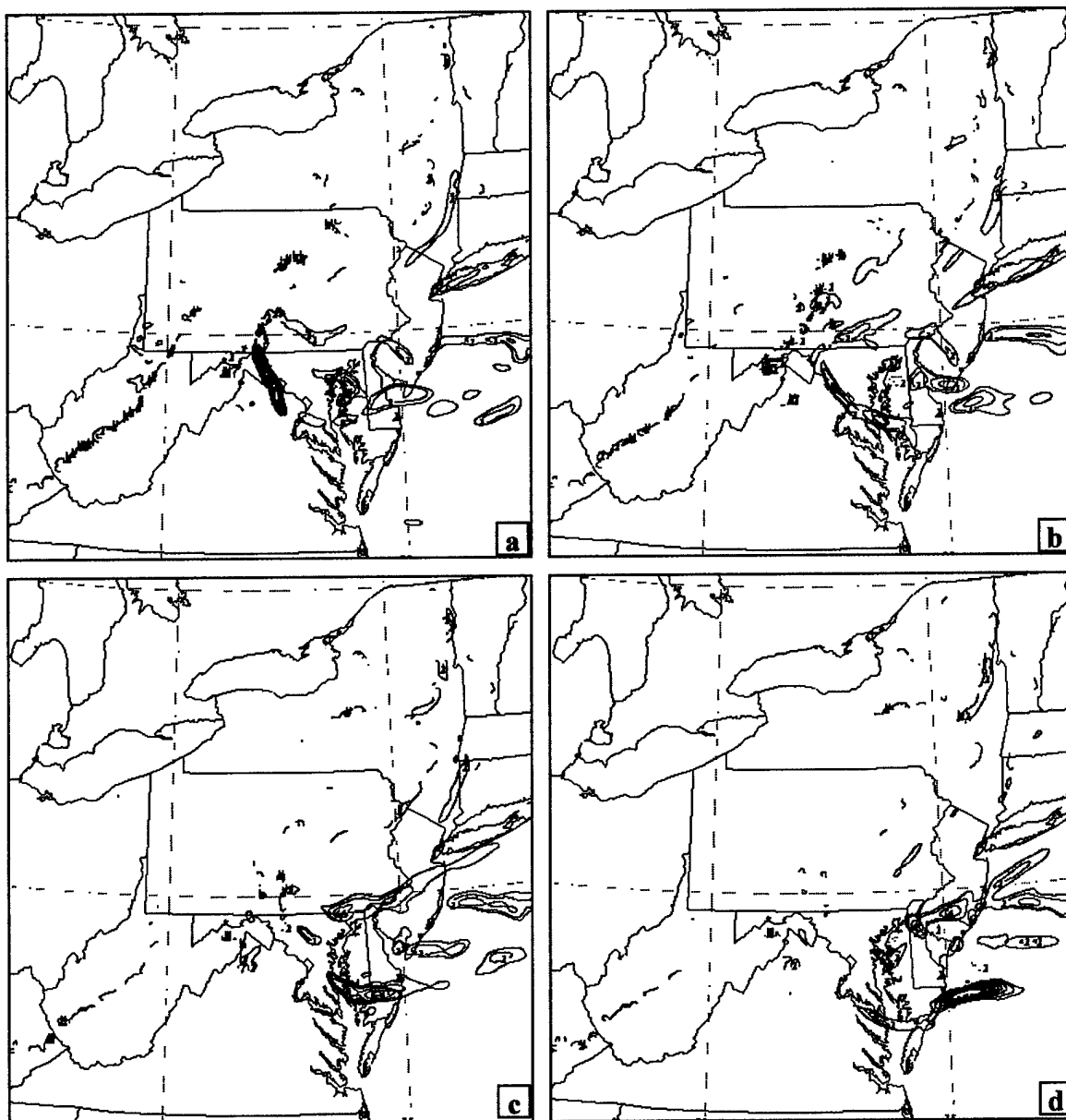
Figure 48. Simulated surface 2-d frontogenesis (^{0}C/100km/3h) valid 13 Jan 2000 (a) 1730 UTC, (b) 1830 UTC, (c) 1930 UTC, (d) 2030 UTC.
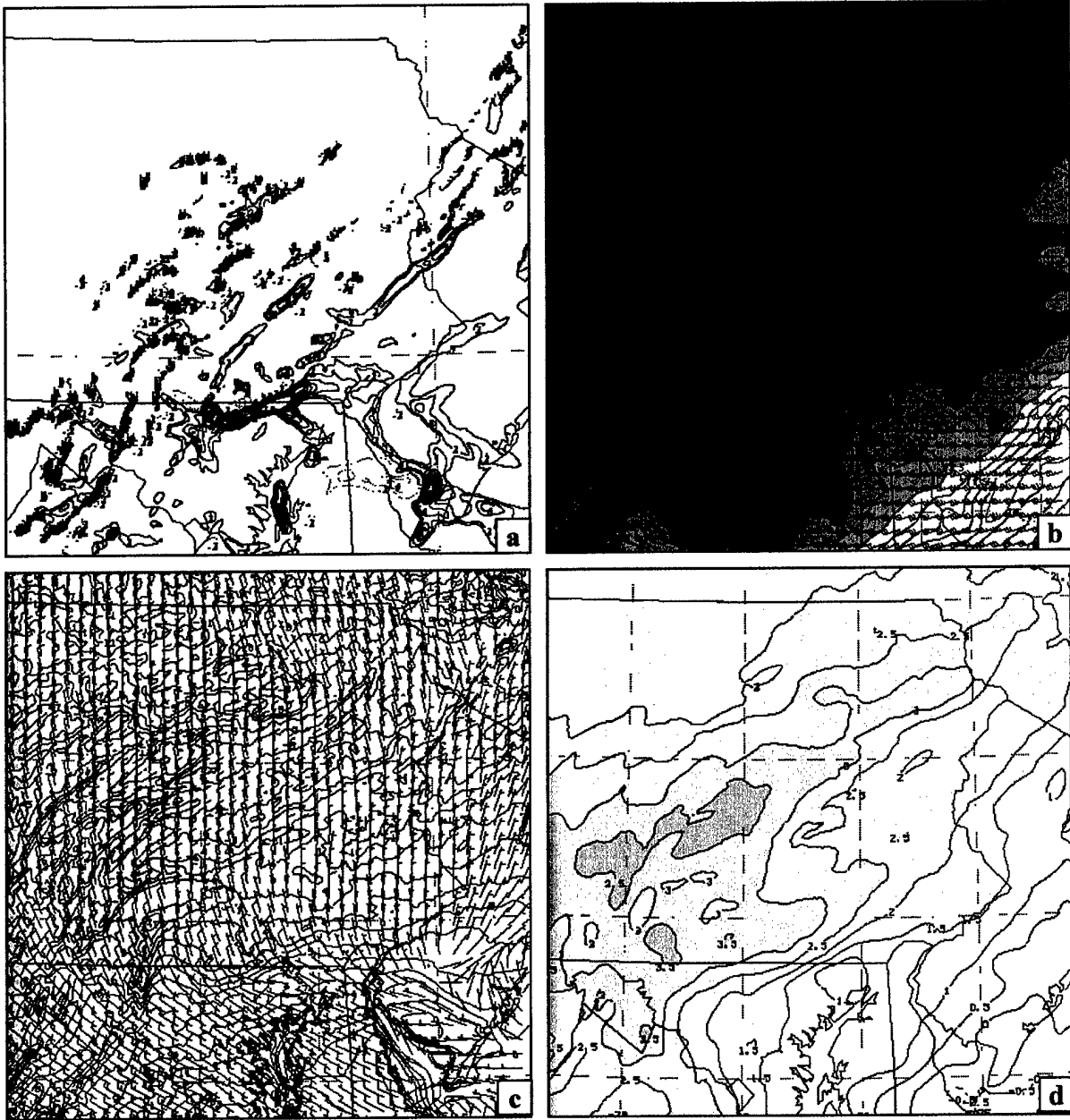
Figure 49. (a-d) Valid 1930 UTC 13 Jan 2000. Simulated (a) 2-d surface frontogenesis (^{0}C/100km/3h), (b) 700 hPa temperature (^{0}C), (c) surface temperature (^{0}C) and wind (ms^{-1}), (d) hourly pressure change (hPa/hr).
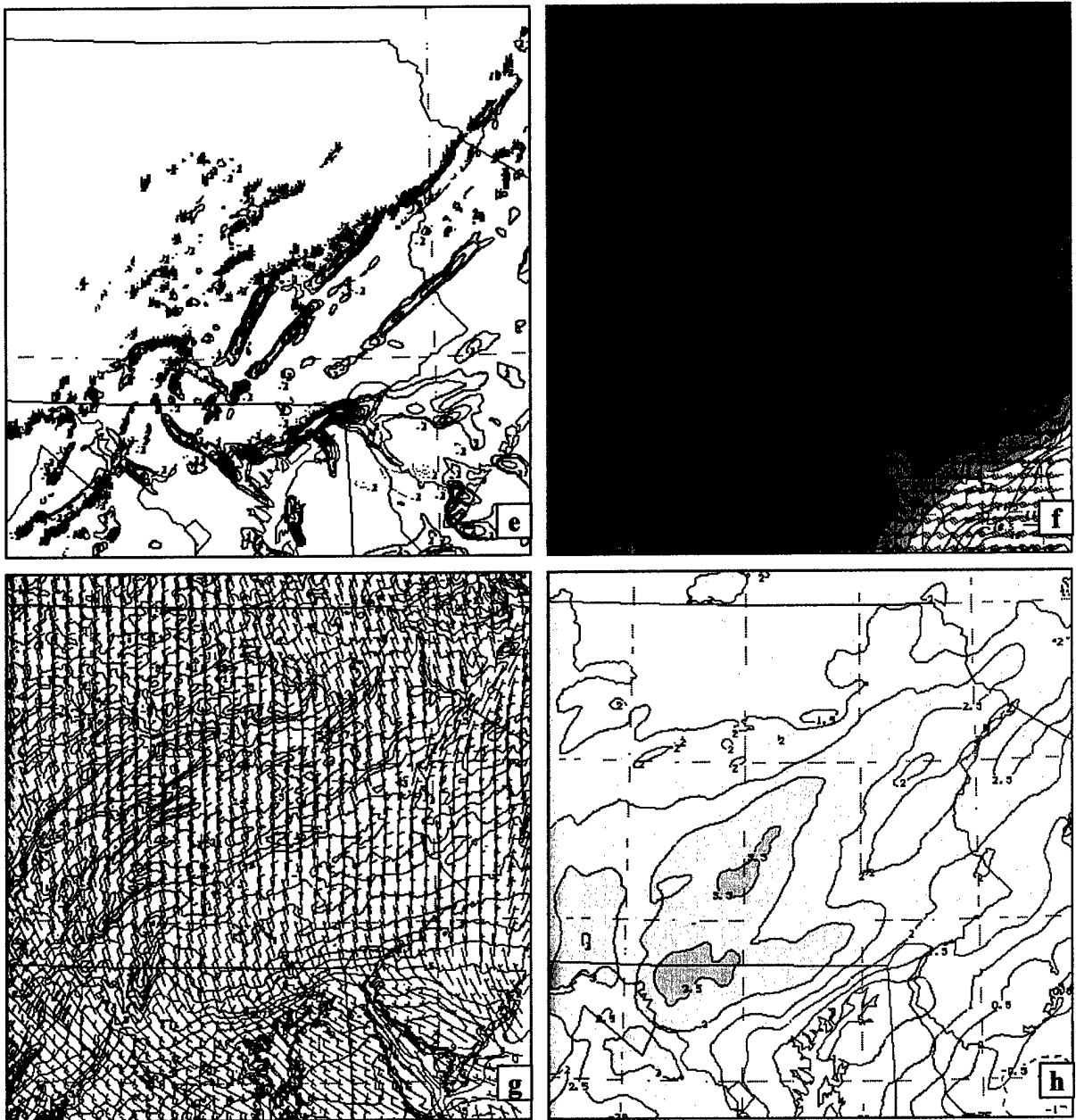
Figure 49 concluded. (e-h) Valid 2000 UTC 13 Jan 2000. Simulated (e) 2-d surface frontogenesis (^{0}C/100km/3h), (f) 700 hPa temperature (^{0}C), (g) surface temperature (^{0}C) and wind (ms^{-1}), (h) hourly pressure change (hPa/hr).

212
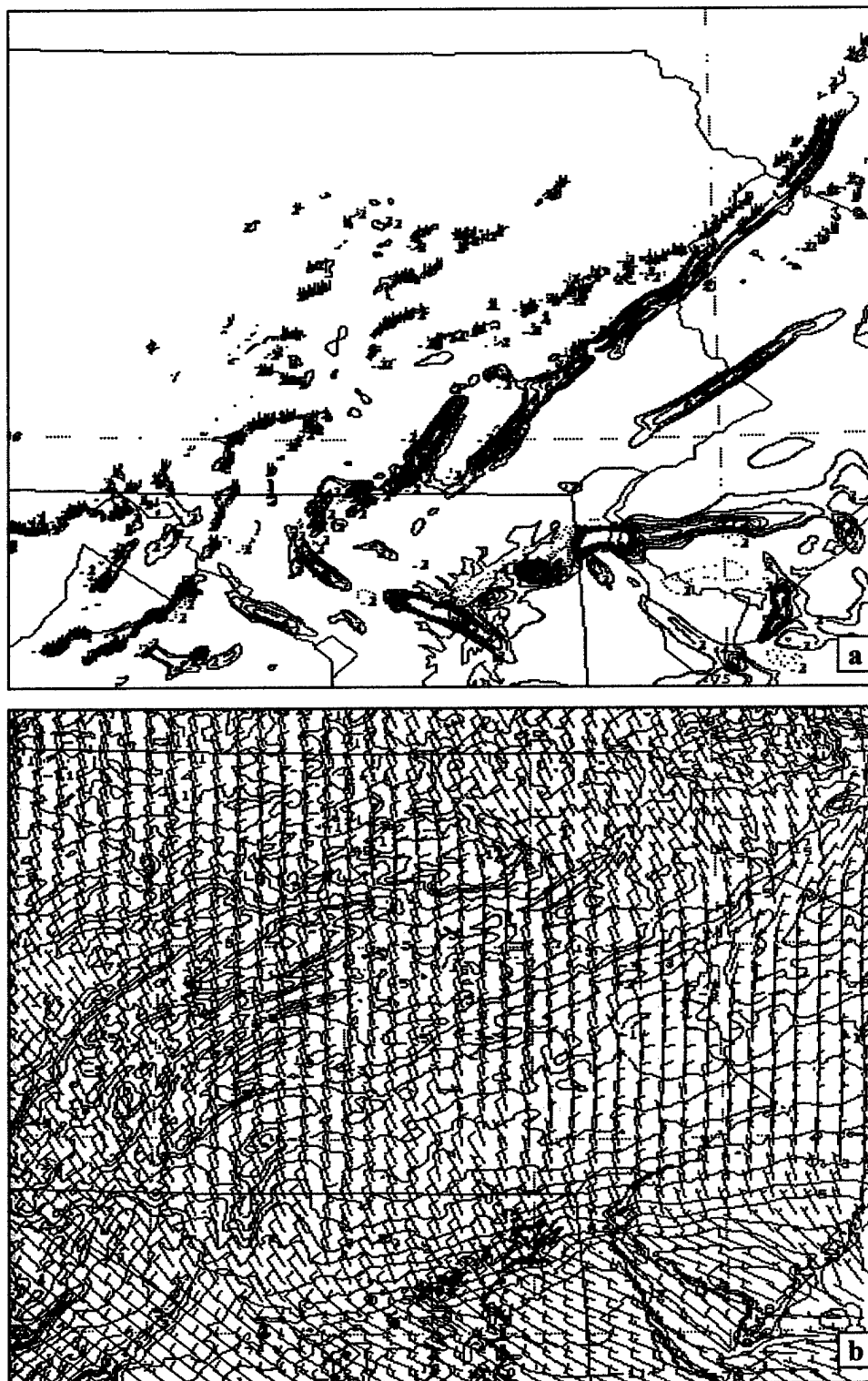
Figure 50. (a) Simulated 2-d surface frontogenesis (^{0}C/100km/3h) valid
2030 UTC 13 Jan 2000, (b) surface temperature (^{0}C) and wind (ms^{-1}).
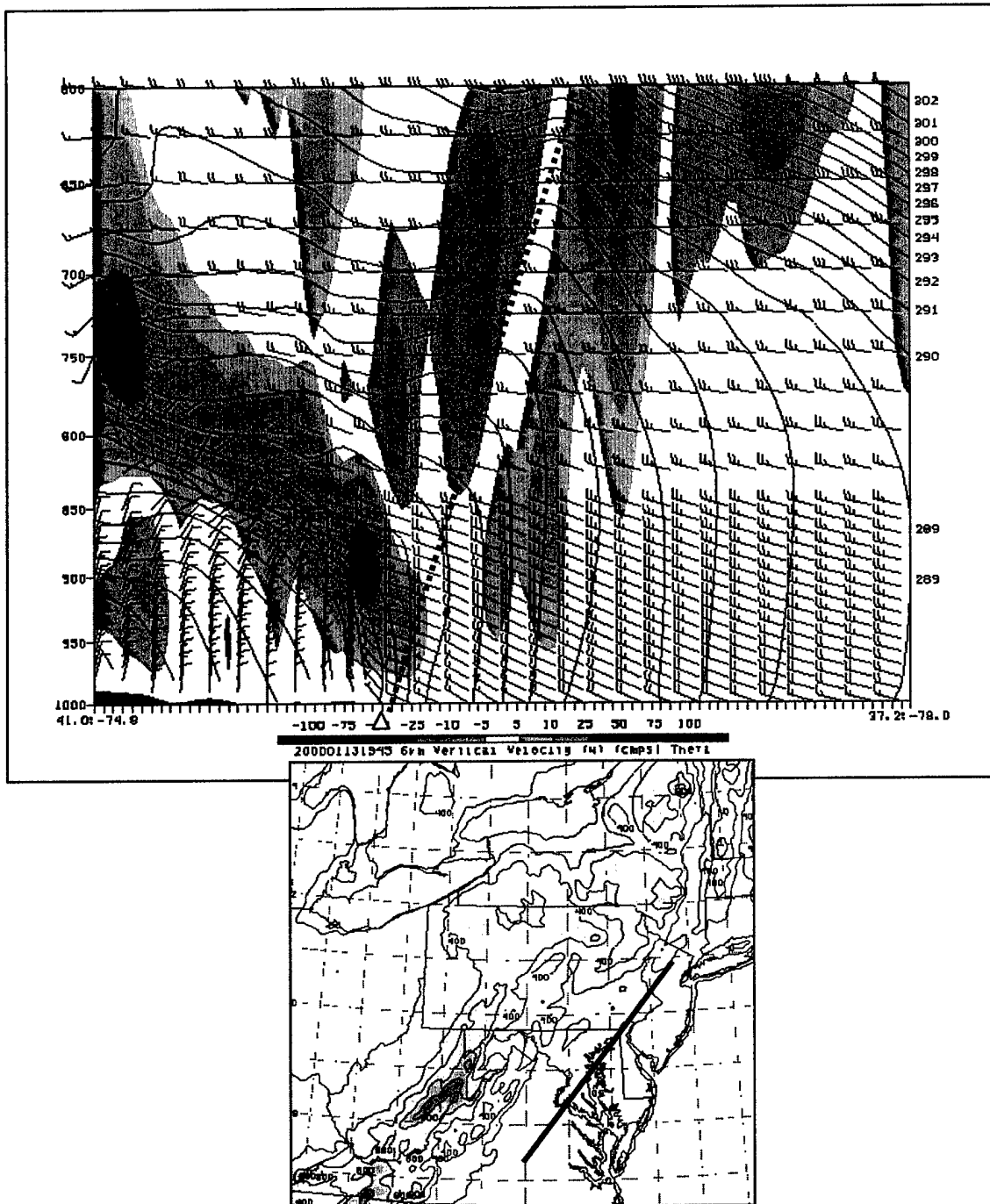
Figure 51. Simulated cross section depicting potential temperature (K), wind (ms^{-1}), and vertical velocity (cms^{-1}). Blue shading indicates upward vertical motion and red shading indicates downward. Cross section location denoted by solid line in inset. Valid 1945 UTC 13 Jan 2000.

214

CHAPTER 4

MESOSCALE SIMULATIONS OF DYNAMICS AND STRUCTURE FOR TWO DIFFERING LOW-LEVEL TURBULENCE EVENTS EAST OF THE APPALACHIAN MOUNTAINS. PART III: CONVECTIVE INDUCED TURBULENCE

4.1 Introduction

Atmospheric turbulence is the leading cause of non-fatal accidents to airline passengers and flight attendants. Low-level turbulence is of particular concern as aircraft take-off and landing are considered the most dangerous stages of flight and there is much less room to react or compensate for unexpected turbulent motions. Accurate forecasts of moderate or greater turbulence would significantly benefit the aviation field. Unfortunately, the very fine scale nature of turbulence combined with the rather coarse observational network make this difficult. Precursors at the large scale must be identified and related to the various scale-interactive processes leading to the turbulence in order to adequately identify regions prone to this dangerous phenomenon. A thorough review detailing the numerous explanations and expected locations for turbulence is provided in Chapter 1 and a brief description in Chapter 2.

Recently, Kaplan et al. (2003a,b) utilized 40 accident reports and four in-depth severe turbulence case studies to determine that turbulence should be forecast in regions with the following synoptic signatures: jet stream entrance region, upstream curvature, cold advection, and nearby convection. Their study focused primarily on upper-level turbulence where effects of terrain are typically minimal. Terrain effects can be significant—as described in previous chapters. As shown in both Chapter 2 and Chapter 3, the effects of terrain at the larger scale can impact subsequent atmospheric response downscale. And these

215

responses can ultimately lead to severe turbulence.

In this research, two cases of low-level turbulence (between 800 and 700 hPa) east of the Appalachian Mountains are investigated. The first case occurred on 28 Dec 1988 and has been investigated previously in the literature as an event where a strong narrow cold frontal rainband (NCFR) formed east of the Appalachian Mountains (Koch and Kocin 1991, henceforth KK91; Chen et al., 1997). The amount of low-level turbulence associated with this event was significant, but the majority of reports were of moderate or lighter intensity. The second case investigated occurred on 13 Jan 2000 in the same region. This event also involved a multitude of low-level turbulence reports, but the vast majority of reports were categorized as severe.

The large-scale (synoptic and meso-α) patterns as well as similarities and differences between these cases were detailed in Chapter 2. Both events occurred during the winter at the same time of day (17-20 UTC) and at similar altitudes (2000-2400m). Surface analyses were similar—both cases featured a cold front along the Appalachian Mountains that moved through the region of reported turbulence between 1700 and 2100 UTC. Additionally, both cases possess many of the large-scale precursors detailed in Kaplan et al. (2003a,b,c) as favorable for turbulence formation (i.e., nearby jet entrance region, upstream curvature, strong cold advection, and nearby convection). In addition to these similarities, some key large-scale differences were identified.

The 28 Dec 1988 (D88) and 13 Jan 2000 (J00) events exhibit different large-scale wave patterns. D88 has a meridional pattern with ridging over the East Coast while J00 is more zonal with a blocking vortex over Quebec and a distinct southern stream which combine to enhance convergence east of the Appalachian Mountains. In addition, flow in

216

D88 is less orthogonal to the terrain in advance of the cold front and is essentially uni-directional at all levels (i.e., less helical). Flow for J00 is more perpendicular to terrain and multi-directional in the vertical. Differences in jet-front structure in the 72 hours prior to the turbulence events and the impact these have on the low-level environment downstream of the Appalachians were also detailed in Chapter 2.

The presence of a subtropical jet (STJ) and its associated transverse ageostrophic circulations distinguishes J00 from D88 and ultimately plays an important role in the advection of low-level warm air (as well as IPV) along and east of the Appalachian Mountains. The interaction between the STJ and PJ (and their concomitant ageostrophic circulations) prior to the 13 Jan 2000 event enabled warm air from the Mexican Plateau to advect east and northeast where it was situated over the colder surface air east of the Allegheny Mountains in south central Pennsylvania, thereby increasing the static stability, effecting the blocking of the J00 cold front, and increasing the subsequent strength of the downstream isentropic upfold elemental to the low-level frontogenesis, convection, and turbulence as described in the hypothesis presented in Chapter 3.

The first five stages of the following hypothesis were examined in detail in the previous chapter. It is hypothesized that the orography of the East Coast of the United States in combination with identifiable meteorological signals of decreasing scale can combine in the following, logical scenario resulting in convection and the generation of severe low-level turbulence:

(1) Strong flow orthogonal to the Appalachian Mountains results in large-amplitude hydrostatic mountain wave formation.

(2) Mountain-wave induced vertical motions produce a downstream isentropic upfold

(mid-level cold pool) oriented northeast to southwest as a reflection of the Allegheny Mountains. This cold pool is deformed by the large-scale background jet and its concomitant ageostrophic motions (to include an indirect circulation that enhances frontogenesis). This process (detailed in Chapter 3) is similar to that described by Kaplan and Karyampudi (1992a) except applied on the Appalachian Mountains.

(3) Intensification of the cold pool aloft and mass flux convergence results in a leeside pressure ridge and a building edgewave that propagates to the south-southeast in a manner previously described by Tilley (1990) and Colle and Mass (1995). This hybrid Kelvin wave-like response results in increased surface convergence and frontogenesis as the front at the surface becomes oriented ENE-WSW.

(4) Leeside warming due to downslope adiabatic effects results in a temperature ridge (leeside trough) east of the Appalachians.

(5) These features (leeside trough, cold pool aloft, surface cold surge) coalesce to form a system somewhat similar to a cold occlusion and results in a lapse rate much greater than moist adiabatic as cold air resides over low-level warm air in a region of tightening surface temperature (and pressure) gradient and convergence east of the Appalachian Mountains.

(6) This combination in the vertical results in convection, cold downdrafts, formation of a density current-like feature, and ultimately breaking vortices. These microscale features are believed to result in a helicity-rich low-level environment highly predisposed to strong low-level turbulence near their level of interaction (i.e., 800 – 700 hPa).

The synoptic and meso-α signals and precursors were identified and a comparison between the two cases studied in this research was made in Chapter 2 in an effort to identify

218

the larger, identifiable signals prior to turbulence formation east of the Appalachians. Chapter 3 bridged the transition from the meso-α to meso-β signals detailed in the first five stages of the presented hypothesis. The degree of conformity and validity of the hypothesis were investigated. The focus in the previous chapter was on the atmospheric response to and the impact of the meso-α and meso-β scale differences in cold frontal propagation, hydrostatic mountain wave formation, isentropic upfold (mid-level cold pool) generation and deformation, and the surface response leading to convection in two cases of differing low-level turbulence intensity east of the Appalachian Mountains. As the feature scale contracts, the similarities between the two cases diminish and differences become more apparent. These differences have a direct effect on the subsequent atmospheric response along and downstream of the Appalachian Mountains.

Early differences in jet-front structure (primarily the existence of a subtropical jet in J00) resulted in different low-level temperature structures east of the Appalachians prior to cold frontal passage. An elevated warm layer (advected from the Mexican Plateau) helped set up a strong inversion on the leeside of the Alleghenies in J00 and resulted in blocking of the windward front and deflection of the low-level flow around the Alleghenies and aloft downstream. No such inversion was present for D88 and frontal propagation is essentially unimpeded. Internal Froude number computations (see previous chapter) indicated that as the cold front approached the mountains, flow in D88 was in the supercritical to partially-blocked regime. On the other hand, cold frontal propagation in J00 was retarded as it traversed the terrain (prior to 13/1700 UTC) and internal Froude number computations placed this case near the junction of the subcritical, completely-blocked, to partially-blocked regime as described in Simpson (1997). Additionally, the strength of the hydrostatic

219

mountain waves formed and the resultant downstream isentropic upfolds generated in these two events are significantly different.

Hydrostatic mountain waves were observed for both cases and investigated in detail in Chapter 3. The stronger cross-mountain flow in J00 resulted in a more vigorous mountain wave and a more substantial upslope upfold, downslope downfold, and downstream isentropic upfold (mid-level cold pool). Additionally, the strong downstream inversion in J00 combined with the stronger hydrostatic mountain wave results in a more significant (700 hPa) cold pool in J00 than in D88.

As shown in Chapter 3, the stronger downstream mid-level cold pool in J00 resulted in a deep katafront structure and stronger, downstream surface pressure rises ahead of the large-scale jet-front system. This mid-level pool of cold air is deformed by the large-scale jet as it progresses eastward (above the terrain-slowed cold front) and results in a mid-level cold front in advance of the surface cold front. The mid-level cold pool in D88 is much weaker, is situated closer to the large-scale cold advection (and trough), and has no significant, distinct impact.

The strong mid-level cold pool in J00 ultimately results in surface pressure rises to the lee of the Alleghenies that are downstream from those associated with the large-scale system. The surface pressure increase and subsequent low-level mass increase east of the Alleghenies results in a low-level cold surge (Tilley 1991) that propagates to the south and east and tightens the surface temperature gradient upon converging with warm air from the south. This scenario, brought about by the terrain-induced isentropic upfold in addition to low-level cold air forced around the terrain, results in enhanced convergence, frontogenesis, reduced stability, and cellular convection near the Pennsylvania-Maryland border as the

220

surface cold surge, warm tongue, and mid-level cold pool merge in space and time. No such north to south surface cold surge is evident in D88 as surface pressure rises in that event are tied to the large-scale (west to east moving) surface cold front and PJ-entrance region circulations (and tropopause fold), behind the primary cold front (i.e., not downstream). The convection pattern in D88 is lineal (as opposed to cellular in J00) and is essentially coupled with the larger-scale jet-front forcing. As discussed in the previous chapter, terrain forcing (at the low levels) enhances convergence in D88, but does not play a dominant, distinct role as does the terrain-induced mid-level cold pool and resultant surface cold surge in J00.

This chapter will investigate the resultant convection for these two cases in more detail and will focus on stage 6 of the hypothesis presented earlier (i.e., convective initiation, frontal contraction, and turbulence). Both events investigated featured multiple low-level turbulence reports and, in agreement with the findings of Kaplan et al. (2003a,b,c), were in proximity to convection. Pilots avoid flying near convection whenever possible and the Federal Aviation Administration (FAA) provides guidelines for avoiding convectively-induced turbulence (CIT) (FAA 2000). Aircraft are supposed to avoid thunderstorms by 37 km in the horizontal and are to fly over convection by at least 305 m for every 5 ms^{-1} of cloud top wind speed. Of course, developing convection can be unpredictable and, as shown in Kaplan et al. (2003a), turbulence is often reported in the vicinity of convection. Additionally, it is not known whether the FAA guidelines (as stated) ensure turbulence avoidance in all cases (Lane et al. 2003). It seems certain that the presence of convection plays a significant role in the generation of turbulence for the two events studied in this research. In addition to the convection (and subsequent frontal contraction), vorticity effects (vertical and horizontal), vortex tube formation, and wave breaking will be analyzed in this

221

chapter in order to appropriately identify the smaller-scale signals likely responsible for the low-level turbulence present in these cases.

Several recent studies have indicated that non-linear flow contraction processes can focus enstrophy (i.e., three-dimensional vorticity-squared) into a specific region in space and time and produce a vortex tube (obstacle) potentially causing severe (and greater) turbulence to an aircraft traversing it (Kaplan et al. 2003c). Andreassen et al. (1998) used numerical simulations and Clark et al. (2000) used numerical simulations and observations to demonstrate the presence of vortex tubes and their possible interaction at the mesoscale to microscale as important elements in the organization of severe clear air and terrain-induced turbulence. Kaplan et al. (2003c) utilized numerical and idealized simulations to demonstrate a sequence of events culminating with the scale contraction of three-dimensional vorticity (at the meso-γ scale) along a tilted, convergent outflow jet and an upfolding isentropic surface that presumably resulted in CIT. They found that a sequence of events that focused maxima of kinematic forcing, frontogenesis, and minima in Richardson number in space and time with an upfolding isentropic surface and intense three-dimensional vorticity convergence most likely accompanied the turbulence events studied. These processes will be investigated in this chapter and a derived indicator (and comparison) of the turbulence for D88 and J00 will be presented.

The remainder of this chapter is organized as follows: Section 2 provides a brief summary of the numerical model utilized in this study. Section 3 describes the convective initiation and convection present in both cases. Section 4 presents an analysis of vorticity (both vertical and horizontal)—both at the meso-γ and microscale, and Section 5 provides details about the turbulent kinetic energy, wave breaking, and other possible signals of

turbulence as well as a potential index for determining probable regions and altitudes of low-level turbulence. Lastly, Section 6 summarizes the results.

4.2 Numerical Model Description

In order to increase the spatial (both horizontal and vertical) and temporal coverage necessary to adequately diagnose the multi-scale phenomena involved in the two low-level turbulence events studied in this research, a mesoscale model is utilized. The non-hydrostatic Mesoscale Analysis and Simulation System (NHMASS) model version 6.0 (Kaplan et al. 2000) produced the simulations used for this study. The numerical experiments, model specifics, grid resolution, and coverage are detailed in Chapter 2.

4.3 Convection and Convective Initiation

As described in the previous chapter, convection was present on both 28 Dec 1988 and 13 Jan 2000. The initiation of this convection as well as the geometry, coverage, and intensity were substantially different for these two cases. Additionally, the role terrain played with respect to this convection and subsequent turbulence differs for these two events. The focus of this section will be to discuss the convective initiation and convection present for D88 and J00.

4.3.1 Convection on 28 Dec 1988

The 28 Dec 1988 event was previously studied by KK91 as an unusual weather event where an intense narrow cold frontal rainband (NCFR) developed along the leading edge of an anafront. The NCFR developed over the Appalachian Mountains at approximately 28/1900 UTC and was accompanied by nearly 40 ms^{-1} wind gusts that broke windows, downed trees and power lines, and caused multiple injuries and several deaths. KK91 identified the rapid intensification of an ageostrophic momentum surge associated with the formation of a sub-synoptic surface pressure ridge directly upstream (as was also shown in our simulations, cf. Ch. 3, Fig. 33) that resulted in strong frontogenesis and intensification of convection. A deep tropopause fold and concomitant mid-tropospheric subsidence with the left entrance region of the upper-level jet was observed at the time of NCFR formation and frontal contraction (as well as a maximum in frontogenesis) was observed just prior to NCFR development. KK91 noted a quadrupling of the two-dimensional frontogenesis function between 28/1700 and 1900 UTC (cf., KK91 Figs. 6b and 6c) with a maximum of 32 ^{0}C/100 km/3 h based on an objective mesoanalysis. This maximum is comparable in location and

225

intensity to our frontogenesis computations using the Miller's 1948 frontogenesis function

$$F = \frac{1}{2}|\nabla_H \theta|(|Def|\cos 2\beta - Div)$$ (4.1)

where *Def* is the horizontal deformation, β is the angle from the isentropes to the axis of dilitation, and *Div* the horizontal divergence. Computations performed on our simulations indicate the contraction of the front where the maximum of frontogenesis is west of DCA and the contours are tightly packed. Fig. 1 displays the 970 hPa 2-d frontogenesis (Miller 1948) and temperatures from the 500-m simulation valid at 28/1900 UTC. The frontogenesis function (Fig. 1a) maximizes just west of DCA in the center of the plot with a maximum in excess of 30 ^{0}K/100km/3h. A plot of 970 hPa temperature and wind (Fig. 1b) indicates a contracted front with a temperature spread of greater than 4 ^{0}C over a region less than 10-km wide collocated with the frontogenesis maximum. This is the same region where precipitation intensified just east of the Cacoctin Mountains as described in the previous chapter (and reviewed later in this section).

The convective band was lineal in structure and essentially formed and lined up along the surface cold front. Initial convection began near MRB just east of the Alleghenies at approximately 28/1830 UTC (see Fig. 2) and continued to move east as the cold front propagated with individual cells moving from SW to NE. Note the cumiliform convective signature in the eastern panhandle of West Virginia extending to the NE and SW along and east of the westernmost Appalachian Mountain Chain (refer to Fig. 3, Ch. 1). This incipient line of convection was well simulated both temporarily and spatially as was its evolution (model verification is discussed in Chapter 2). Radar echoes with the system reached a maximum of almost 60dBs with rain rates associated with a narrow band of the NCFR as

high as 56-114 mm/hr recorded over a 5-10 minute period over 10 km (KK91) as the line of convection moved through the Washington, D.C. area. Modeled rainfall rates could not achieve this intensity although the intensity increased with resolution with a maximum of 40 mm/hr in the finest resolution (500-m) simulation—also located properly in space and time (Fig. 3). National Weather Service radar indicated maximum convective tops of 7 to 8 km (the tropopause was at approximately 11 km) and indicated several bulges along the intense rainband indicative of "line element" echoes (James and Browning, 1979). KK91 noted that the NCFR possessed features similar to those of line convection or 2-d convection occurring at the surface anafront (Browning and Harrold, 1970). One of the lifting mechanisms proposed for the convection by KK91 was an orographically-forced hydraulic jump. Results based on our 2-km simulations seem to support this scenario.

As momentum associated with the primary cold front traverses the Allegheny Mountain peak, an apparent hydraulic jump forms and by 1700 UTC the rapidly moving cold front catches up to the downstream jump. This merger results in enhanced vertical motion and incipient precipitation (cf., Ch. 3, Fig. 38). As the frontal system traversed the remaining two downstream mountain peaks (the Shenandoah and the Blue Ridge) a similar response occurred with a jump-front merger and enhanced vertical motion and precipitation along the Shenandoah between 1745-1800 UTC (cf., Ch. 3, Fig. 39) and along the Cacoctin Mountains (easternmost Blue Ridge) between 1830-1845 UTC (cf., Ch. 3, Fig. 40). This enhanced vertical motion and increased precipitation does not occur between terrain peaks or during the intermittent times when the front is not crossing elevated terrain (i.e., it appears the enhanced vertical motions and precipitation are a byproduct of the front-terrain interaction). This convection is inherently tied to the convergence associated with the

primary cold front as its momentum is maintained (and actually increased) east of the Alleghenies due to the deep tropopause fold and ageostrophic (direct) circulation in the left entrance region of the southwesterly polar jet (as discussed in Chapter 3 and detailed in KK91), with the greatest intensification occurring after 1900 UTC.

Clearly, the convection in D88 is lineal in extent and closely linked to the larger-scale frontal system and subsequent smaller-scale contractions of the front. These contractions are due to subsidence associated with the thermally direct jet-entrance circulation, which are potentially enhanced by a tightened temperature gradient due to precipitation-induced evaporative cooling behind the cold front (as documented by KK91). Our simulations indicated the terrain, and in particular the three elevated peaks of the Allegheny, Shenandoah, and Blue Ridge Mountains, enhanced the precipitation and resulted in intermittent increases in upward vertical motion as hydraulic jumps formed to the lee of the mountain peaks (as speculated by KK91). The effect of terrain on convective initiation for the 28 Dec 1988 event is more indirect and the resultant convection and associated CIT substantially different than that of the 13 Jan 2000 event.

4.3.2 Convection on 13 Jan 2000

The structure, areal coverage, intensity, and initiation of convection for the 13 Jan 2000 event are substantially different from those of the 28 Dec 1988 event. The convection in D88 is inherently linked to the scale-contracted large-scale front and the convergence associated with it (as well as the concomitant jet-front circulations and surface pressure effects). The convection in J00 is detached from the larger-scale system and aligned with the phasing of the downstream mesoscale phenomena (mid-level cold pool, leeside trough,, and

surface cold surge (edgewave)) described in the hypothesis and detailed in the previous chapter. Additionally, the impact of terrain on the convection in J00 is more direct. The Allegheny Mountain-induced isentropic upfold (mid-level cold pool) as well as the leeside trough and surface cold surge all owe their existence to the Appalachian Mountains (as shown in Chapter 3) and it is the phasing of these phenomena that results in the convection in J00 (as will be shown). No such combination of features occurred in D88.

As discussed in the previous chapter, the 13 Jan 2000 event conforms to the first five stages of the presented hypothesis much more closely than does the 28 Dec 1988 event. The formation of the primary mechanisms responsible for the convective initiation—and ultimately turbulence—in J00 is covered in detail in the previous chapter. The focus of this section is on the phasing of these elements and how their phasing produces meso-γ scale phenomena critical to convection and convectively-induced frontogenesis and turbulence.

The key elements responsible for the convection and subsequent CIT in J00 are the mountain-induced mid-level cold pool, leeside temperature ridge, and the surface cold surge (edge wave). The mid-level cold pool (isentropic upfold) owes its genesis to the hydrostatic mountain wave created by strong cross-mountain flow early (before 1400 UTC) on 13 Jan 2000. The result of this terrain-orthogonal flow is an upslope upfold (cold pool), a downslope downfold (low-level warm pool), and a downstream isentropic upfold (mid-level cold pool) whose strength is enhanced by the tightly packed isentropes in the vertical east of the Alleghenies—the result of large-scale processes described in Chapter 2. This terrain-induced mid-level cold pool is readily apparent in simulated output from the 6-km control simulation (Fig. 4). These plots of temperature at 700 hPa clearly denote the elliptically-shaped cold pool in southern and central Pennsylvania east of the Allegheny Mountains.

This pool is deformed by the jet streak (in the manner described in the previous chapter) and becomes oriented NE-SW as a reflection of the topography. Figure 4a depicts the deforming cold pool at 1700 UTC. Note both the eastward extent (near 77^0W) and the southern extent (near 40^0N) of the cold pool. This mid-level cold pool is clearly distinct from the larger-scale cold advection and trough denoted by the plum shading in the figure (-16^0 to -16.5^0 isotherm) and the wind shift from NNW to WNW in the upper left corner of the figure. By 1800 UTC (Fig. 4b), the eastern and southern definition of the mid-level cold pool is more apparent as is the thermal ridging bisecting them (40^0N, 76.5^0W). As will be shown, this cold pool will phase with the surface cold surge (edge wave) and tightening surface temperature gradient and result in reduced static stability, upward vertical motion, and convection along the boundary. This phasing represents the coupling of two predominantly streamwise thermally indirect ageostrophic frontogenetical circulations.

The formation mechanisms responsible for the surface cold surge were described in detail in the previous chapter. Fig. 5 depicts the cold surge (denoted by the thick black line and bound by the 0^0 isotherm and northerly momentum) between 1800 and 2000 UTC (the period during which convection was initiated). Also evident in this figure (Fig. 5a) is the leeside warm tongue visible in central Virginia (12^0C isotherm) and focused just south of the surface cold surge along the Pennsylvania-Maryland border and in northern Delaware. The surface temperature (and hence, frontal) gradient is tightening (contracting) in this region in space and time and surface convergence is enhanced as the northerly momentum associated with the edgewave collides with the west to southwesterly flow to the south. At the same time, the mid-level cold pool moves over the region and further destabilizes the environment. This combination of the mid-level cold pool, surface warm tongue, and surface cold surge

230

results in enhanced vertical motion and convection along the boundary—initially in south-central Pennsylvania through Maryland, and ultimately in the Delaware-New Jersey region in the vicinity of the severe low-level turbulence report. This phasing can be clearly seen in plots combining the surface and mid-level features.

Figs. 6 and 7 depict the 970 hPa and 700 hPa temperature as well as the 850 hPa vertical velocity. The collocation of the mid-level cold pool (see Fig. 4), surface cold surge and leeside warm tongue (see Fig. 5) phase in space and time in these plots and act to enhance upward motion in the location of this phasing. In these two figures, the 700 hPa temperature is contoured in solid red. As with Fig. 4, the mid-level cold pool is located north and west of the 12.5 ^{0}C 970 hPa isotherm. At 1800 UTC (Fig. 6a), this cold pool is located in south- and east-central Pennsylvania through northern and central Maryland. At this time, the nascent surface cold surge is essentially collocated, to just south of the mid-level cold pool through southern Pennsylvania. The 970 hPa temperature is contoured in black (dashed). Notice that the upward vertical motion (shaded in blue) coincides with this feature and essentially mirrors the mid-level cold pool. By 1900 UTC (Fig. 6b), the mid-level cold pool and surface edgewave are essentially collocated in south central and southeast Pennsylvania. By 1930 UTC (Fig. 7a), the surface temperature gradient tightens over the southeast Pennsylvania-northeast Maryland border where the surface cold surge, surface warm tongue, and mid-level cold pool phase. This region can best be identified in the figure by the closed cellular-shaped contour of upward motion along the eastern Maryland-Pennsylvania border. This is the precise location where convection developed as will be shown later in this section. By 2030 UTC (Fig. 7b), this region of phasing and maxima in upward vertical motion resides in northeastern Delaware in proximity to the low-level

231

turbulence/accident location as the observed surface front and temperature gradient contracts further. This convective initiation, cellular structure, and storm motion is confirmed in visible satellite imagery.

Figs. 8 and 9 depict GOES-8 1-km visible satellite imagery and radar (Fig. 9b) for the time of interest (1800-2000 UTC). The cellular convection is encircled in the satellite imagery. These images indicate excellent agreement with the phasing of the mid-level cold pool, surface cold surge, and warm tongue as described earlier and depicted in Figs. 6 and 7 as the convection tracks from south-central Pennsylvania (1815 UTC) to the accident location (1932 UTC). Storm motion is estimated at 320/20 ms^{-1} and peak radar reflectivities at the time of the accident report were 27 dBs with 40 dBs recorded nearby (Fig. 9b). Maximum convective cloud tops in the region were 5500 m. A comparison of visible satellite imagery to the 500-m numerical simulations indicates that the nascent convection in south-central Pennsylvania that tracks to the ESE to the accident location (near Wilmington, Delaware) corresponds with the 850 hPa vertical velocity peaks as well as the simulated convection although the simulated convection is approximately 60-70 minutes tardy when compared to the observed convection.

In order to pinpoint the upward motion and associated convection and its relationship to the phasing between the mid-level cold pool, leeside warm tongue, and surface cold surge (edge wave), the 850 hPa vertical velocity from the 500-m NHMASS numerical simulations was analyzed and compared to the 2-d frontogenesis at low- and mid levels as well as the simulated precipitation. As shown previously, the phasing of these features coincides with maxima in upward motion. Fig. 10 depicts the 850 hPa vertical velocity with upward motion shaded in blue and subsiding motion in red. These maxima are of greater intensity (3+ ms^{-1})

than those shown earlier for the coarser (6-km) simulation and are in the same location corresponding to the mid-level cold pool phasing with the tightening, contracting surface front at the boundary between the warm air from the south and the cold surge from the north. As with the convection in the satellite imagery, the vertical velocity maximum first appears in south central Pennsylvania (along the Pennsylvania-Maryland border in Fig. 10a) and tracks to the ESE toward the accident location in east central Delaware/New Jersey by 2030 UTC (Fig. 10d). A comparison with Figs. 11 and 12 indicates the upward vertical motion (blue shade) due to the phasing of the mid-level cold pool and surface features is essentially collocated with maxima in frontogenesis at the surface and mid levels as well as the simulated convection (Fig. 13). A careful comparison indicates that frontogenesis associated with the surface cold surge and leeside warm tongue extends west of the strongest upward motion (greater than 3 ms^{-1} easternmost blue-shaded region in Fig. 10) and is associated with the weaker upward vertical motion (less than 1 ms^{-1}) that traverses the Potomac River (as does the low-level frontogenesis (see Fig. 11c)). Fig. 12 indicates frontogenesis associated with the deformed mid-level cold pool to be better correlated with the strongest upward motion and precipitation. The destabilization of the atmosphere by this cold pool in combination with the surface cold surge is the key element responsible for the convection, and ultimately turbulence in this event. This coupling of the 775 and 970 hPa fronts is an example of a streamwise thermally-indirect circulation (e.g., Kaplan and Karyampudi 1992) with rising motion in the cold air and sinking in the warm. It should also be noted that deficient moisture in the initial field for J00 (as described in Chapter 2) resulted in under-simulated rainfall (and latent heating) in J00 as peak simulated rainfall was only 6 $mmhr^{-1}$. Nevertheless, the location and motion of the simulated convection compares favorably with

233

observations (although it lags observed convection by approximately an hour). The initiation of convection in J00 due to the described phasing process conforms to the hypothesis presented earlier in a much more coherent fashion than does that of D88—where the convection is essentially coupled to the convergence and vertical motion associated with the surface cold front (and larger-scale jet-front system) and enhanced by low-level terrain effects. Vertical coupling of the fronts in J00 is in proximity to convection and the severe turbulence report. The following section will detail differences in vorticity structure (both vertical and horizontal) as well as vorticity tendencies in the regions near convection as we attempt to identify the smaller-scale signals associated with the low-level turbulence in these two events.

4.4 Vorticity Analysis

An analysis of the three-dimensional vorticity structure in the environment surrounding the convection present in these two low-level turbulence cases will further elucidate the identification of signals present in and around the turbulence locations, as well as highlight the differences between the two events studied in this research. Convection affects the three-dimensional vorticity in several ways, to include motions induced by the convective outflow jet and disruption to the momentum field as flow splits around the storm cell (which acts as an obstacle). These effects can result in large gradients of vorticity away from the storm center. Cloud scale processes further intensify ambient vorticity through convergence, tilting, and solenoidal forcing. The 500-m resolution simulations allow for the diagnosis of vorticity (and vorticity tendency) in all three dimensions.

Vorticity can best be visualized as the rotation (or spin) of a fluid as it is contracted to a point and is defined as the curl of the velocity field:

$$\nabla \times \overline{V} = \left(\frac{\partial w}{\partial y} - \frac{\partial v}{\partial z}\right)\hat{i} + \left(\frac{\partial u}{\partial z} - \frac{\partial w}{\partial x}\right)\hat{j} + \left(\frac{\partial v}{\partial x} - \frac{\partial u}{\partial y}\right)\hat{k} \qquad (4.2)$$

which can be broken down into the horizontal and vertical components of vorticity :

$$\text{X-space vorticity} = \xi = \frac{\partial w}{\partial y} - \frac{\partial v}{\partial z} \qquad (4.3)$$

$$\text{Y-space vorticity} = \eta = \frac{\partial u}{\partial z} - \frac{\partial w}{\partial x} \qquad (4.4)$$

$$\text{Z-space vorticity} = \varsigma = \frac{\partial v}{\partial x} - \frac{\partial u}{\partial y} \qquad (4.5)$$

$$\text{H-space vorticity} = \left(\xi^2 + \eta^2\right)^{\frac{1}{2}} \qquad (4.6)$$

The X-space and Y-space vorticity terms are comprised of vertical shear and

horizontal variation of vertical velocity and are dominated by the vertical shear terms when vertical motion is weak. The vertical velocity terms can dominate the horizontal vorticity in regions of strong updrafts and downdrafts. Z-space vorticity (vertical vorticity) is comprised of horizontal shears, which tend to be weak when compared to vertical shear although the horizontal shear can be comparable to vertical shear near convection. H-space vorticity is a representation of the horizontal vorticity and allows for comparison between two cases of different velocity orientation. In order to examine how three-dimensional vorticity is generated and how it changes with time, we utilize the vorticity tendency equations.

The vorticity tendency equations—in the horizontal and vertical—are defined as follows:

$$\frac{\partial(\xi)}{\partial t} = -u\frac{\partial\xi}{\partial x} - v\frac{\partial\xi}{\partial y} - w\frac{\partial\xi}{\partial z} - (\xi)\left(\frac{\partial v}{\partial y} + \frac{\partial w}{\partial z}\right) - \left(\frac{\partial u}{\partial y}\frac{\partial w}{\partial x} - \frac{\partial u}{\partial z}\frac{\partial v}{\partial x}\right) + \frac{1}{\rho^2}\left(\frac{\partial p}{\partial z}\frac{\partial p}{\partial y} - \frac{\partial p}{\partial y}\frac{\partial p}{\partial z}\right), \quad (4.7)$$

$$\frac{\partial(\eta)}{\partial t} = -u\frac{\partial\eta}{\partial x} - v\frac{\partial\eta}{\partial y} - w\frac{\partial\eta}{\partial z} - (\eta)\left(\frac{\partial u}{\partial x} + \frac{\partial w}{\partial z}\right) - \left(\frac{\partial v}{\partial z}\frac{\partial u}{\partial y} - \frac{\partial v}{\partial x}\frac{\partial w}{\partial y}\right) + \frac{1}{\rho^2}\left(\frac{\partial p}{\partial x}\frac{\partial p}{\partial z} - \frac{\partial p}{\partial z}\frac{\partial p}{\partial x}\right), \quad (4.8)$$

$$\frac{\partial(\zeta)}{\partial t} = -u\frac{\partial\zeta}{\partial x} - v\frac{\partial\zeta}{\partial y} - w\frac{\partial\zeta}{\partial z} - (\zeta)\left(\frac{\partial u}{\partial x} + \frac{\partial v}{\partial y}\right) - \left(\frac{\partial w}{\partial x}\frac{\partial v}{\partial z} - \frac{\partial w}{\partial y}\frac{\partial u}{\partial z}\right) + \frac{1}{\rho^2}\left(\frac{\partial p}{\partial x}\frac{\partial p}{\partial y} - \frac{\partial p}{\partial y}\frac{\partial p}{\partial x}\right) \quad (4.9)$$

Terms→   1   2   3   4

Term 1 is the advection term and represents the horizontal and vertical advection of vorticity. This term can be significant where strong vorticity gradients coexist with strong horizontal and vertical motions. This term defines the movement of vorticity and does not generate vorticity.

Term 2 is the convergence term. This term generates vorticity by the convergence of the corresponding vorticity (either horizontal or vertical) itself. Divergence of the

236

corresponding vorticity acts to reduce it.

Term 3 is the tilting term. This term translates vorticity through the tilting of vertical vorticity into the horizontal or by the tilting of horizontal vorticity into the vertical as the result of differential horizontal or vertical motion.

Term 4 is the solenoidal term and represents the baroclinic generation of vorticity by density gradients oriented orthogonally to the axis of rotation (and at some angle relative to the pressure gradient). This term tends to have more of an impact on horizontal vorticity generation due to the fact that vertical pressure and density gradients are often several orders of magnitude greater than the horizontal pressure and density gradients. In general, the solenoidal term is smaller than the other terms in the vorticity tendency equation, but can be significant if the density gradient becomes contracted. Despite its relative size, this term is important because it can act as a source term for the other vorticity production terms to act on.

These vorticity tendency equations are useful in these high resolution analyses because they enable a cogent comparison of the forcing terms responsible for the production of vorticity and facilitate understanding of how airflow (and vorticity) is affected by and near convection. Various vorticity and vorticity tendency parameters will be examined for both cases in order to better understand and identify the small-scale signals present in and around the low-level turbulence events.

As demonstrated in the previous section, initiation of convection as well as the amount, orientation, and intensity of convection differed for the two events studied in this research. Convection in D88 was widespread and lineal in extent accompanying the surface cold front. Simulated and observed coverage and intensity (as well as latent heating) were

237

substantially stronger in D88. Convection in J00 was the result of a complicated phasing process between a mid-level cold pool, surface cold surge, and low-level warm tongue as previously described. Convection was cellular and less intense. These differences are further reflected in wind, temperature, and vorticity analyses surrounding the convection.

4.4.1 December 28, 1988

Fig. 14 depicts simulated precipitation, as well as the 775 hPa wind, vertical velocity, and temperature for the 28 Dec 1988 event (at 1930 UTC). The convection is aligned in a lineal fashion along the surface cold front (as described in the previous section). There are two regions of more intense precipitation apparent in this figure—one to the north of Washington, DC (bisecting the 39.1^0N latitude line) and a stronger cell southwest of DCA between 38.8 and 38.9^0N latitude. The temperature field isn't substantially perturbed at this altitude although the warming on the backside of the southernmost cell coincides with the strongest downward motion depicted in Fig. 14d. The wind field is clearly perturbed around the southern cell (note the bifurcation of the flow at approximately 38.8^0N, 77.4^0W in Fig. 14b) with westerly flow to the east of the storm cell and southwesterly flow to the west of the cell. The wind field is also disrupted with the northern cell (near 39.05^0N, 77^0W). Isotachs indicate a maximum downstream (north and east) with the weakest horizontal velocity corresponding to the cell location. Deformation is strongest on the eastern and downstream flank of the storms as is the upward motion. The strongest vertical vorticity (see Fig. 15a) is observed in an elongated band along the eastern fringe of the heaviest precipitation and is essentially collocated with the deformation maxima (Fig. 15b). Positive vorticity is situated on the eastern flank and negative to the west. This positive region of vertical vorticity

corresponds to the tightly packed isotachs in Fig. 14c where both $\partial v / \partial x$ and $\partial u / \partial y$ are changing rapidly as a result of the lineal convection and the rapid spatial change of wind speed and direction.

The effect of this lineal convection and the northeast to southwest anafront on horizontal vorticity is depicted in Fig. 16 and Fig. 17. Note that the horizontal vorticity is generally an order of magnitude larger than the vertical vorticity shown in Fig. 15. Fig. 16a depicts the X-space vorticity as defined in Eq. 4.3. The bulk of the X-space vorticity is depicted as negative as a result of the dominance of the vertical shear term with and behind (i.e., west of) the cold frontal system and associated convection. A zone of positive X-space vorticity is present near 77.3^0W and is due to the strong meridional variation of vertical velocity associated with the strong convective cell (in addition to the enhanced vertical motions associated with the jump front in this region as discussed in the previous section). The Y-space vorticity (as defined in Eq. 4.4) is depicted in Fig. 16b. For the 28 Dec 1988 event, the u-component of the wind doesn't vary much with height in the northern half of the domain and the stronger Y-space vorticity is found to the south where both vertical shear and longitudinal changes in vertical motion are fairly substantial—particularly near the most intense convection and vertical motion gradient (near 77.4^0W). Aside from the X- and Y-space vorticity associated with the stronger cell to the southwest, the vast majority of horizontal vorticity is either upstream of or collocated with the line of convection. This pattern can be clearly seen in Fig. 17 which depicts the combination of X- and Y-space vorticity (Fig. 17a) and the enstrophy (Fig. 17b). Enstrophy is defined as the sum of the squares of X-, Y-, and Z-space vorticity. The horizontal vorticity, as defined in Eq. 4.6, is greatest where the vertical shears maximize in combination with a minimum in the

239

streamwise variation of vertical velocity. Since enstrophy is comprised of both horizontal and vertical vorticity—and the horizontal vorticity is generally an order of magnitude larger—it is not surprising to find the measure of three-dimensional spin approximately lined up with the maxima and minima of horizontal vorticity. For D88, the enstrophy maxima are almost exclusively confined to the region along and upstream of the surface anafront and convective line. There is a secondary line of high enstrophy located farther upstream of that attached to the surface front and convection (running from northeast to southwest from 39.4^{0}N, 76.5^{0}W to 39^{0}N, 77.4^{0}W). This maximum is almost entirely due to vertical shear behind the surface anafront and ahead of the mid-level trough (note: soundings through this zone indicate 800 hPa winds of 290/15 and 750 hPa winds of 240/30).

In order to ascertain which terms are primarily responsible for the production of three-dimensional vorticity (and hence, vortex tubes), the vorticity tendency equations are utilized (see Eq. 4.7 – 4.9). Fig. 18 depicts the total vorticity tendency (contribution of all terms) for X-, Y-, and Z-space vorticity as well as the total 3-d vorticity tendency. As expected, the contribution of the vertical vorticity tendency to the total vorticity tendency is small when compared to the contributions of the X- and Y-space vorticity tendency terms. Patterns for the horizontal vorticity tendency terms are similar (Fig. 19 a-b), with the primary contribution collocated with the frontal system and convection (just west of DCA) in a lineal pattern with the exception of the more arc-like pattern to the south associated with the strongest convection. Contributions from the X- and Y-space tendency terms are roughly equivalent and advance with the frontal system and convection with time. In order to determine the key mechanisms (and pattern) responsible for this vorticity generation, the various terms in the vorticity tendency equation are examined (with the exception of the

advection term, which doesn't generate vorticity).

Fig. 19 depicts the total vorticity tendency and the contributions from the convergence, tilting, and solenoidal terms. The total vorticity tendency maximizes along the cold front and concomitant convection in a NE-SW pattern that is a reflection of this feature and also in an arc-like pattern essentially surrounding the stronger convection to the southwest of DCA (surrounding 38.8^0N, 77.4^0W). Contributions from the convergence term (Fig. 19b) and the tilting term (Fig. 19c) are very similar in magnitude and location. Production with the convergence term comes from the variation in the horizontal wind and, in particular, the variation of vertical velocity with height (see Fig. 20). Both $\partial u / \partial x$ and $\partial v / \partial y$ are fairly large as air is accelerated away from the convection both to the north and east. The tilting term redistributes existing vorticity through vertical motions—both in terms of vertical wind shear and the horizontal variation of vertical velocity. As discussed earlier, the primary contributor is the vertical shear along the front and the horizontal variation of vertical velocity near the most intense convection. Lastly, the contribution from the solenoidal term is approximately one to two orders of magnitude less than that of the convergence and tilting terms. This term increases as the density and pressure gradients contract and maximizes in D88 downstream from the convection (with the rising motion along the frontal boundary indicative of a thermally-direct streamwise circulation) and near the vertical velocity maxima with the stronger convection to the southwest (near 38.85^0N, 77.4^0W).

The horizontal and vertical vorticity, enstrophy, and vorticity tendencies for the 28 Dec 1988 event all essentially line up along and upstream (west) of the lineal convection accompanying the surface anafront. There is some indication of a more arc-like pattern

241

associated with the stronger southern convective cell, although the enstrophy, vorticity, and vorticity tendencies are generally located upstream and along the convection in this location as well with the exception of a small eastern extension associated with the flow splitting around the convective cell. Differences between this event and J00, to include frontal structure and propagation as well as convection geometry and initiation, have been previously discussed. As expected, differences in vorticity, enstrophy, and vorticity tendency are also present. The 13 Jan 2000 will be discussed in the next subsection.

4.4.2 January 13, 2000

Fig. 21 depicts simulated precipitation, as well as the 775 hPa wind, vertical velocity, and temperature for the 13 Jan 2000 event (at 2020 UTC). As discussed in Section 4.3, the convection in this event differs from that of 28 Dec 1988. It is much more isolated, less intense (as defined by precipitation rate), and cellular in structure and formed as a result of the frontal phasing process described earlier in this chapter. The cell depicted in Fig. 21a originated in south central Pennsylvania near the Pennsylvania-Maryland border and moved essentially ESE through the 500-m domain as it approached the severe turbulence site in eastern Delaware-New Jersey after 2020 UTC. The temperature field is clearly perturbed by the convection as an arc of warm temperatures (1^0 to 2^0C warmer than the immediate surroundings) surrounds the convection to the north and south and a $1+^0$C cold perturbation is present downstream (northeast and southeast—just upstream from the Delaware River). The wind field is also disrupted by the convective cell (Fig. 21b). As with the stronger convective cells in D88, the horizontal wind minimizes within the cell and accelerates downstream—particularly to the right of the convection (east of 75.7^0W longitude) as a result

of the increased pressure gradient force with the latent heating. This pattern of a downstream and rightward jetlet emanating from the region of weakest horizontal wind is readily apparent in a plot of wind and isotachs (Fig. 21c) and is similar in formation to that described in Kaplan et al. (1998) and Hamilton et al. (1998). The isotach analysis indicated the maximum in wind speed downstream (south and east) as in D88. An analysis of vertical motion (Fig. 21d) indicates a wavelike pattern with the strongest downward motion on the cell's rear flank (along the Maryland-Delaware border) and the strongest upward motion on the front flank of the storm cell in central Delaware (just west of the Delaware River). Note the oscillating pattern in vertical motion along the path of the storm from approximately 39.65^0N, 75.82^0W to 39.5^0N, 75.6^0W. This reinforces the pattern of streamwise rising in the cold air and sinking in the warm air analogous to that described earlier in Section 4.3.2.

For the 13 Jan 2000 event, the deformation is largest in a large arc encompassing and surrounding the convective cell (Fig. 22a). The region is much broader in extent than either of the maxima in the 28 Dec 1988 event and is arc-like in appearance as opposed to lineal. Additionally, the area of large (> 40 s^{-1}) deformation covers a significantly larger area than does the convection. The deformation maxima in D88 are much more closely aligned with the convection (i.e., the sphere of deformation doesn't extend far from the line of convection). The strongest vertical vorticity in J00 is oriented in a similar pattern to that of deformation (Fig. 22b). Strong positive vorticity is aligned with the strongest deformation in an arc-like pattern with the strongest positive vorticity to the right and the strongest negative vorticity to the left. The positive region of vorticity—particularly the strong, southernmost arc—corresponds to the tightly packed isotachs in Fig. 21c in the area of strongest outflow and near the larger-scale southern stream of westerly momentum (> 30 ms^{-1}) traversing the

region. This is a region of significant $\partial v / \partial x$ and small or negative $\partial u / \partial y$ in the accelerating westerlies.

The effect of this convection on the horizontal vorticity is depicted in Figs. 23 and 24. As with D88 (and in general), the horizontal vorticity is an order of magnitude greater than the vertical vorticity shown in Fig. 22. Figure 23a depicts the X-space vorticity as defined in Eq. 4.3. The majority of X-space vorticity is depicted as negative due to the general dominance of the vertical shear term over the meridional variation of vertical velocity. There are two enclosed contours of positive X-space vorticity and these correspond to the zones of strongest vertical motion as shown in Fig. 21d. As with both the deformation and vertical vorticity, the X-space vorticity pattern is somewhat circular and broad, not lineal and elongated as in D88. Another distinction is that the maxima in X-space vorticity for J00 are located downstream from the convection as opposed to upstream as in D88. This downstream orientation is likely a reflection of the increased vertical shear downstream due to the katafront structure in J00 compared to the upstream maximum accompanying the anafront structure present in D88 and consistent with the tilt of the thermally indirect circulation. The Y-space vorticity (as defined in Eq. 4.4) is shown in Fig. 23b. Again, an arc-like pattern surrounding and downstream from the convection is apparent in central Delaware. The pattern is similar in shape and orientation to both the deformation and vertical vorticity and also the curved, tight temperature pattern shown earlier (Fig. 21a) although extending farther downstream. When compared to the Y-space vorticity for D88, it is clear the intensity is greater (by nearly a factor of two) for J00 than D88. These large Y-space vorticity values are the result of a combination of large vertical shear and low to negative $\partial w / \partial x$. Note that the strongest arc of positive Y-space vorticity (defined by the

244

westernmost and southernmost tight contours) conforms to the region surrounding and sandwiched between the two vertical velocity peaks (compare Figs. 23b and 21d). As with the X-space vorticity, a major distinction between the Y-space vorticity on 13 Jan 2000 and that shown earlier for 28 Dec 1988 is that the maximum values primarily extend downstream from the convection and not upstream. The arc-like vorticity pattern as well as the intensity and downstream location of these maxima can be more clearly seen in the horizontal vorticity and enstrophy plots (Fig. 24). The horizontal vorticity (as defined in Eq. 4.6) is greatest where the vertical shears maximize and the streamwise variation of vertical velocity minimizes. In this event, the horizontal vorticity is driven by the Y-space vorticity (compare Figs. 23b and 24a). Additionally, since enstrophy is comprised of the individual horizontal vorticities and vertical vorticity, the enstrophy tends to reflect the vorticity patterns shown earlier—and the horizontal (and hence, Y-space) vorticity more prominently due to the order of magnitude difference between the horizontal and vertical vorticities. A comparison of the horizontal vorticity shows horizontal vorticity maxima in J00 are more than 1.5 times as large as those present in D88. The maximum of enstrophy for J00 is concentrated in an arc-like pattern along and downstream from the convection in central Delaware and extends eastward well in advance of the convection (across the Delaware River). Enstrophy maxima for J00 were nearly 1.8 times as large as those for D88, even though the intensity of convection was much larger for D88. The magnitude of the enstrophy maximum is due in large part to the vertical shears and the horizontal variation of vertical vorticity as was the case for the Y-space vorticity.

As with D88, the vorticity tendency equations (Eq. 4.7 – 4.9) are utilized in order to determine which terms are primarily responsible for the production of three-dimensional

vorticity. Fig. 25 depicts the total vorticity tendency (contribution of all terms) for X-, Y-, and Z-space vorticity, as well as the total 3-d vorticity tendency. The contribution of the vertical vorticity tendency to the total vorticity tendency is relatively small for J00 as a result of order of magnitude considerations (previously described). The X- and Y-space vorticity tendencies for this case (as they were in D88) are similar to each other—both in orientation and magnitude (Fig. 25 a-b). Both are arc-like with a void in the center corresponding to the maximum vertical updraft (refer to Fig. 21d). The Y-space vorticity tendency is more encompassing (largely as a reflection of the Y-space vorticity itself) and mirrors the total vorticity tendency (Fig. 25d) which is essentially the sum of the X- and Y-space vorticity tendencies. In order to determine the primary mechanisms responsible for this vorticity generation, the various terms in the vorticity tendency equation are examined (with the exception of the advection term, which doesn't generate vorticity).

Fig. 26 depicts the total vorticity tendency and the contributions from the convergence, tilting, and solenoidal terms. The total vorticity tendency maximizes in an arc around the convective updraft (Fig. 26a) with downstream maxima with the convective cell and to the south and east. As with D88, contributions from the convergence term (Fig. 26b) and the tilting term (Fig. 26c) are similar in magnitude and location. Production with the convergence term is due to the variation of the horizontal wind and the variation of vertical velocity with height (see Fig. 27). Both $\partial u / \partial x$ and $\partial v / \partial y$ are large as the wind is deformed near the convection and accelerated to the south and east. As discussed earlier, the tilting term redistributes existing vorticity through vertical motions via vertical wind shear and the horizontal variation of vertical motion. These maximize near the oscillating vertical velocities (see Fig. 21d) with the northernmost maximum (near 39.56^0N) and with the rapidly

246

accelerating outflow jet near the southernmost maximum (near 39.50^0N). The pattern with the solenoidal term is more chaotic although it maximizes in the region near the tight temperature (and density) gradient shown earlier (Fig. 21a). This term is several orders of magnitude less than that of the convergence and tilting terms. A comparison of the various vorticity tendency terms between J00 and D88 indicates differences in both orientation and magnitude. The various terms in the 28 Dec 1988 case are primarily lineal in extent and aligned along the surface anafront and convection as well as upstream (i.e., to the west). The vorticity tendencies in the 13 Jan 2000 event are aligned in an arc-like pattern coincident and downstream (i.e., south and east) from the surface katafront and convection. Additionally, the convergence and tilting terms for J00 are more than three times as large as those in D88 and the overall vorticity tendency is nearly four times greater in the 13 Jan 2000 event. *This result is particularly interesting considering the precipitation rates in D88 are much larger than those in J00.*

Differences in horizontal and vertical vorticity, enstrophy, and vorticity tendency between two low-level turbulence events have been analyzed. In the 28 Dec 1988 event, these parameters all essentially line up along and upstream of the lineal convection accompanying the surface anafront. In the 13 Jan 2000 event, the maxima of vorticity, enstrophy, and vorticity tendency appear in an arc-like configuration along and downstream of the convective cell and surface katafront. The implications for convectively-induced turbulence and an index for identifying regions of potential turbulence will be discussed in the next section.

4.5 Convectively-Induced Turbulence

The three-dimensional vorticity and vorticity tendency were defined and identified for two cases of low-level turbulence east of the Appalachian Mountains. Analyses in the previous section indicate that large concentrations of vertical and, in particular, horizontal vorticity were present (and developing) with the deformation and microfronts generated by convection and its concomitant outflow jet. These regions of maximum vorticity and vorticity production are fairly broad and elongated and in all likelihood cover a more expansive area than that of the low-level turbulence. Additionally, the analyses in the previous section were limited to the horizontal and give little (if any) indication of the vertical extent and intensity of the vorticity and any vortex tubes or turbulence. Lastly, the issue of turbulence avoidance bears some discussion. As discussed earlier, pilots know to avoid flying near convection and the FAA has specific guidelines for thunderstorm avoidance in the horizontal and vertical (as discussed in Section 4.1). In the two cases studied in this research, one event featured a very intense line of convection and the other fairly weak cellular convection. While the initiation of convection and convective growth can be somewhat unpredictable and lead to CIT encounters, it seems also likely that turbulence encounters are more probable in proximity to innocuous looking storms (e.g., J00) than near organized, intense convection. These issues, as well as the storm relative location and influence in regards to potential turbulence will be the focus of this section. In addition, we will provide a potentially useful index for better identifying preferred regions of turbulence.

In an effort to further diagnose probable turbulence regions, several parameters often associated with turbulence will be examined and related to the previously identified large vorticity (both horizontal and vertical) and enstrophy locations. The turbulent kinetic energy

248

(TKE) is often used to denote the presence of mean wind shear and thermal stratification responsible for the generation and maintenance of turbulence. The TKE equation for horizontally homogenous flow (Stull, 1988) is

$$\frac{\partial \overline{e}}{\partial t} = -\overline{u'w'}\frac{\partial \overline{u}}{\partial z} - \overline{v'w'}\frac{\partial \overline{v}}{\partial z} + \frac{g}{T_0}\overline{w'\theta'} - \frac{\partial}{\partial z}\left(\overline{e'w'} + \frac{1}{\rho_0}\overline{p'w'}\right) - \varepsilon \qquad (4.10)$$

The first two terms on the RHS are the shear production terms, the third term is the buoyancy production term, the fourth term represents vertical diffusion, and the final term viscous dissipation. The shear production terms are composed of momentum flux and mean vertical wind shear and represent the conversion of the kinetic energy of the mean motion to turbulent motion. These terms are most significant near the surface and diminish rapidly with height. The buoyancy term represents the conversion of potential energy to TKE and is a source of TKE in unstable stratification or convection and a sink in stable stratification. As a result, large values of TKE should roughly approximate the maxima in vorticity (and enstrophy) as well as align with the convection shown earlier in the chapter. This is indeed the case, as Fig. 28 demonstrates. Unfortunately, the regions of maximum TKE are somewhat chaotic and cover an even broader, less distinct region than the enstrophy maxima shown in the previous section (especially for D88). Additionally, the TKE maxima for the 28 Dec 1988 case are larger than those for the 13 Jan 2000 case. This result is contrary to the vorticity, enstrophy, and vorticity tendency analyses and is likely the result of the large amount of convection present as well as the larger kinetic energy in the background flow. As with the vorticity tendency analyses presented in the previous section, maxima of TKE occurred predominantly upstream of the convection in D88, and downstream of the convection in J00. *What is potentially significant in Fig. 28 is that the change in magnitude*

249

of TKE maxima for J00 is much larger (particularly when normalized relative to the maxima)

than that for D88—possibly reflecting a larger eddy dissipation rate (EDR) in J00 often

associated with turbulence (e.g., Kaplan et al. 2000). Another frequently used measure of

turbulent potential that combines wind shear and static stability (buoyancy) is the Richardson

number (discussed in more detail in Chapter 1). The gradient Richardson number is defined

as the ratio of static stability to the mean vertical wind shear-squared:

$$Ri = \frac{\dfrac{g}{\theta_0}\dfrac{\partial\theta}{\partial z}}{\left(\dfrac{\partial\bar{V}}{\partial z}\right)^2} \qquad (4.11)$$

and is a measure of the relative effects of buoyancy and shear on turbulence. A requirement

for the instability of flow and the possible transition to turbulence is given by $Ri < 0.25$

(Miles 1961, Howard 1961). The Richardson number for both events is plotted and

contoured in Fig. 29 between 2200 and 2600 m to coincide with the turbulence reports in

space and time. The patterns for both events are remarkably similar to those of vorticity,

vorticity tendency, and enstrophy presented in the previous section. Note the arc-like pattern

in Delaware (between 39.5^0 and 39.6^0N) for J00 in Fig. 29a and across the Delaware River in

Fig. 29b. A contour of $Ri < 0.25$ is evident in both of these plots in proximity to the

convective cell (refer to Figs. 21b and 13d). As with the vorticity (and enstrophy) analyses,

the majority of low Richardson numbers (i.e., $Ri < 0.5$) occur with and downstream of the

convective cell in J00. The phasing of the mid-level cold pool, surface cold surge, and warm

tongue from the south in this region results in decreased static stability and increased wind

shear (as shown previously). On the other hand, minima in Richardson number for D88

(Figs. 29c and d) are elongated and line up   along and upstream from the surface anafront

250

and concomitant convection. There is some evidence of an arc-like structure in Ri (near 38.8⁰N, 77.55⁰W) with a stronger cell to the southwest (also apparent in the vorticity plots shown in the previous section), but the general pattern is lineal and the minima are higher than those for J00 with no $Ri < 0.25$ contours in the entire domain. As with J00, these plots (both in pattern and magnitude) line up well with the maxima of vorticity, vorticity tendency, and enstrophy.

A comparison of Richardson number and enstrophy is particularly revealing. Fig. 30 depicts the enstrophy valid at the same height and time as the Richardson number displayed in Fig. 29. Even a cursory comparison reveals the remarkable correlation between these parameters—both in orientation and value. The enstrophy maxima are essentially coincident with the Richardson number minima in every instance. This close correlation indicates that the vertical shear terms might be dominant in these cases as the square of vertical velocity appears in the numerator of enstrophy (inherent in the horizontal vorticity) and in the denominator of Richardson number. In order to further highlight the correlation between the enstrophy (measure of three-dimensional spin) and Richardson number (ratio of static stability to mean wind shear), the ratio of these two parameters (enstrophy/Ri) is computed and displayed in Fig. 31. This index (referred to here as the rienstrophy) will maximize in regions of high enstrophy and low Richardson number—in other words, locations where spin, vortex tube potential, and the ratio of vertical wind shear to static stability are the greatest. In the event vertical shear is dominant, this ratio will essentially reduce to the vertical velocity terms raised to the fourth power divided by the buoyancy frequency. Additionally, maxima of this ratio greatly focus the region of interest for both cases. Figs. 31a and b depict somewhat of a broken arc-like pattern with the largest values focused

around and downstream of the convective cell in central Delaware for J00. As with the previous parameters, rienstrophy values for D88 are somewhat elongated and located upstream (i.e., west) of the line of convection. Additionally, maxima for D88 are two to five times less than those of J00 and the time tendencies in J00 are much larger than in D88. Thus far, we have only looked at these parameters in the horizontal plane. Although a small-scale phenomenon, turbulence (by its nature) possesses vertical extent and it is possible the maxima for the parameters studied could be at slightly different altitudes. In order to more thoroughly investigate this, vertical cross sections along the maximum storm cell motion vectors are analyzed for both cases.

The locations of the vertical cross sections utilized for D88 and J00 are shown in Fig. 32. Horizontal wind, vertical wind, and potential temperature are displayed for these cross sections in Fig. 33. Plots of the horizontal wind (Figs. 33a and c) depict the deformation due to convection (visible with the most significant wave activity in both events) with the outflow jet apparent downstream as the isotachs increase in the right section of the cross sections. In these plots, the wind appears more deformed in J00 (Fig. 33a) than in D88 (Fig. 33c). Vertical velocities are intense with strong upward motion (2.5 to 10 ms^{-1}) at the surface front locations and strong downdrafts (2 to 7.5 ms^{-1}) associated with the convection and gravity wave. Note the variation in the horizontal and vertical wind for 13 Jan 2000 in the vicinity of the folding isentropes (and possible breaking wave) near 750 hPa. These horizontal and vertical winds have an impact on the horizontal and vertical vorticity and in the differences observed between these two events.

The cross sectional plots of horizontal and vertical vorticity reveal some interesting differences between J00 and D88. They also indicate the greatest concentration of vorticity

252

(or vortex tubes) may be at slightly different altitudes than previously plotted. Fig. 34 (a-h) depicts the horizontal and vertical vorticity for the cross section shown in Fig. 32. Figs. 34a and e depict the X-space vorticity. The X-space vorticity maximizes in J00 downstream from the potentially breaking wave and convection between approximately 2000 and 2700 m. This vorticity is positive indicating a dominance by the meridional variation of vertical velocity over vertical wind shear. On the other hand, the X-space vorticity in D88 maximizes upstream from the surface anafront and convection and at a lower altitude (800 – 2000 m). In this case, the bulk of X-space vorticity is negative indicating dominance of vertical wind shear over the zonal variation of vertical velocity. Both the lower altitude and sign of this X-space vorticity can likely be explained by the surface anafront structure itself. Vertical wind shear behind the surface front (and the approaching mid-level trough) decreases with altitude and slopes to the left (west) as directional and speed shear are stronger behind the front than in ahead of it.

Figs. 34b and f depict the Y-space vorticity over the same cross section. As with the horizontal plots showed earlier, the Y-space vorticity maximizes in a wishbone-type pattern in the region immediately above and downstream from the convection and largest upward vertical velocity (shown in Fig. 33b). This maximum extends from approximately 2200 – 3100 m (maximizing at 2600 m). The Y-vorticity for J00 indicates a dominance of vertical wind shear over the horizontal variation of vertical velocity. Analysis of Y-space vorticity for D88 indicates there is little significant Y-space vorticity although a relative (positive) maximum (associated with increased vertical wind shear above 2600 m) is apparent in the northwest quadrant of the cross section between 2600 – 3000 m. Figs. 34c and g depict the horizontal vorticity (as defined in Eq. 4.6) for both cases and highlights the downstream

tendency in J00 and the upstream tendency in D88. The large maxima ($> 20 \times 10^{-3}$ s^{-1}) of positive horizontal vorticity further emphasizes the dominance of the vertical wind shear over horizontal variation of vertical velocity in determining these maxima. Figs. 34d and h depict the vertical vorticity. These maxima are an order of magnitude smaller than the horizontal vorticities with positive vertical vorticity aligned vertically with the frontal system and storm updraft and negative vorticity on the upstream (left) side with the storm downdraft. Note also the downstream maximum in J00 (to the east of the strong vertically-oriented maximum). As shown earlier, the primary deformation and distortion of the winds occurred downstream for J00 and upstream for D88 and these horizontal and vertical vorticity cross sections provide additional validation of this. In addition, cross sections of enstrophy and Richardson number provide more clues as to possible turbulence locations.

Fig. 35 depicts cross sections of enstrophy and Richardson number for J00 and D88. As with the horizontal plots of enstrophy, the vertical cross sections (Figs. 35a and c) are primarily a reflection of the horizontal vorticity (and hence vertical wind shear and, to a lesser extent, horizontal variation of vertical velocity). This vertical display of enstrophy actually indicates a higher maximum with D88 than J00. This maximum (roughly between 1200 – 2200 m, upstream from the surface anafront and convection) is located along the transition zone between upward and downward motion (see Fig. 33d) and in the region of strong vertical wind shear with the downfolding isentropes (see Fig. 33c). The mid-level maximum in J00 is situated downstream from the convection and a potentially overturning wave. This maximum in enstrophy also brackets a zone of rapidly changing vertical velocity (see Fig. 33b) and vertical wind shear (see Fig. 33a). In order to further ascertain the potential for turbulence in these regions of concentrated vorticity (vortex tube signatures), the

254

Richardson number is plotted in Figs. 35b and d (only values less than 1.0 are depicted). As was shown with the horizontal comparisons performed earlier, Richardson number correlates very well with enstrophy (and hence, horizontal vorticity). The Richardson number for J00 coincides with the maximum enstrophy (between 2500 – 2800 m in Fig. 35a) and values are less than 0.25 for a broad region in advance of what appears to be a nearly overturning wave. While enstrophy was slightly higher in the D88 cross section, there are no Richardson numbers less than or equal to 0.25 (the smallest contour is 0.5—between approximately 1400 – 2200 m). Nevertheless, locations where these parameters overlap (i.e., maximum enstrophy and minimum Richardson number) should indicate areas with a high probability for turbulence.

Since the vertical cross sections of enstrophy and Richardson number appear to indicate a high turbulence potential at various altitudes, horizontal plots of the ratio of enstrophy to Richardson number (rienstrophy) are provided at 2600 m for the 13 Jan 2000 event and at 1600 m for the 28 Dec 1988 event. The precipitation is overlaid on these plots in order to better depict the location of these maxima with respect to convection. Fig. 36a depicts an arc of high rienstrophy downstream (south and east) from the convective cell in central Delaware for J00. The influence of this maximum extends 11+ km downstream and is located very close in space (both horizontal and vertical) and time to the observed severe low-level turbulence event on this date. Values for D88 are depicted in Fig. 36b and display a more lineal pattern. Additionally, the maximum value for this event is approximately 29 x 10^{-4} s^{-2} as opposed to 50 x 10^{-4} s^{-2} for J00. As with the previous plots, as well as the analyses of vorticity, TKE, enstrophy, and Richardson number, maxima for D88 appear upstream of the surface anafront and convection as opposed to downstream from the surface katafront and

convection as was the case for J00. This difference in orientation is most likely the result of frontal orientation (anafront vs. katafront) as well as differences in shear structure due to differences denoted earlier for the larger scales (e.g., two-jet system and stronger mid-level cold pool in J00) which resulted in lineal convection closely tied to the large-scale jet-front system for D88 and cellular convection associated with the complicated mountain-induced phasing for J00. These differences impact the amount and intensity of turbulence encountered and reported. A strong line of convection is more likely to be avoided by aircrews (or attempted to be avoided) than an innocuous-looking convective cell of small vertical extent. It is often these storm cells that catch pilots unaware and result in severe turbulence reports. The 28 Dec 1988 event was far more convectively unstable than that of 13 Jan 2000 with negative $\partial\theta_e / \partial z$ (computed between 900 – 700 hPa) in the region of interest through 28/19 UTC (and an overall range of -6 to $+1$ ^{0}K/km) as opposed to a complete absence of negative $\partial\theta_e / \partial z$ prior to 13/17 UTC (and an overall range of -2 to $+10$ ^{0}K/km) for J00. The 13 Jan 2000 case demonstrates the potential for large concentrations of vorticity (implied vortex tubes), wave breaking, and severe turbulence that fairly weak convection can have given the right circumstances. In addition, the time rate of enstrophy change is consistent with large values of EDR.

The difference in wave structure between J00 and D88 is clearly evident in a comparison of potential temperature cross sections. Fig. 37a depicts the potential temperature at 0.5^0K intervals for the 13 Jan 2000 event with the cross section located as in Fig. 32. A convectively-induced gravity (buoyancy) wave that appears close to overturning is visible above the surface front and strongest near the level of reported turbulence and simulated large vorticity, enstrophy, and rienstrophy, and low Richardson number as

shown earlier (between 800 and 600 hPa). The wave pattern for the 28 Dec 1988 event is of much smaller amplitude and essentially quiescent. A comparison of isentropes over a 30-minute interval further indicates the disparity in wave pattern, dispersion, and ducting.

Fig. 38 demonstrates the relatively non-dispersive nature of the wave in J00 as it propagates from northwest to southeast atop the low-level front. Note how well this wave maintains its shape throughout the time period. On the other hand, the relatively minor wave activity in D88 appears more dispersive (Fig. 39) and much less likely to result in wave breaking. The wave packet in J00 is essentially indistinguishable from the front (i.e., it moves with the front) whereas the modest waves in D88 are more transient in nature. In order to prevent energy loss and wave dispersion, a sufficient wave duct is necessary. The wave ducting capability of these two cases is investigated and compared by looking at the wave ducting factor of each (Koch and O'Handley, 1997). The ducting factor (DF) is computed from the numerically simulated layer output and determined as follows:

$$DF = (\theta_{800} - \theta_{950}) - (\theta_{e800} - \theta_{e400}) \qquad (4.12)$$

and is based on the criteria necessary for an efficient wave duct (i.e., strong near-surface static stability and conditional instability in the layer above (Lindzen and Tung, 1976)). For wave maintenance, a duct factor exceeding 10^0C (and in most cases greater than 15^0C) is required and the wave duct must be of sufficient strength within the projected corridor of wave propagation. The duct factors for J00 and D88 are contoured and plotted in Fig. 40. DF values for the 13 Jan 2000 event are greater than 23^0C throughout the 500-m NHMASS domain (Fig. 40a) and a comparison with the DF values for the 28 Dec 1988 event (Fig. 40b)—generally less than 15^0C—indicates that J00 is more prone to ducting and wave breaking than D88.

257

This analysis of wave behavior indicates J00 is more likely to exhibit wave breaking than D88. Similarly, vertical and horizontal analyses of vorticity, enstrophy, Richardson number, and the rienstrophy index indicate greater vortex tube and turbulence likelihood for J00 although vertical analyses indicate the greatest probability of parameter maximization at lower altitude in D88 and slightly higher than accident level in J00.

4.6 Summary and Conclusions

In this chapter, we investigated the convective initiation and the role of convection, frontal contraction, and vorticity effects (to include vortex tube formation) on low-level turbulence east of the Appalachian Mountains. A thorough comparison between two cases of convectively-induced low-level turbulence was made and an index incorporating the three-dimensional vorticity, vertical wind shear, and static stability was suggested to help better identify regions where turbulence would be expected.

Convection in the 28 Dec 1988 case was lineal in extent and closely linked to the larger-scale frontal system and subsequent scale contractions of the front due to subsidence associated with a thermally-direct jet-entrance circulation and potentially enhanced by a tightened temperature gradient due to precipitation-induced evaporative cooling behind the rearward-sloping cold front. Our simulations indicated the terrain, and in particular the three elevated peaks of the Allegheny, Shenandoah, and Blue Ridge Mountains, resulted in intermittent increases in upward vertical motion and enhanced precipitation as hydraulic jumps formed to the lee of the mountain peaks. The effect of terrain on convective initiation for D88 is more indirect and the resultant convection and associated CIT and vorticity patterns substantially different than that of the 13 Jan 2000 event.

The convection in J00 is detached from the larger-scale system and aligned with the phasing of the downstream mesoscale phenomena (mid-level cold pool, leeside trough, and surface cold surge (edgewave)). Additionally, the impact of terrain on the convection is more direct (the terrain is essentially responsible for each of the mesoscale features that eventually combined to initiate the convection). The Allegheny Mountain-induced isentropic upfold (mid-level cold pool) as well as the leeside trough and surface cold surge all owe their

259

existence to terrain interactions (as detailed in the previous chapter) and it is the phasing of these phenomena that results in the convection in J00. No such combination of features occurred in D88. In J00, the combination of the mid-level cold pool, surface warm tongue, and surface cold surge resulted in enhanced vertical motion and convection along the boundary of their intersection—initially in south-central Pennsylvania through Maryland, and ultimately in the Delaware-New Jersey region in the vicinity of the severe low-level turbulence report. The initiation of convection in J00 due to the described phasing process conforms to the presented hypothesis in a much more coherent fashion than does that of D88—where the convection is essentially coupled to the convergence and vertical motion associated with the surface cold front (and larger-scale jet-front system) and enhanced by low-level terrain effects. These differences affect the momentum and vorticity fields in different ways.

An analysis of the deformation and three-dimensional vorticity structure in the environment surrounding the convection in both cases was performed. The deformation, horizontal and vertical vorticity, enstrophy, and vorticity tendency maxima for the 28 Dec 1988 event all occurred along and upstream (west) of the lineal convection accompanying the surface anafront. On the other hand, the deformation for J00 was largest in an arc encompassing and surrounding the cellular convection and was much broader in extent than the maxima in D88. Additionally, the area of large deformation covered a significant region outside of the convection—deformation maxima in D88 were much more closely aligned with the convection. This relationship (or orientation) could have an impact on turbulence reporting as flight inside or through convection is rare. Horizontal and vertical vorticity and enstrophy maxima patterns for J00 were circular (arc-like) and broad, not elongated as in

260

D88. Horizontal vorticity maxima were also primarily located downstream from the convection as opposed to upstream as in D88—likely due to the increased downstream vertical shear due to the katafront (forward-sloping) structure in J00 compared to the upstream maximum accompanying the anafront (rearward-sloping) structure in D88. Horizontal vorticity maxima in J00 were more than 1.5 times as large and enstrophy nearly 1.8 times as large as those in D88. A comparison of the various vorticity tendency terms between J00 and D88 indicated similar differences in orientation and magnitude. The various terms in the 28 Dec 1988 case were primarily lineal in extent and aligned along and upstream from the surface anafront and convection. The vorticity tendency terms in the 13 Jan 2000 case were arc-like in appearance and located primarily downstream from the surface katafront and convection. In addition, the convergence and tilting terms for J00 were more than three times larger and the overall vorticity tendency nearly four times larger than those for D88. The difference in magnitude of these parameters as well as the orientation and location of these maxima likely played in a role in the higher turbulence intensities reported on 13 Jan 2000. In order to diagnose these events further, parameters traditionally associated with turbulence were computed and compared for both cases.

An analysis of the turbulent kinetic energy (TKE) revealed patterns similar to those of vorticity, enstrophy, and vorticity tendency. TKE maximized primarily upstream of the convection in D88 and downstream of the convection in J00. Similar results were observed for Richardson number (Ri). The majority of Ri minima were arc-like in appearance and located downstream from convection in J00 and were elongated and upstream from the surface anafront and convection in D88. Additionally, Ri was consistently lower for J00 as several contours of Ri < 0.25 were observed for J00 and none for D88.

A comparison of Ri and enstrophy revealed a remarkable correlation—both in orientation and inverse magnitude. Enstrophy maxima were essentially coincident with minima of Richardson number. The ratio of these parameters (enstrophy/Ri) should maximize in regions where spin, vortex tube potential, and the ratio of vertical wind shear to static stability are largest (i.e., regions ripe for turbulence). This ratio, referred to here as rienstrophy, is offered as a potentially valuable index for identifying turbulence potential. As with the parameters previously discussed, rienstrophy maxima were elongated, lineal, and located upstream of the convection and surface cold front in D88 (although these maxima are much more focused that those provided by any of the previous parameters). Maxima of this ratio for J00 are similarly focused and as with the high concentrations of vorticity, enstrophy, vorticity tendency, TKE, and Ri minima, are arc-like and located downstream from the convection and surface katafront. Maxima for J00 were two to five times larger than those for D88 despite the fact that the convection was much more intense in D88 as inferred from precipitation rates. The location of the J00 maxima (in the vertical) occurred in the vicinity of an apparent breaking wave. In addition to rienstrophy, future research should consider the investigation of helicity of 3-D vortex tubes as a possible turbulence indicator.

Wave patterns for these two cases were significantly different as well. The convectively-induced gravity (buoyancy) wave in J00 appeared non-dispersive and traveled on the surface katafront, which acted as a moving wave duct. Wave activity in D00 was transient and dispersive. The wave ducting factor was computed for both cases and that of J00 far exceeded the minimum required for sufficient wave ducting (throughout the entire domain), whereas the ducting factor computed for D88 was marginal upstream of the surface front and below the threshold downstream from the front.

This chapter detailed the smaller-scale differences between two cases of low-level CIT east of the Appalachian Mountains. Results showed that the larger-scale differences detailed in Chapters 2 and 3 significantly influenced the initiation of convection, frontal slope, deformation, vorticity and vorticity tendency, and ultimately turbulence downscale. The 13 Jan 2000 event demonstrates the potential for high concentrations of vorticity (implied vortex tubes), wave breaking, and severe turbulence that fairly weak convection can have given the scenario set forth in the hypothesis. *Key to these differences are the more intense terrain-induced mesoscale frontal coupling in the vertical and its implications for rapid fluctuations of TKE.*
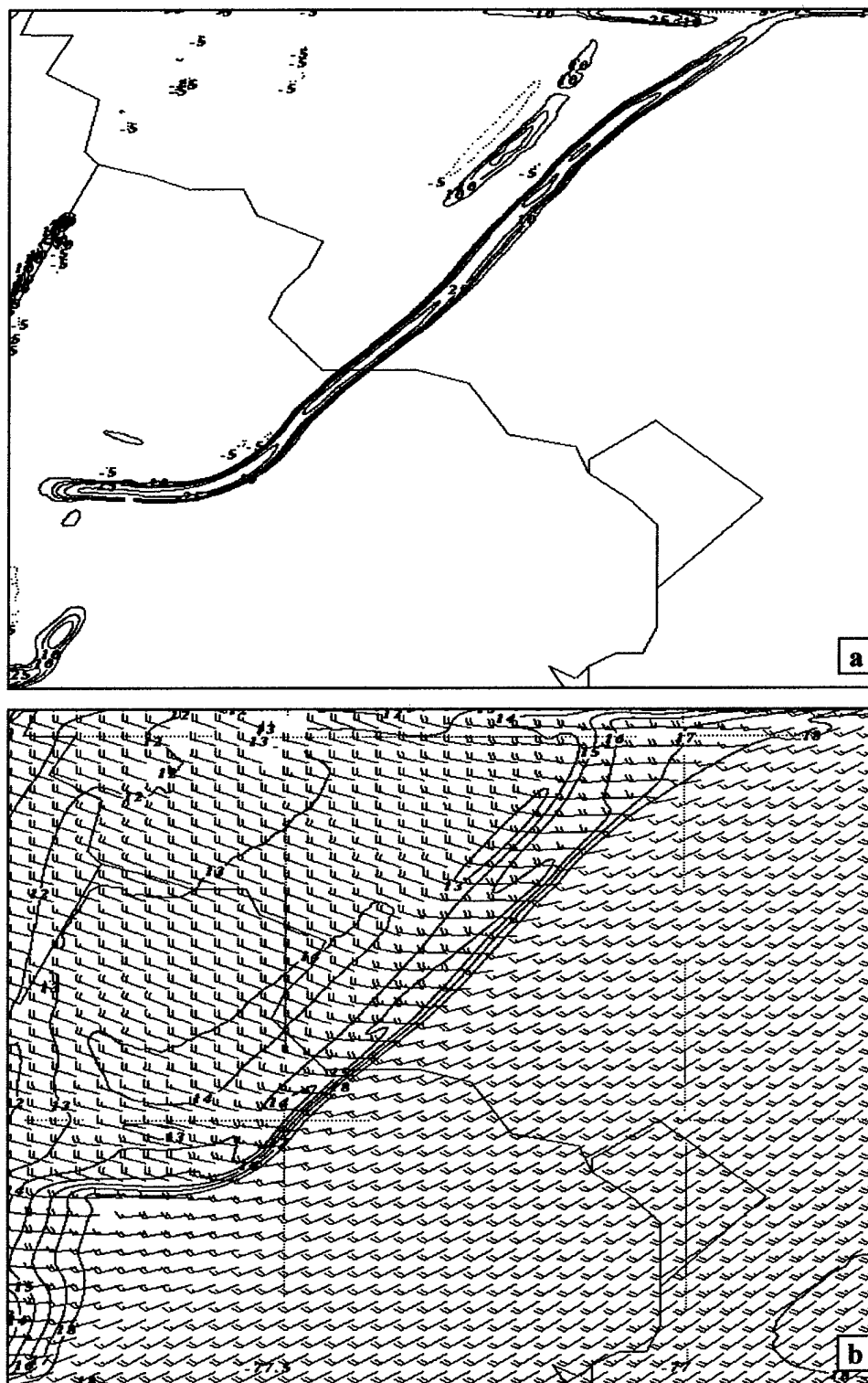
Figure 1. (a) 970 hPa frontogenesis (deg C/100km/3hr) valid 1900 UTC
28 Dec 1988, (b) 970 hPa temperature (^{0}C) contoured every degree and
wind (ms^{-1}) valid 1900 UTC 28 Dec 1988.
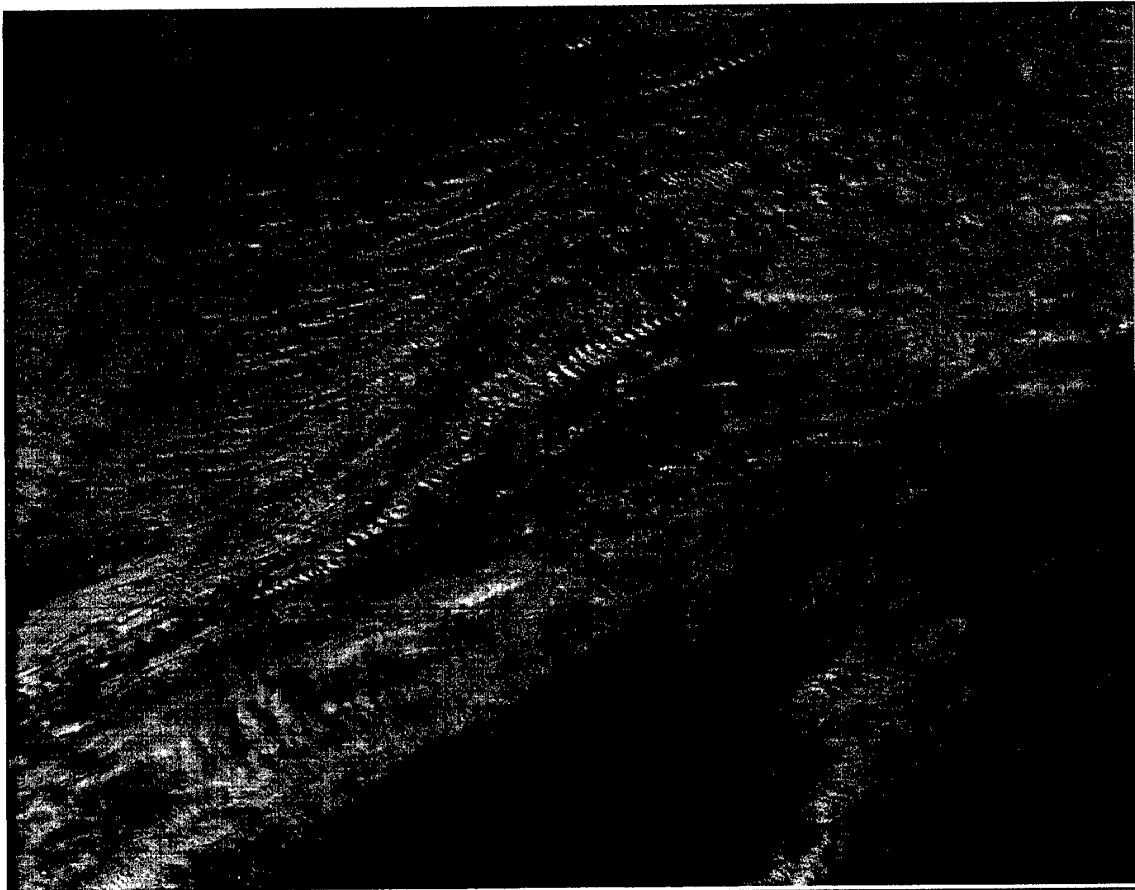
Figure 2. 1-km visible satellite imagery valid 1830 UTC 28 Dec 1988.
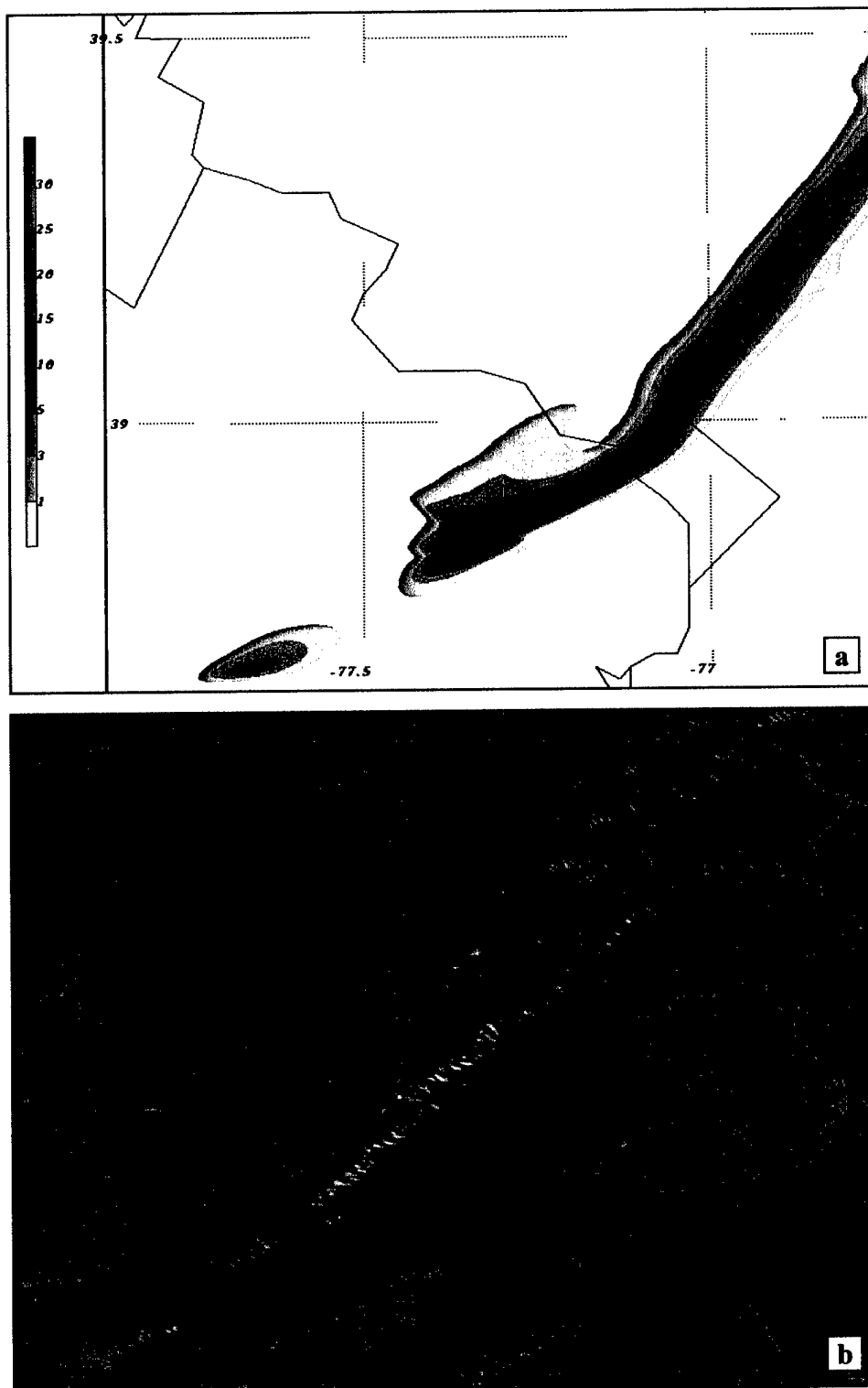
Figure 3. (a) 500-m NHMASS simulated precipitation (mm/hr) valid 1930 UTC 28 Dec 1988, (b) 1-km visible satellite imagery valid 1930 UTC 28 Dec 1988.

Figure 4. Simulated 700 hPa temperature (^{0}C) and wind (ms^{-1}) valid (a) 1700 UTC 13 Jan 2000, (b) 1800 UTC 13 Jan 2000.
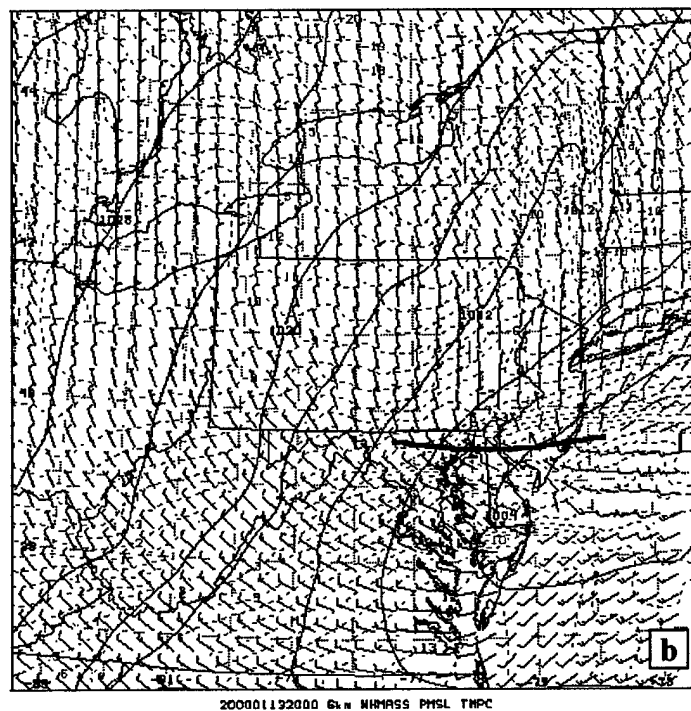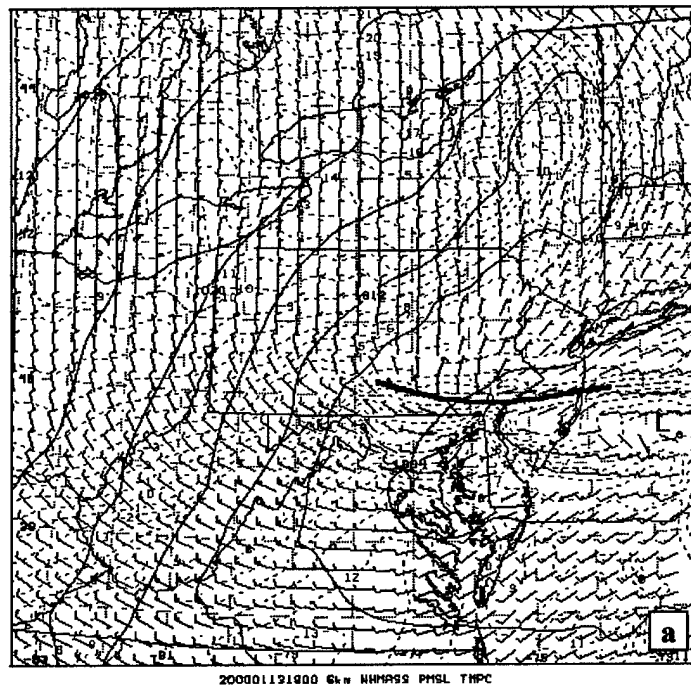
Figure 5. Simulated surface PMSL, wind (ms⁻¹), and temperature (⁰C) valid (a) 1800 UTC 13 Jan 2000 and (b) 2000 UTC 13 Jan 2000. Low-level cold surge identified by bold line.

268
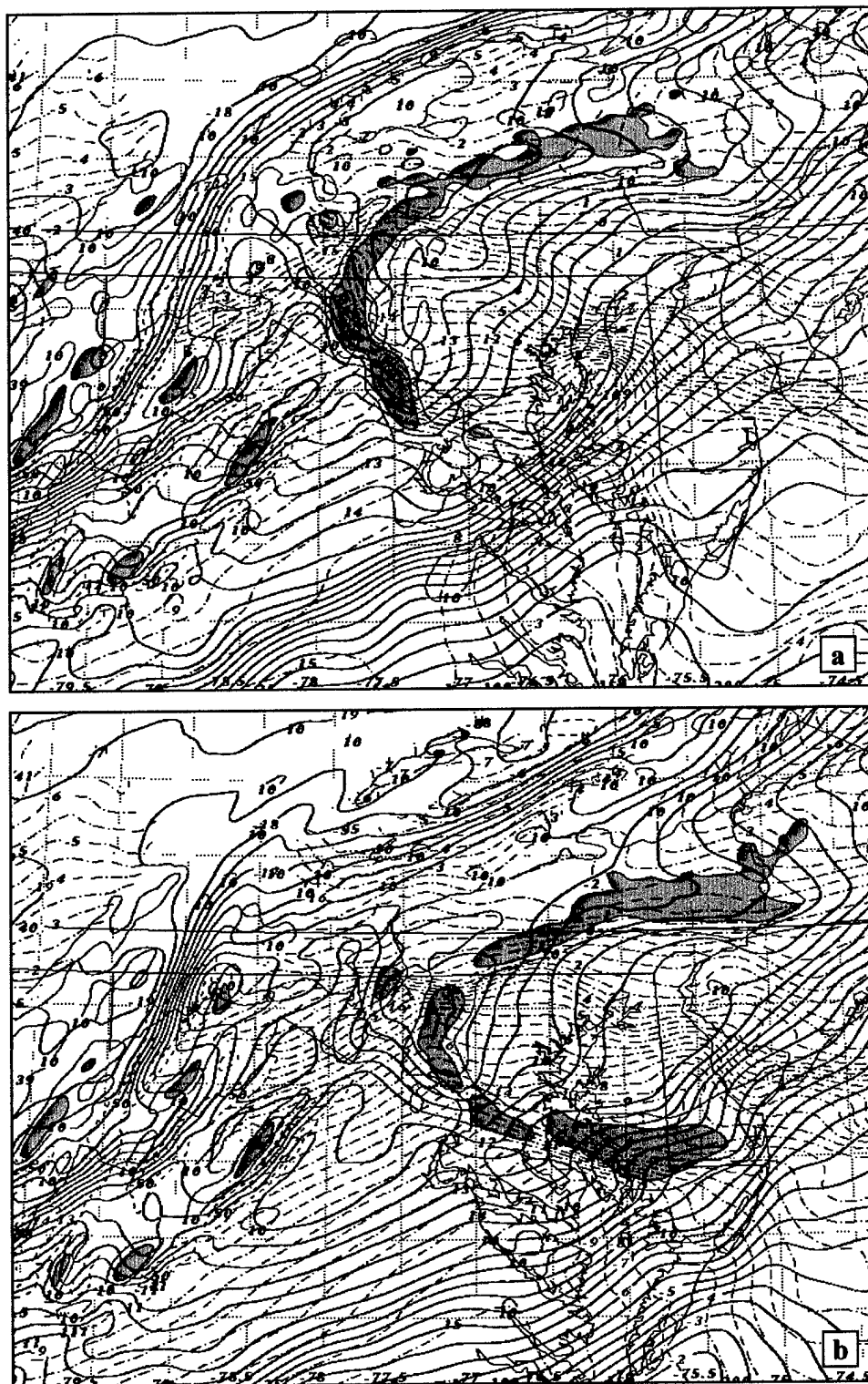
Figure 6. Simulated 970 hPa temperature (^{0}C, dashed black line), 700 hPa temperature (^{0}C, thick red line), and 850 hPa vertical velocity (25+ cms^{-1} shaded blue). Valid 13 Jan 2000 (a) 1800 UTC, (b) 1900 UTC.
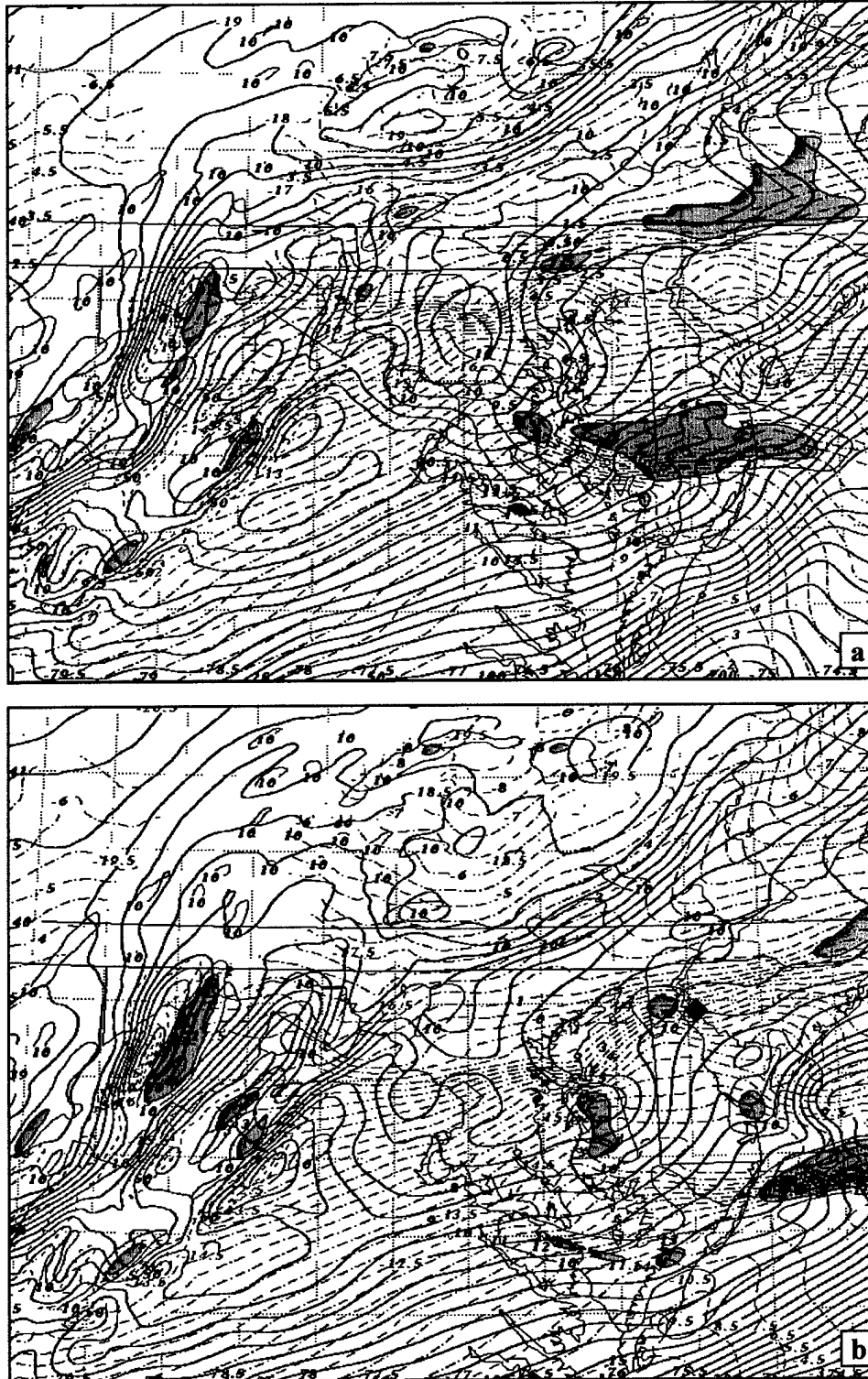
Figure 7. Simulated 970 hPa temperature (^{0}C, dashed black line), 700 hPa temperature (^{0}C, thick red line), and 850 hPa vertical velocity (25+ cms^{-1} shaded blue). Valid 13 Jan 2000 (a) 1930 UTC, (b) 2030 UTC. Approximate accident location identified by blue diamond in (b).
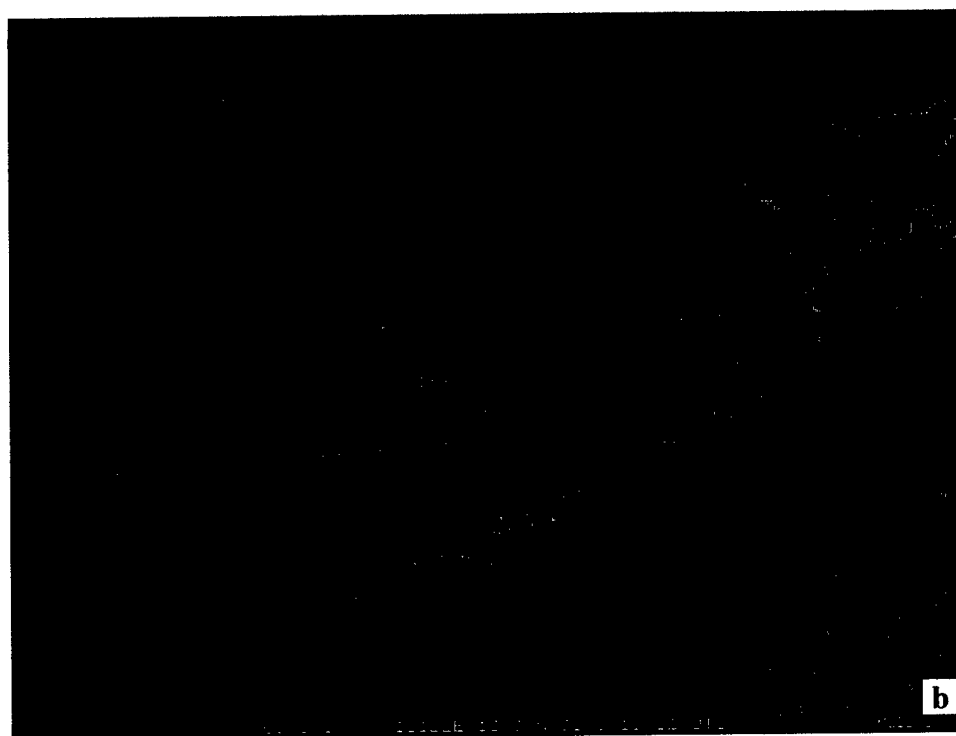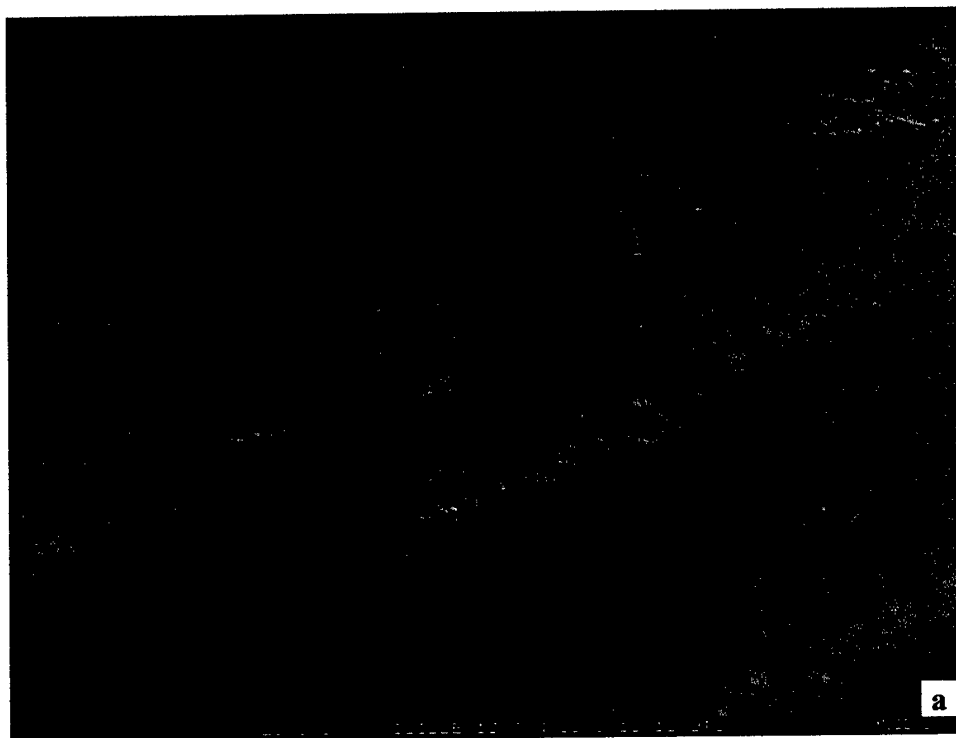
Figure 8. GOES-8 1-km Visible satellite imagery valid (a) 1815 UTC 13 Jan 2000, (b) 1902 UTC 13 Jan 2000. Cellular convection discussed in the text is encircled in blue.
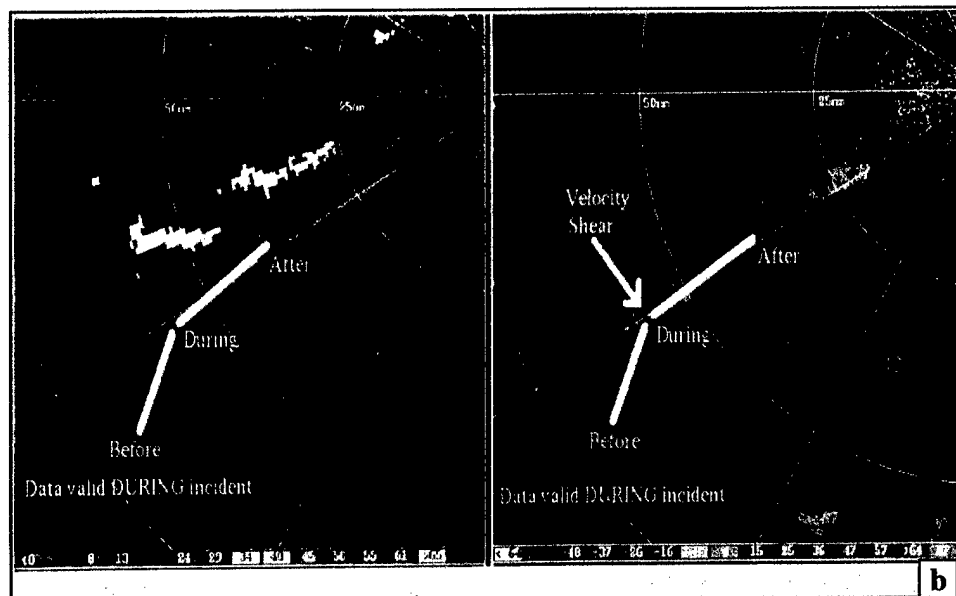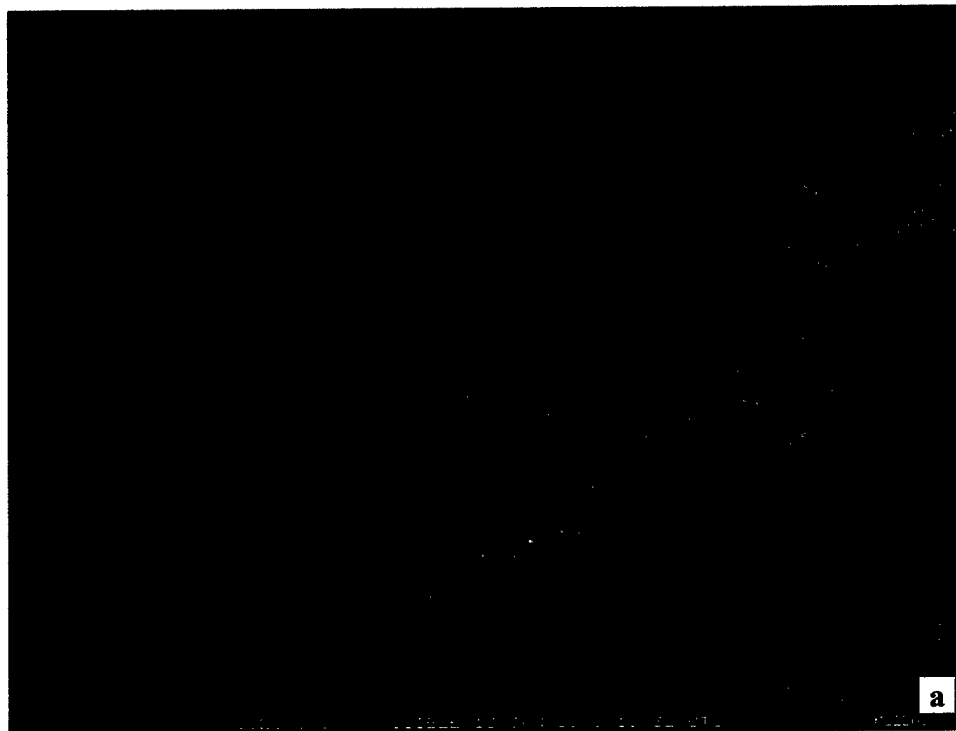
Figure 9. (a) GOES-8 1-km Visible satellite imagery valid 1932 UTC 13
Jan 2000. Cellular convection discussed in the text is encircled in blue,
(b) NEXRAD Radar image valid 1932 UTC 13 Jan 2000. Note: The
image on the left depicts dB rate as discussed in the text and the image on
the right depicts velocity shear. Aircraft flight path is indicated by solid
white line.
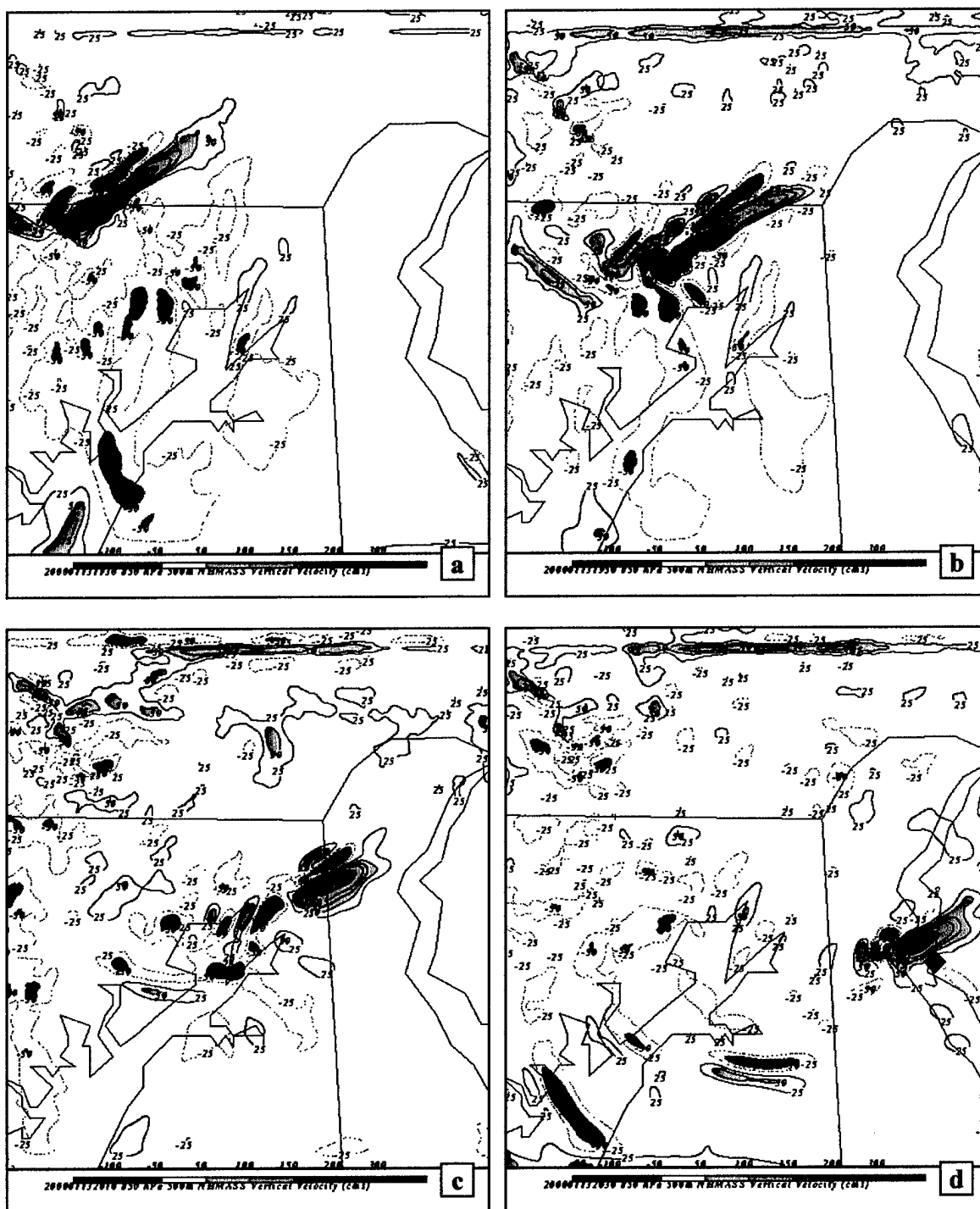
Figure 10. 500-m NHMASS simulated 850 hPa vertical velocity (cms^{-1}) valid 13 Jan 2000 (a) 1930 UTC, (b) 1950 UTC, (c) 2010 UTC, (d) 2030 UTC. Upward motion is indicated by blue-filled contours (maximum 3+ ms^{-1}) and downward motion in red. Approximate accident location identified by blue diamond in (d).

273
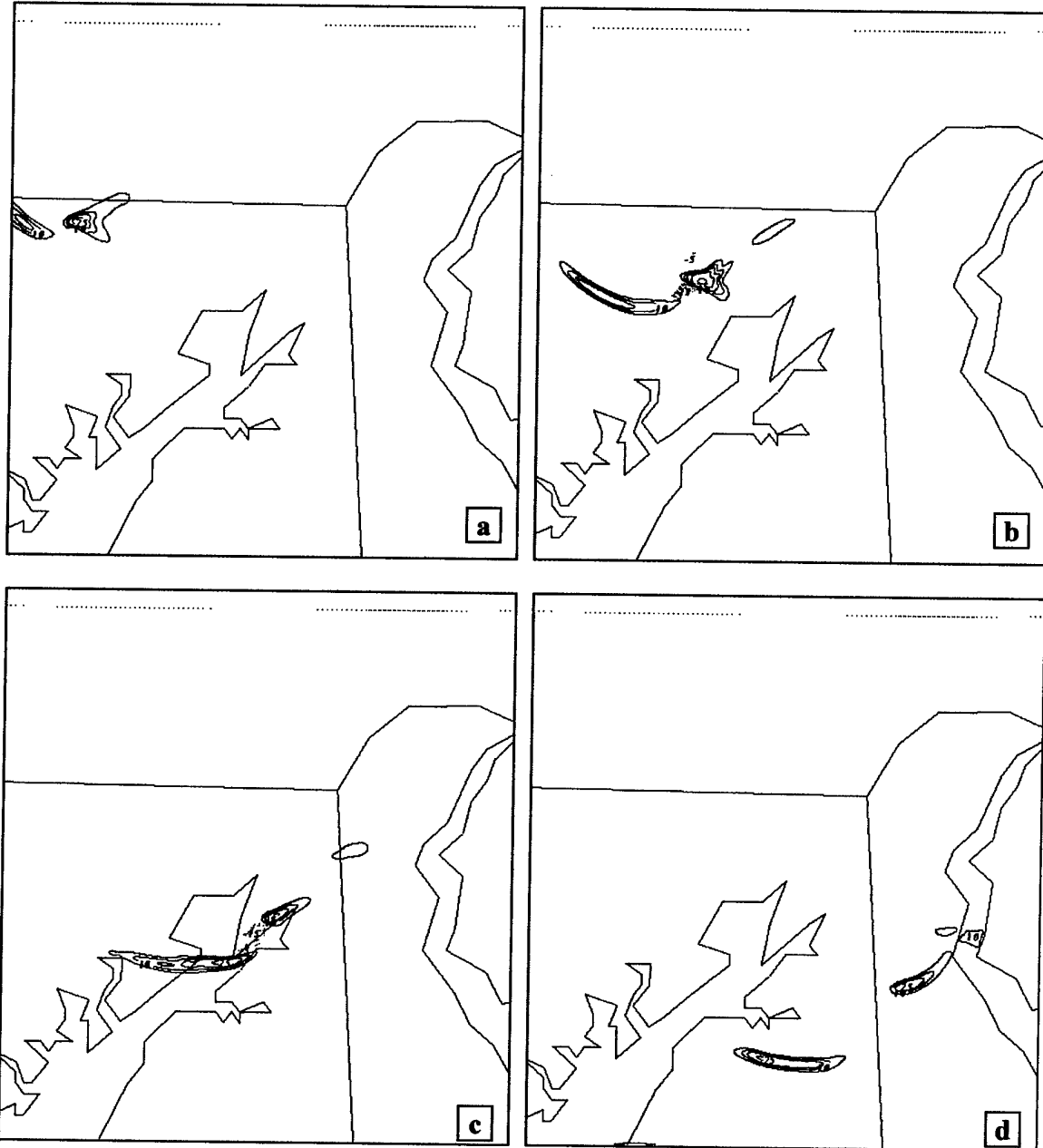
Figure 11. 500-m NHMASS simulated 970 hPa 2-d frontogenesis (deg C/100km/3hr) valid 13 Jan 2000 (a) 1930 UTC, (b) 1950 UTC, (c) 2010 UTC, (d) 2030 UTC.
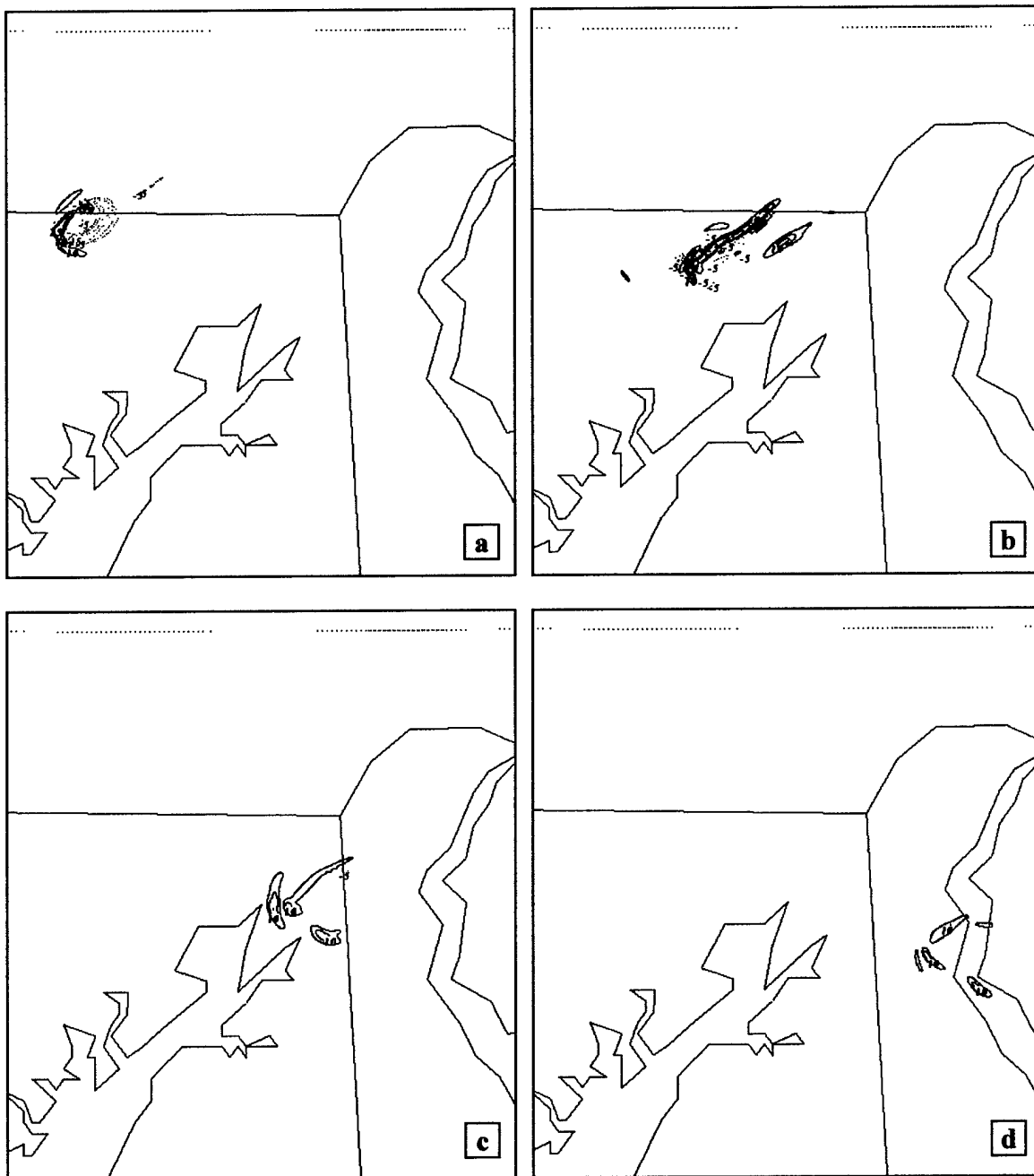
Figure 12. 500-m NHMASS simulated 775 hPa 2-d frontogenesis (deg C/100km/3hr) valid 13 Jan 2000 (a) 1930 UTC, (b) 1950 UTC, (c) 2010 UTC, (d) 2030 UTC.
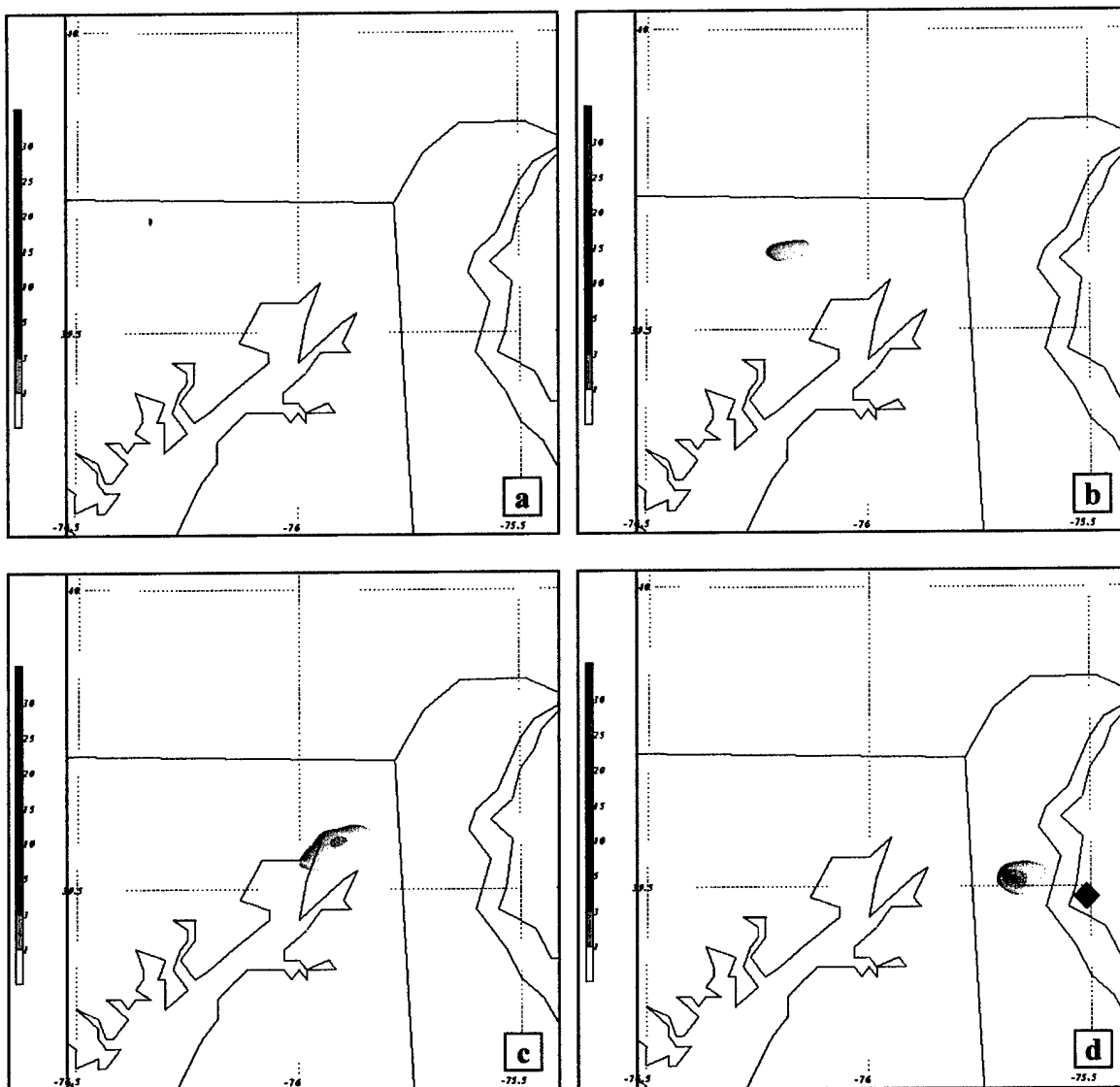
Figure 13. 500-m NHMASS simulated precipitation (mmhr⁻¹) valid 13 Jan 2000 (a) 1930
UTC, (b) 1950 UTC, (c) 2010 UTC, (d) 2030 UTC. Approximate accident location
identified by blue diamond in (d).
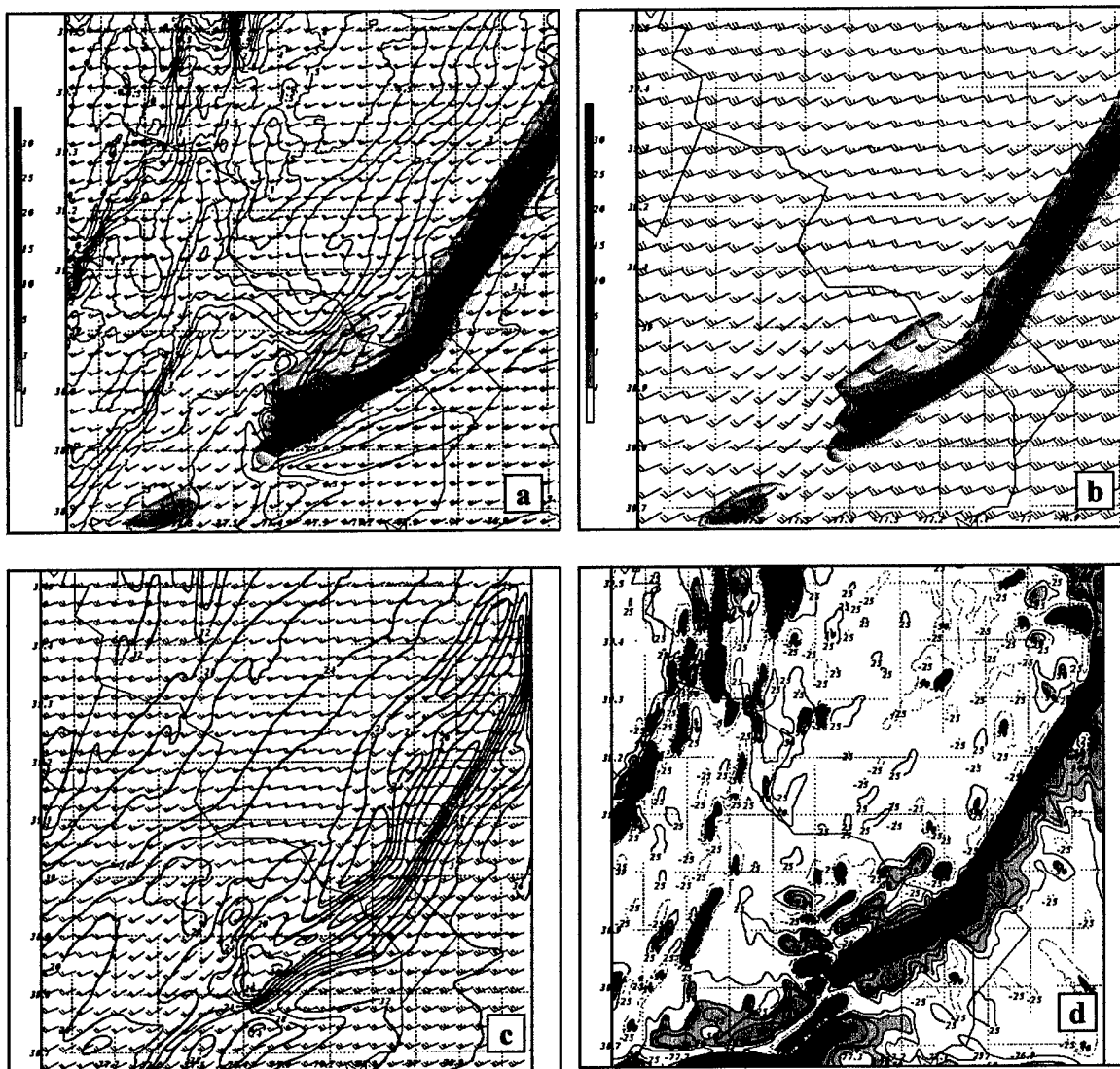
Figure 14. (a) 500-m NHMASS 775 hPa temperature (^{0}C), wind (ms^{-1}), and precipitation (mmhr^{-1}), (b) 500-m NHMASS precipitation (mmhr^{-1}) and 775 hPa wind (ms^{-1}), (c) 500-m NHMASS 775 hPa wind (ms^{-1}) and isotachs (contoured every 2 ms^{-1}), (d) 500-m NHMASS 775 hPa vertical velocity (cms^{-1}). All plots valid 1930 UTC 28 Dec 1988.
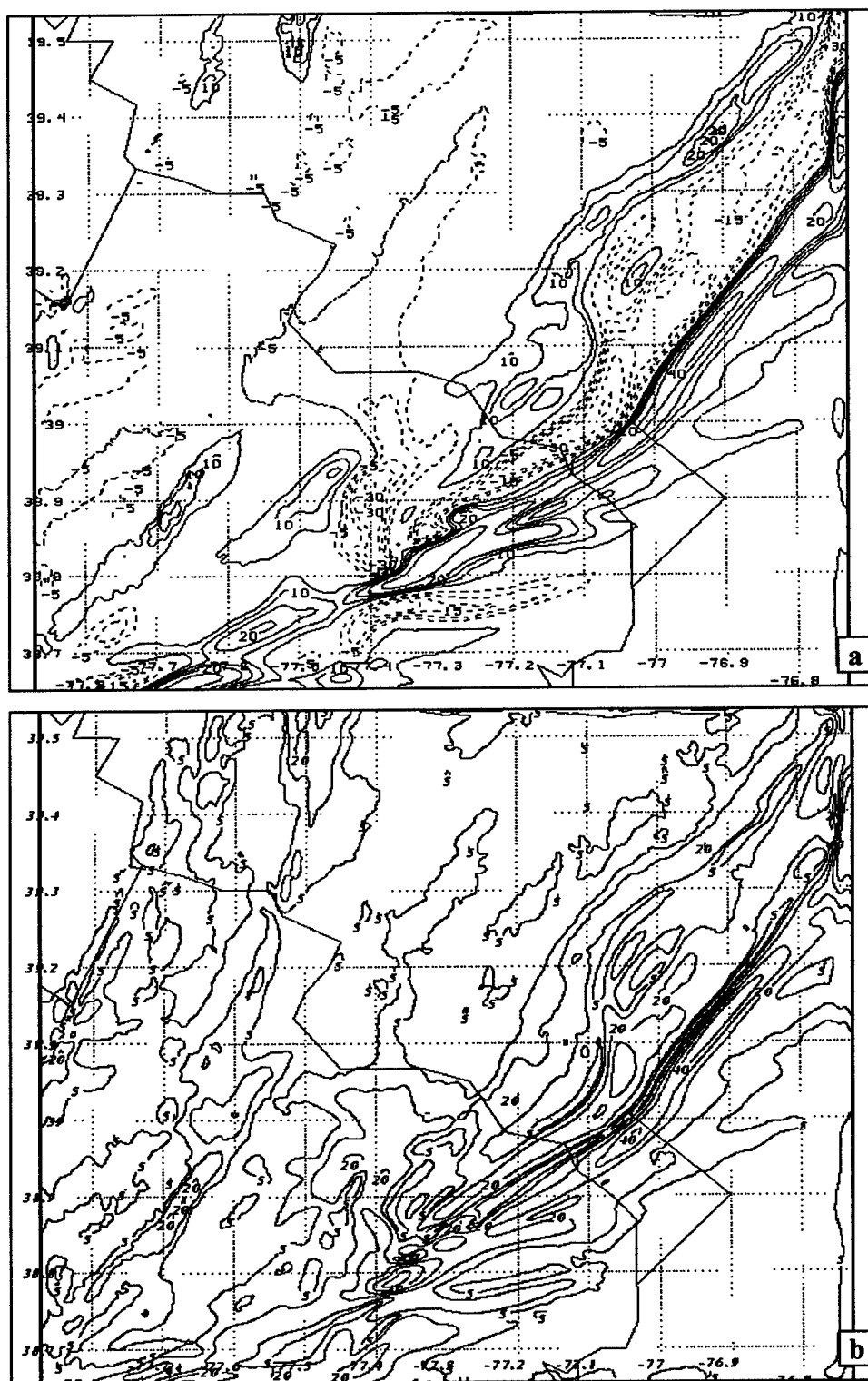
Figure 15. 500-m NHMASS (a) 775 hPa vertical vorticity $(x10^{-4}s^{-1})$, (b) 775 hPa deformation $(x10^{-4}s^{-1})$. Valid 1930 UTC 28 Dec 1988.

278
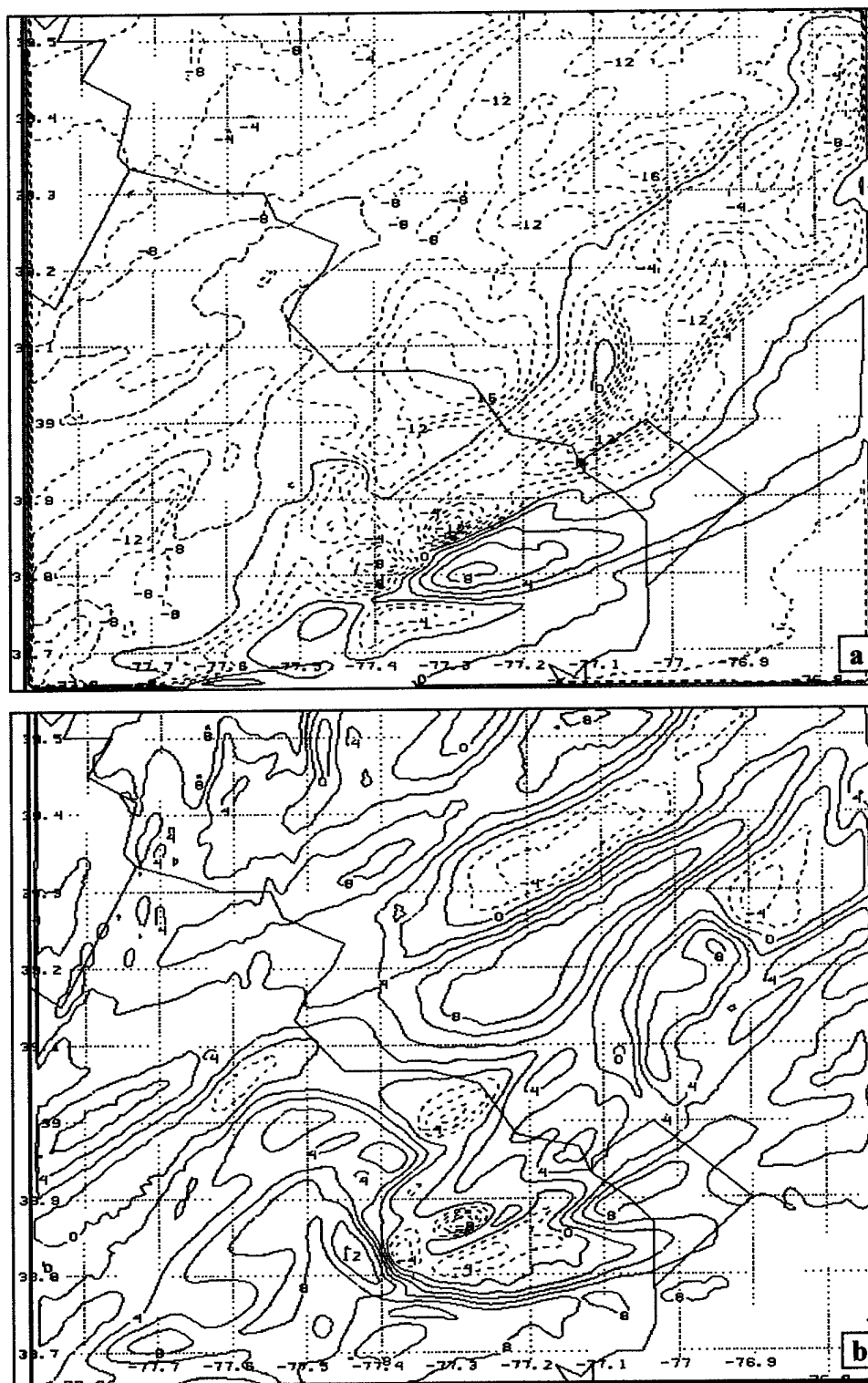
Figure 16. Valid 1930 UTC 28 Dec 1988. 500-m NHMASS (a) 2400m
X-space vorticity (x10^{-3}s^{-1}), (b) 2400m Y-space vorticity (x10^{-3}s^{-1}).
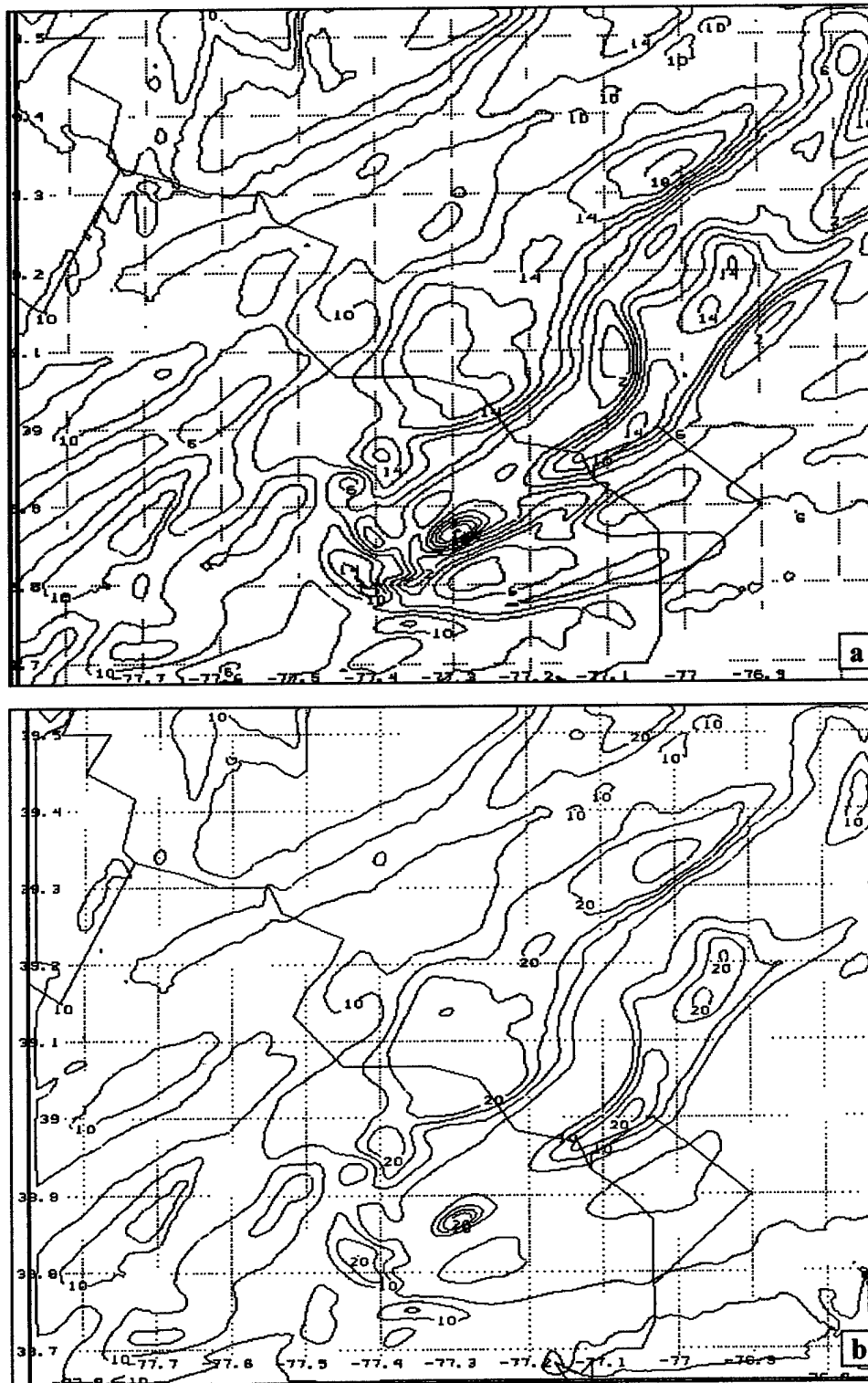
Figure 17. Valid 1930 UTC 28 Dec 1988. 500-m NHMASS (a) 2400m
horizontal vorticity (x10^{-3}s^{-1}), (b) 2400m enstrophy (x10^{-5}s^{-1}).
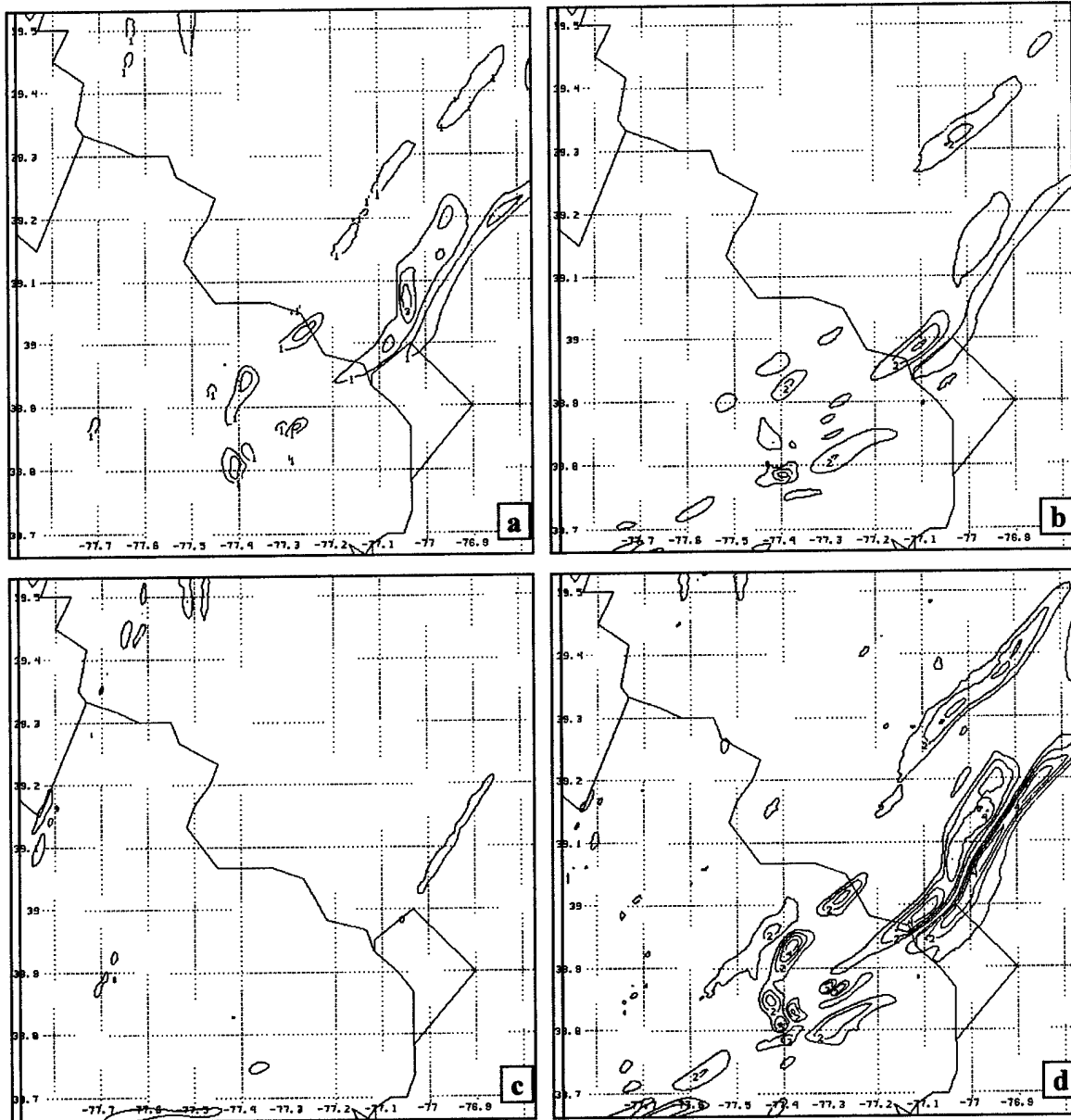
Figure 18. Valid 1930 UTC 28 Dec 1988. 500-m NHMASS (a) 2400m X-space vorticity tendency (x10^{-5}s^{-2}), (b) 2400m Y-space vorticity tendency (x10^{-5}s^{-2}), (c) 2400m Z-space vorticity tendency (x10^{-5}s^{-2}), (d) 2400m total vorticity tendency (x10^{-5}s^{-2}).
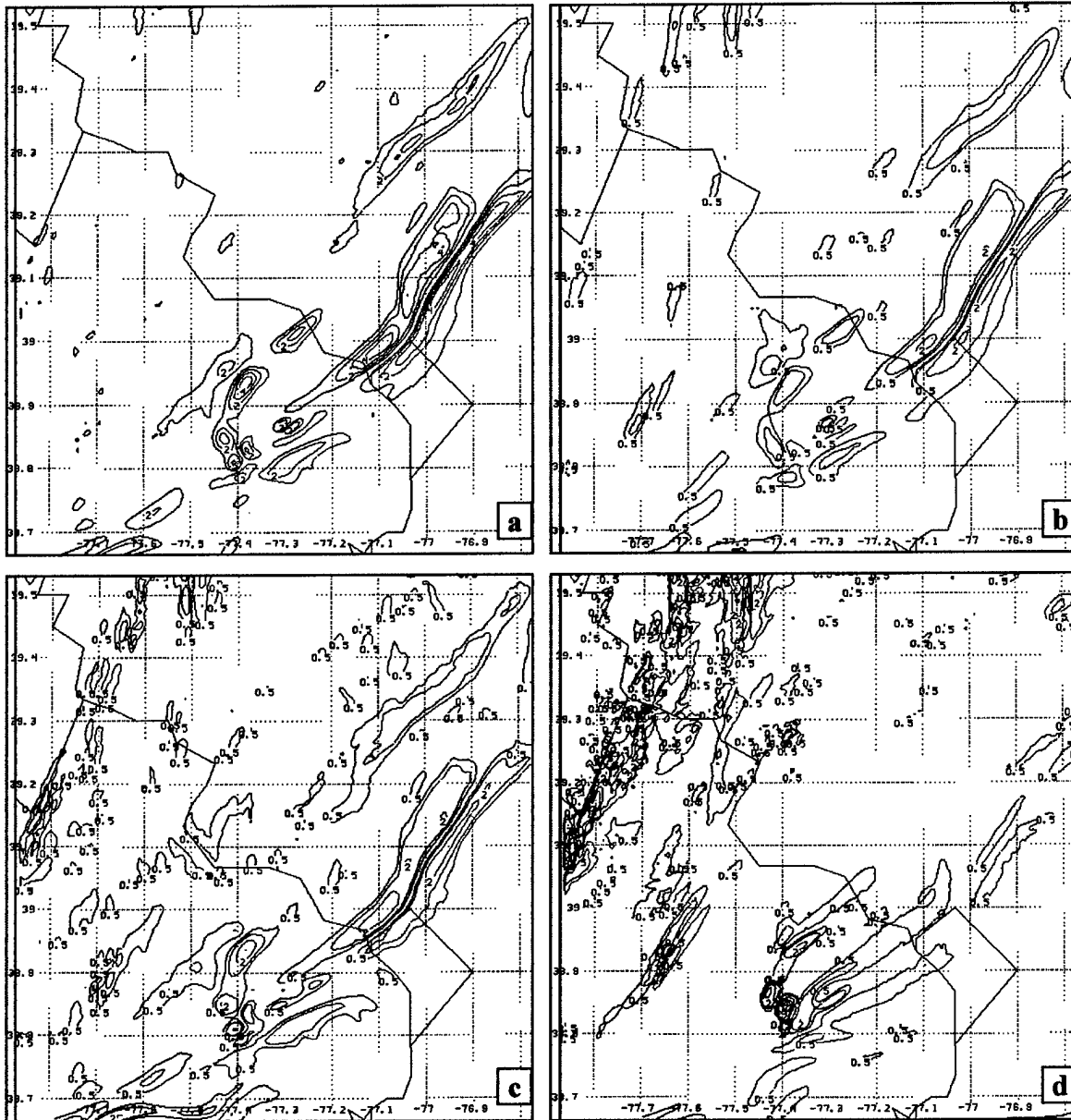
Figure 19. Valid 1930 UTC 28 Dec 1988. 500-m NHMASS (a) 2400m total vorticity tendency (x10^{-5}s^{-2}), (b) 2400m vorticity tendency CONV (x10^{-5}s^{-2}), (c) 2400m vorticity tendency TILT (x10^{-5}s^{-2}), (d) 2400m vorticity tendency SOL (x10^{-5}s^{-2}).
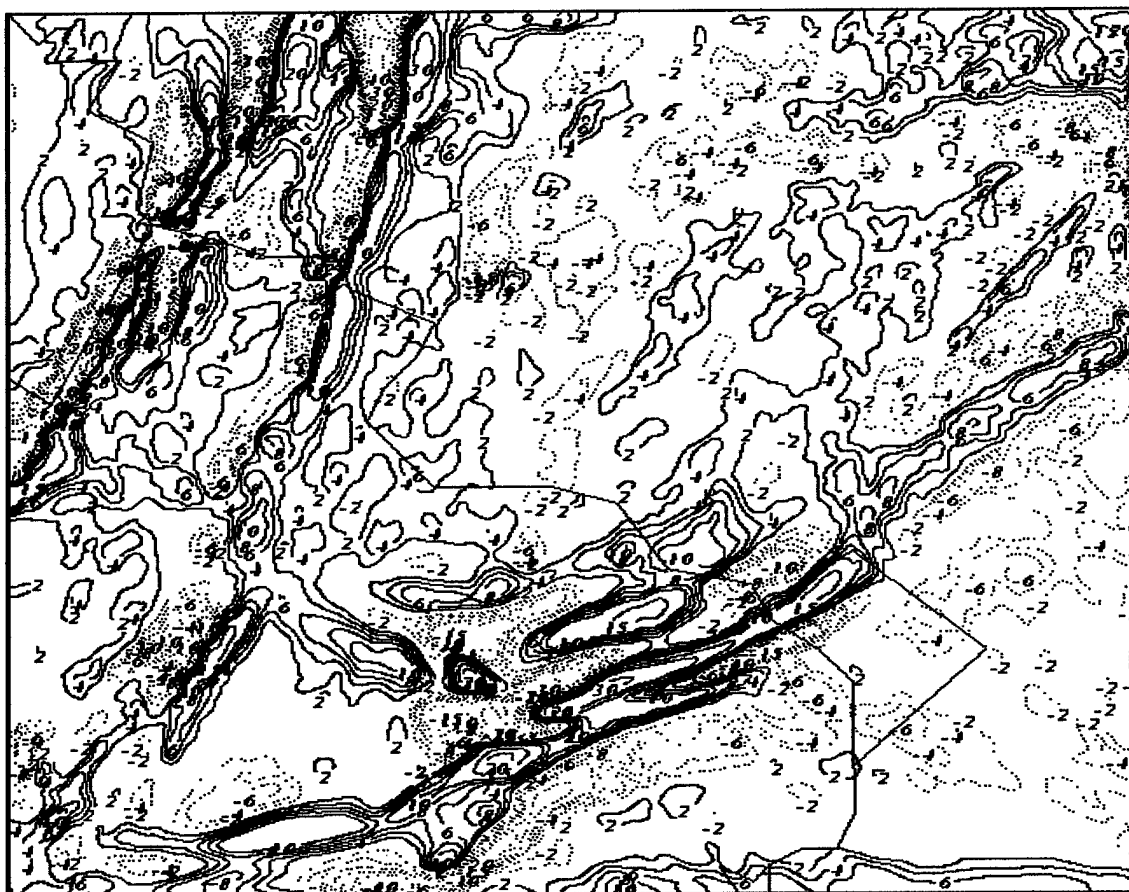
Figure 20. 500-m NHMASS 700-900 hPa dw/dz ($\times 10^{-1} s^{-1}$) valid 1930 UTC 28 Dec 1988.
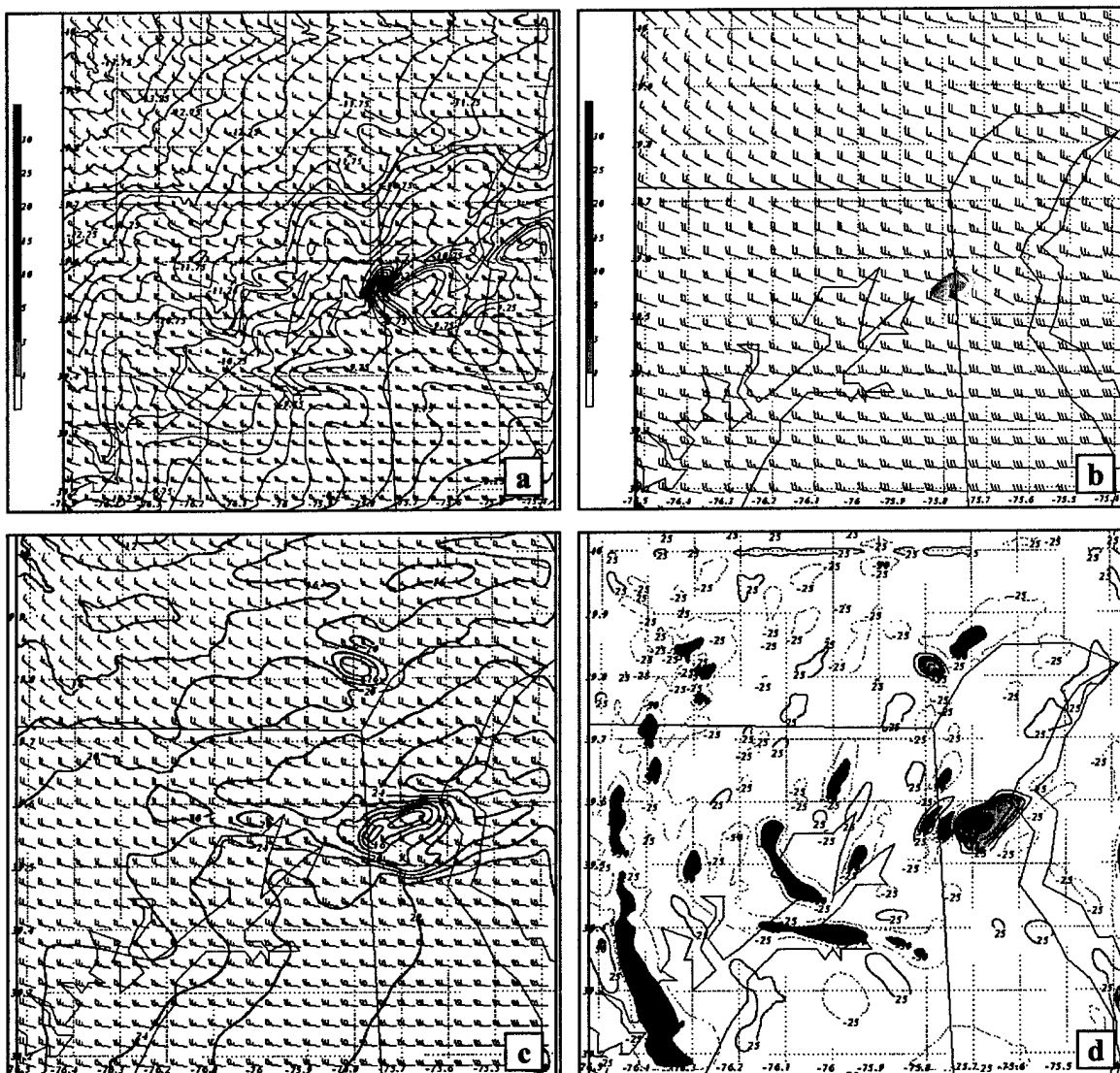
Figure 21. (a) 500-m NHMASS 775 hPa temperature (^{0}C), wind (ms^{-1}), and precipitation (mmhr^{-1}), (b) 500-m NHMASS precipitation (mmhr^{-1}) and 775 hPa wind (ms^{-1}), (c) 500-m NHMASS 775 hPa wind (ms^{-1}) and isotachs (contoured every 2 ms^{-1}), (d) 500-m NHMASS 775 hPa vertical velocity (cms^{-1}). All plots valid 2020 UTC 13 Jan 2000.
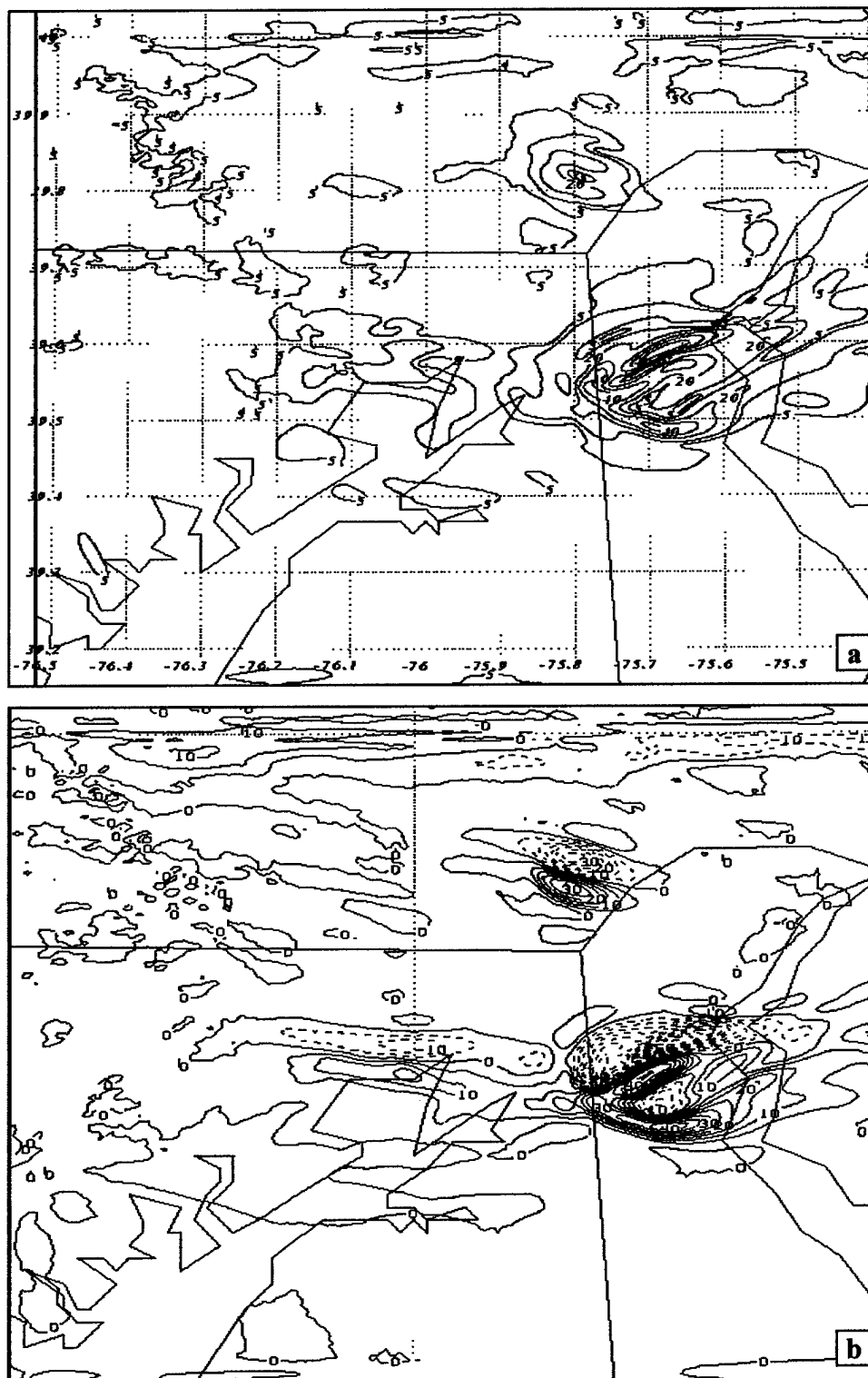
Figure 22. 500-m NHMASS (a) 775 hPa deformation $(x10^{-4}s^{-1})$, (b) 775 hPa vertical vorticity $(x10^{-4}s^{-1})$. Valid 2020 UTC 13 Jan 2000.
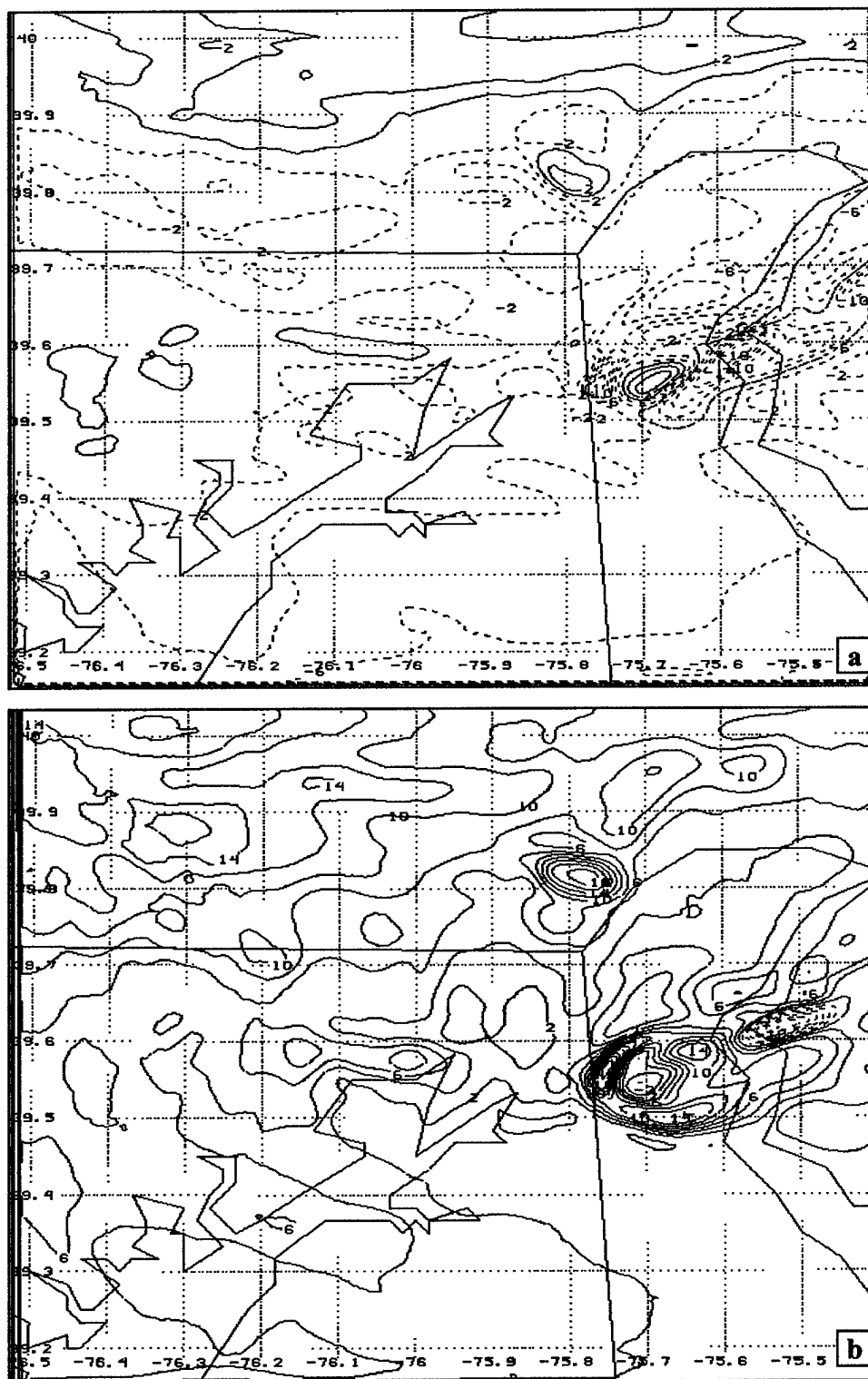
Figure 23. 500-m NHMASS (a) 2400m X-space vorticity (x10^{-3}s^{-1}), (b) 2400m Y-space vorticity (x10^{-3}s^{-1}). Valid 2020 13 Jan 2000.
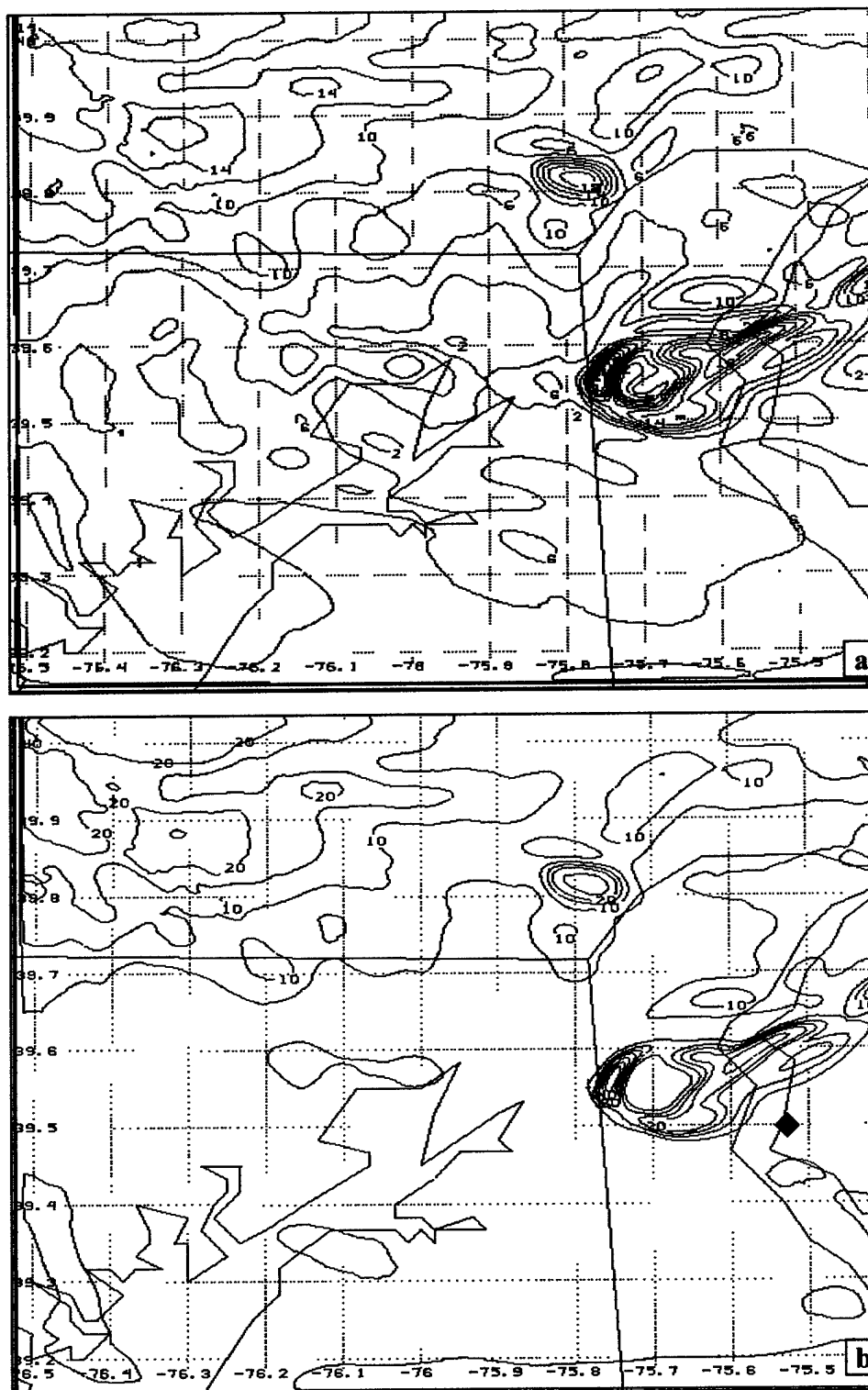
Figure 24. 500-m NHMASS (a) 2400m horizontal vorticity (x10^{-3}s^{-1}), (b)
2400m enstrophy (x10^{-5}s^{-1}). Valid 2020 UTC 13 Jan 2000. Approximate
accident location identified by blue diamond in (b).

287

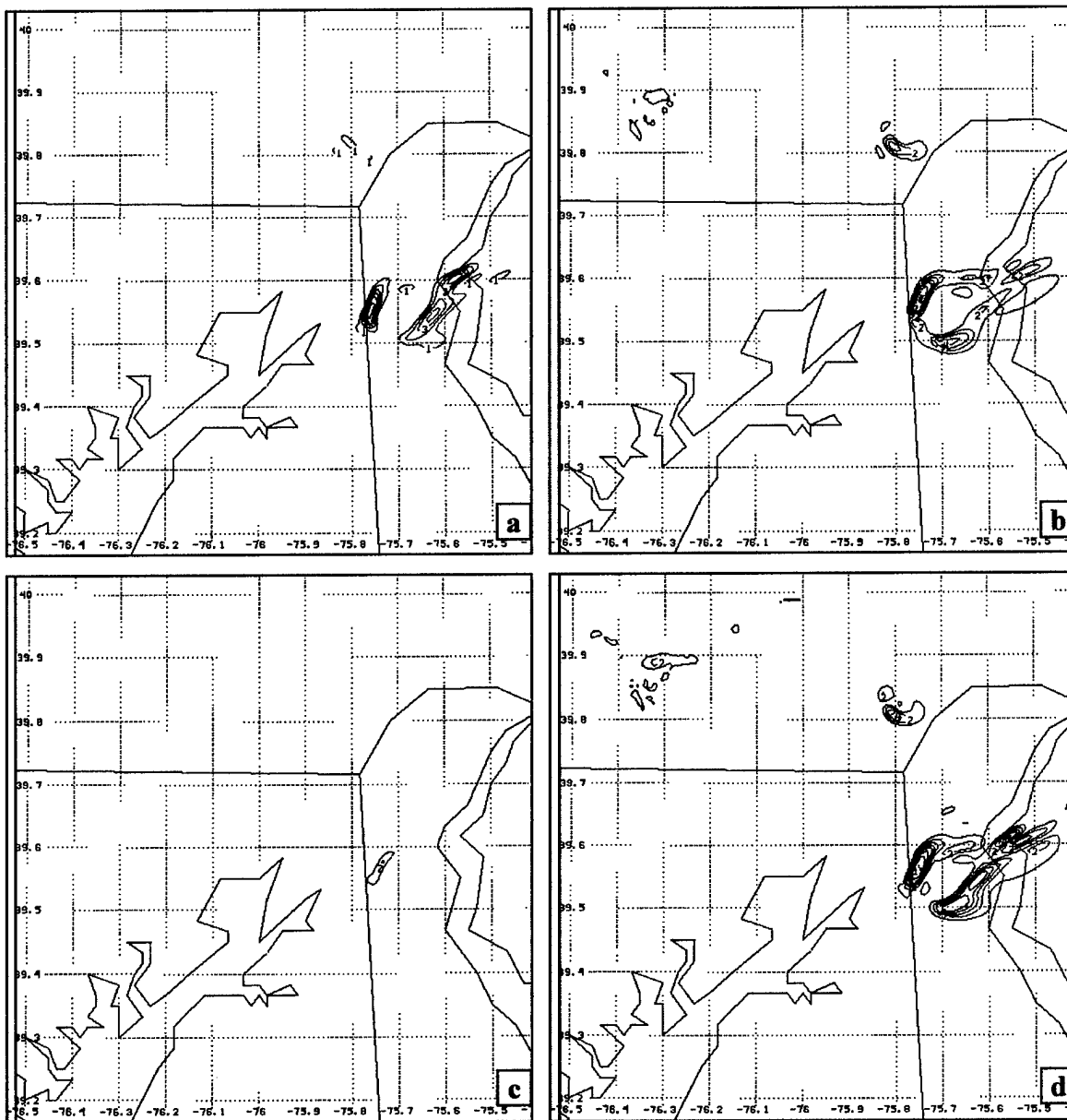Figure 25. 500-m NHMASS (a) 2400m X-space vorticity tendency (x10^{-5}s^{-2}), (b) 2400m Y-space vorticity tendency (x10^{-5}s^{-2}), (c) 2400m Z-space vorticity tendency (x10^{-5}s^{-2}), (d) 2400m total vorticity tendency (x10^{-5}s^{-2}). Valid 2020 UTC 13 Jan 2000.
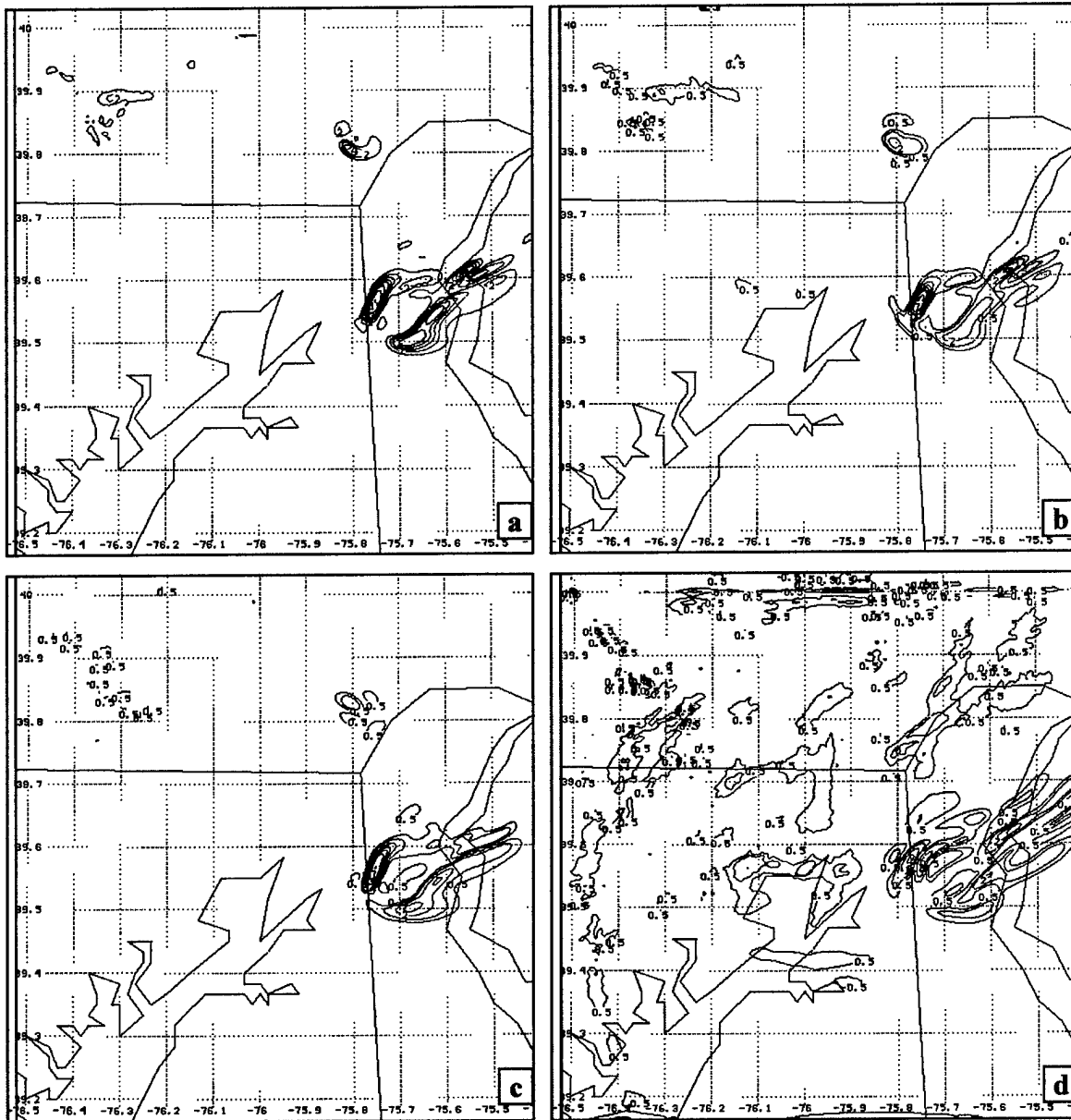
Figure 26. 500-m NHMASS (a) 2400m total vorticity tendency (x10^{-5}s^{-2}), (b) 2400m vorticity tendency CONV (x10^{-5}s^{-2}), (c) 2400m vorticity tendency TILT (x10^{-5}s^{-2}), (d) 2400m vorticity tendency SOL (x10^{-5}s^{-2}). Valid 2020 UTC 13 Jan 2000.
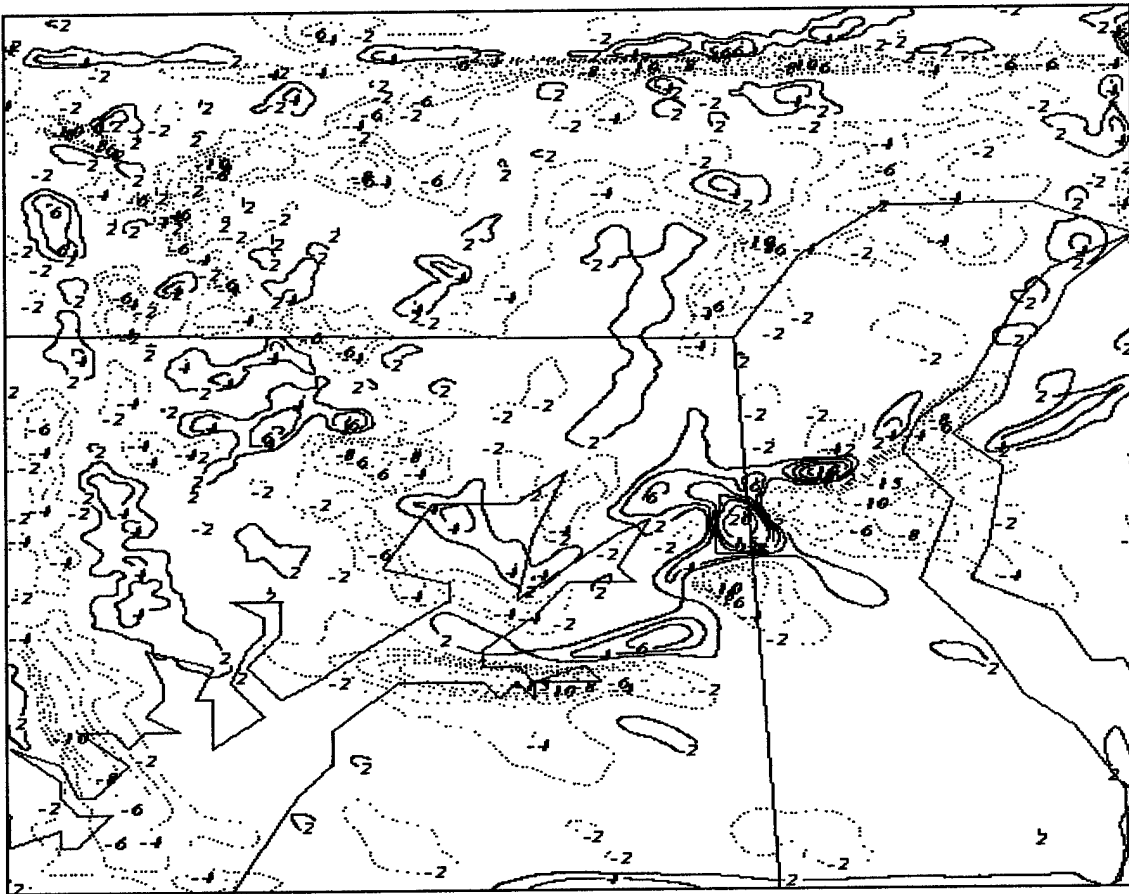
Figure 27. 500-m NHMASS 700-900 hPa dw/dz ($\times10^{-1}s^{-1}$) valid 2020 UTC 13 Jan 2000.

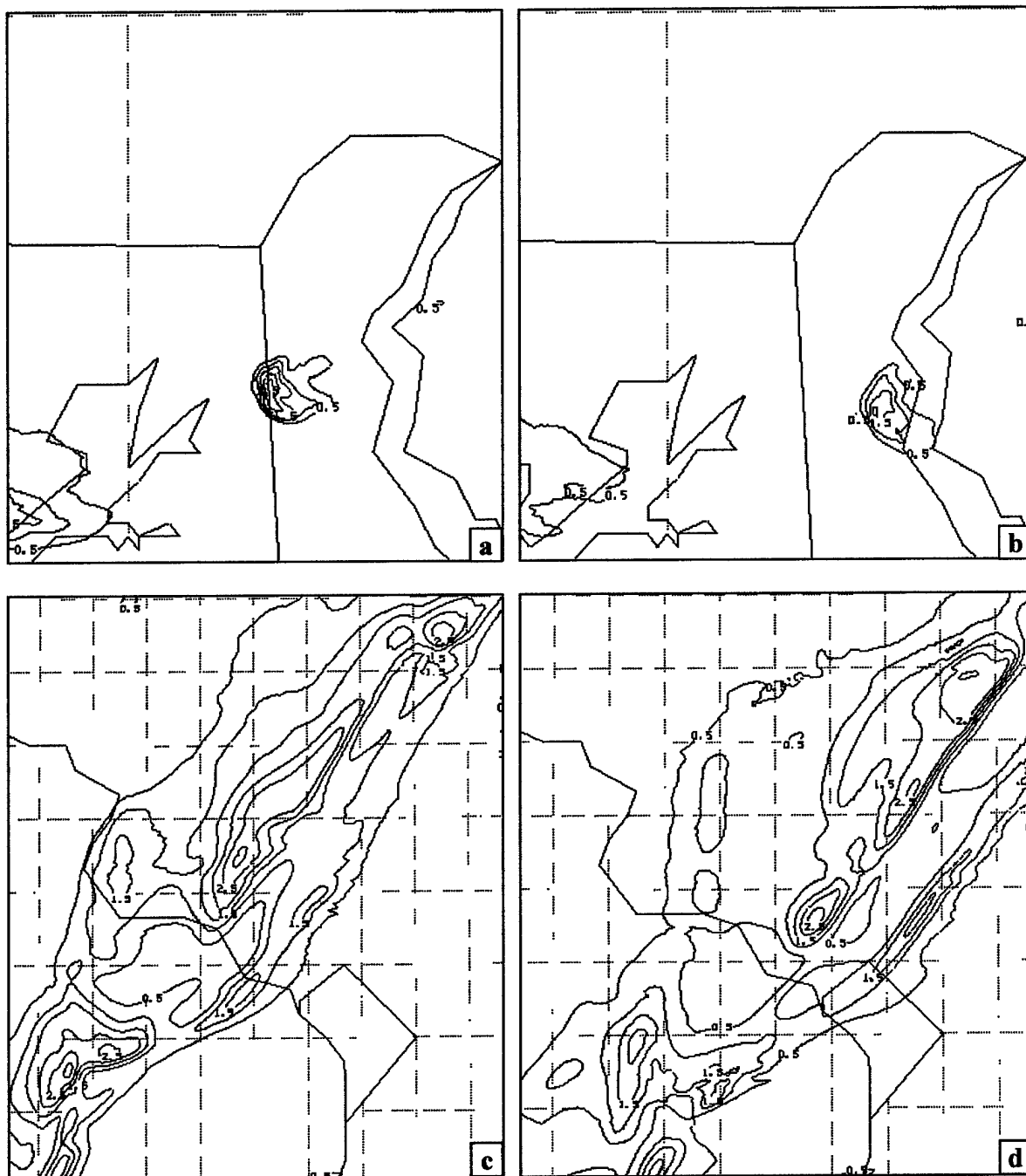Figure 28. NHMASS 500-m 700 hPaTKE (m^{2}s^{-2}) valid (a) 2020 UTC 13 Jan 2000, (b) 2030 UTC 13 Jan 2000, (c) 1920 UTC 28 Dec 1988, (d) 1930 UTC 28 Dec 1988.

Figure 29. 500-m NHMASS 2200-2600m Richardson Number valid (a) 2020 UTC 13 Jan 2000, (b) 2030 UTC 13 Jan 2000, (c) 1920 UTC 28 Dec 1988, (d) 1930 UTC 28 Dec 1988.
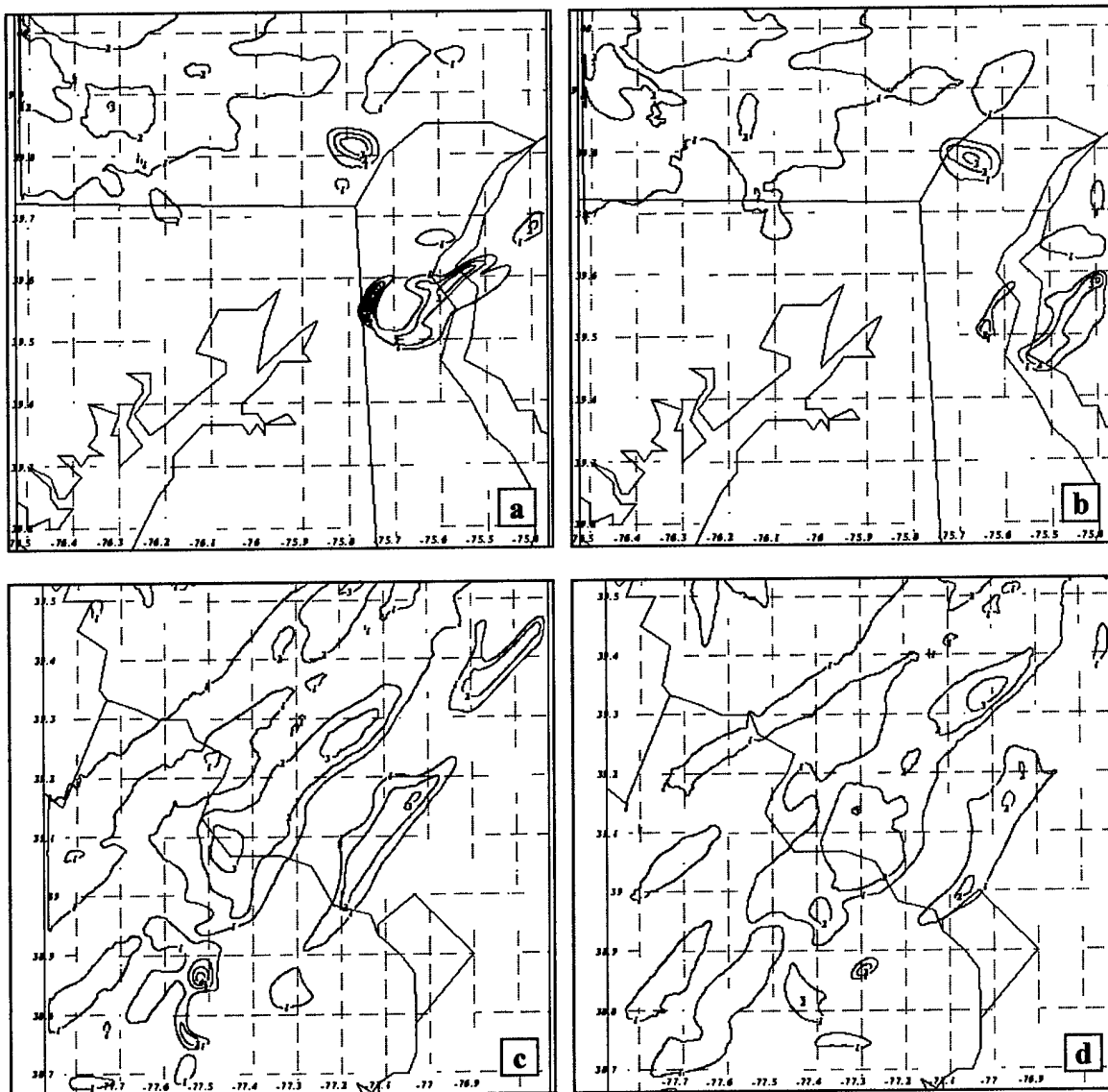
Figure 30. 500-m NHMASS 2400m Enstrophy ($\times 10^{-4}$ s^{-2}) valid (a) 2020 UTC 13 Jan 2000, (b) 2030 UTC 13 Jan 2000, (c) 1920 UTC 28 Dec 1988, (d) 1930 UTC 28 Dec 1988. Enstrophy greater than 2 x 10^{-4} s^{-2} is shaded.
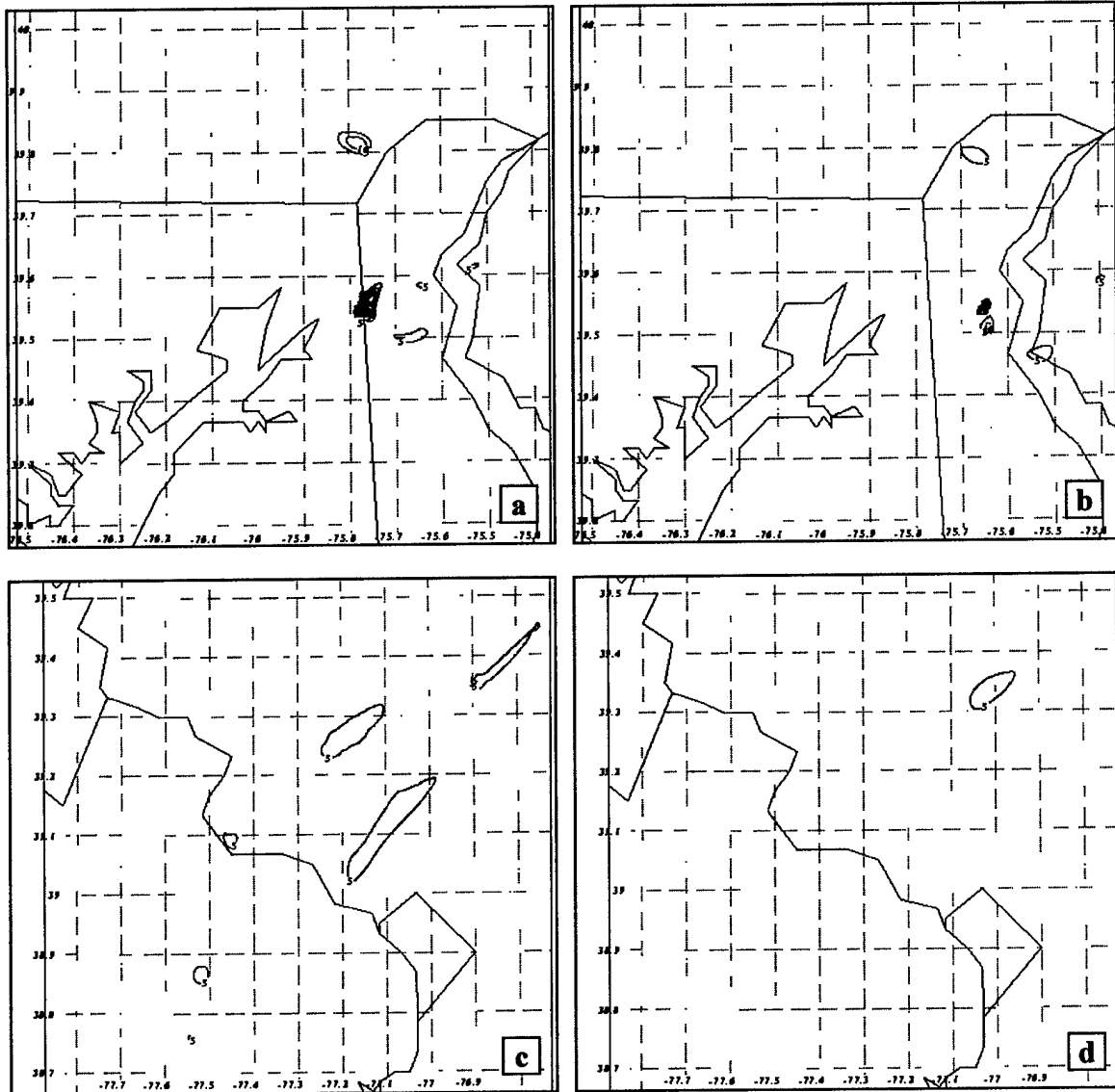
Figure 31. 500-m NHMASS 2400m Enstrophy/Richardson Number Quotient (x 10^{-4}s^{-2})
valid (a) 2020 UTC 13 Jan 2000, (b) 2030 UTC 13 Jan 2000, (c) 1920 UTC 28 Dec 1988,
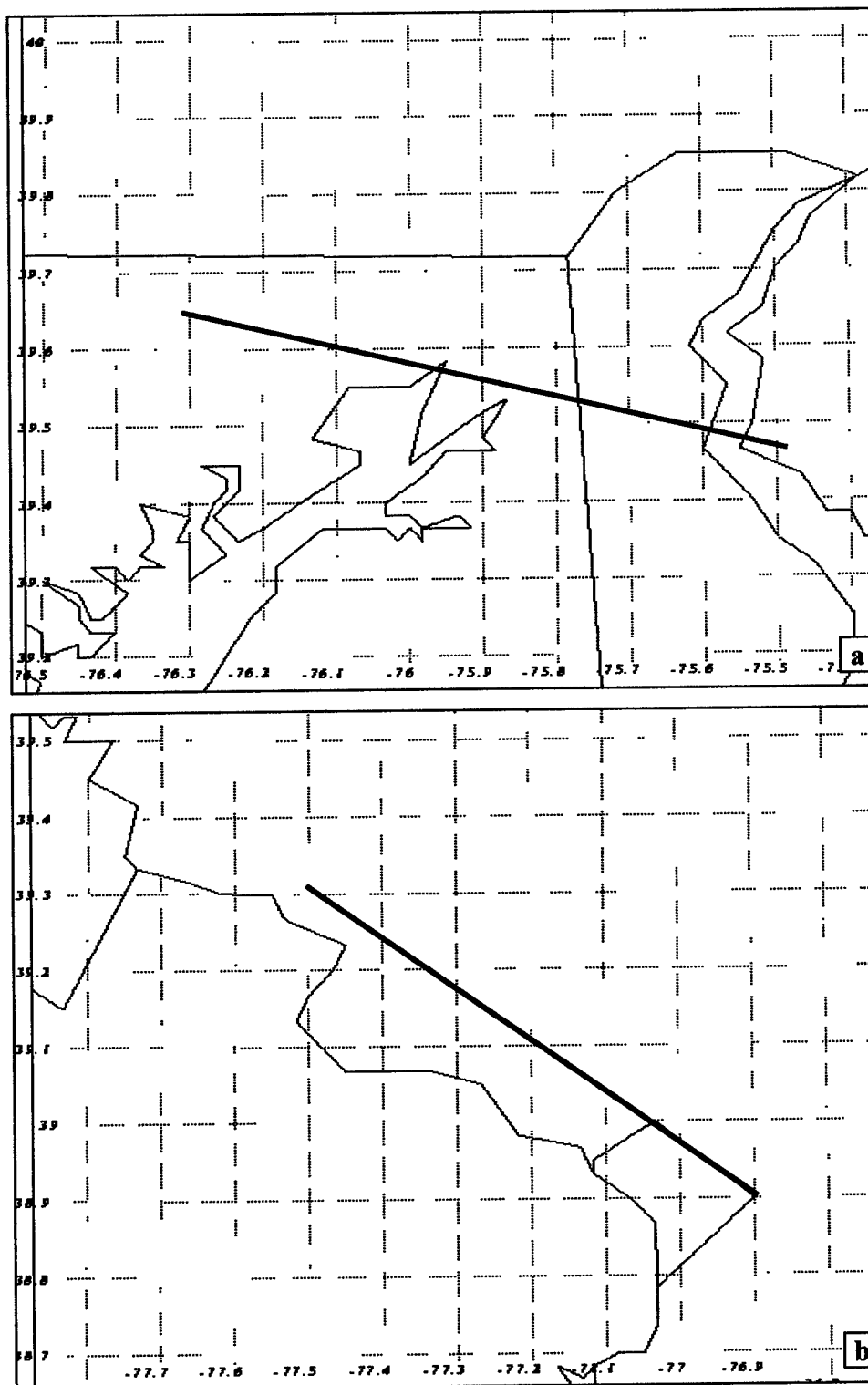(d) 1930 UTC 28 Dec 1988. Rienstrophy greater than 20 x 10^{-4} s^{-2} is shaded.

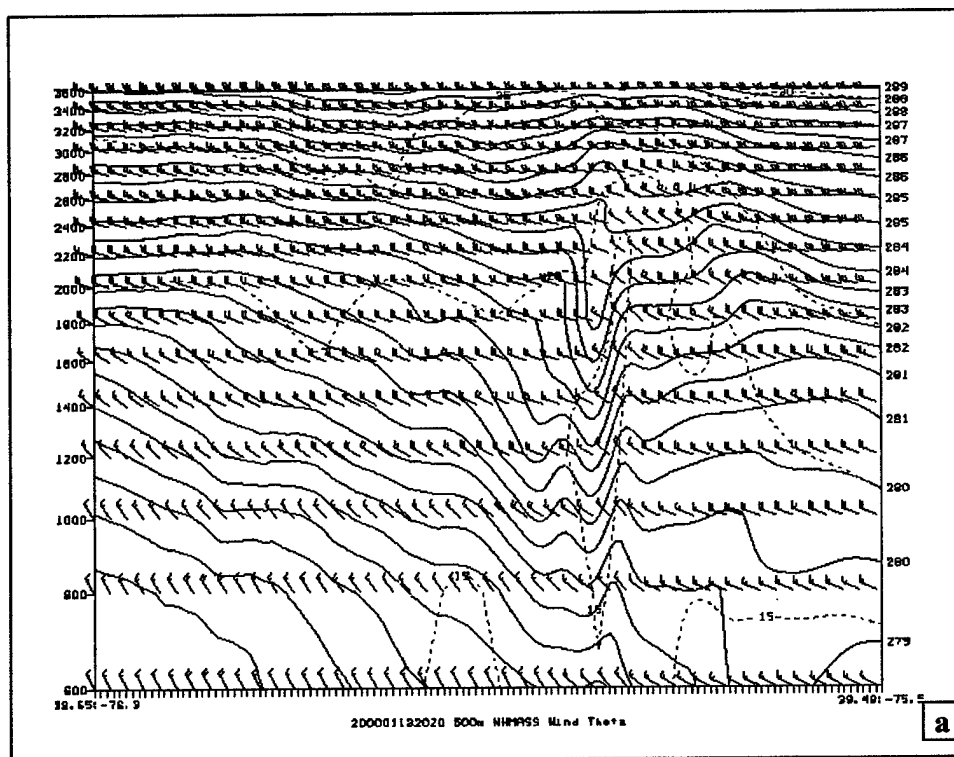Figure 32. Location of 500-m NHMASS cross sections for (a) 13 Jan
2000, (b) 28 Dec 1988.

Figure 33. (a) potential temperature (K) and wind (ms⁻¹), (b) potential temperature (K)
and vertical velocity (cms⁻¹) valid 2020 UTC 13 Jan 2000, (c) potential temperature (K)
and wind (ms⁻¹), (d) potential temperature (K) and vertical velocity (cms⁻¹) valid 1930
UTC 28 Dec 1988.

296
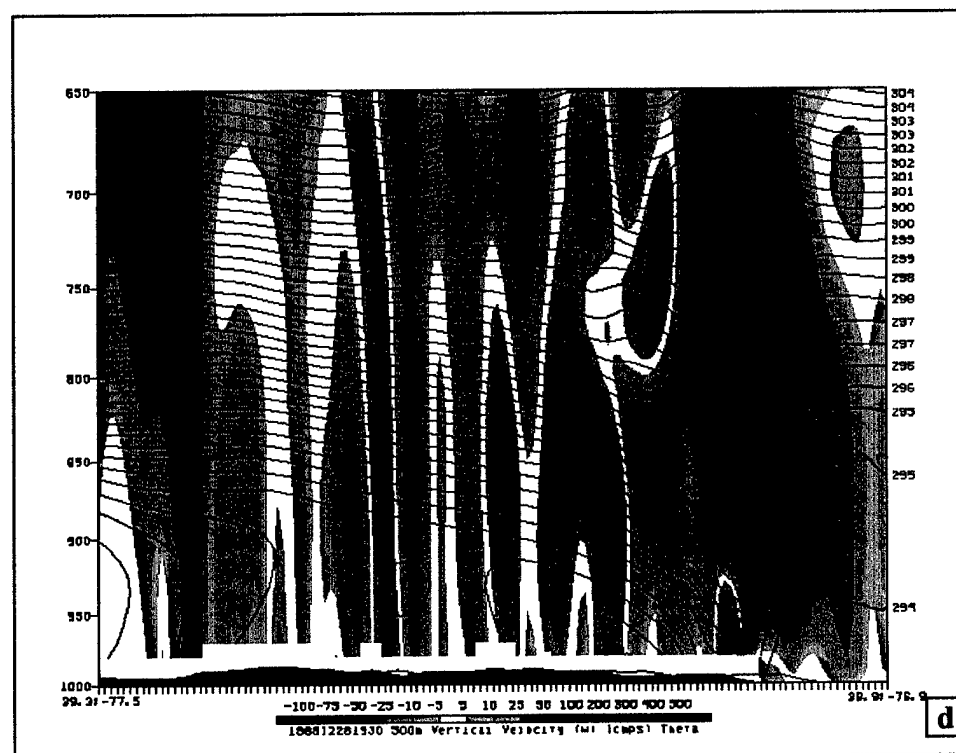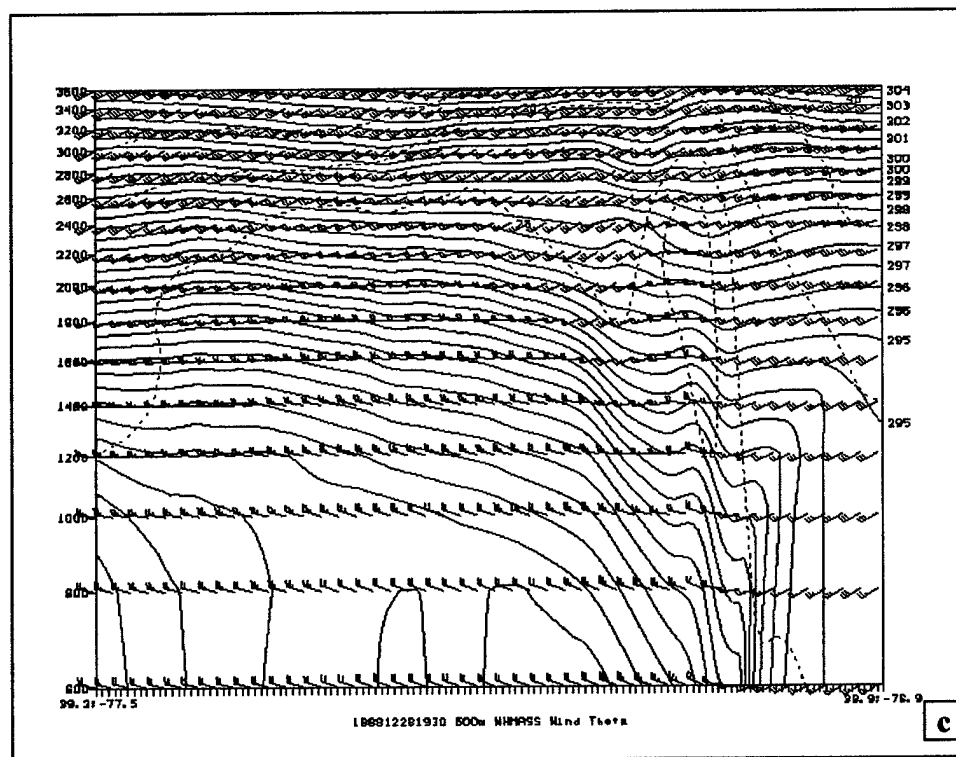
Figure 33. Concluded.

297
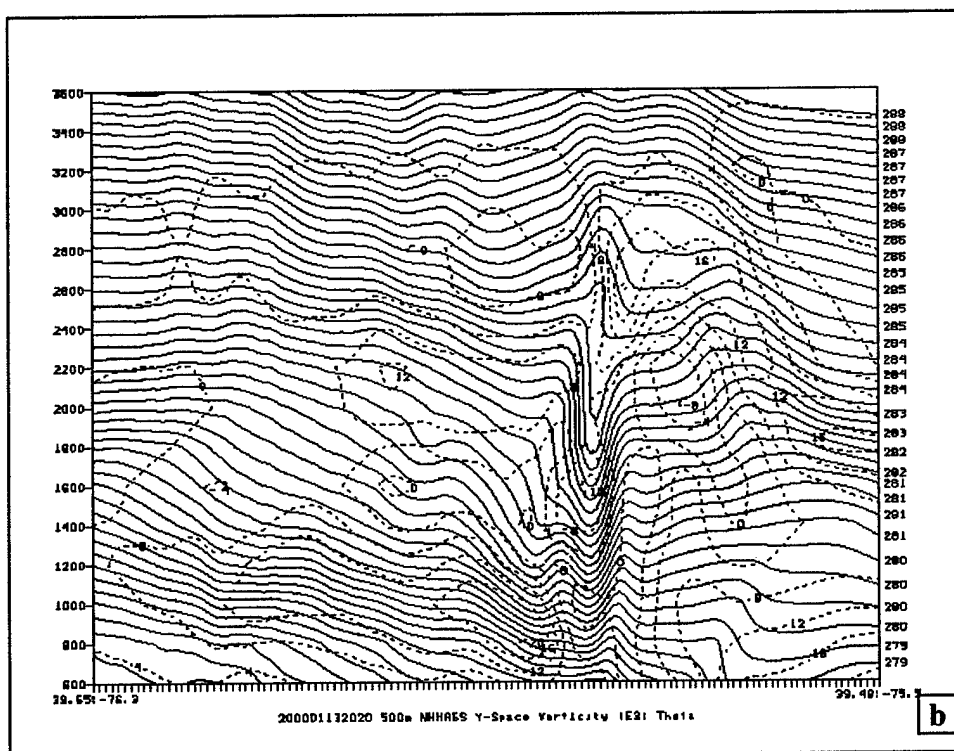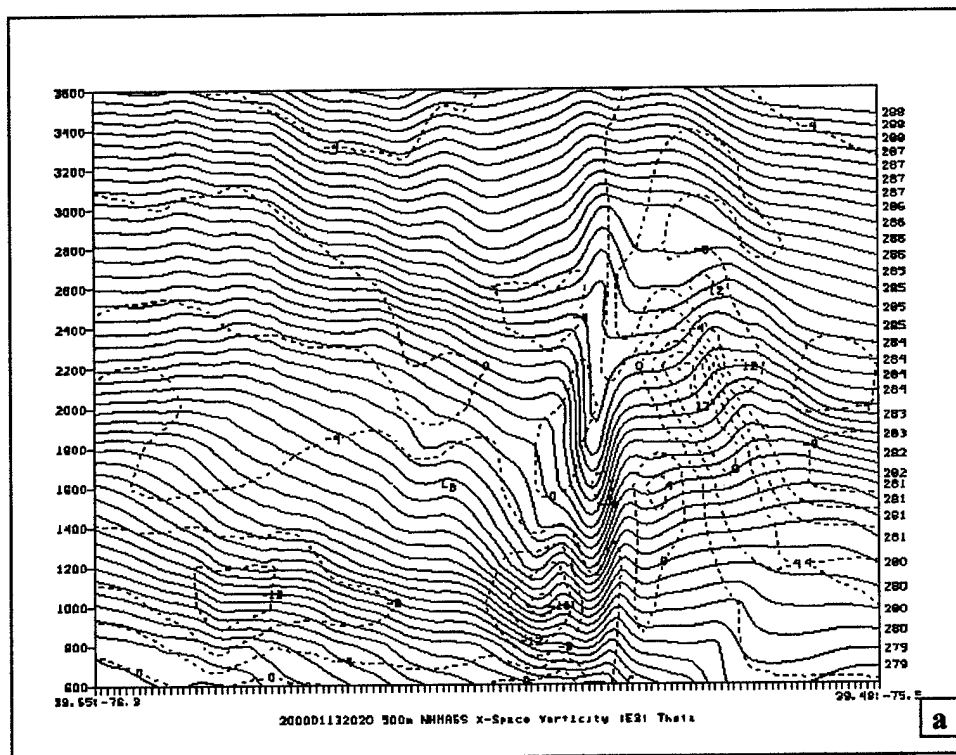
Figure 34. (a) X-space vorticity (x 10^{-3}s^{-1}), (b) Y-space vorticity (x 10^{-3}s^{-1}), (c) H-space vorticity (x 10^{-3}s^{-1}), (d) Z-space vorticity (x 10^{-4}s^{-1}). (a-d) valid 2020 UTC 13 Jan 2000. (e) X-space vorticity (x 10^{-3}s^{-1}), (f) Y-space vorticity (x 10^{-3}s^{-1}), (g) H-space vorticity (x 10^{-3}s^{-1}), (h) Z-space vorticity (x 10^{-4}s^{-1}). (e-h) valid 1930 UTC 28 Dec 1988.

298
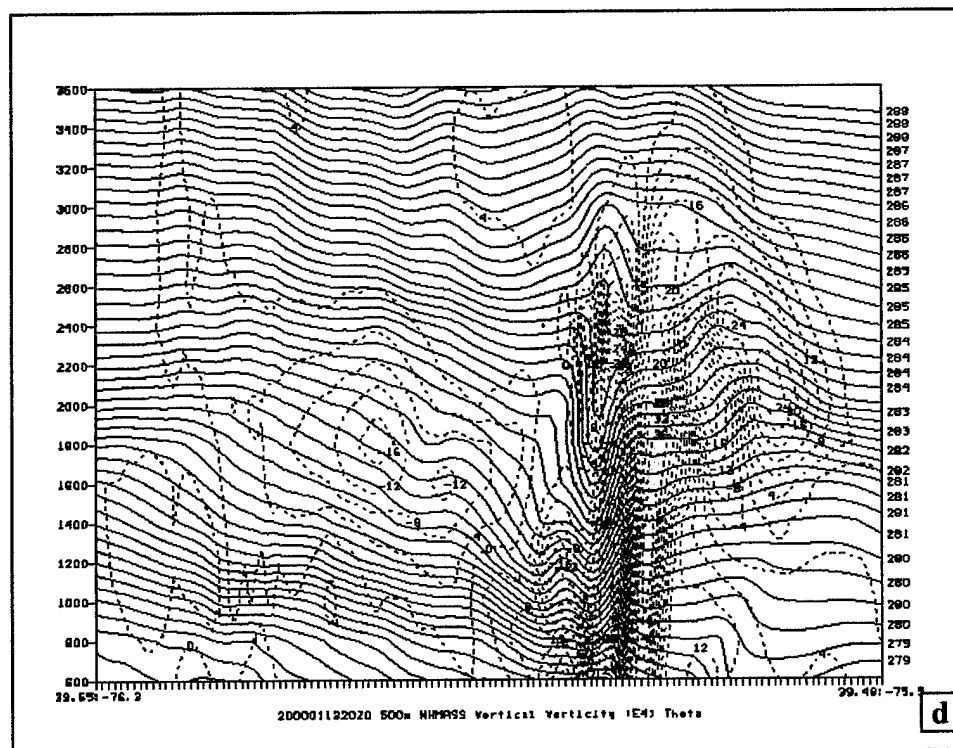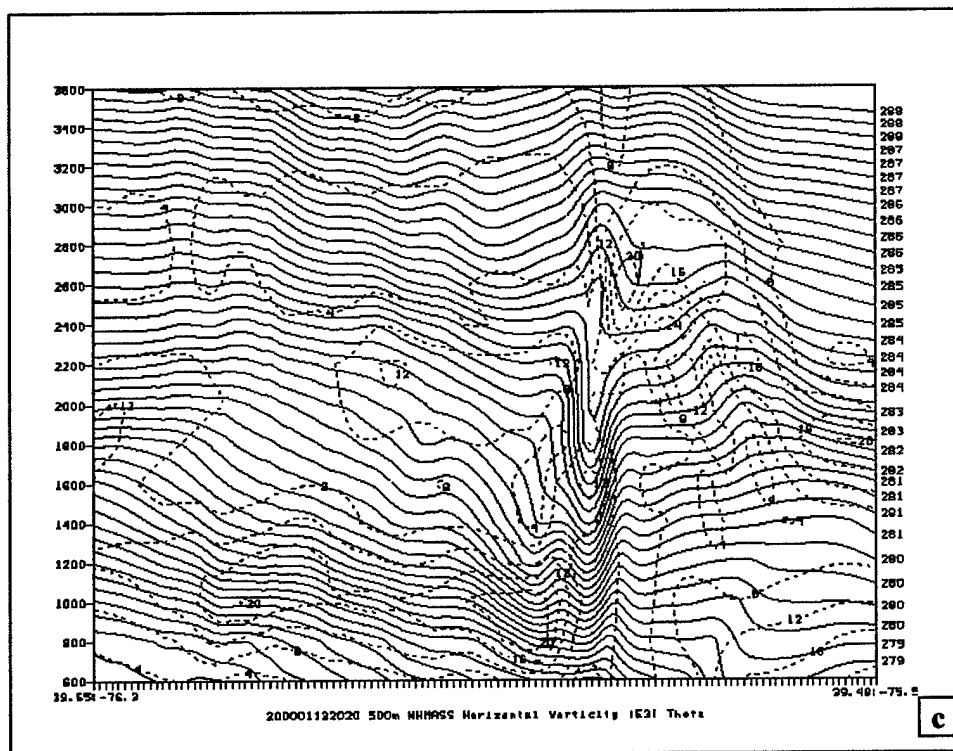
Figure 34. Continued.
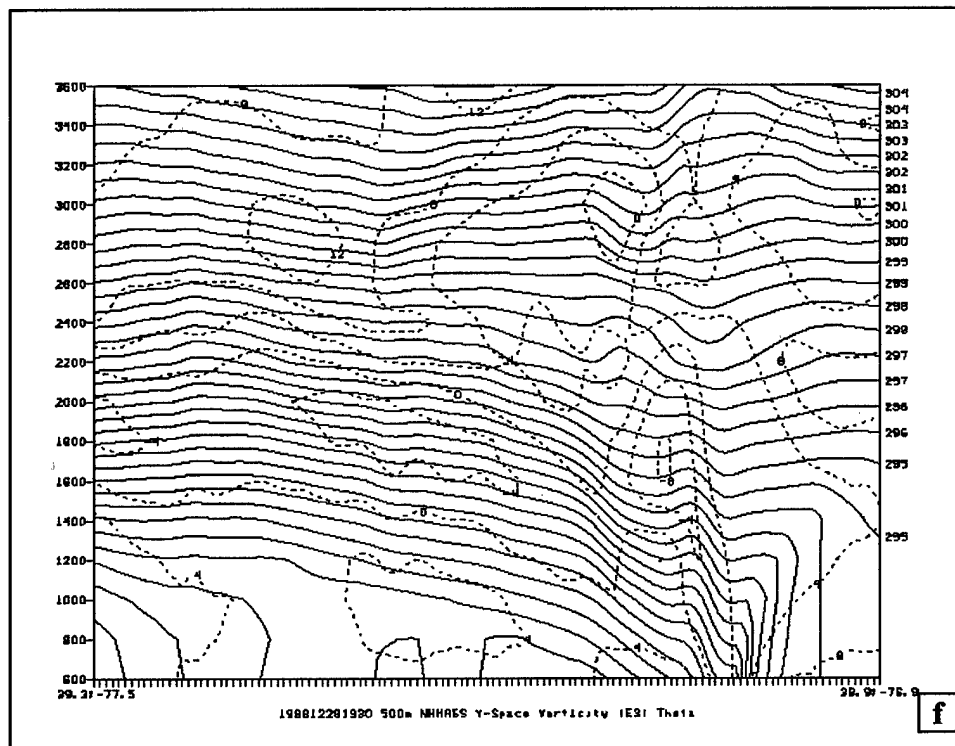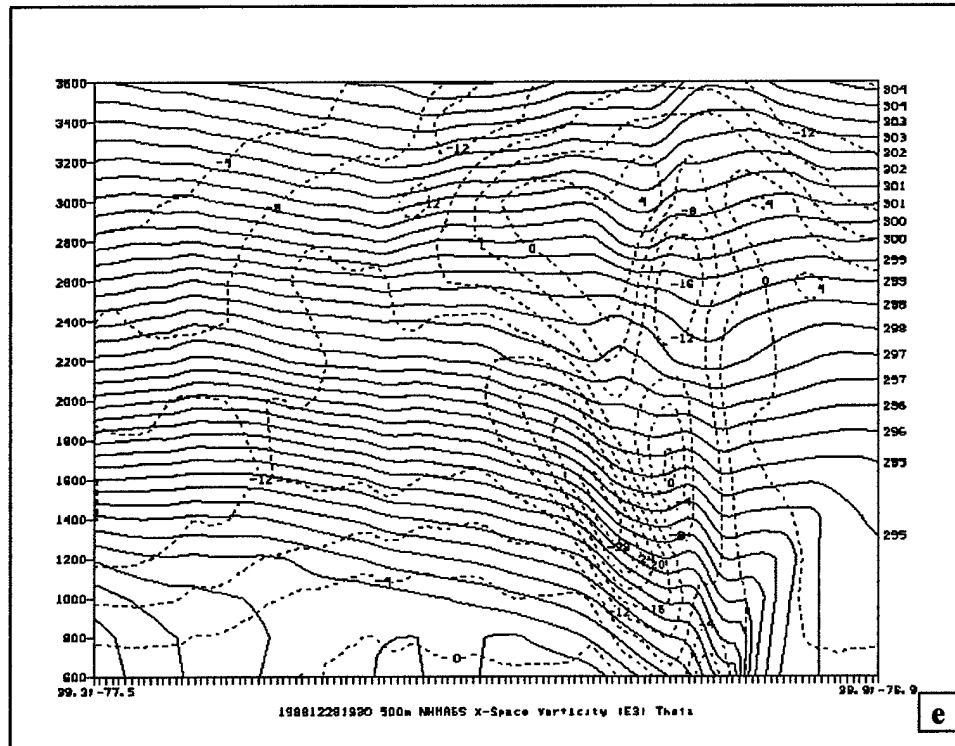
Figure 34. Continued.
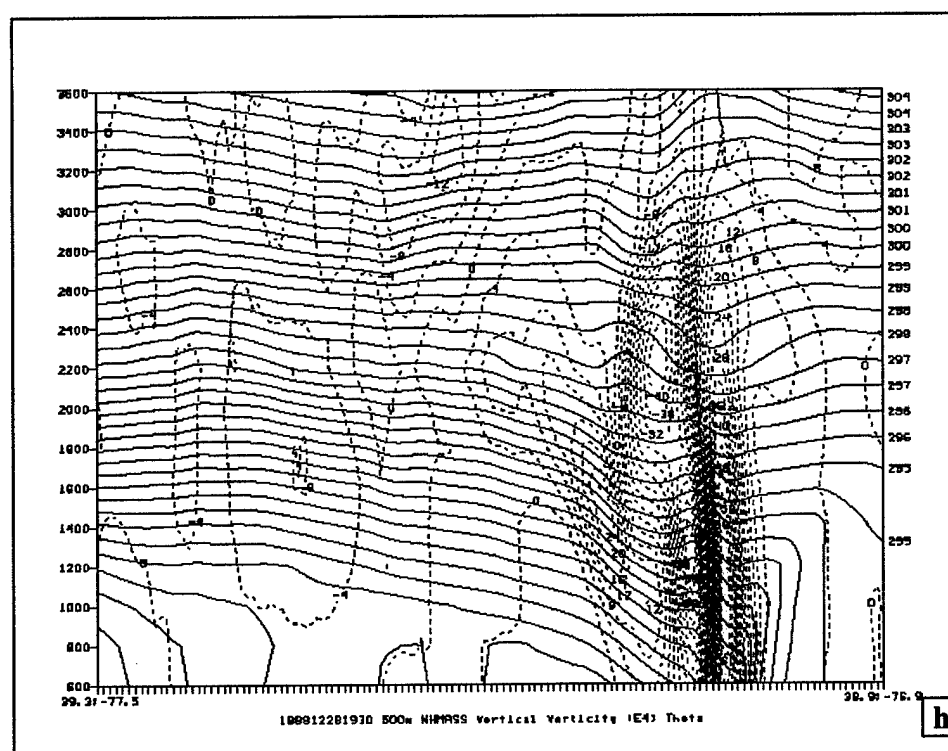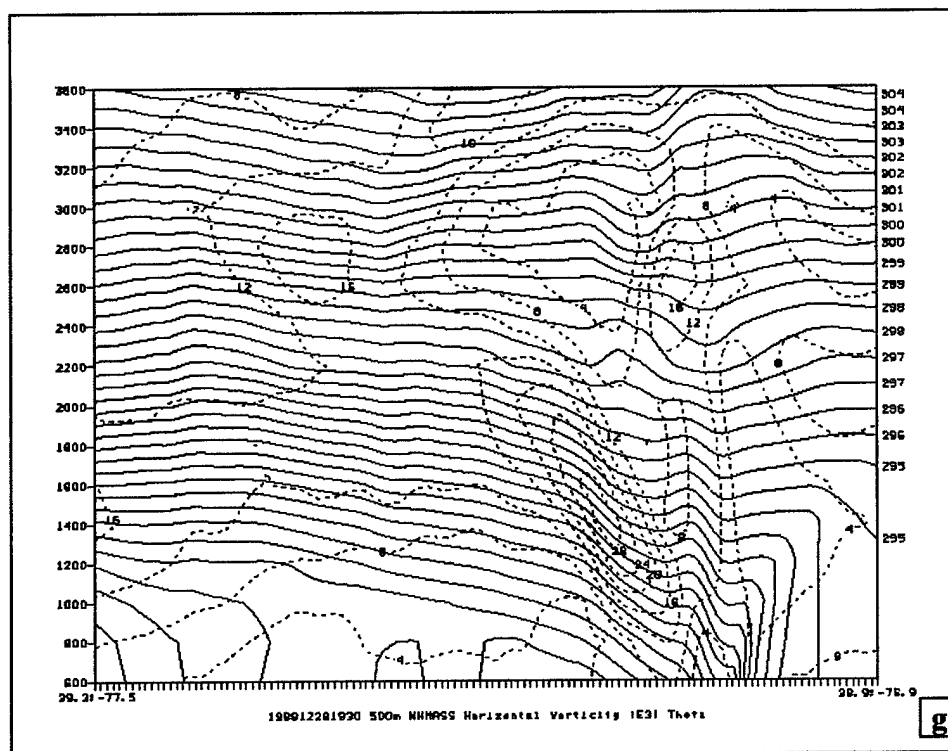
Figure 34. Concluded.

301
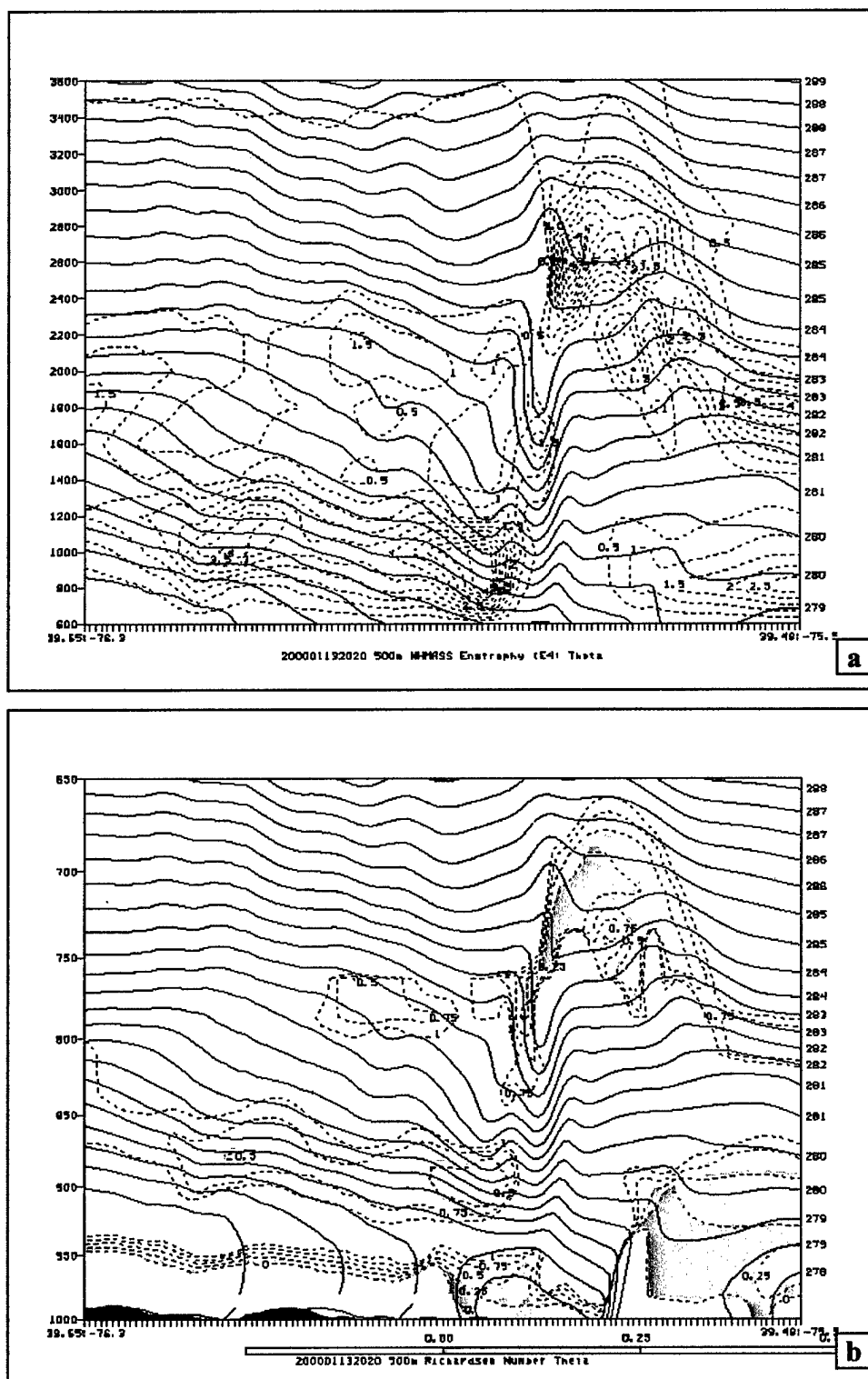
Figure 35. (a) Enstrophy (x $10^{-4} s^{-2}$), (b) Richardson number. Valid 2020 UTC 13 Jan 2000, (c) Enstrophy (x $10^{-4} s^{-2}$), (d) Richardson number. Valid 1930 UTC 28 Dec 1988. Enstrophy > 2 and Ri < 0.5 shaded.
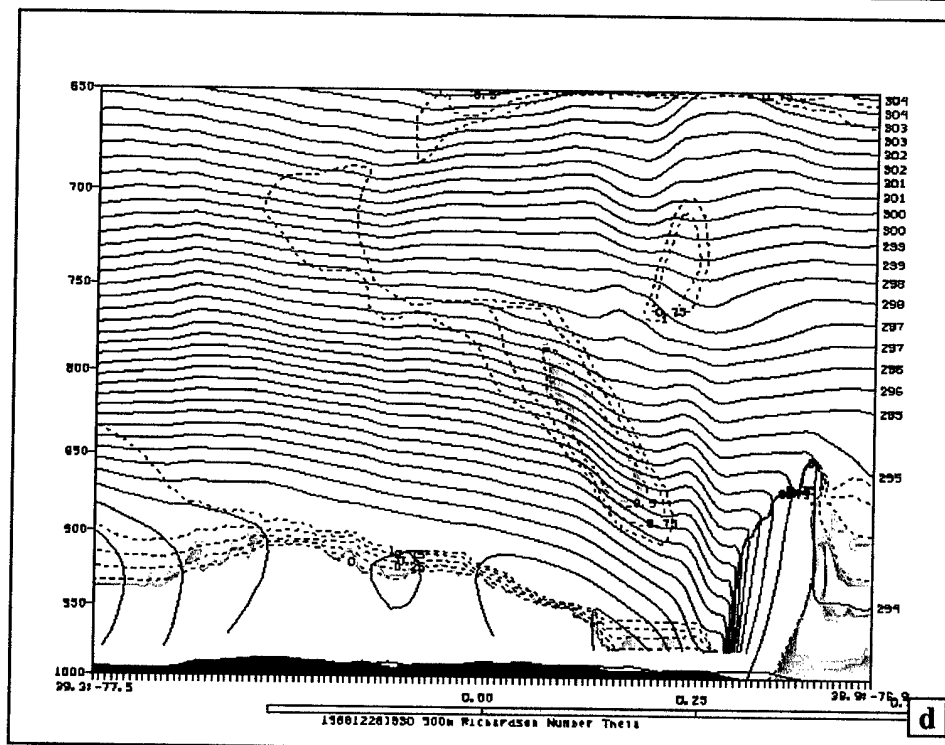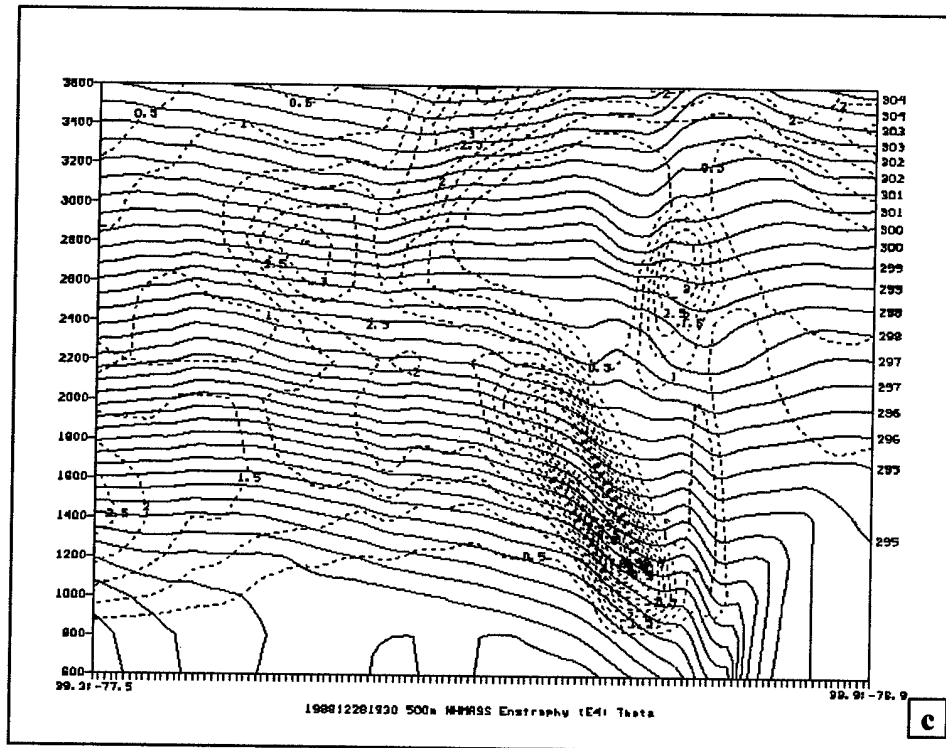
Figure 35. Concluded.

303
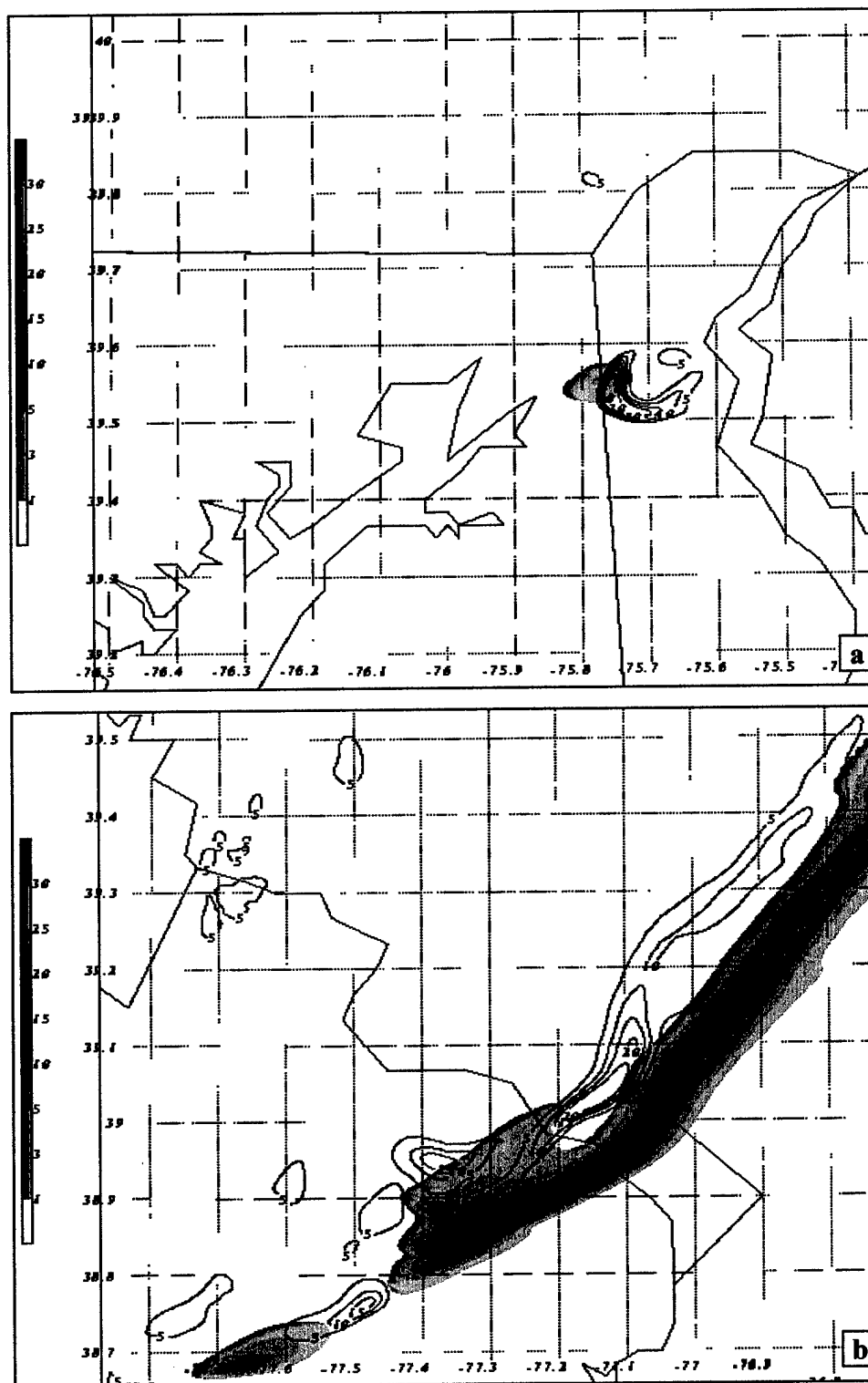
Figure 36. 500-m NHMASS precipitation (mm/hr) and rienstrophy (x $10^{-4}s^{-2}$) at 2600 m (J00) and 1600 m (D88) valid (a) 2020 UTC 13 Jan 2000, (b) 1930 UTC 28 Dec 1988.
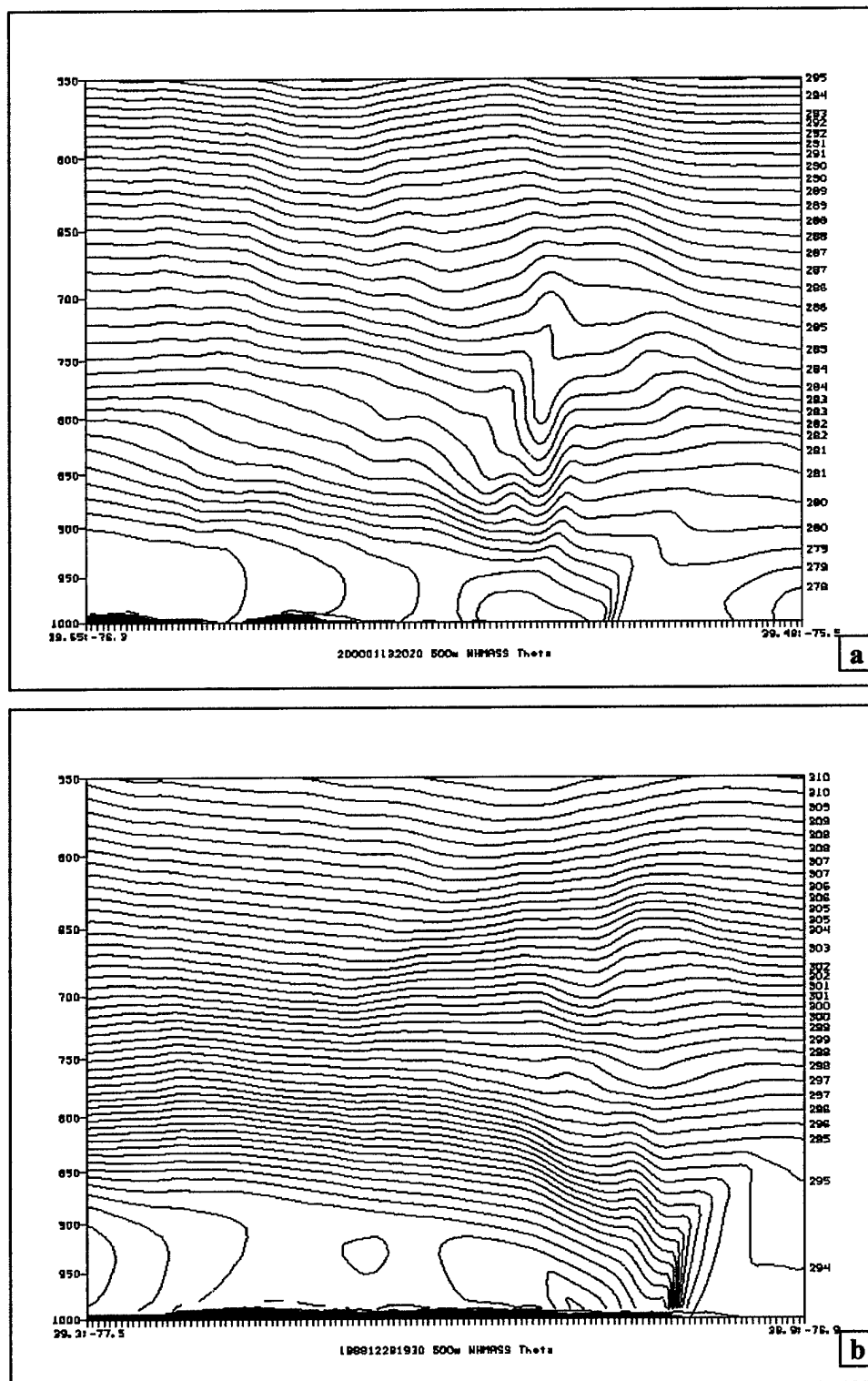
Figure 37. 500-m NHMASS potential temperature (K) cross section valid
(a) 2020 UTC 13 Jan 2000, (b) 1930 UTC 28 Dec 1988.

305
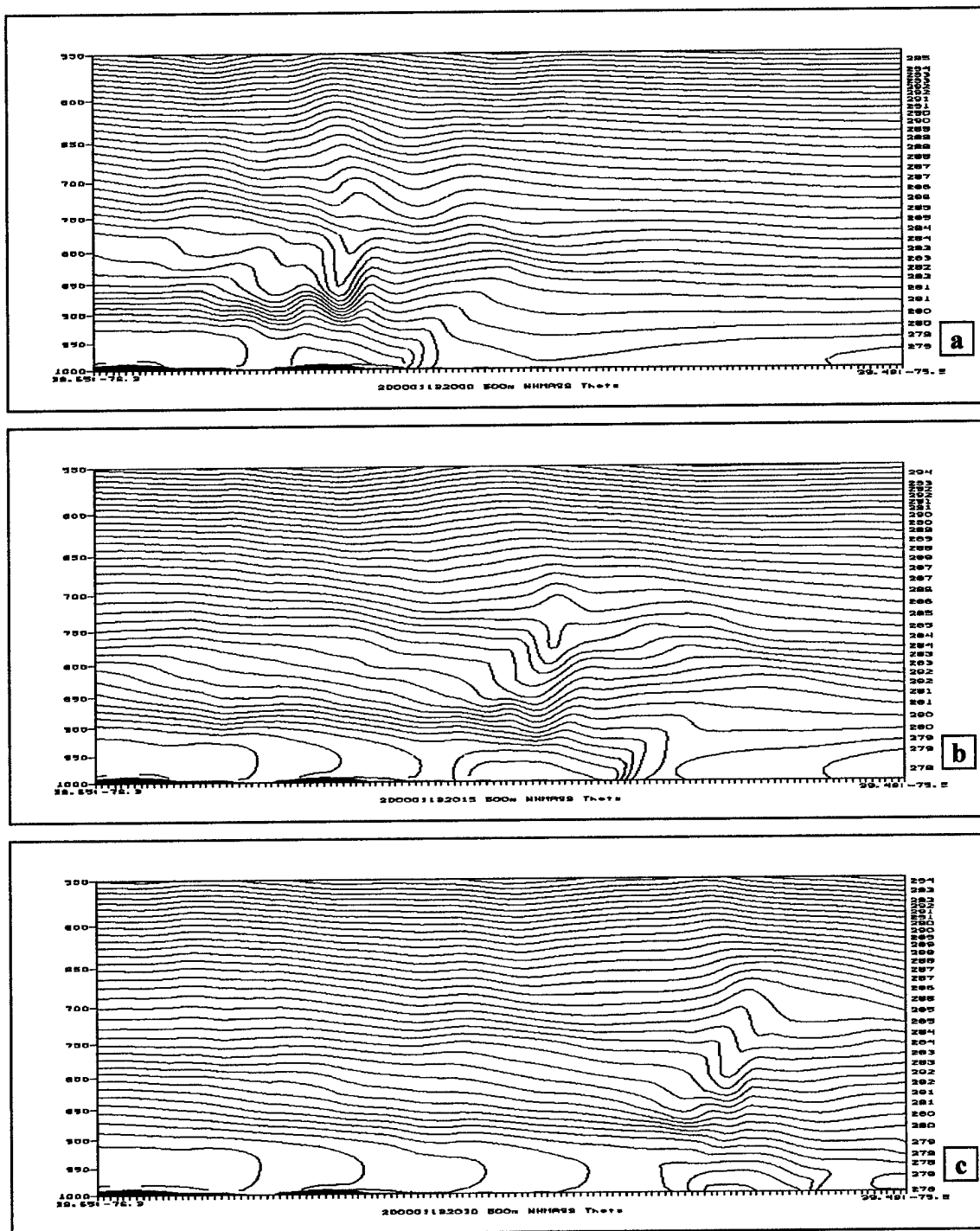
Figure 38. 500-m NHMASS potential temperature (K) cross sections valid (a) 2000 UTC 13 Jan 2000, (b) 2015 UTC 13 Jan 2000, (c) 2030 UTC 13 Jan 2000.
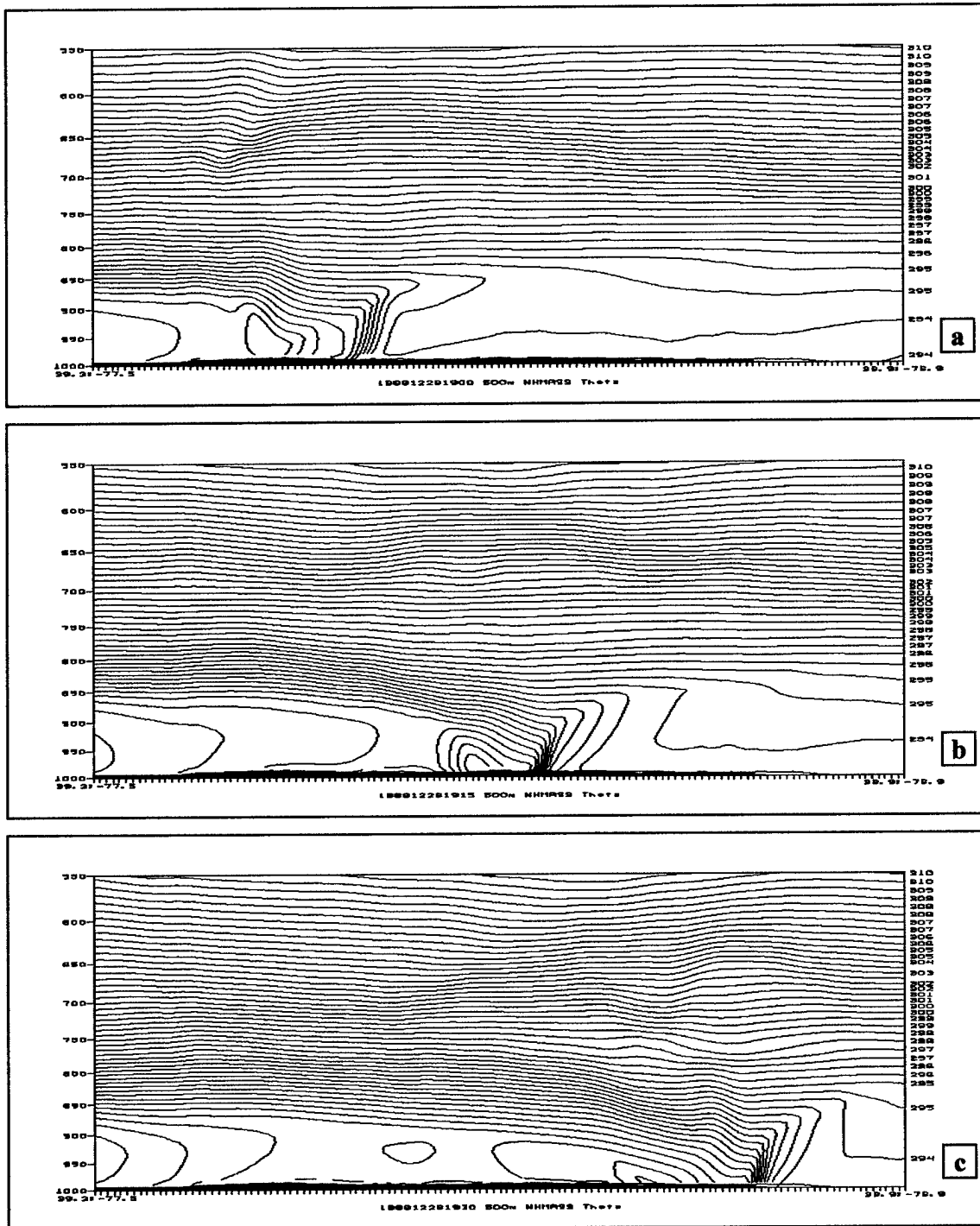
Figure 39. 500-m NHMASS potential temperature (K) cross sections valid (a) 1900 UTC 28 Dec 1988, (b) 1915 UTC 28 Dec 1988, (c) 1930 UTC 28 Dec 1988.
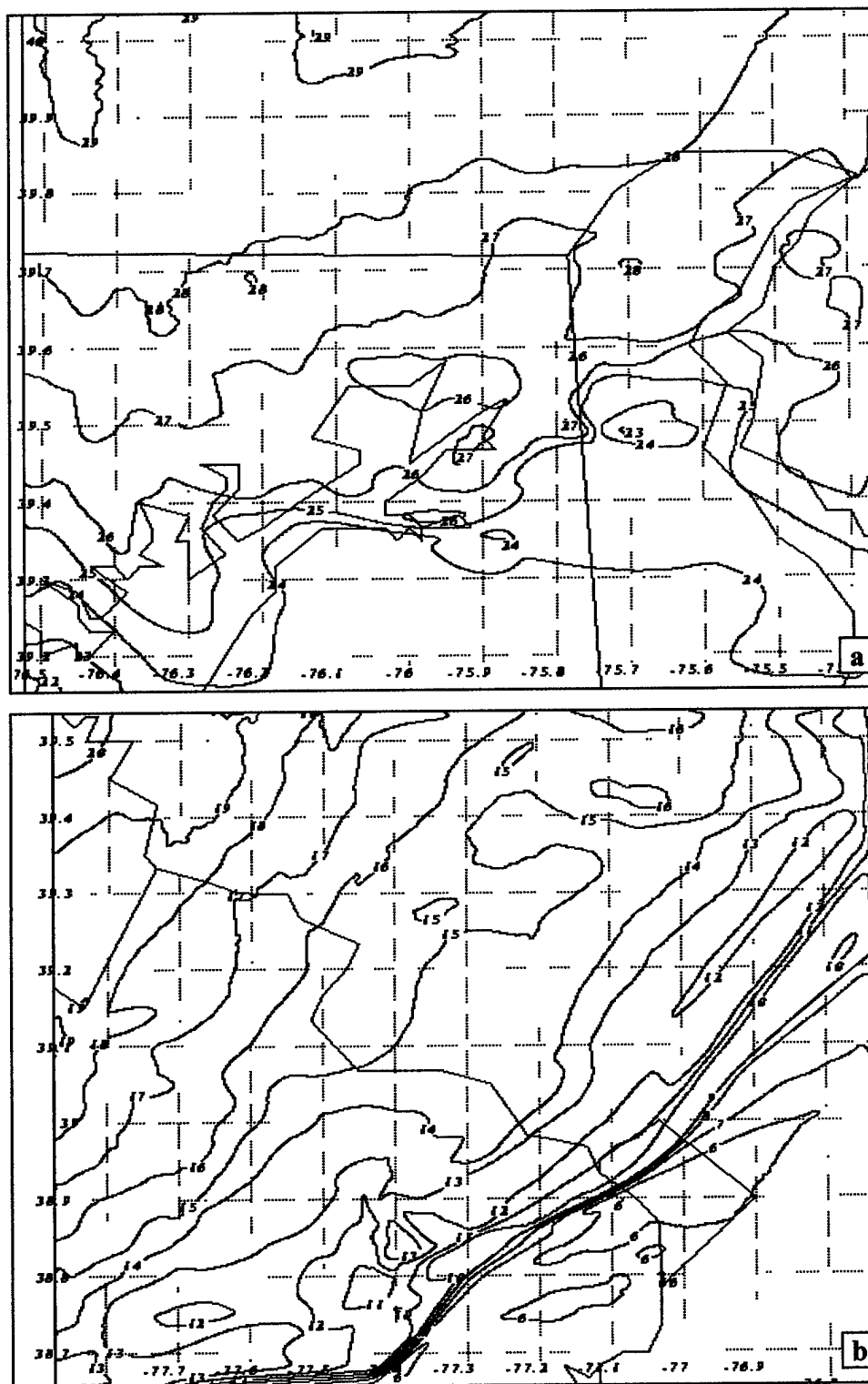
Figure 40. 500-m NHMASS ducting factor (^{0}C) valid (a) 2020 UTC 13 Jan 2000, (b) 1930 UTC 28 Dec 1988.

308

CHAPTER 5

SUMMARY AND CONCLUSIONS

The atmospheric environments prior to and during two cases of widespread low-level turbulence east of the Appalachian Mountains were examined. Analysis indicated both the 28 Dec 1988 (D88) and 13 Jan 2000 (J00) turbulence events occurred in jet entrance regions with upstream curvature and that both occurred in a region of strong cold advection with convection located within 100 km. While these two cases displayed some similarities— particularly at the large scale—the reported intensity of low-level turbulence differed (there was a similar number of low-level turbulence reports, but the percentage of severe and greater turbulence for J00 was more than twice that of D88).

Large-scale wave patterns for these two events were distinctly different. The D88 event displayed a meridional wave pattern with ridging over the East Coast. The J00 wave pattern is more zonal and there is a vortex over Quebec and a southern stream (associated with the subtropical jet (STJ)) which combined to enhance deformation, convergence, and frontogenesis east of the Appalachian Mountains. In addition, large-scale flow in J00 arrived from different directions at different altitudes, whereas flow in D88 was essentially unidirectional at all levels. These wave patterns also affected the orthogonality of wind to terrain—flow for D88 was generally from the southwest (i.e., similar to the orientation of the Appalachians); flow for J00 was much more westerly, and as a result, more perpendicular to the Appalachian Mountains. Jet-front structures in the 24 to 72 hours preceding the turbulence events also displayed differences.

The presence of the STJ and its associated transverse ageostrophic circulations distinguished J00 from D88 and ultimately enabled the advection of low-level warm air

along and east of the Appalachians. As a result of the absence of a STJ in the D88 case, the surge of low-level warm air was essentially coupled to the single polar jet (PJ)-frontal system and its exit region's transverse ageostrophic circulation. As a result, the warmer temperatures in D88 were west of the Appalachian Mountains prior to mountain wave formation and before cold frontal passage on 28 December. There was no warm advection east of the mountains downstream from the advection coupled to the primary large-scale system. In contrast, there were two surges of warm air at low levels in J00, including an additional surge along and east of the Appalachians due to the presence of the STJ. The low-level warm air in J00—east of the Allegheny Mountains advected over the colder surface air (already in place), increased the static stability, and played an important role in the blocking of flow over the elevated terrain as well as the subsequent strength of the isentropic upfold (mid-level cold pool) vital to low-level mesoscale and microscale frontogenesis, convection, and turbulence.

Differences in low-level PV structure and advection patterns were also identified. These differences were associated with the upper-level wave patterns and jet structures present prior to the turbulence events. The low-level PV advection in D88 was primarily associated with the large-scale QG frontal system and the tropopause fold associated with the PJ's left entrance region. This low-level PV maximum was meridional and tracked to the east with the large-scale cold frontal system as it advanced. As with the low-level temperature pattern for D88, there was no significant low-level maximum of PV east of the Appalachians prior to cold frontal passage. On the other hand, two distinct low-level PV maxima were evident for J00. The first, associated with the STJ and the first of two PJ streaks to traverse the region, was coherent and traceable from west Texas (early on 11 Jan

2000) to the northeast through Tennessee and the Carolinas. Ultimately, this PV maximum ended up in south central Pennsylvania in advance of a second low-level PV maximum associated with the left entrance region of the second PJ streak that traversed the region. The presence of the additional low-level PV maximum in J00 helped create an environment high in cyclonic vorticity ahead of the large-scale cold front. These large-scale differences had a direct impact on cold frontal propagation, hydrostatic mountain wave formation, mid-level cold pool generation, strength, and deformation, and the subsequent surface response that initiated convection in these two cases of low-level turbulence east of the Appalachian Mountains.

In the 13 Jan 2000 event, the STJ (acting in concert with the northerly PJ) enabled the transport of warm Mexican Plateau air to the leeside of the Alleghenies early on 13 Jan 2000. This elevated warm layer helped set up a strong inversion on the leeside of the mountains and enabled blocking of the windward front and deflection of the low-level flow around the Allegheny Mountains and aloft downstream. No such inversion was evident downstream of the Alleghenies on 28 Dec 1988 and frontal propagation was more or less unimpeded. This difference, combined with the difference in wave structure and low-level temperature patterns, resulted in a more blocked/dammed regime for J00 and a partially-blocked hydraulic structure for D88.

Internal Froude number computations indicated that as the cold front approached the mountains, flow in D88 was in the supercritical to partially-blocked regime. In contrast, cold frontal propagation in J00 (prior to 13/1700 UTC) was retarded as it crossed the mountains. Froude number computations placed J00 near the junction of the sub-critical, completely-blocked, to partially-blocked regime. Frontal propagation was unimpeded in D88 but was

311

retarded in J00. Additionally, the strength of the hydrostatic mountain waves formed and the resultant downstream isentropic upfolds generated in these two events varied substantially (in large part due to the larger-scale differences in wind and temperature structure on both sides of the Alleghenies).

Hydrostatic mountain waves were observed for both events. Cross-mountain flow on 28 Dec 1988 resulted in a mountain wave with the downstream upfold located near the lee slope due to southwesterly flow at mountain level prior to frontal passage. Relatively strong cross-mountain flow on 13 Jan 2000 resulted in a more vigorous mountain wave with concomitant upslope upfold, downslope downfold, and downstream isentropic upfold (mid-level cold pool). Consequently, and enhanced by the strong downstream inversion, the mid-level (700 hPa) cold pool is more significant and located farther downstream in J00 than in D88.

The stronger downstream mid-level cold pool resulted in a deeper katafront structure and stronger, downstream pressure rises in advance of the large-scale frontal system for J00. As the large-scale jet crossed above the Alleghenies, it acted on (and deformed) the mid-level cold pool and created an upper-level cold front in advance (downstream) of the retarded surface cold front. The mid-level cold pool on 28 Dec 1988 was much weaker and situated closer to the large-scale cold advection and trough—and had no distinct effect of its own.

The mid-level cold pool on 13 Jan 2000 resulted in surface pressure rises to the lee of the Alleghenies—downstream from those associated with the large-scale system. As a result of the strong downstream mid-level cold pool and subsequent surface pressure rises, the low-level mass increase in south central Pennsylvania (east of the Alleghenies) resulted in a low-level cold surge (edgewave-like feature) that surged to the south and east and tightened the

312

surface temperature gradient—ultimately merging with warm air from the south. This surface cold surge resulted in enhanced convergence, frontogenesis, and cellular convection near the Pennsylvania-Maryland border. No such north-to-south moving cold surge was present in the 28 Dec 1988 event as surface pressure rises were tied to the large-scale (west-to-east moving) surface cold front and PJ-entrance region circulations (and tropopause fold), behind the primary cold front and not downstream.

The combination of the mid-level cold pool, leeside warm air, and low-level cold surge in space and time acted to enhance frontogenesis in a scale contraction process near the accident location in J00. No such combination existed in D88 as there was no discernible mid-level cold pool or surface cold surge in advance of the large-scale cold front. Forcing in D88 was tied to the large-scale frontal system and not closely associated with a mountain-induced mid-level cold pool (and resultant surface response) as in J00. Additionally, as a result of the downstream mid-level cold pool on 13 Jan 2000, the J00 frontal structure is essentially forward-sloping (i.e., a katafront) as opposed to the traditional rearward-sloping (anafront) structure present in D88. Although friction and terrain effects played an important role in retarding surface features and allowed the upper-level system to advance, the mid-level cold pool (isentropic upfold) clearly aided this process in J00. These differences in frontal structure affect the initiation of convection and resultant vorticity patterns east of the Appalachian Mountains.

We investigated the convective initiation and the role of convection, frontal contraction, and vorticity effects (to include vortex tube formation) on low-level turbulence east of the Appalachian Mountains. A thorough comparison between two cases of convectively-induced low-level turbulence was made and an index incorporating the three-

313

dimensional vorticity, vertical wind shear, and static stability was suggested to help better identify regions where turbulence would be expected.

Convection in the 28 Dec 1988 case was lineal in extent and closely linked to the larger-scale frontal system and subsequent scale contractions of the front due to subsidence associated with a thermally-direct jet-entrance circulation and potentially enhanced by a tightened temperature gradient due to precipitation-induced evaporative cooling behind the rearward-sloping cold front. Our simulations indicated the terrain, and in particular the three elevated peaks of the Allegheny, Shenandoah, and Blue Ridge Mountains, resulted in intermittent increases in upward vertical motion and enhanced precipitation as hydraulic jumps formed to the lee of the mountain peaks. The effect of terrain on convective initiation for D88 was more indirect and the resultant convection and associated CIT and vorticity patterns substantially different than that of the 13 Jan 2000 event.

The convection in J00 was detached from the larger-scale system and aligned with the phasing of the downstream mesoscale phenomena (mid-level cold pool, leeside trough, and surface cold surge (edgewave)). Additionally, the impact of terrain on the convection was more direct (the terrain was essentially responsible for each of the mesoscale features that eventually combined to initiate the convection). The Allegheny Mountain-induced isentropic upfold (mid-level cold pool) as well as the leeside trough and surface cold surge all owe their existence to terrain interactions and it was the phasing of these phenomena that resulted in the convection in J00. No such combination of features occurred in D88. In J00, the combination of the mid-level cold pool, surface warm tongue, and surface cold surge resulted in enhanced vertical motion and convection along the boundary of their intersection—initially in south-central Pennsylvania through Maryland, and ultimately in the Delaware-

314

New Jersey region in the vicinity of the severe low-level turbulence report. The initiation of convection in J00 due to the described phasing process conformed to the presented hypothesis in a much more coherent fashion than did that of D88—where the convection was essentially attached to the convergence and vertical motion associated with the surface cold front (and larger-scale jet-front system) and enhanced by low-level terrain effects. These differences affected the momentum and vorticity fields in different ways.

An analysis of the deformation and three-dimensional vorticity structure in the environment surrounding the convection in both cases was performed. The deformation, horizontal and vertical vorticity, enstrophy, and vorticity tendency maxima for the 28 Dec 1988 event all occurred along and upstream (west) of the lineal convection accompanying the surface anafront. On the other hand, the deformation for J00 was largest in a large arc encompassing and surrounding the cellular convection and was much broader in extent than the maxima in D88. Additionally, the area of large deformation covered a significant region outside of the convection—deformation maxima in D88 were much more closely aligned with the convection. This alignment could have an impact on turbulence reporting as flight inside or through convection is rare. Horizontal and vertical vorticity and enstrophy maxima patterns for J00 were circular (arc-like) and broad, not elongated as in D88. Horizontal vorticity maxima were also primarily located downstream from the convection as opposed to upstream as in D88—likely due to the increased downstream vertical shear due to the katafront (forward-sloping) structure in J00 compared to the upstream maximum accompanying the anafront (rearward-sloping) structure in D88. Horizontal vorticity maxima in J00 were more than 1.5 times as large and enstrophy nearly 1.8 times as large as those in D88. A comparison of the various vorticity tendency terms between J00 and D88

indicated similar differences in orientation and magnitude. The various terms in the 28 Dec 1988 case were primarily lineal in extent and aligned along and upstream from the surface anafront and convection. The vorticity tendency terms in the 13 Jan 2000 case were arc-like in appearance and located primarily downstream from the surface katafront and convection. In addition, the convergence and tilting terms for J00 were more than three times larger and the overall vorticity tendency nearly four times larger than those for D88. The difference in magnitude of these parameters as well as the orientation and location of these maxima likely played a role in the higher turbulence intensities reported on 13 Jan 2000. In order to diagnose these events further, parameters traditionally associated with turbulence were computed and compared for both cases.

An analysis of the turbulent kinetic energy (TKE) revealed patterns similar to those of vorticity, enstrophy, and vorticity tendency. TKE maximized primarily upstream of the convection in D88 and downstream of the convection in J00. Similar results were observed for Richardson number (Ri). The majority of Ri minima were arc-like in appearance and located downstream from convection in J00 and were elongated and upstream from the surface anafront and convection in D88. Additionally, Ri was consistently lower for J00 as several contours of Ri < 0.25 were observed for J00 and none for D88.

A comparison of Ri and enstrophy revealed a remarkable correlation—both in orientation and inverse magnitude. Enstrophy maxima were essentially coincident with minima of Richardson number. The ratio of these parameters (enstrophy/Ri) should maximize in regions where spin, vortex tube potential, and the ratio of vertical wind shear to static stability are largest (i.e., regions ripe for turbulence). This ratio, referred to here as rienstrophy, is offered as a potentially valuable index for identifying turbulence potential. As

316

with the parameters previously discussed, rienstrophy maxima were elongated, lineal, and located upstream of the convection and surface cold front in D88 (although these maxima are much more focused that those provided by any of the previous parameters). Maxima of this ratio for J00 are similarly focused and as with the high concentrations of vorticity, enstrophy, vorticity tendency, TKE, and Ri minima, are arc-like and located downstream from the convection and surface katafront. Maxima for J00 were two to five times larger than those for D88 despite the fact that the convection was much more intense in D88 as inferred from precipitation rates. In addition, the location of the J00 maxima (in the vertical) occurred in the vicinity of an apparent breaking wave.

Wave patterns for these two cases were significantly different as well. The convectively-induced gravity (buoyancy) wave in J00 appeared non-dispersive and traveled on the surface katafront, which acted as a moving wave duct. Wave activity in D00 was transient and dispersive. The wave ducting factor was computed for both cases and that of J00 far exceeded the minimum required for sufficient wave ducting (throughout the entire domain), whereas the ducting factor computed for D88 was marginal upstream of the surface front and below the threshold downstream from the front.

The smaller-scale differences between two cases of low-level CIT east of the Appalachian Mountains were detailed. Results showed that differences at the larger scales significantly influenced the initiation of convection, frontal slope, deformation, vorticity and vorticity tendency, and ultimately turbulence downscale. The 13 Jan 2000 event demonstrates the potential for high concentrations of vorticity (implied vortex tubes), wave breaking, and severe turbulence that fairly weak convection can have given the scenario set forth in the hypothesis. *Key to these differences was the more intense terrain-induced*

317

mesoscale frontal coupling in the vertical and its implications for rapid fluctuations of TKE.

318

REFERENCES

Attié, J.L., A. Druilhet, P. Durand, and B. Bénech, 1997: Two-dimensional structure of mountain wave observed by aircraft during the PYREX experiment. *Ann. Geophysicae*, **15**, 823-839.

Bender, Morris A., and Hans Panofsky, 1976: Temperature gradients and clear-air turbulence probabilities. *Final Report, National Environmental Satellite Service*, NOAA, 18pp.

Browning, K.A., and T.W. Harrold, 1970: Air motion and precipitation growth at a cold front. *Quart. J. Roy. Meteor. Soc.*, **96**, 369-389.

Buzzi, A., and S. Tibaldi, 1978: Cyclogenesis in the lee of the Alps: A case study. *Quart. J. Roy. Meteor. Soc.*, **104**, 271-287.

Charney, J.J., and J.M. Fritsch, 1999: Discrete frontal propagation in a non-convective environment. *Mon. Wea. Rev.*, **127**, 2083-2101.

Chen, C., C.H. Bishop, G.S. Lai, and W.K. Tao, 1997: Numerical simulations of an observed narrow cold-frontal rainband. *Mon. Wea. Rev.*, **125**, 1027-1045.

Colle, B.A., and C.F. Mass, 1995: The structure and evolution of cold surges east of the Rocky Mountains. *Mon. Wea. Rev.*, **123**, 2577-2610.

Cowen, R., 1998: Clearing the air about turbulence. *Weatherwise*, **51**, 24-28.

Dutton, M.J.O., 1980: Probability forecasts of clear-air turbulence based on numerical model output. *Meteor. Mag.*, **109**, 293-310.

Ellrod, Gary P., 1985: Detection of high level turbulence using satellite imagery and upper air data. *NOAA Tech. Memo NESDIS 10*, 30pp.

Ellrod, G.P., and D.I. Knapp, 1992: An objective clear-air turbulence forecasting technique: Verification and operational use. *Wea. Forecasting*, **7**, 150-165.

Endlich, Roy M., 1964: The mesoscale structure of some regions of clear-air turbulence. *J. Appl. Met.*, **3**, 261-276.

FAA, cited, 2002: Safety of flight: Meteorology—Thunderstorm flying. Aeronautical Information Manual, The Federal Aviation Adminstration.

Fairall, C.W., A.B. White, and Dennis W. Thomson: A stochastic model of gravity-wave-induced clear-air turbulence. *J. Atmos. Sci.*, **48**, 1771-1790.

Hamilton, D.W., Y-L Lin, R.P. Weglarz, and M.L. Kaplan, 1998: Jetlet formation from diabatic forcing with applications to the 1994 Palm Sunday tornado outbreak. *Mon. Wea. Rev.*, **126**, 2061-2089.

Hopkins, Robert H., 1977: Forecasting techniques of clear-air turbulence including that associated with mountain waves. *WMO Tech. Note 155*, 31 pp.

Howard, L.N., 1961: Note on a paper of John Miles. *J. Fluid Mech.*, **10**, 509-512.

Huffman, Allan, 2001: Analysis of the synoptic and mesoscale environment for selected cases of severe aircraft turbulence. Masters Thesis, North Carolina State University, 141 pages.

James, P.K., and K.A. Browning, 1979: Mesoscale structure of line convection at surface cold fronts. *Quart. J. Roy. Meteor. Soc.*, **105**, 371-382.

Jinliang, Liu, and Li Jianzhong: Diagnostic analysis of the dynamics and numerical simulation of clear air turbulence. *Acta Met. Sinica*, **10**, 331-345.

Kain, J.S., and J.M. Fritsch, 1993: Convective parameterization for mesoscale models: The Kain-Fritsch Scheme. *The Representation of Cumulus Convection in Numerical Models, Meteor. Monogr., No. 46*, Amer. Meteor. Soc., 165-170.

Kaplan, M.L., and V.M. Karyampudi, 1992a: Meso-beta scale numerical simulations of terrain drag-induced along-stream circulations. Part I: Midtropospheric frontogenesis. *Meteorol. Atmos. Phys.*, **49**, 133-156.

Kaplan, M.L., and V.M. Karyampudi, 1992b: Meso-beta scale numerical simulations of terrain drag-induced along-stream circulations. Part II: Concentration of potential vorticity within dryline bulges. *Meteorol. Atmos. Phys.*, **49**, 157-185.

Kaplan, M.L, R.P. Weglarz, Y.-L. Lin, D.B. Ensley, J.K. Kehoe, and D.S. DeCroix, 1999: A Terminal Area PBL Prediction System for DFW. *Preprints, 37th AIAA Aerospace Sciences Meeting and Exhibit, AIAA 99-0983, January 11-14, 1999*, Reno, NV, 27 pp.

Kaplan, M.L., A.W. Huffman, K.M. Lux, J.J. Charney, A.J. Riordan,, and Y-L Lin, submitted Feb 2003 to *Meteorol. Atmos. Phys.*: Characterizing the severe turbulence environments associated with commercial aviation accidents. Part I: A 44 Case study synoptic observational analyses.

Kaplan, M.L., A.W. Huffman, K.M. Lux, J.D. Cetola, J.J. Charney, A.J. Riordan,, Y-L Lin, and K.T. Waight III, submitted Feb 2003 to *Meteorol. Atmos. Phys.*: Characterizing the severe turbulence environments associated with commercial aviation accidents. Part II: Hydrostatic mesoscale numerical simulations of supergradient wind flow and streamwise ageostrophic frontogenesis.

Kaplan, M.L., A.W. Huffman, K.M. Lux, J.D. Cetola, J.J. Charney, A.J. Riordan,, Y-L Lin, and K.T. Waight III, submitted Feb 2003 to *Meteorol. Atmos. Phys.*: Characterizing the severe turbulence environments associated with commercial aviation accidents. Part III: Nonhydrostatic numerical simulations of unbalanced supergradient wind flow and the transformation of streamwise ageostrophic vorticity gradients into horizontal vortex tubes.

Kaplan, M.L., J.J. Charney, K.T. Waight III, K.M. Lux, J.D. Cetola, A.W. Huffman, A.J. Riordan, S.W. Slusser, and Y-L Lin, submitted Feb 2003 to *Meteorol. Atmos. Phys.*: A real-time turbulence model (RTTM) designed for the operational prediction of moderate-severe aviation turbulence environments.

Keller, John. L., and Patrick A. Haines: Case studies of clear air turbulence using the diagnostic Richardson number tendency formulation. *NASA Contractor Report 3378*, 50pp.

Keller, John L., 1986: The physical and empirical basis for a specific clear-air turbulence risk index. *NASA Contractor Report 3971*, 39pp.

Keller, John L., 1990: Clear air turbulence as a response to meso- and synoptic-scale dynamic processes. *Mon. Wea. Rev.*, **118**, 2228-2242.

Kennedy, P.J., and M.A. Shapiro, 1975: The energy budget in a clear air turbulence zone as observed by aircraft. *Mon. Wea. Rev.*, **103**, 650-654.

Kennedy, P.J., and M.A. Shapiro, 1980: Further encounters with clear air turbulence in research aircraft. *J. Atmos. Sci.*, **37**, 986-993.

Knox, John A., 1997: Possible mechanisms of clear-air turbulence in strongly anticyclonic flows. *Mon. Wea. Rev.*, **125**, 1251-1259.

Koch, S.E., and P.J. Kocin, 1991: Frontal contraction processes leading to the formation of an intense narrow rainband. *Meteorol. Atmos. Phys.*, **46**, 123-154.

Koch, S.E., and C. O'Handley, 1997: Operational forecasting and detection of mesoscale gravity waves. *Wea. Forecasting*, **12**, 253-281.

Lane, T.P., R.D. Sharman, T.L. Clark, and H-M. Hsu, 2003: An investigation of turbulence generation mechanisms above deep convection. *J. Atmos. Sci.*, **60**, 1297-1321.

Lee, David R., Roland S. Stull, and William S. Irvine, 1984: Clear air turbulence forecasting techniques. *AFGWC TN-79/001 (Rev)*, 74pp.

Lin, Y-L., R.D. Farley, and H.D. Orville, 1983: Bulk parameterization of the snow field in a cloud model, *J. Climate Appl. Meteor.*, **22**, 1065-1092.

Lin, Y-L., N-H., Lin, and R.P. Weglarz, 1992: Numerical modeling studies of lee mesolows, mesovorticies and mesocyclones with application to formation of Taiwan mesolows. *Meteorol. Atmos. Phys.*, **49**, 43-67.

Lindzen, R.S., and K.K. Tung, 1976: Banded convective activity and ducted gravity waves. *Mon. Wea. Rev.*, **104**, 1602-1617.

McCann, D.W., 1998: Is clear air turbulence caused by wind shear? *Unpublished manuscript*, 31pp.

McCann, D.W., 1999: A simple turbulent kinetic energy equation and aircraft boundary layer turbulence. *Nat. Wea. Digest*, **23**, 13-19.

Miles, J.W., 1961: On the stability of heterogeneous shear flows. *J. Fluid Mech.*, **10**, 496-508.

Murakami, T., and H. Nakamura, 1983: Orographic effects on cold surges and lee-cyclogenesis as revealed by a numerical experiment. Part II: Transient aspects. *Journal of the Meteorological Society of Japan*, **61**, 547-567.

Peltier, W.R., and T.L. Clark, 1979: The evolution and stability of finite amplitude mountain waves—II: Mountain wave drag and severe downslope windstorms. *J. Atmos. Sci.*, **36**, 1499-1529.

Pepler, S.J., G. Vaughan, and D.A. Hooper, 1998: Detection of turbulence around jet streams using a VHF radar. *Q.J.R. Meteorol. Soc.*, **124**, 447-462.

Queney, P., 1948: The problem of airflow over mountains. A summary of theoretical studies. *Bull. Amer. Meteorol. Soc.*, **29**, 16-26.

Reed, R.J., and K.R. Hardy, 1972: A case study of persistent, intense clear air turbulence in an upper-level frontal zone. *J. Appl. Met.*, **11**, 541-549.

Reiter, E.R., and A. Nania, 1964: Jet-stream structure and clear-air turbulence (CAT). *J. Appl. Met.*, **3**, 247-260.

Rutledge, S.A., and P.V. Hobbs, 1983: The mesoscale and microscale structure and organization of clouds and precipitation in midlatitude cyclones. VIII: A model for the "seederfeeder" process in warm-frontal rainbands. *J. Atmos. Sci.*, **40**, 1185-1206.

Smith, R.B., 1976: The generation of lee waves by the Blue Ridge. *J. Atmos. Sci.*, **33**, 507-519.

Smith, R.B., 1979: The influence of the mountains on the atmosphere. *Adv. Geophys.*, **21**, 87-230.

Smith, R.B., 1982a: Synoptic observations and theory of orographically disturbed wind and pressure. *J. Atmos. Sci.*, **39**, 60-70.

Smith, R.B., 1982b: A differential advection model of orographic rain. *Mon. Wea. Rev.*, **110**, 306-309.

Smith, R.B., 1989: Hydrostatic airflow over mountains. *Adv. Geophys.*, **31**, 1-41.

Starr, J.R., and B. Kemp, 1974: Mesoscale structure of jet streams and associated clear-air turbulence. *Meteor. Mag.*, **103**, 313-329.

Stull, R.B., 1988. *An Introduction to Boundary Layer Meteorology*. Kluwer Academic Pub., Boston.

Sumi, A., 1985: A study of cold surges around the Tibetan Plateau by using numerical models. *Journal of the Meteorological Society of Japan*, **63**, 377-396.

Tilley, J.S., 1990: On the application of edge wave theory to terrain-bounded cold surges: A numerical study. PhD Thesis, The Pennsylvania State University, University Park, PA, and NCAR, Boulder, CO, 353pp.

Uccellini, L.W., K.F. Brill, R.A. Petersen, D. Keyser, R. Aune, P.J. Kocin, and M. des Jardins, 1986: A report on the upper-level wind conditions preceding and during the shuttle Challenger (STS 51L) explosion. *Bull. Amer. Met. Soc.*, **67**, 1248-1265.